Étude expérimentale des interactions aérodynamiques pneu/véhicule

Yifei Wang

To cite this version:

Yifei Wang. Étude expérimentale des interactions aérodynamiques pneu/véhicule. Autre. ISAE-ENSMA Ecole Nationale Supérieure de Mécanique et d'Aérotechique - Poitiers, 2019. Français. NNT : 2019ESMA0002 . tel-02157958v1

HAL Id: tel-02157958

https://theses.hal.science/tel-02157958v1

Submitted on 17 Jun 2019 (v1), last revised 17 Jun 2019 (v2)

THÈSE

Pour l'obtention du grade de

DOCTEUR DE L'ÉCOLE NATIONALE SUPÉRIEURE DE MÉCANIQUE ET D'AÉROTECHNIQUE

(Diplôme National - Arrêté du 25 mai 2016)

École Doctorale :
Sciences et Ingénierie en Mécanique, Matériaux, Energétique et Aéronautique

Secteur de Recherche : MÉCANIQUE DES MILIEUX FLUIDES

Présentée par

Yifei WANG

Experimental study of wheel-vehicle aerodynamic interactions

Directeur de thèse : **M. Jacques Borée**

Co-encadrant : **M. Christophe Sicot**

Soutenue le 29 Mars 2019 devant la Commission d'Examen

JURY

Rapporteurs:	
S. Aubrun	Professor, Centrale Nantes, France
M. Passmore	Professor, Loughborough University, UK
Membres du jury:	
L.-E. Brizzi	Professor, University of Poitiers, France
V. Herbert	Ingénieur-Docteur, PSA Peugeot Citröen, France
T. Castelain	Maître de conférence, University of Lyon, France
M. Grandemange	Ingénieur-Docteur, **Référent Cifre**, MFP Michelin, France
J. Borée	Professor, ISAE-ENSMA, France
C. Sicot	Maître de conférence, ISAE-ENSMA, France

Acknowledgements

On this moment of submission of my thesis, I would like to thank all those whom I have come across in this path of my journey, who have helped me and from whom I have learnt to live the life.

First and foremost, I am deeply grateful for my supervisor J. Borée. It was him who inspired me to pursue my education in France as well as my research work in fluid mechanics. I would also like to express my sincerest gratitude to my supervisors C. Sicot and M. Grandemange for their patient teaching, guidance, support and trust. All of my supervisors have been tremendous mentors for me. Their insight into the subject has always made me realize and understand the subject in a broader perspective. Their advice on both research as well as my career have been invaluable.

I am indebted to Michelin for its funding and technical support. Particularly, without the reduced-scale tires made by Michelin, it would be impossible to conduct the experimental studies in such realistic conditions.

I would also like to thank the rest of my thesis committee: Prof. M. Passmore, S. Aubrun, L.-E. Brizzi, T. Castelain and Dr. V. Herbert. I want to thank them for letting my defense be an enjoyable moment, and for their brilliant comments and suggestions, which allow me to widen my research from various perspectives.

I am deeply grateful for the help of J.M. Breux and F. Paillé, with whom I have performed my experiments. Without their contribution to the design and implementation of the experimental set-ups, this thesis would not have been completed. Additional thanks to R. Bellanger and P. Braud for the implementation of laser techniques, and to M. Rossard, B. Robert, O. Delage for their assistance with the wind tunnel equipment.

Thanks to the following colleagues from the department, for the countless invaluable discussions and at times, motivation, throughout: R. Li, Y. Liu, X. Wang, Y. Haffner, A. Carusone, etc.

Last, and most of all, thanks to my family for being there for me, even far away in distance. They have always encouraged me, which enables me to get to where I am today. Thanks to my partner M. Boisdron for always supporting me and providing moments of well-needed respite from the occasionally stressful work.

Résumé étendu

La réduction de la traînée aérodynamique des véhicules terrestres est devenue un enjeu crucial en raison des normes strictes des émissions de CO_2. Ce travail se focalise sur les roues et leur interaction aérodynamique avec le véhicule. A titre indicatif, entre 20% à 40% de la traînée aérodynamique est originaire de la traînée des roues et des passages de roue. De ce fait, l'optimisation du système roue--passage de roue--véhicule nous offre la possibilité d'une réduction substantielle de la traînée aérodynamique ainsi que de la consommation d'énergie. Pour mieux comprendre l'interaction entre les roues et le véhicule, les expérimentations sur une maquette à l'échelle 2/5ième équipée d'un diffuseur et de pneus Michelin sont effectuées. La géométrie du véhicule, basée sur le modèle ASMO, a été modifiée précédemment à ce travail afin d'obtenir un angle d'attaque de l'écoulement sur les roues avant et un équilibre du sillage réaliste en présence de quatre roues tournantes. Cette configuration a servi de référence dans le cadre de cette étude.

Chapitre 1

Avec le durcissement des objectifs de réduction des émissions de CO_2 et autres gaz à effet de serre, les constructeurs automobiles du monde entier cherchent les moyens de rendre les véhicules plus économes en énergie et plus écologiques. Le système pneumatique constitue une piste de recherche prometteuse car il joue un rôle essentiel non seulement dans la performance du véhicule et la sécurité, mais aussi dans la consommation d'énergie. En effet, leur contribution représente entre 20% à 40% de la traînée aérodynamique totale, et peut ainsi permettre une réduction importante de trainée, et donc de consommation d'énergie. Néanmoins, l'influence des roues sur l'aérodynamique des véhicules devra être étudiée plus en profondeur. Dans ce contexte, le travail vise à améliorer la compréhension de l'interaction aérodynamique roue-véhicule. Cette partie bibliographique présente et analyse les études précédentes portant sur l'écoulement au soubassement, l'aérodynamique des roues, puis sur l'aérodynamique des véhicules en conditions de roulement. Ainsi, on sait que l'équilibre du sillage d'un corps en proche paroi peut être modifié par un changement de garde au sol, de pertes de charge au soubassement, ou de direction ou et de l'état turbulent de l'écoulement du soubassement… Ensuite, on a dégagé le comportement 3D et complexe de l'écoulement autour des roues isolées et des roues à l'intérieur du passage de roues. Pour une voiture, les roues étant situées dans le soubassement, les éléments bibliographiques ont mis en contexte l'importance de l'aérodynamique des roues par rapport à l'ensemble du véhicule.

Chapitre 2

La première partie du Chapitre 2 décrit l'expérience réalisée ainsi que les outils de traitement mis en place. La maquette de véhicule utilisée tout au long de l'étude est basée sur le modèle ASMO (Section 2.1.2). Sa géométrie a été modifiée précédemment à ce travail de sorte que lorsque quatre roues tournantes sont présentes, l'angle d'incidence de l'écoulement sur la roue avant est compris entre 10° à 15°, et que le sillage du véhicule soit bien équilibré. Pour étudier les efforts aérodynamiques d'interférences entre le véhicule et les roues, agissant sur le véhicule seulement, on adopte une méthode de

mesure dit "wheel-off", ce qui signifie que les roues sont mécaniquement découplées du véhicule, et qu'uniquement les efforts sur le véhicule sont mesurés. L'écrasement des pneumatiques à échelle réduite est réglé, afin de reproduire la déformation réaliste du pneu à l'échelle 1 sous charge. Les mesures du torseur aérodynamique ont été réalisées avec une balance fixée à l'intérieur de la maquette, composée de capteurs piézoélectriques. La distribution de pression à la surface du véhicule est mesurée en 203 prises de pression reliées à deux scanners de pression. Les mesures du champ de vitesse dans le sillage du véhicule sont effectuées avec la technique PIV en trois plans différents.
La deuxième partie du chapitre expose une brève présentation du modèle numérique employé pour simuler certaines configurations. Il s'agit de la méthode lattice Boltzmann. Les calculs ont été réalisés par l'entreprise GANHTHA, selon notre cahier de charges. Les résultats numériques servent à compléter l'analyse physique de l'écoulement.

Chapitre 3

Comme présenté dans le chapitre précédent, la maquette est basée sur le modèle ASMO. Pour analyser les caractéristiques aérodynamiques autour de cette géométrie modifiée, la maquette sans roues et avec les passages de roue fermés (configuration notée par *N*) a été analysée (Section 3.1). Cette configuration a une déportance importante et une faible traînée. L'écoulement au soubassement présente une forte tridimensionnalité avec des lignes de courant divergentes puis convergente. Le sillage du véhicule est aussi très 3D en raison de sa géométrie. Deux paires de tourbillons longitudinaux sont détectés dans le sillage proche.
Le gradient de pression vertical sur la ligne centrale du culot est négatif. Il est cohérent avec l'asymétrie du sillage dans le plan y=0. Mais cet équilibre du sillage est inversé par rapport à une voiture de tourisme classique dans les conditions de roulement. Cela vient de la proximité du sol, et de la géométrie du véhicule, où l'angle du toit (10°) est supérieur à l'angle du diffuseur (5°).

Les roues dans différents états (en rotation ou pas) et avec différents pneumatiques peuvent être considérées comme des perturbations placées au soubassement du véhicule. Afin de simplifier ces perturbations et d'étudier l'impact du blocage au soubassement, nous avons monté une paire d'obstacles profilés (demi-ellipse) au-dessous des passages de roue arrière bouchés, rien n'ayant été monté à l'avant du soubassement. Nous définissons le taux de blocage géométrique, noté τ, par le rapport entre la largeur totale des obstacles (qui est deux fois le petit axe elliptique) et la largeur du véhicule. L'étude paramétrique est effectuée avec τ= 10, 15, 20, 25, 30, 35,40 %. Deux régimes peuvent être observés en fonction de la largeur des obstacles. Le premier régime correspond aux configurations pour lesquelles les sillages des obstacles se ferment, en moyenne temporelle, en amont de la sortie du soubassement ($\tau \leq$ 25 %). Dans ce régime, la pression au soubassement diminue considérablement par rapport à la configuration *N*. L'augmentation de la taille des obstacles, dans ce régime, a seulement des effets locaux sur la répartition de pression au soubassement et au culot, mais ne modifie pas la pression dans le plan de symétrie du véhicule. Dans le second régime ($\tau >$ 25 %), les sillages d'obstacles «non fermés» (vitesse longitudinale moyenne négative observable à la sortie du soubassement) fusionnent avec le sillage du véhicule. Cela conduit à une modification plus globale de l'écoulement, se traduisant par une chute de pression à la surface entière du culot, et une augmentation importante de la pression à l'arrière du soubassement. En résumé, l'augmentation du taux de blocage au soubassement augmente lentement la dépression au culot et la pression au soubassement dans le premier régime, mais beaucoup plus rapidement lorsque on est dans le deuxième régime.

En ce qui concerne le sillage du véhicule, quel que soit le régime, l'organisation du sillage n'est pas significativement modifiée. Pour tous les obstacles profilés testés, les sillages moyens du véhicule semblent avoir une organisation similaire, avec une grande structure de recirculation moyenne dans le sens horaire et une plus petite structure en sens inverse. Cependant, comparés à N, leurs sillages présentent une asymétrie plus prononcée dans la direction verticale. De plus, il y a une nette réduction de la longueur de la recirculation lorsque le taux de blocage du soubassement augmente, ce qui indique une courbure croissante des lignes de courant moyennes au décollement sur le culot.

Une expérience supplémentaire avec un modèle à échelle réduite a été réalisée dans le but de reproduire les deux régimes, avec une taille fixe d'obstacle au soubassement, mais à différentes positions longitudinales par rapport au culot. Les résultats suggèrent qu'avec une paire d'obstacles progressivement éloignée du culot, nous pouvons discerner deux régimes : «proche» et «éloigné» du culot. La sensibilité des coefficients aérodynamiques globaux vis-à-vis de cette distance diffère grandement entre les deux régimes. Les deux régimes ont une analogie avec respectivement le régime de «grand» et de «petit» blocage. Les deux expérimentations soutiennent l'hypothèse que le sillage non fermé de l'obstacle au soubassement génère une interaction beaucoup plus forte avec le sillage du véhicule et donc une influence plus importante sur la distribution de la pression à la surface du véhicule.

Chapitre 4

Dans ce chapitre, les obstacles profilés sont d'abord remplacés par des roues arrière tournantes, configuration XR (Section 4.1). Les structures d'écoulement autour des roues arrière tournantes sont présentées en s'appuyant sur les résultats issus de la simulation numérique. Les phénomènes caractéristiques des roues tournantes présentés dans la littérature, telles que le $jetting$, le pic de pression positive ($Cp > 1$) situé en amont de la surface de contact et la dépression importante ($Cp < -1$) immédiatement derrière la surface de contact, sont confirmés par la simulation. Le schéma général des structures tourbillonnaires s'accorde bien avec ce qui existe dans la littérature. Par rapport à la configuration N, la présence de roues arrière tournantes diminuent la pression au soubassement entre elles car elles empêchent partiellement l'écoulement extérieur de pénétrer dans cette zone de basse pression, comme les obstacles de petit blocage (Chapitre 3). Cependant, elles augmentent légèrement la pression à l'entrée du soubassement et considérablement la pression devant elles, ce qui augmente la pression totale au soubassement et donc le coefficient de portance. Les roues arrière tournantes ainsi que les passages de roue créent des zones de basse pression dans leur sillage. La réduction de la pression au culot se traduit finalement par une augmentation de la traînée du véhicule. Cette diminution de pression au culot est associée à la réduction de la longueur de recirculation du sillage du véhicule. Les fortes fluctuations générées par les roues augmentent l'instabilité de l'écoulement à la sortie du soubassement. De ce fait, l'entraînement dans le sillage du véhicule est augmenté, ce qui entraîne la fermeture plus tôt du sillage moyen. L'effet des roues arrière peut être vu, au premier ordre, comme un effet de blocage. La rotation ou non des roues fait varier le taux de blocage dans le soubassement. Les roues fixes générant des sillages plus larges et donc un blocage plus important. Pour les roues arrière en rotation ou fixes, aucune modification n'a été constatée en termes d'organisation de sillage moyen par rapport à la configuration N.

Dans la Section 4.2, on ajoute des roues avant tournantes. Cette configuration de base, notée RR, est étudiée par rapport à XR. Trois aspects principaux peuvent être notés à partir des résultats de la simulation numérique. Premièrement, l'angle d'attaque sur les roues est différent. Deuxièmement, les roues avant de la configuration RR ont un déficit de vitesse relativement faible dans leur sillage. Troisièmement, dans cette configuration, les roues arrière ont un sillage plus large.

La présence de la roue avant augmente considérablement la pression au soubassement, ce qui montre une réduction du flux au soubassement. La position du point d'arrêt au nez de la voiture est plus basse, ce qui est conforme à la variation de portance observée. Cette diminution importante du flux soubassement, couplé avec la présence du diffuseur, conduit à une inversion de l'équilibre du sillage du véhicule dans le plan de symétrie. On retrouve alors un sillage du véhicule bien équilibré. Le sillage des roues arrière est plus large, ce qui entraîne une interaction plus intense entre le sillage des roues et le sillage du véhicule. Cependant, la diminution de la pression au culot localement en aval des roues arrière est compensée par la recompression en haut du culot, en raison de l'inversion de l'équilibre du sillage. Par conséquent, la pression moyenne du culot et la traînée restent inchangées par rapport à la configuration sans roue avant.

Enfin dans la Section 4.3, différents états de roue sont testés sur les essieux avant et arrière par rapport à la configuration de base RR. Tout d'abord, le champ d'écoulement autour des roues fixes avant et arrière à l'intérieur des passages de roue est analysé en utilisant les résultats de la simulation numérique. Les roues fixes créent un sillage plus large. Lorsque la rotation de la roue avant est arrêtée (configurations SR et SS), le sillage des roues est plus large et une pression plus faible est mesurée dans leur sillage, ce qui entraîne un coefficient de portance plus bas. L'équilibre du sillage du véhicule est légèrement affecté. Lorsque la rotation de la roue arrière est arrêtée (configurations RS et SS), l'effet de blocage créé par la roue arrière fixe est accentué par le diffuseur. Il y a une augmentation de la pression entre les roues arrière au soubassement, entraînant une augmentation de la portance. La diminution du flux au soubassement se traduit par une déviation du sillage du véhicule vers le sol.

Chapitre 5

Dans ce chapitre un fond supplémentaire à l'arrière du soubassement est ajouté pour éliminer le diffuseur du véhicule. Cela permet une première analyse de la sensibilité de nos résultats à une modification de la géométrie du véhicule. Cette configuration est notée $\underline{RR}$. Par rapport à la configuration avec diffuseur (RR), une augmentation de la pression est observée au soubassement, en particulier sur la partie arrière. Cette diminution du flux au soubassement provoque la plongée du sillage moyen vers le sol.

Cet effet global conduit à une insensibilité des coefficients aérodynamiques aux perturbations au soubassement (présence des roues, état des roues, ...). Autrement dit, la présence du diffuseur accentue (par son effet global sur l'aérodynamique du véhicule) les effets locaux introduits par les perturbations au soubassement.

La deuxième partie du chapitre présente l'analyse de l'effet d'un changement du type de pneumatique. Nous étudions ainsi (en plus du pneu de référence à 3 sillons longitudinaux) un pneu ayant 3 sillons et des rugosités sur le flanc et un pneu lisse. Il est démontré que le changement de pneu (avant ou arrière) peut être interprété comme une modification du taux de blocage des roues (roue plus ou moins large) avec les mêmes conséquences sur les distributions de pression au culot et au soubassement que celles analysées dans les chapitres précédents (mais avec un effet plus faible). Il a aussi été observé que le changement de pneu arrière peut, dans certaines configurations, avoir un effet significatif sur l'équilibre du sillage.

Enfin, la contribution des passages de roues sur la traînée du véhicule est étudiée pour toutes les configurations mesurées. La roue en rotation équipée de rugosités sur le flanc semble provoquer une force de «poussée» dans les passages de roue. La traînée du véhicule et la somme des traînées du culot et des quatre passages de roue suivent une dépendance linéaire. La pente, égale à 1, indique que le changement de traînée est corrélé à environ 100 % à la modification de la pression au culot et dans les passages de roue. La fonction affine entre la pression au culot et la traînée du véhicule présente une pente de 0,81. Ce qui signifie que la variation de la traînée des passages de roue représente à peu près 19% de la modification de la traînée du véhicule.

Chapitre 6

Le chapitre 6 résume les résultats présentés dans cette thèse. Pour les perspectives à ce travail, il serait intéressant d'analyser plus finement la généralité des résultats obtenus au regard de modifications de géométrie du véhicule. En ce qui concerne les stratégies de réduction de la traînée, l'existence de deux régimes contrôlés par une paire d'obstacles à l'arrière du soubassement fournit des indications pour améliorer la traînée des véhicules. Il semble ainsi préférable d'éloigner la roue arrière du culot pour limiter la traînée, ou utiliser des roues plus minces, tout en veillant aux autres performances telles que la sécurité et la stabilité.

Table of contents

Chapter 1

Introduction and literature review

With the current conditions of the toughening of environmental legislation for CO_2 and other greenhouse gas emissions, automobile manufacturers around the world are looking into the ways to make the vehicle more energy efficient and therefore more environmentally friendly. The pneumatic system is a crucial area as it plays an essential role not only in vehicle performance and security, but also in energy consumption. Indeed, they are responsible for approximately 20% to 40% of the total aerodynamic drag. This evaluation quantifies the potential of drag reduction by optimization of the wheel-wheelhouse-vehicle system. Nevertheless, the influence of the wheels on the flow around the vehicles remains open issues. In this context, this work aims at improving the comprehension of wheel-vehicle aerodynamic interaction. We provide an overview of the current studies related to wheel aerodynamics. The scope of the investigations undertaken in this work is then outlined.

Contents

1.1 Global context

Human activities are estimated to have increased approximately 1°C of the average temperature on Earth since around 1880 (IPCC, 2018). While with the melting of polar ice sheets and glaciers, the acidification of oceans, the accelerated rise in sea levels, the higher frequency of heat wakes and more powerful hurricanes ... the effects of this climate upheaval are already very tangible. At the current rate of greenhouse gas emissions, global warming is likely to reach 4.8°C by 2100, compared with the period between 1986-2005, which will doubtlessly cause dreadful consequences. In 2015, 195 nations signed onto the Paris agreement to curb greenhouse gas emissions sufficiently to limit global warming to 2°C above pre-industrial levels by 2100. At the same time, more than 100 nations called for a lower warming target of 1.5 °C instead of 2°C. To respond this request, in October 2018, the Intergovernmental Panel on Climate Change (IPCC) released a special report on the impact of global warming of 1.5°C. They revealed that this half a degree can make a world of difference. We would see fewer life-threatening heat, drought, precipitation extremes, less sea level rise, less ecosystems damage, fewer species lost, with far-reaching consequences for humans and their activity. However, this goal is far from easy. To do so we must achieve a net-zero carbon footprint by 2030. This means carbon capture process in the atmosphere will need to offset emissions at that date. Thus it is essential to curb greenhouse gas emissions, which requires rapid and unprecedented transitions in all aspects of society: reducing industrial emissions, controlling urban sprawl, limiting animal-based protein consumption, ensuring energy sobriety, increasing the percentage of renewable in the electricity mix and revolutionizing transportation ...

Transport is the only sector in which greenhouse gas emissions are still higher than they were in 1990 (EU, 2018). In the automotive sector, cars and vans produce about 15% of the EU's CO_2 emissions. Average emissions by new cars rose to 118.5g CO_2/km in 2017, following a steady decline over the past few years. Under current rules, the average new car must not emit more than 95g/km by 2021. In a plenary vote on October 3, 2018, MEPs (Member of the European Parliament) proposed emissions should be cut respectively by 20% in 2025 and 40% in 2030, than in 2021. New targets are expressed in percentages because the 95 g/km standard (in 2021) will have to be recalculated according to the new more rigorous emissions test that better reflects real driving conditions. Moreover, they propose that 35% of new cars sold from 2030 should be electric or hybrid.

With these stricter regulations and tax rates being introduced every year on CO_2 emissions, automobile manufacturers are pushed into seeking solutions that do not compromise the vehicle's global performance. Aerodynamics is one of the several fields where such solutions are pursued.

The actual CO_2 emissions of a vehicle depend on the vehicle's driving resistances, the powertrain's efficiency and the energy demand of potentially activated auxiliary consumers. The efficiency of the powertrain describes those parts of the total fuel's energy content that can be used for the mechanical propulsion of the vehicle. The majority of the employed chemical energy gets lost by heat dissipation and friction in the powertrain. Engine efficiency varies between different types of engines and also between different loads within the engine maps, described by engine speed and engine power (or torque). The total driving resistance F_x of a vehicle follow basic physical principles, which consists of four parts: rolling resistance F_{R}, aerodynamic drag F_{A}, acceleration F_{Acc} and slope of the road F_{S}:

$$F_x = F_{\mathrm{R}} + F_{\mathrm{A}} + F_{\mathrm{Acc}} + F_{\mathrm{S}} \tag{1.1}$$

Assuming a passenger car traveling at constant speed on a level road, the driving resistance can be simplified into the following form:

$$F_x = F_{\mathrm{R}} + F_{\mathrm{A}} = f_{\mathrm{R}} m g + \frac{1}{2} C_x S \rho V_\infty^2 \tag{1.2}$$

The two terms F_{R} and F_{A} as a function of driving velocity is given in Figure 1.1. The rolling resistance is proportional to the vehicle load. The coefficient of rolling resistance f_{R} depends on wheel and road properties, and some other factors. It is rather constant at low velocities, but increases strongly at high speeds. The aerodynamic drag is determined by the aerodynamic shape of the body, described by the drag coefficient (C_x), and by the projected frontal area of the vehicle (S). As the aerodynamic drag increases as the square of driving speed, it rises much faster than the rolling resistance. At above $60 km/h$, the aerodynamic drag dominates over the rolling resistance, and becomes the main source of driving resistance. However it should be noted that the figure is only schematic, as the real distribution of the forces and their absolute values strongly depend on vehicle and tire characteristics.

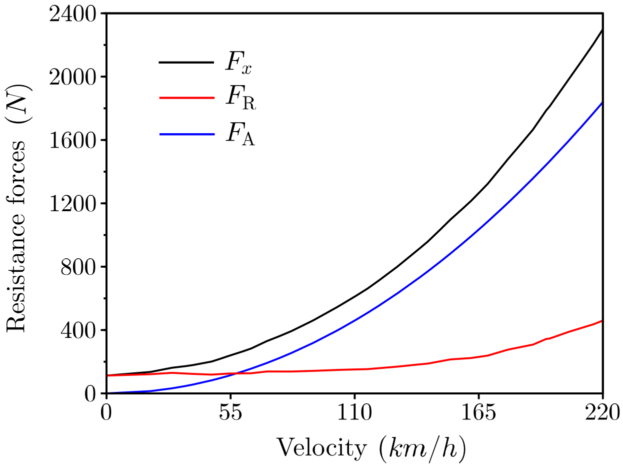

Figure 1.1: Aerodynamic drag and rolling resistance versus vehicle velocity for a typical passenger car (Elena, 2001).

The focal point of this work is the wheel and its aerodynamic interaction with the vehicle. To give some specific numbers on their importance, it is estimated that for a typical passenger car, the wheels and wheelhouses account for approximately 20% to 40% of the total aerodynamic drag (Pfadenhauer *et al.*, 1996; Wickern & Lindener, 2000; Elofsson & Bannister, 2002). Consequently, the optimization of the wheel-wheelhouse-vehicle system provides us the possibility of a substantial reduction of the aerodynamic drag as well as energy consumption.

As the lower half of the wheels are exposed to the underbody flow, their presence will undoubtedly modify the underbody flow condition compared to the basic vehicle body. Moreover, wheels themselves create complex flow structures that will convect downstream, interfere in the vehicle wake. To broaden our understanding of these behaviors, the following literature review will start with individually the underbody flow and the wheels aerodynamics, then the existing investigations on vehicle in on-road conditions will be presented.

1.2 Influence of the underbody flow

In a conventional vehicle, the underbody embodies exhaust pipes, mufflers, gearbox, propulsion shaft, etc, which is far from smooth. These parts are important contributors to aerodynamic drag and account for about 10%-30% of the total drag force (Passmore & Le Good, 1994; Rossitto, 2016).

First stage studies are focused on the underbody flow effect on simplified vehicle geometries by removing the complications of wheels. Then, once the wheels are ignored, at the ground proximity, the underbody flow can be controlled by pressure loss system, passive devices, ground clearance, unsteady actuation, etc. Their impact on the wake organization and the base pressure level can be analyzed.

To simulate the underbody roughness and examine their aerodynamic impact, Perry & Passmore (2013) introduced 5 horizontal roughness strips of different size in the underbody of a square-back Windsor model. They revealed a significant impact of the underbody flow condition on the base pressure and near wake structure, chiefly at lower ground clearance. With an increase in underbody roughness, the drag raises as the lower vortex near the base becomes stronger and larger. The underbody roughness was also investigated in real car geometry. Jakirlic *et al.* (2016) conducted computational study using VLES (Very Large Eddy Simulation) on a 'DrivAer' car model with smooth and detailed underbody. A higher drag coefficient is obtained with detailed underbody configuration than smooth underbody configuration.

Similar disturbance facility as used in Perry & Passmore (2013) was also applied in Barros *et al.* (2017). Apart from one horizontal strip, they also tested a centralized circular cylinder and uniform grid, with variable size, in the underbody of a rectangular bulff body in ground proximity. The application of small disturbance facilities increases the wake lower vortex size, sets flow symmetry in the wall-normal plane, and triggers bimodal lateral wake reversals. Further increase of perturbation size additionally enhances wake lower vortex, and the wake lateral bistability is suppressed.

It can be conjectured that, in the previous studies, if they continued decreasing underbody flow momentum by even larger perturbation, the wall-normal asymmetry will once again reverse. This is what have been observed in Grandemange *et al.* (2013*a*), while they increase gradually the underbody flow momentum by augmenting the ground clearance of a parallelepiped body with rectangular blunt trailing edge. Three regimes can be identified when increasing the ground clearance. When the ground clearance is small, the wake is similar to that of the 3D backward facing step as a result of the strong viscous effect in the underbody. While increasing progressively the ground clearance, the underbody flow gains higher momentum but separation occurs more downstream on the floor. It forms a curved jet that reattaches on the upper part of the base. The recirculation length is significantly reduced, leading to an important drag increase. For even higher ground clearance, the underbody flow has enough momentum to prevent separation on the ground, and two counter-rotating vortices are formed in the mean wake symmetrical plane. The drag decreases compared to the second regime but then stabilizes. This evolution of the near wake characteristics is also confirmed by McArthur *et al.* (2016) varying ground clearance with a GTS (Ground Transportation System) model. In addition, in certain range of the body aspect ratio, lateral bistability behavior is observed in the first regime, and in the third regime the near wake undergoes bistability in either lateral or vertical direction.

At a constant ground clearance, similar flow regimes to those observed in Grandemange *et al.* (2013*a*); McArthur *et al.* (2016) could be achieved by modifying underbody flow velocity. It is the case in Castelain *et al.* (2018) where they mounted a pressure loss system to control the underbody velocity from 0.15 of the free stream velocity to 0.86, beneath a simplified tractor-trailer model with side skirts.

The preceding researches bring to evidence different wake wall-normal balance due to underbody flow momentum variation. While by involving flow deviation devices at the rear trailing edge of a bluff body, for example tapers and flaps (Grandemange *et al.*, 2013*c*; Littlewood & Passmore, 2010; Perry *et al.*, 2016), the shear layer is directly deflected, so does the mean wake. The linear dependence between the lift coefficient and the bottom flap angle in Grandemange *et al.* (2013*c*) demonstrates that, in addition to the bottom shear layer deviation by bottom flap, the underbody flow momentum is equally modified. Further observations indicate a quadratic dependence of drag versus lift, revealing the potential of reaching drag minimum in road vehicle applications by empirically setting the angles of the flow separations at the trailing edges. This approach using flap and taper corresponds to the underbody diffuser applied in real vehicles.

The diffuser is a passage of increasing area at the underbody exit. It can increase the underbody flow at its entry while reduce the velocity at the exit, and thereby recovering pressure. They were initially applied to race cars to increase downforce and improve high speed stability.

Now they are commonly used in road vehicles to improve lift and drag performance. Cooper *et al.* (1998) investigated the influence of ground clearance combined with different diffuser angle using a rounded nose bluff body with side plates. With underbody diffuser, the effect of the ground clearance is still consistent with those observed in Grandemange *et al.* (2013*a*); McArthur *et al.* (2016). They reported increasing downforce and drag with the decreasing ride height to a maximum, followed by a sharp decrease in downforce due to viscous effect at ground proximity. Moreover, the optimum diffuser angles for downforce are between $13° \sim 16°$. Above 25°, the diffuser is completely stalled. In terms of the drag, at high ground clearance, it is similar to the drag variation seen in fastback vehicles, where increasing the back slant angle from 0° reduces drag up to an angle of about 12°-15° (Ahmed *et al.*, 1984). While at lower ground clearance, the range over which the diffuser reduces drag is smaller (0°-5°) compared to the fastback data (0°-15°). Eventually, one can mention multiple channel underbody diffusers, they are proved to be more efficient than single channel diffuser, as with increasing diffuser angle, significant downforce production is achieved with little increase in drag (Jowsey, 2013).

Another mechanism that can influence underbody flow condition is related to the experimental set-up, the moving ground. More and more wind tunnels are equipped with different moving ground systems with proper boundary-layer treatment to better reproduce the on-road condition. Krajnović & Davidson (2005) showed that the influence of the floor motion on the wake structure of a slanted surface body is qualitatively limited to the region near the floor and near the slanted surface. It is anticipated that in a realistic case with a moving ground, the flow regime classifications as evidenced in Grandemange *et al.* (2013*a*); Castelain *et al.* (2018) depending on underbody flow momentum persist, however the transition between two regimes may occur at different ground clearance or underbody velocity values.

1.3 Wheels aerodynamics

1.3.1 Isolated wheels

Before attempting to study wheel-wheelhouse-vehicle interaction, a more fundamental approach is to start with the aerodynamics of isolated wheels.

A wheel is a bluff body thus the flow field around it exhibits strong three-dimensional properties and complex vortex dynamics phenomena (Pirozzoli *et al.*, 2012).

The first aerodynamic research aimed at the automobile wheels was carried out by Morelli (1969). In fact, when the wheel is in contact with the ground, it is required to separate the aerodynamic forces from the reaction forces due to the ground. In order to avoid this, in their experiment, a wheel was suspended without contact, onto a recess of a stationary plate simulating the ground. The wheel was driven to rotate by a DC motor. The drive-shaft was connected to a force balance. Due to the gap underneath the tire, a Venturi effect plus a Magnus effect lead to important suction underneath the tire, eventually results in a negative lift. However the observed downforce of the rotating wheel and the increase of the drag due to the rotation of the wheel compared to the stationary one are their major results that are contrary to the subsequent observations. This is because in reality the wheels are in contact with the ground, and air can not pass underneath.

Fackrell & Harvey (1975) were one of the first who investigated experimentally the isolated rotating wheel in contact with the ground. Their results are also the most accepted and referenced in this subject area. They indicated that only in this realistic flow conditions could

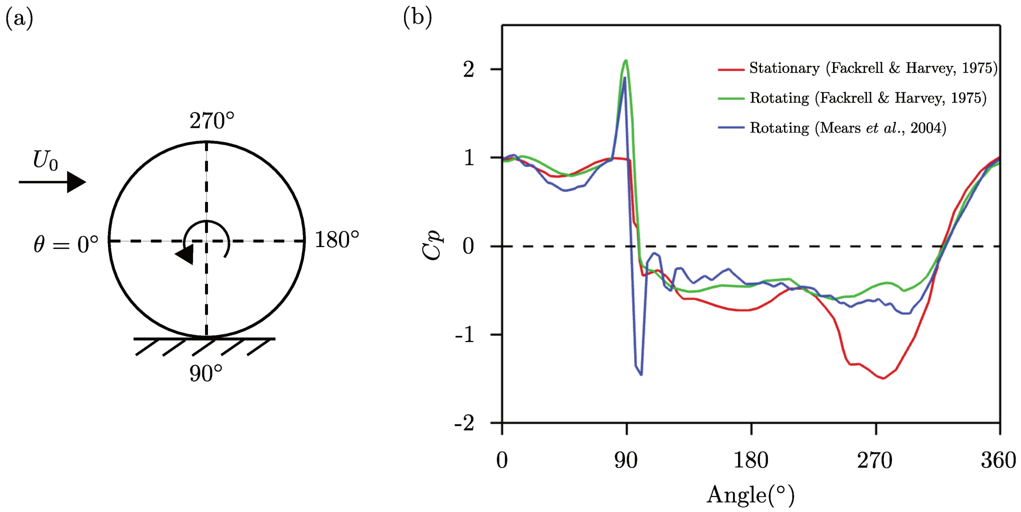

Figure 1.2: (a) The angle convention of a rotational wheel; (b) Static pressure distribution on the centerline around stationary and rotational wheels (Fackrell & Harvey, 1975; Mears *et al.*, 2004).

appropriate lift and drag be acquired. They performed wheel surface pressure measurements by a set of pressure tappings across the tread connected to a microphone located inside the wheel. The measured data was transported out from the rotating wheel via slip rings. The distribution of the static pressure in the wheel centerline was measured for rotating and stationary wheels (Figure 1.2). Neglecting the viscous force, and by integration of the surface pressure, drag and lift coefficients were derived. They revealed that a rotating wheel has a lower drag and lift than those of a stationary wheel, which is proven by later investigations (Wäschle *et al.*, 2004; Mears *et al.*, 2004). The rotation of the wheel leads to a downward shifting stagnation point, and an earlier separation from the top wheel tread, as shown in Figure 1.3. Compared to rotating wheel, the later separated flow creates large suction region on the tire tread (approximately from 130° to 310° in the Figure 1.2), accounting for a higher drag and a higher lift. Moreover, in their measurements, a sharp rise of C_p to greater than 1 was discernible at the upstream region of the contact patch (Figure 1.2). This is due to the interaction between the oncoming flow and the wheel/road juncture, producing an effective and significant 'pumping' of the air out into the free-stream from either side of the wheel. This phenomena is called *viscous jetting*.

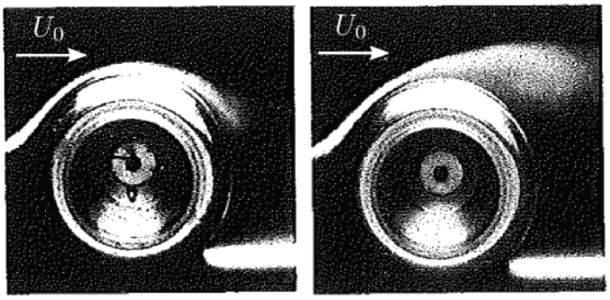

Figure 1.3: Smoke visualization of flow pass stationary wheel at left and rotational wheel at right, flow coming from left to right (Fackrell & Harvey, 1975)

With this high pressure peak, Fackrell & Harvey (1975) expected a higher transverse velocity of the flow emerging from the front contact patch underneath the wheel. Therefore, the lower wake of a rotational wheel would be wider. However the contrary is often observed (McManus & Zhang, 2006; Axerio & Iaccarino, 2009; Heyder-Bruckner, 2011; Diasinos *et al.*, 2015). Two reasons were proposed in the literature to explain the thinner wake of a rotating wheel: the first is that the flow emerging from the front contact patch underneath the rotating wheel is deflected by full free-stream velocity, while the stationary wheel sits in a boundary layer of the stationary ground, resulting in a slower dissipation of the transverse velocity of the emerging flow (McManus & Zhang, 2006); the second is that for a stationary wheel, the late separated flow on the wheel tread creates a stronger downwash behind the tire which fuels the formation of the strong counter rotating ground vortex pair that enlarges the wake (Axerio & Iaccarino, 2009).

In addition to the high pressure peak, Fackrell & Harvey (1975) also predicted that the sharp rise of the surface pressure would be accompanied by a drastic drop. A negative pressure peak would exhibit immediately after the line of contact due to the divergence of the moving surface. However it was not observed in their measurements. It is probably attributed to the rising of the moving belt increasing the pressure immediately downstream the contact patch. While it was subsequently observed by Mears *et al.* (2004) (Figure 1.2). The oscillations after the negative pressure peak was believed to be induced by instrumental error.

The first detailed general schematic of the flow structures around an isolated wheel in contact with the ground was presented by McManus & Zhang (2006) using unsteady RANS, delineated in Figure 1.4. For a stationary wheel, the flow stays attached on the top tire tread, as precedent observations, creating a strong downwash behind the wheel and forming a pair of counter rotating vortices. For a rotating wheel, the flow separates earlier than in the stationary case, giving rise to an upper arch shaped vortex. In the lower wake, a recirculation region forms in the separation region. In general, an isolated rotating wheel creates a taller yet thinner wake than a stationary one. Furthermore, the DES simulation of Heyder-Bruckner (2011) revealed that both the upper and lower wake of a rotating wheel are composed of periodically shed vortices released from the shear layer which is created as the flow separates from the wheel surface.

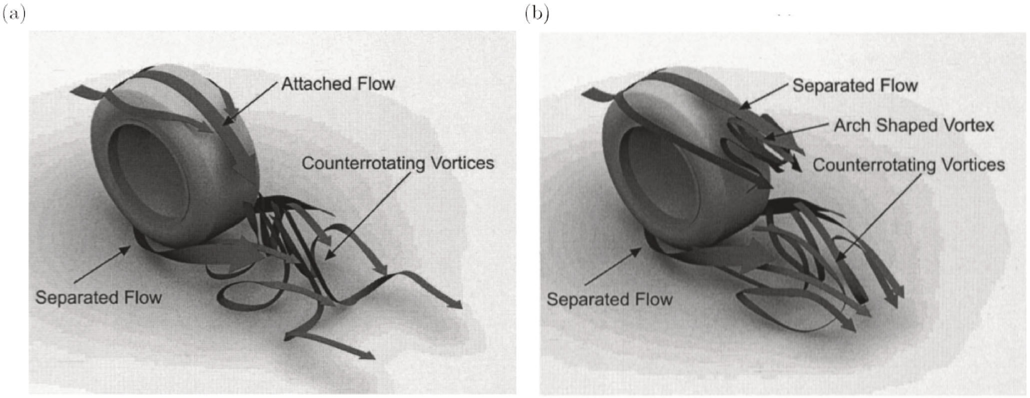

Figure 1.4: Schematic diagrams of the general isolated wheel flow (a) Stationary; (b) Rotating (McManus & Zhang, 2006).

In addition to the rotation of the wheel and the contact with the ground, another on-road condition proved to be essential is the contact patch size. Rigid wheels made of carbon fiber or aluminum are often used for scaled aerodynamic experiments, as the process of manufacturing such a wheel is more accessible. Besides, to reproduce corrected deformable tire, it needs to be preloaded, which would result in excessive wear of the moving belt. While the rigid tire ensures durability and longevity of the test equipment. The investigation on contact patch surface was carried out numerically by Diasinos *et al.* (2015) using steady-state RANS. They included a small step around the wheel's contact patch to simulate the contact with the ground. However, they did not apply a real deformable tire shape on the wheel. By varying the height of the step from $0.0028d$ to $0.0085d$ (d is the wheel diameter), they observed a reducing wake width with the increasing step height, and a decrease of drag up to 20% (0.1 in C_d). In their numerical set-ups, increasing the step height increases the length of the contact patch more than its width, resulting an aspect ratio change. Therefore the flow separation point moves towards the rear of the wheel with a reduction in the lateral departure angle of the jetting from the contact patch. The experimental research of Purvis (2003) seems to find the opposite conclusion. They used a 50% scale deformable tire constructed from polyurethane foam, while their tire did not have an accurate side profile. They demonstrated that the width of the wheel lower wake increases significantly with the contact patch width. It may be difficult to conclude which trend is correct, while from the results in Diasinos *et al.* (2015) it can be said that the wheel wake is effectively dictated by the shape of the contact patch. Their findings emphasize the importance of applying correct contact patch.

1.3.2 Wheels inside wheelhouses

The wheelhouses add considerable complexity on the system compared to isolated wheels. Understanding the wheelhouse flow allows us to further investigate its interaction with the remainder of the vehicle.

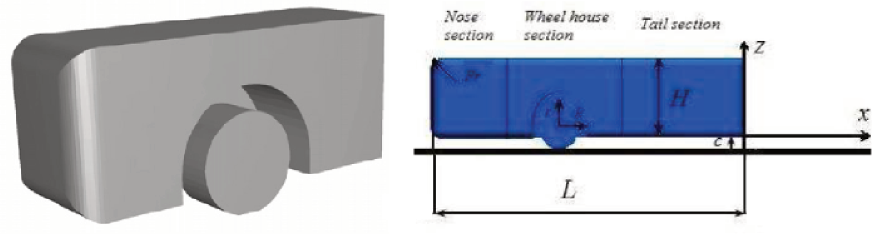

Figure 1.5: The investigated simplified models, at left : Regert & Lajos (2007), at right: Krajnović *et al.* (2010).

A detailed structure of the flow field inside a generic wheelhouse around rotating wheel was first published by Regert & Lajos (2007) using RANS and URANS, and later supported by LES simulations of Krajnović *et al.* (2010) on simplified models (Figure 1.5). Wheel-specific vortices were identified, independent of the grid, numerical scheme, turbulence model and the shape of the body (Figure 1.6). Two longitudinal vortices correspond with the *jetting* vortices in the case of an isolated rotating wheel, which are marked with L and R. The only discrepancy of the two works lies in the existence of an additional pair L_1 and R_1 observed behind the wheel by Krajnović *et al.* (2010), which arises from the entrained upward air by the rotation of the wheel. The interaction of the up-flow entering the wheelhouse and the running surface of the wheel moving in the opposite direction results in boundary layer separation over the upper part of the wheel, which gives rise to the formation of vortex A. The upper arch shaped vortex in an isolated configuration (Figure 1.4(b)) does no longer exist. Vortex B mainly results from the flow entering the wheelhouse from its front leading edge, getting entrained by the wheel rotation, recirculating inside the wheelhouse and eventually leaving the wheelhouse from the rear upper part. Vortex H is generated by the recirculation of the separated flow at the entry of the wheelhouse. Vortex C and S are the results of boundary layer separations over the front and rear edges of the wheel arch. Vortex E originates from the flow entering at the front of the wheelhouse between the wheel and the inner wall, impinges on the downstream part of the wheel arch and then stretched downwards to the underbody.

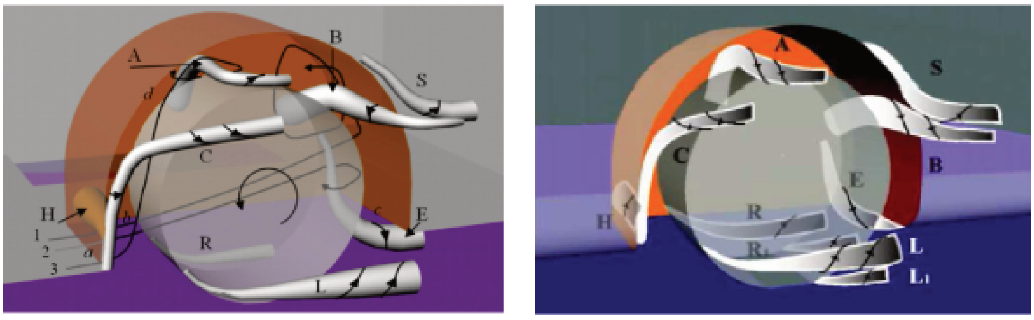

Figure 1.6: Vortex skeleton of flow in a wheelhouse, at left : Regert & Lajos (2007), at right: Krajnović *et al.* (2010).

The flow entering the wheelhouse mainly leaves the volume from the upper part of the wheel arch due to the wheel rotation. Gulyás *et al.* (2013) carried out PIV measurements in several horizontal planes besides a rotating wheel inside the wheelhouse of an Ahmed body. By analyzing the streamlines and flow-fields in these planes, they found a maximum amount of outflow leaving the wheelhouse between the top of the wheel and the highest point of the wheel arch curve. Bonitz *et al.* (2018) conducted unsteady surface pressure measurements downstream a front wheel arch of a full-scale Volvo S60 production car of notchback type. They found out a dominant frequency at the wheel rotational frequency in the upper part behind the wheelhouse, revealing a coherent structure exiting the wheelhouse. It can be analogous to the A structure found in Regert & Lajos (2007) and Krajnović *et al.* (2010). The low pressure and high pressure fluctuation region behind the front wheel arch corresponds the reattachment area of this vortex exiting the wheelhouse. It then propagates horizontally downstream. In a real life scenario, this vortex will cause most of the side contamination on the vehicle. It is further confirmed that this coherent structure presents even under large yaw angle (±15°), no matter at leeward or windward side. While it is not observed when the wheel is stationary.

It should be mentioned that in the experiment of Bonitz *et al.* (2018) it was the vehicle being yawed to leeward and to windward. While even though this yaw angle is zero, the front wheel approaching flow does not have a zero angle, as pointed out in Regert & Lajos (2007). When the model is aligned with the oncoming flow, for a 1D fore-body, where the distance between the fore-body and the front wheelhouse equals approximately to one diameter of the wheelhouse, the yaw angle of the front wheel approaching flow is approximately 9.18°; for 2D fore-body, it is 7.5°; for infinite fore-body, the yaw angle reduces towards 2.85°. For a typical passenger car, this value is around $10 - 15°$ (Pfadenhauer *et al.*, 1996). This yaw angle importantly influences the intensity and position of vortices A and B, while the position and size of other vortices are less dependent of this parameter (Regert & Lajos, 2007). Bonitz *et al.* (2018) also observed more or less pronounced frequency signals of the vortex at the upper part behind the wheelhouse, when the measurement area was located leeward or windward.

The size of the wheelhouse also assumes important influence on the wheelhouse vortex development as well as the global aerodynamic coefficients. When reducing the diameter of the wheel arch, A, E decrease in size, while B gradually dominates the outflow from the upper part as it is fed by unchanged inflow in the internal part of the wheelhouse (Regert & Lajos, 2007). A decrease in depth of the wheelhouse mainly reduces the size and intensity of vortex B and E. The drag of the simplified model including wheelhouse and wheel globally decreases with the reducing wheel arch volume but the effect of radial space on drag is more important (Fabijanic, 1996; Thivolle-Cazat & Gilliéron, 2006). However, it was not easy to know whether the increase of drag came from the simplified body or the wheel as the drag was measured globally.

1.3.3 Aerodynamics of road vehicle including wheels

In vehicle aerodynamics, detailed numerical and experimental studies have been focused on generic, simplified geometries, such as the Ahmed body (Ahmed *et al.*, 1984; Krajnoviä & Davidson, 2005; Östh *et al.*, 2014; Grandemange *et al.*, 2013*b*; Barros *et al.*, 2016; Li, 2017), Asmo body (Perzon & Davidson, 2000; Nakashima *et al.*, 2008; Tsubokura *et al.*, 2009; Xflow, 2010; Aljure *et al.*, 2014), and Windsor models (Howell, 1994; Littlewood *et al.*, 2011; Perry & Passmore, 2013; Perry *et al.*, 2015, 2016). These simplified models are widely investigated as they can reproduce importation flow structures around realistic road vehicles and favor the comparison between different experimental and numerical studies. Recently, with the advances in wind-tunnel equipment, more thorough investigations have become possible. Aerodynamic investigations of generic models including wheels and wheelhouses are receiving more attention, as they are more representative of real vehicles. Moreover, the wheels and wheelhouses are also important contributors to the aerodynamic drag. For a typical passenger car, the wheels and wheelhouses together are responsible for approximately 20% to 40% of the total drag (Pfadenhauer *et al.*, 1996; Wickern & Lindener, 2000; Elofsson & Bannister, 2002).

The experimental study of Pavia & Passmore (2017) demonstrates that the inclusion of the front wheelhouses and front wheels into a 1/4 scale Windsor model modifies mildly the drag. The lateral bi-stable motion that exhibits in the wake of a Windsor model without wheels is still recognizable. Moreover the state of the front wheels (stationary or rotating) shows negligible difference. However, when rear axle is additionally included, significant pressure drop can be noticed in the bottom half of the base. This results from the formation of a stable counter rotating vortice pair in the gap between the two rear wheels, which also tends to stabilize the bi-stable motion. Elofsson & Bannister (2002) claimed that in a wake balance point of view, the inclusion of (four) wheels create interference effects between the wheel wakes and the vehicle wake, causing the vehicle wake being far from balanced or elliptical [1]. Consequently, significant drag increase is induced compared to the basic vehicle body.

The more important influence of rear wheels on the vehicle aerodynamic was also confirmed by varying the state of the wheels separately at the front axle and at the rear. The experimental studies of Elofsson & Bannister (2002) on a Volvo Sedan and a Volvo Squareback, and the numerical investigations by Koitrand & Rehnberg (2013) on a Jaguar XF Saloon and a Jaguar XF Sportbrake all illustrate higher variation in global lift and drag coefficients when altering rear wheel state. Rear wheel rotation contributes to a decrease in the vehicle total drag ($\delta C_d = -0.03 \sim -0.02$) and rear lift ($\delta C_l = -0.04 \sim -0.02$) compared to rear stationary wheel cases. Wäschle (2007) interpreted the increase in base pressure as additional energy being transferred into the vehicle wake by the rear wheel rotation and thus reduces the losses and the wake size. Elofsson & Bannister (2002) assumed that rotating rear wheel creates local upwash (Figure 1.7), compared to the large wake of the stationary wheel, and thus results in smaller interference effect with the base region. However, it can be argued that, the upwash or upward velocity downstream a rotating wheel is not observed in isolated situations at equivalent distance, as shown in their PIV measurements in the wake (Axerio & Iaccarino, 2009; Heyder-Bruckner, 2011; Sprot, 2013; Diasinos *et al.*, 2015). It is thus conjectured that the observed upwash visualized by the smoke is due to the vehicle diffuser (or its Coanda shape). While in

---

[1] put forth by Morelli (2000), an elliptical cross-section of a vehicle wake is considered well-balanced.

a stationary case, the wheel wake extends more downstream and can not be vectored by the diffuser.

Figure 1.7: Smoke flow visualization behind the rear wheel, at left: rear stationary wheel, at right: rear rotating wheel (Elofsson & Bannister, 2002)

It is sufficient to remark that in open-wheeled race car aerodynamics, the flow field around the whole race car is severely affected by the front wheel (Sprot, 2013), in contrast to passenger cars where the presence of the front wheels or the front wheel state has less significant impact than rear wheels.

In context of vehicle with diffuser, Huminic & Huminic (2017) exposed a combined effect of the wheels and the diffuser. By RANS simulation on a 1/4-th scaled 35°-slant-angle Ahmed body without and with wheels at various diffuser length and angle, they brought to evidence an increase of lift and drag in on wheels condition compared to same geometry without wheels, as a result of the formation of the vortices originated from the rear wheelhouses. They showed that the lift coefficients of the model without and with wheels both decrease with increasing diffuser length and angle. While the decreasing rate becomes smaller with the increasing of the diffuser angle when wheels are included (Figure 1.8(a)), revealing a reduced diffuser efficiency. Moreover, from the drag measurements (Figure 1.8(b)) it can be noted that, there is possibility of reaching drag minimum over the range of diffuser angle and length when the generated vortices from the rear wheelhouses have a smallest size.

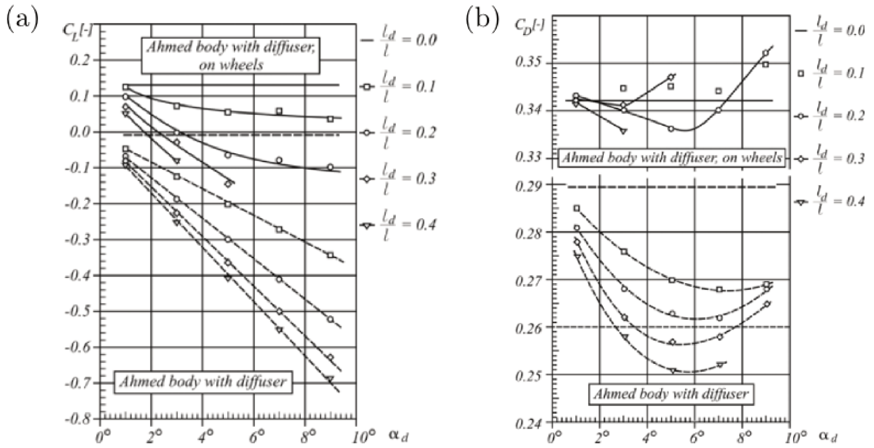

Figure 1.8: Lift and drag coefficient of a 1/4-th scaled 35°-slant-angle Ahmed body without and with wheels at various diffuser length and angle (Huminic & Huminic, 2017).

In parallel, there are also investigations on the effect of more detailed parameters of the wheel upon global aerodynamic forces and flow-field, for example, the rim design, tire edge patterns...

It is reported that the wheel rim has an impact not only on wheelhouse flow but also on the underbody and cooling flow and the base wake of the vehicle (Wäschle, 2007; Kuthada & Wiedemann, 2008; Landström *et al.*, 2009). A covered rim was found to be more favorable in terms of aerodynamic drag. The CFD analysis of Bastian *et al.* (2015) ascribed the decrease in vehicle total drag by applying covered rims mainly to the smaller drag generated at the wheels. For a total reduction of 20 counts, up to 6 drag counts reduction is observed for front wheels and 11 for rear wheels, while the base and integral wheelhouse drag is only slightly affected. Moreover, Landström *et al.* (2011*b*,*a*) proposed that optimizing the rear rims design has larger potential in decreasing the aerodynamic resistance of the vehicle. Using statistical design of experiment (DOE) methods, Berg & Brandt (2018) ranked the tested rim parameters (Figure 1.9) as follows, from the most relevant to the least in decreasing aerodynamic drag: Coverage area (high), Rim cover distance (high), Rim cover depth (low), Rim cover angle (low), Depth of center (low), Drop angle (high). The maximum drag difference induced by the most relevant parameter, coverage area, reaches up to -0.017 in Cd for a Volvo S90 Sedan and -0.012 for a Volvo V90 Estate.

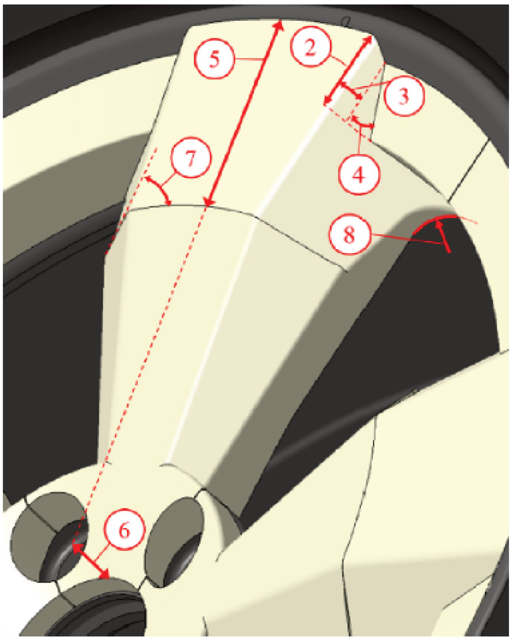

Figure 1.9: The rim parameters investigated in Berg & Brandt (2018): 1. Coverage area; 2. Rim cover distance; 3. Rim cover depth; 4. Rim cover angel; 5. Position of break; 6. Depth of center; 7. Drop angle.

It is noteworthy that the different drag variations for different car geometries due to same modification in wheels also present when altering the wheel state. The Volvo sedan tested in Elofsson & Bannister (2002) also benefits more drag reduction with wheel rotation than Volvo Squareback. These results reveal that the vehicle geometry plays an important role in wheel-vehicle interaction.

The edge patterns on the tire are less investigated in the literature, as experimentally, tires with different edge patterns are less accessible, and numerically, their simulation exhibits limitations (see next section). Hobeika *et al.* (2013) investigated the tire edge pattern by applying a rotating moving wall boundary condition on the tire surface. They claimed that the edge pattern introduces a high vorticity in the flow. The interaction between the generated vorticity and vehicle wake shows visible influence in base pressure plots, resulting up to 7 drag counts increase for a Volvo Sedan and 14 for a Volvo Sportswagen.

In a more realistic approach, vehicle ride height can be elevated by both aerodynamic lift and the radial expansion of the tires due to centrifugal forces. Given the sensitivity of the underbody flow to the ground clearance (Section 1.2), the rise in ride height is likely to modify the underbody flow condition. The experiments of Bastian *et al.* (2015) on a BMW 3 Series sedan demonstrated that when driving at $140kph$, the on-road vehicle is measured to be elevated by $5mm$–$7mm$ at the front body. Moreover, when applying the elevated ride height in wind tunnel they observed approximately 4 counts drag increase.

1.3.4 Rotating wheel modeling

An essential part of modeling the wheel rotation is in assigning boundary conditions to the geometry, which affects the shear layers and developing flow-physics. The methods of implementing wheel rotation in CFD have been investigated to some extent over recent years. In the following we will present briefly the commonly used numerical approaches in rotating systems.

The simplest approach is to apply a Rotating Wall (RW) condition on the surface of the rotating part by imposing the velocity at the wall tangential to their cell surface. However, due to the complexity of the wheel geometry, this method alone sometimes fails to represent the appropriate flow condition around the wheels. It is due to the fact that non-zero velocity component could not be introduced to any cell surface whose movement is normal to the velocity vector, as physically a solid wall could not have inflow or outflow. It is the case for certain parts as inside the rim spokes and in the lateral grooves on the tire tread, shown in Figure 1.10 framed by the red boxes. It can be perceived that if rotating wall condition is applied on the whole surface of the wheel, the velocity magnitude set in these areas becomes much lower than reality. To address these problems, other approaches as Multiple Reference Frame (MRF) and Sliding Mesh (SM) have been put forth.

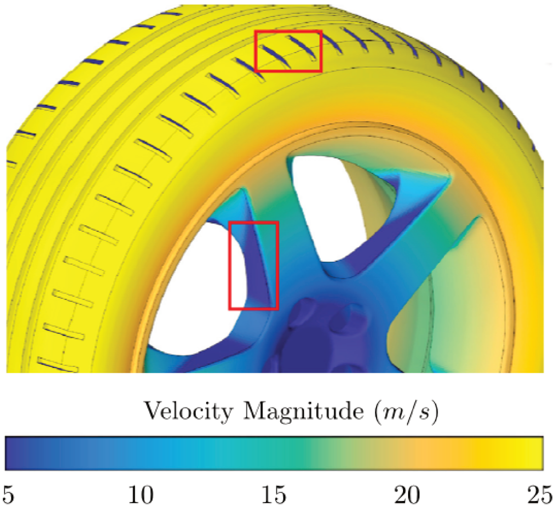

Figure 1.10: Velocity distribution on a wheel obtained by Rotating Wall approach (Hobeika & Sebben, 2018); The red boxes indicate the regions where RW approach fails to apply correct surface velocity.

The MRF is a steady-state approximation in which individual cell zones move at different rotational/translational speeds. Centrifugal accelerations and Coriolis effects are introduced to cell zones having rotational motion. This approach is appropriate when the flow at the boundary between these zones is nearly uniform. For example, the MRF can be used for turbomachinery application in which rotor-stator interaction is small. While in the case of a rotation wheel in a vehicle, if MRF is applied to the whole wheel, the flow around the wheel can never be rotationally uniform over the interface with the main flow. Mlinaric (2007); Wäschle (2006) claimed that MRF volumes could only be used to each open region in-between the spokes. The sensitivity study of wheel orientation in Landström *et al.* (2010) using MRF shows the position of the spokes affects the flow field and aerodynamic forces. Therefore the MRF is not considered the ideal method for modeling the rim or complete wheel rotation.

The SM model is considered to be the most realistic method for simulating flows in multiple moving reference frames. With this approach, two cell zones are allowed to slide relative to each other with an interface zone between them. At each time step the interface zones will vary as the adjacent zones move relative to each other and the flux across the interface zones from one to another are computed for the next time step. That is why this method is very computationally demanding. In vehicle simulations, it is not very easy to be implemented for the whole wheel due to the contact patch on the ground, yet it is a good method for the regions containing the rim, spokes and wheel hub and when high fidelity is required in modeling rotating wheels. Figure 1.11(a) shows the implementation of SM on the rim.

Most of the CFD investigations on rotating wheels made many compromises, particularly involving the blocking of through-hub flow, the lack of a rotating mesh (for non axially symmetric geometry rotations such as spokes), or a lack of rotating wall treatment (such as the tread). Most of these are a consequence of resource restrictions. To compromise the accuracy and the computational costs, the study of Hobeika & Sebben (2018) proposed a hybrid approach for simulating tire rotation. RW is applied on the external tire area; SM is applied on the not closed rim (in the case of a closed rim, the RW method is sufficient as the closed rim surface is tangential to the rotational velocity); And MRF is applied on the repetitive small size lateral grooves (Figure 1.11(b)). This combined method is proved to be promising solution as it can predict reasonably flow field and aerodynamic coefficients compared to a full sliding mesh approach.

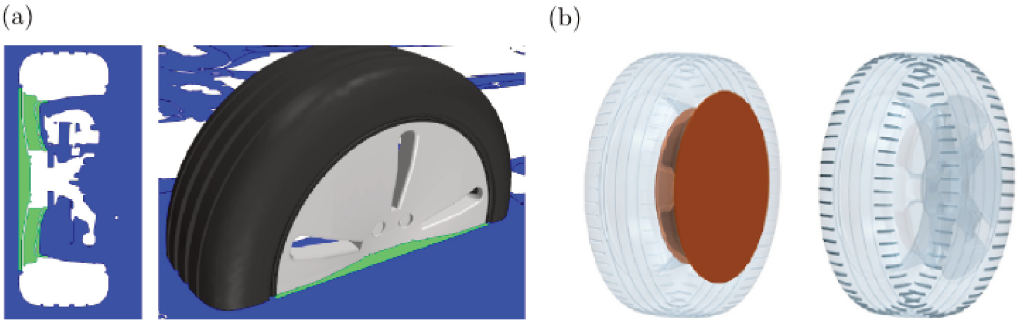

Figure 1.11: (a) The sliding mesh setup (Berg & Brandt, 2018), with the sliding mesh domain (green) and the outer domain (blue); (b) The hybrid approach proposed by Hobeika & Sebben (2018), with sliding mesh applied on the not closed rim (brown) and MRF applied on the lateral grooves.

1.4 Outline of the thesis

The above sections have addressed the sensitivity of the global aerodynamic forces and wake flow to underbody modifications, followed by the description of complex 3D flow behavior around isolated and shrouded wheels. For a passenger car, as the wheels are situated in the underbody, these bibliographical elements have put into context the importance of the wheel aerodynamics in relation to the whole vehicle.

Furthermore, as encouraged by MEPs, the electric vehicles will be more prevalent in the future. The electric vehicles have a smoother underbody, as the battery package is located between the wheelbase of the underbody, and there is no exhaust pipes. These lead to the lowering of the drag contribution coming from the underbody, whereas the increase of the drag ratio in other areas, including the wheels. However, due to the functionality of the wheels, they are not likely to have a more aerodynamically favorable shape. Therefore, to achieve further drag reduction, a better understanding of the wheel-vehicle interaction is of crucial interest. Nevertheless, the influence of the wheels on the flow around the vehicles remains open issues. For example, from an industrial point of view, the ranking by aerodynamic drag of different tires sometimes depends on vehicle geometry (Wittmeier *et al.*, 2013). While the mechanisms behind it remains poorly understood. The objective of the study is to clarify this interaction, by viewing the wheels as underbody perturbations, and analyzing their impact on the aerodynamic around a reduced-scale vehicle. We will give a detailed analysis in terms of the aerodynamic forces, base and underbody pressure distributions, vehicle wake and wheel wakes. The work is structured as follows:

Chapter 2 details the experimental and computational environments. The vehicle model used in our study, which originated from the ASMO model, is also presented. This model was chosen by Michelin and optimized with reference rotating wheels prior to the PhD work. This step is of fundamental importance. Indeed, a lot of works in the literature considered model bodies having well balanced wakes without wheels as a starting point of studying the influence of wheels. On the contrary, the strategy in our research will be starting from a body having a well balanced wake with four rotating wheels.

The first part of Chapter 3 describes the smooth model configuration, which is the vehicle model with polystyrene foam perfectly filling the wheelhouses and without wheels. This configuration naturally has a high underbody momentum flux thus a negative lift, and a non balanced mean wake with wall-normal asymmetry. It is used in Section 3.2 to study the influence of perturbations located at the rear part of the underbody. To do so, a pair of profiled obstacles is mounted at the two sides, underneath the plugged rear wheelhouses, to emulate the rear wheels. A parametric study is performed with different obstacle width.

In first section of Chapter 4, the profiled obstacles are firstly substituted by rear wheels as a more realistic approach. Based on Section 3.2, the effect of the rear wheel state (rotating or stationary) is discussed, in comparison with the profiled obstacles configurations. Next in Section 4.2, the front wheels are additionally included, which leads to the baseline configuration. The vehicle wake becomes well balanced, in contrast to the precedent configurations preserving the same wall-normal asymmetry to the smooth model configuration. In Section 4.3, wheel state investigations are carried out at the front or rear axle, modifying the well balanced wake of the baseline configuration.

In Chapter 5, we eliminate the vehicle diffuser in Section 5.1. With the recovered wake wall-normal asymmetry, the vehicle geometry influence on wheel-vehicle interaction is tackled. In Section 5.2 the effects of different tires are addressed, based on the local and global effects of the perturbations that have been investigated in previous chapters.

Finally, in Chapter 6 the overview of the main results and the outlook for future works are provided.

Chapter 2

Experimental and computational environments

In this chapter, the experimental and supplementary computational set-up are elaborated. The vehicle model used throughout the study is based on the Asmo model (Section 2.1.2). Its geometry are modified so that when four rotating wheels are present, the front wheel is subject to reasonable yaw angle, and the model has a realistic wake balance. In order to investigate the interference aerodynamic force between the vehicle and the wheels, acting on the car body, a 'wheel-off' configuration is adopted, which means the wheels are mechanically decoupled from the vehicle, and solely the aerodynamic forces of the vehicle is measured. This method also omit the measurement procedure of subtracting forces generated between the tire and its driven unit as the wheels are not measured. For configurations including wheels, the contact patch of the reduced scale Michelin tire is regulated, aiming at emulating the realistic tire deformation under load.

Contents

2.1 Experimental method

The design and implementation of the experimental set-up were performed during the PhD work. Figure 2.1 gives a general picture of the experimental set-up inside the wind tunnel, which will be elaborated in the following subsections.

Figure 2.1: General picture of the experimental set-up inside the wind tunnel working section.

2.1.1 Wind-tunnel apparatus

The experiments were undertaken inside the test section of the subsonic closed-loop wind tunnel S620 (Figure 2.2) in Institute Pprime in Poitiers, France. It has a contraction ratio of 7 : 1, with a rectangular test section of $6.2m^2$ ($2.4m$ (width)×$2.6m$ (height)). The maximum free-stream velocity can reach $60m/s$ and flow stability in the tunnel is ensured for velocities greater than $5m/s$. The turbulence intensity is approximately 0.5%.

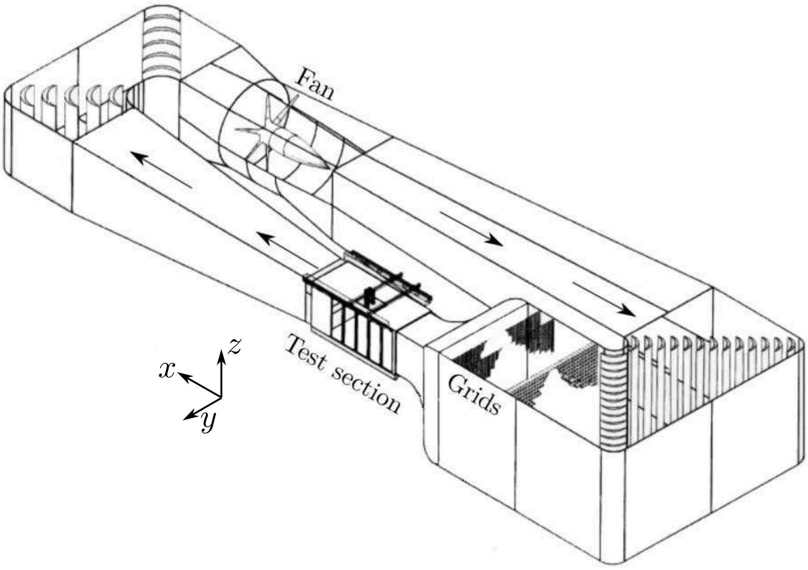

Figure 2.2: Schematic of wind tunnel facility. The arrows inside the tunnel indicate the direction of the generated flow.

According to the experimental set-up, a sketch of the vehicle model in the test section is portrayed in Figure 2.3. The geometry of the vehicle model will be presented in detail in

Section 2.1.2. The vehicle is held by a profiled support overhead throw the ceiling of the wind-tunnel, above a raised floor. The raised floor is a flat plate with an elliptical leading edge to control the boundary layer thickness. At the end of the elliptical leading edge, a band of rough tape is applied to trigger the transition to turbulent boundary layer.

With 16 pressure taps, symmetrically drilled through the upper and lower surface of the raised floor immediately downstream the leading edge, and an adjustable trailing edge flap at the end of the raised floor, we managed to control the incident angle of the flow contouring the leading edge. To obtain a zero incident angle, same pressure level needed to be ensured at the upper and lower surface of the raised floor. This is achieved without the vehicle model, and with the flap angle set at $\alpha_{\text{Flap}} = 3.1°$. After this adjustment, the model is mounted at $0.3L_V$ downstream the leading edge, and $1.06L_V$ upstream the trailing edge. The ground clearance G is fixed at $0.04L_V$. The blockage ratio of the model's frontal surface with respect to the upper area above the raised floor is 7%. The Cartesian coordinate systems is denoted by X, Y, Z representing streamwise, spanwise (or lateral) and transverse (or wall-normal) directions. $Y = 0$ is the symmetrical plane. For the wake investigations with PIV measurements, the origin of the coordinate system corresponds to the point on the raised floor at the mid-span and rear end of the model, as delineated in Figure 2.3(a). While to describe the geometry of the vehicle and the positions of the pressure sensors, the origin of the X coordinate is set at the front wheel center, and $Z = 0$ corresponds to the lower surface of the vehicle (Figure 2.3(b)).

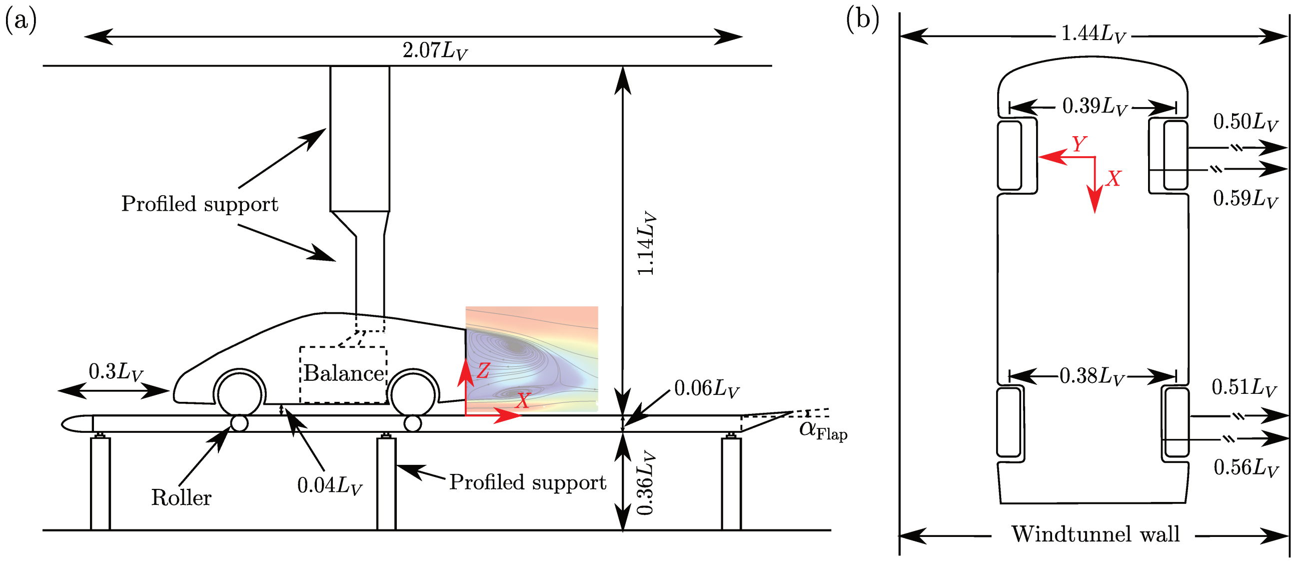

Figure 2.3: Experimental set-up details: (a) Positioning of the model inside the wind-tunnel working section, above the raised floor, in XZ plane. The PIV field in the symmetric $Y = 0$ plane is also illustrated; (b) The positioning in the XY plane and the front and rear tracks. $L_V = 1668mm$.

To focus on the interference aerodynamic force between the vehicle and the wheels, acting on the vehicle body, the four wheels inside the wheelhouses are mounted mechanically decoupled from the vehicle model. This is known as a 'wheel-off' configuration (Knowles, 2007), in contrast to the real suspension system inside the automobile settings. In this approach, we only measured the aerodynamic forces of the vehicle. This method also omit the measurement procedure of subtracting forces generated between the tire and its driven unit as the wheels are not measured.

The wheels are fixed by four individual stings shrouded with symmetric airfoil (Figure 2.1). The tire information and the contact patch regulation will be detailed in Section 2.1.3. The stings are held by four pairs of supports fixed at the outboard side of the wheels near the wind-tunnel inner wall. Four individual drive units placed inside the raised floor allow the rotation of the wheels. The individual drive unit composes of a roller (Figure 2.3(a)), and a motor which drives the roller (Figure 2.8(b)). Each wheel is in direct contact with a roller. For the stationary tests, the motors are shut down so that the rollers and the wheels are still. For the rotating tests, the motors actuate, allowing the rotation speed of the wheel to match with the freestream speed so as to simulate the vehicle moving forward through still air. The experiments are conducted at $V_0 = 28ms^{-1}$, corresponding to $Re_{L_V} = 3.10^6$. The freestream velocity is limited by the operating limitation of the motors in the drive units. At this freesteam velocity, the rotating speed of the motor is 5629 tr/min. The boundary layer thickness on the ground was not measured. While according to the experiments of Barros (2015); Li (2017) in the same wind tunnel with a similar raised floor, at a Reynolds number one order of magnitude lower than ours, the boundary layer was proved to be turbulent. The boundary thickness on the ground based on 99% of the free-stream velocity was typically $10mm$, at a streamwise position approximately at the entry of the underbody, with or without the model in the test section. Thus the boundary layer is estimated to be smaller than $0.15G$ at our operating Reynolds number.

Figure 2.3(b) provides the front and rear axle tracks. At first, they were both set at $640mm$, so that the tire side wall was flush to the vehicle side. However, it has been observed that for these tracks, when wheels were in rotation, the model featured important oscillatory behavior in the yaw and roll motion. This is reminiscent of an isolated rotational wheel investigated by Pirozzoli *et al.* (2012), where significant oscillations in the wheel's side force were recorded yet with a zero time-averaged mean value. The four rotational wheels inside the wheelhouses probably do not have zero mean side force. As a consequence, they may create changing and oscillatory suction to the vehicle which results in the oscillatory motion of the model. In order to limit this oscillation, it is required to enlarge the axle track. After several tests, with each front wheel moved $2mm$ outboard in the Y direction, we achieved to debilitate the oscillation. The front axle track is finally set at $644mm$ and the rear axle track at $640mm$. To better ensure the stability of the vehicle and to help keep the profiled support straight, four guy-wires, which are tensioned cables, are installed, as can be seen in Figure 2.1. One end of the guy is attached to the vertical support, and the other end is anchored to the wind tunnel inner wall. At the operational position, the guy end fixed on the profiled support is lower in vertical position. This ensures that the support can lift vertically the vehicle model without constraint, to facilitate operations like inflating the tires or change the wheels. At the same time, the tensioned cables prevent the model from descending below this ground clearance ($0.04L_V$) position.

2.1.2 Vehicle model

The tested vehicle is a 2/5th-scale model with respect to the size of a typical passenger car. It is originated from the Asmo model. The Asmo model was created in Daimler Benz research department nearly twenty years ago, which was not related to any actual Mercedes cars of the time, in order to achieve a low aerodynamic drag and to test CFD-codes. It is available for the public on internet. It has a square back rear, smooth surface, boat tailing and an underbody diffuser (see Figure 2.4). The model is characterized by no pressure induced boundary layer separation and low drag coefficient: from 0.15 to 0.18 in the literature (Perzon & Davidson, 2000; Aljure *et al.*, 2014), when compared with the typical Ahmed body (0.23-0.38 from Ahmed *et al.* (1984)).

This model is often used to compare with the experimental surface pressure measurements (Perzon & Davidson, 2000) to validate the turbulence models for simulations (Nakashima *et al.*, 2008; Tsubokura *et al.*, 2009; Xflow, 2010). However not much information of the fluid dynamics around the Asmo model was available. The only published detailed flow structures around the Asmo model was made by Aljure *et al.* (2014) using large-eddy simulations. They portrayed

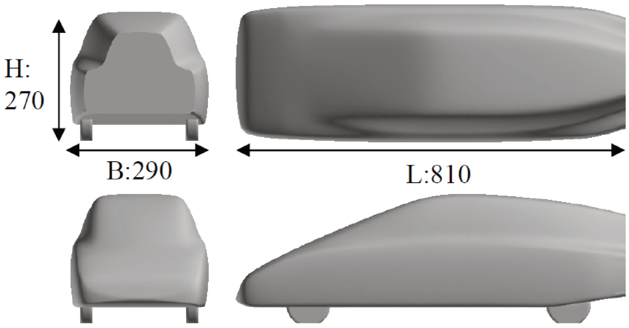

Figure 2.4: The dimension of the 1/5th-scale Asmo model (units in millimeters).

the generation of the main longitudinal vortices (Figure 2.5(a)) as the interaction among the high speed stream along the side, the slow speed stream in the back and the main flow traveling along the top (Figure 2.5(b)). The recirculation region has the shape of a horseshoe toroidal vortex bounded by the flow coming from the sides and the top of the body (Figure 2.5(c)). They also pointed out that the longitudinal structures around the Asmo car are much weaker and exhibit less turbulent behavior than those found around the Ahmed car with the 25° slant back.

However, the Asmo model does not have real wheelhouses and its aspect ratio (length/width) is not much akin to typical passenger cars. ACE (Aero Concept Enginneering) slightly modified its geometry at Michelin's request, by adding wheelhouses, adjusting its fore-body length and aspect ratio to achieve a reasonable angle of attack for the front wheels, in order for wheel aerodynamic studies. The diffuser angle was equally modified to obtain a realistic wake balance, similar to that of an estate and hatchback car. It leads to the model that we use in the experiments, whose geometry is detailed in Figure 2.6. The black dots are positions of the pressure taps. The pressure measurements will be presented shortly in Section 2.1.4.

2.1.3 Tires and contact patch regulation

The wheels are equipped with reduced scale (2/5th-scale) Michelin tires having a realistic deflected shape of a 205/55 R16 tire. The diameter is approximately $254mm$ and the width is around $82mm$. Shown in Figure 2.7(a) is the reference tire, with three longitudinal grooves on the tire tread, and is used in most of the experiments (Chapter 4). Apart from that, two other types of tires are investigated in comparison with the reference one. Figure 2.7(b) is on the basis of the reference tire, additionally having carborundum powder glued on the flank, aiming at representing tire sidewall marking. Figure 2.7(c) is referred to as a 'slick tire' without grooves, which is similar to a competition tire. Their aerodynamic effects will be presented in Section 5.2.

In the experiments the surface of the tire contact patch is regulated to emulate the realistic tire deformation under load. For a typical European market passenger car which weights about $1.4t$, the load of one front wheel is approximately $400daN$, and it is $300daN$ for one rear wheel. Assuming that tire inflation pressure is about $2.5bar$ and is equal to ground contact pressure, the contact patch surface is thus reckoned to be $160cm^2$ for the front tire and $120cm^2$ for the rear tire. For our vehicle model whose scale is 2/5, neglecting the contact patch difference in front and rear tire, this gives roughly a contact patch of $23cm^2 \approx 4.3cm(in\ X) * 5.4cm(in\ Y)$ for each tire. In order to limit tire damage and excessive load on the rolling system, we inflated the 2/5-th scale tires to $1bar$. As the wheels are decoupled from the vehicle, a proper contact patch is then achieved by adjusting the wheel center height at tire inflation pressure of $1bar$.

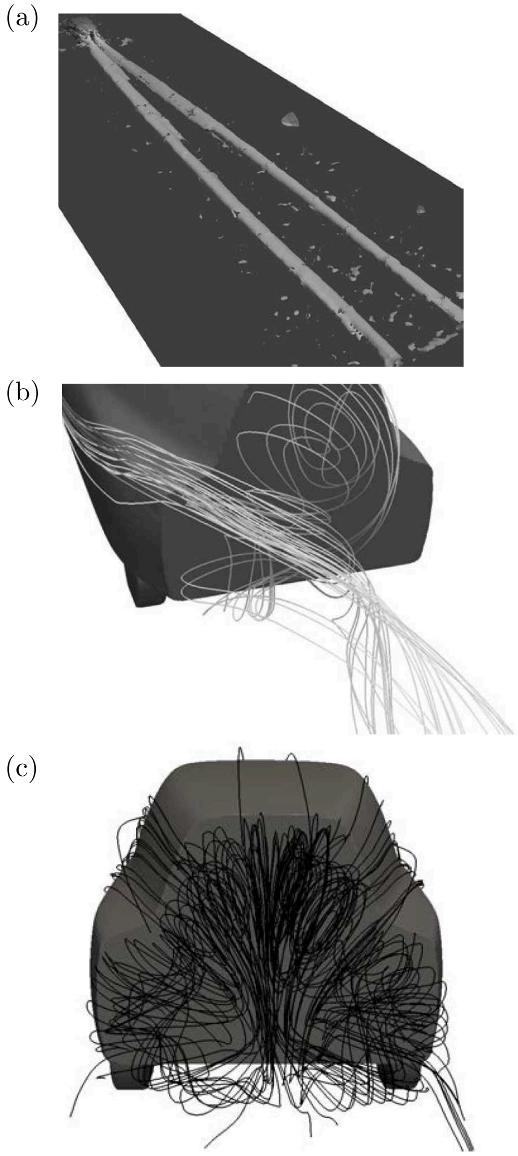

Figure 2.5: (a) Iso-contour of $Q = 0.1$ behind Asmo model indicating the two longitudinal vortices; (b) Time-averaged streamlines illustration the formation of the longitudinal vortices; (c) Recirculation regions in the wake. (Aljure *et al.*, 2014)

With the help of a *Tekscan Pressure Mapping* system the static contact patch can be visualized in real time (Figure 2.8(a)). This system is composed with a thin sensor, which can be put between the wheel and the roller to detect the interface pressure; a data acquisition electronic, that can scan the sensing points within the sensor; and a software, which displays the pressure distribution. The visual footprint displayed by the software is thus deemed as the contact patch. In our configuration, the contact surface is slightly different from the real contact patch because of the small radius of the roller supporting the wheel. There is no doubt that a larger roller radius can better simulate the road. Nevertheless, in order to hide the roller inside the raised floor, with its apex flush to the upper surface of the floor, the size of the roller is limited by the thickness of the raised floor. In this situation, the length (in the X direction) of the contact surface is curved due to the small radius of the roller. As a result it is difficult to guarantee the proper contact patch length ($4.3cm$ in the X direction). Thus we consider the width (in the Y direction) of the output contact surface to be the priority parameter, which is aimed approximately at $5.4cm$.

To determine the correct wheel center height that ensures the proper contact patch width,

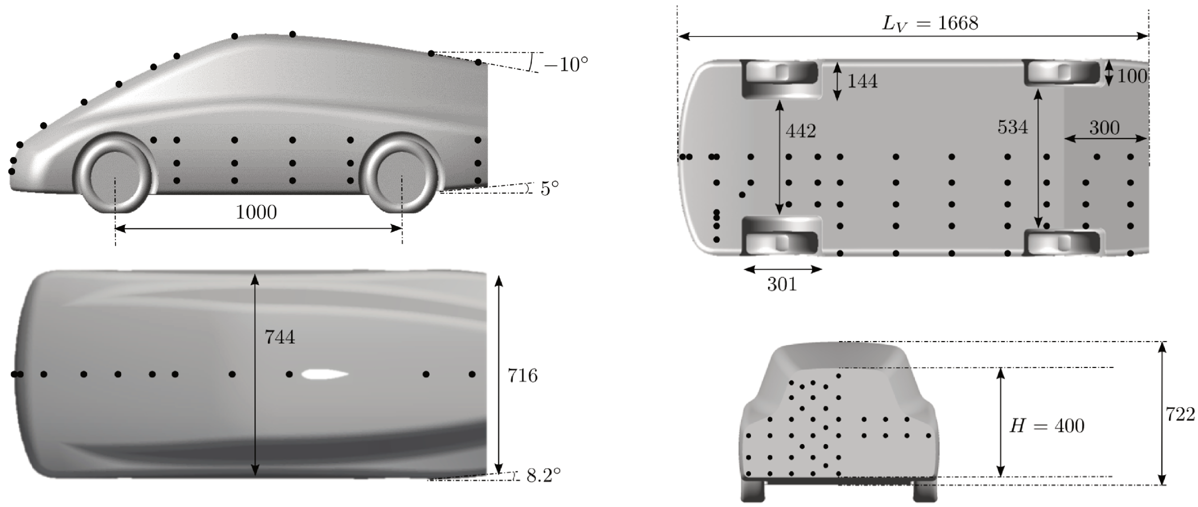

Figure 2.6: The dimension of the vehicle model (units in millimeters) with the locations of the pressure sensors in black dots. The size of the profiled support can be visualized from the top view of the vehicle.

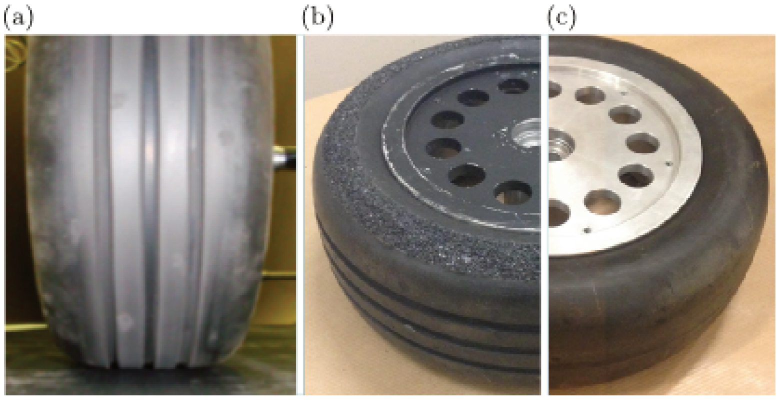

Figure 2.7: Three types of tires investigated in the study. See text for descriptions.

we need to modify the height of the sting supports fixed on the floor, located at the outboard side of the wheels near the wind-tunnel inner wall. The sting supports were initially made with a height equal to the radius of the wheel. With the thin sensor lying between the wheel and the roller, we observed insufficient contact patch width. Thence we gradually elevated the roller vertically in its rail inside the raised floor (Figure 2.8(b): *i.Elevate*) until the visible contact surface displayed on the software reaches the target width. The vertical displacement of the roller was noted down. Then the wheel, the sting and the wheel support were dismantled. We cut out the same distance as the noted displacement from the bottom of the support (Figure 2.8(b): *ii.Cut*). The target height of the support is therefore achieved. Finally we lowered the roller to its initial position inside the raised floor (Figure 2.8(b): *iii.Descend*) and we re-mounted the support, the sting and the wheel. The wheel center height was ultimately settled at $122mm$ for the following experiments.

2.1.4 Pressure measurements

Pressure taps are drilled through the vehicle wall and connected to two ‘miniature electronic pressure scanners’ EPS using vinyl tubes inside the model, to allow the pressure measurements on the vehicle surface. Both scanners are equipped with 64 channels. They are connected to the measurement chain outside the wind tunnel test section by a wire going through the profiled support of the model. Data acquisition duration was $120s$ at $100Hz$, giving access to

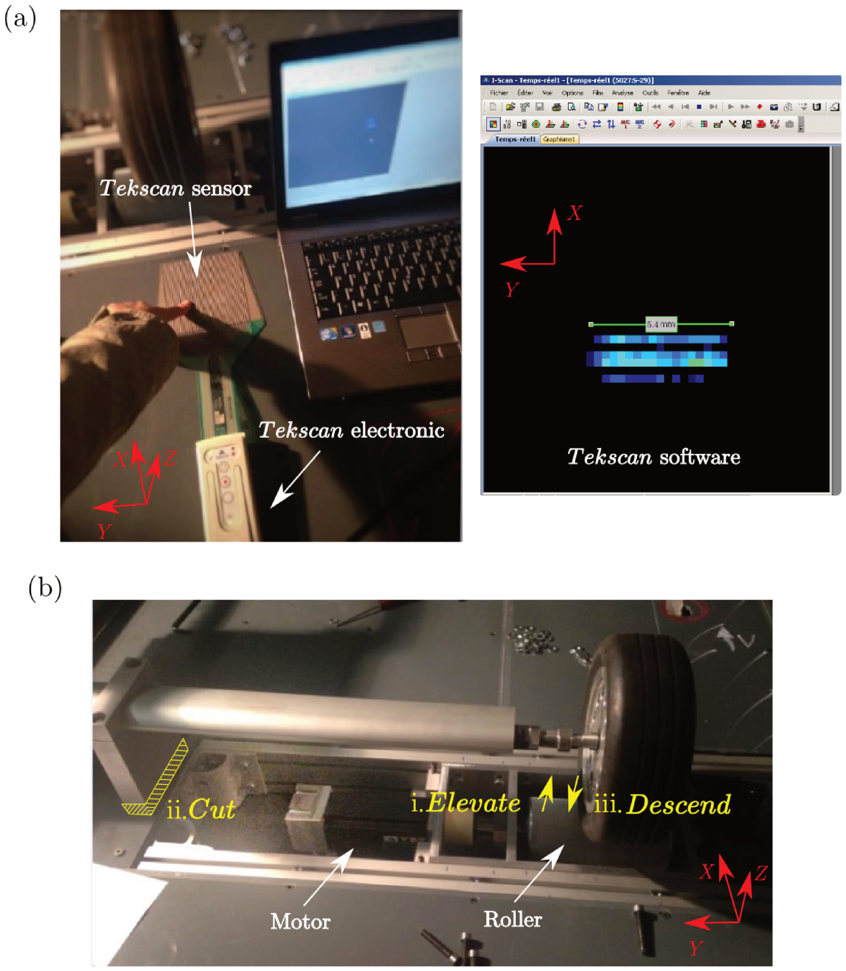

Figure 2.8: (a) *Tekscan Pressure Mapping* system for contact patch visualization; (b) Contact patch regulation steps (see text for details).

the average pressure value. The pressure coefficient is defined as:

$$Cp = \frac{p - p_{ref}}{\frac{1}{2}\rho V_0^2} \tag{2.1}$$

The upstream mounted pitot-static probe at the inlet of the wind tunnel test area gives the reference static p_{ref} and the total pressure, which can be used to determine the average velocity of the wind V_0. The full ranges of the two scanners are respectively $1PSI$ ($1PSI = 6894.76Pa$) and $1000Pa$, with static accuracy of 0.1% of their ranges, which correspond respectively 0.014 and 0.002 in Cp.

The vehicle model is equipped with 203 pressure taps in total. Two rounds are needed to cover all the surface pressure measurements as there are only 128 channels. The locations of the pressure taps (except inside the front and rear wheelhouses) are demonstrated in Figure 2.6. Among them, 196 pressure taps are located on the body's right half ($Y \leqslant 0mm$): 12 taps on the roof symmetrical line, 16 taps on the sidewall, 55 in the front wheelhouse, 29 in the rear wheelhouse, 51 on the underbody surface, 33 in the base; and with another 7 pressure taps on the left half of the base ($Y > 0mm$). The 7 pressure taps on the left can be used to check the symmetry of the time-averaged flow. An indicator Sym_ind is calculated to quantify the degree of asymmetry of the flow, by averaging the differences between the two symmetric (left and right) pressure taps on the base (7 pairs in total). The measurements with a high Sym_ind should be taken with caution. For that a threshold of $Sym\_ind = 0.008$ is set, which corresponds to a left-right pressure average difference of $4Pa$ (the pressure scanner connected with the base pressure taps has a range of $1000Pa$ with an accuracy of $1Pa$). In the following sections, the distributions of the base and the underbody pressure will be presented not only with the measurements at the right side but they will also be symmetrized to the left side to facilitate the visualization. Besides, the coordinates will be normalized by the base height $H = 400mm$: $x = X/H$, $y = Y/H$, $z = Z/H$. In Figure 2.6(a) and (b), the symmetrized pressure distributions on the base and in the underbody after interpolation are shown. Figure 2.6(c) and (d) give an example of the interpolated pressure distribution on the side body and inside the front and rear wheelhouses.

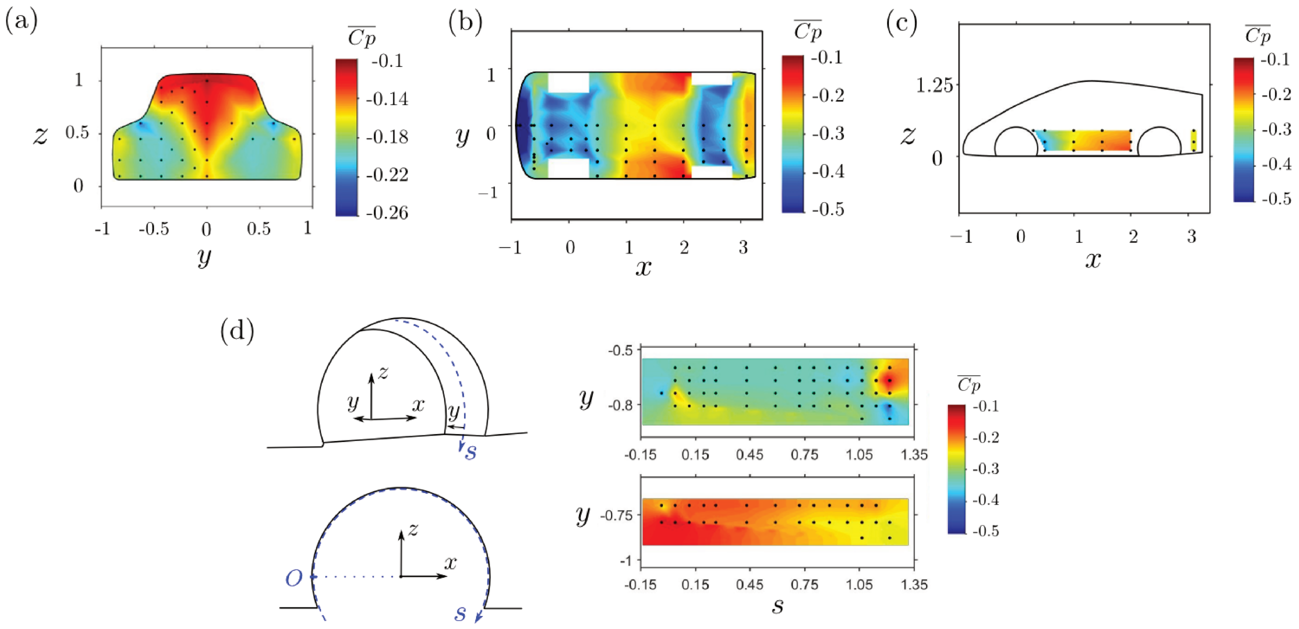

Figure 2.9: Examples of the the pressure distributions on the base (a), in the underbody (b), on the side body (c), and inside the front and rear wheelhouses (d). The coordinates are normalized by the base height.

2.1.5 Force measurements

The aerodynamic drag Fx and lift Fz exerting on the vehicle are measured by a balance embedded inside the vehicle, held by the profiled support (Figure 2.10(a)). The balance is specifically designed for this study and is composed of piezoelectric high sensitive quartz sensors (Figure 2.10(b)). There are 3 lift sensors (9331B Kistler) and one drag sensor (9217A Kistler), which are able to measure compression and tensile forces in the z and x directions.

During the test, induced by the the aerodynamic forces, the piezoelectric quartz crystals in the sensors yield electric charge proportional to the forces. The charge signal is then fed via a screened cable passing through the profiled support to a charge amplifier outside the wind tunnel test section. The charge amplifier converts the signal into proportional output voltage. The forces Fx and Fz are then calculated with the output voltage and with the calibration coefficients. The calibration coefficients were obtained from the balance calibration performed by the use of standard masses up to $10kg$. However, to calculate the time-averaged aerodynamic forces in the conditions of the experiments, the inherent drift in output signal for piezoelectric force measuring devices (Mack, 2003) needed to be taken into consideration. Admittedly, the small linear drift can be easily removed by measuring the drift rate α using signals in quiescent air. To do so, the measurement procedure is set as delineated in Figure 2.11(a). The drift

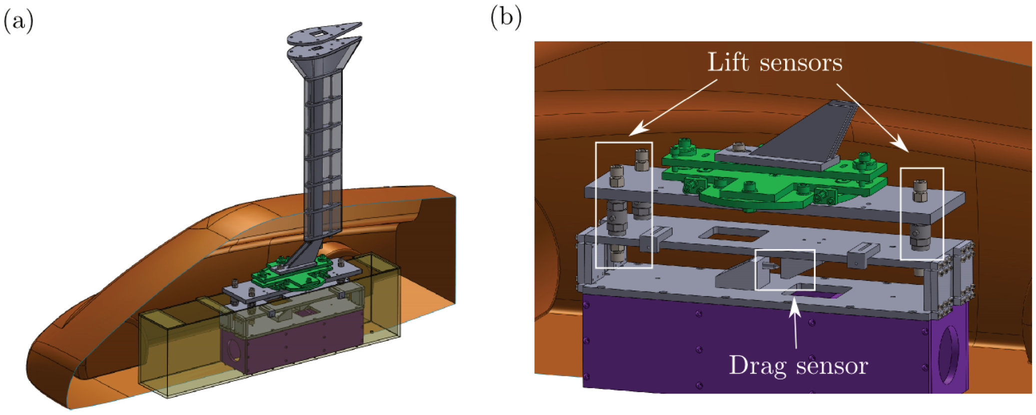

Figure 2.10: (a) Inner view of the vehicle, with the balance inside, and held by the profiled support; (b) The lift and drag sensors in the balance.

rate α is calculated from the force measurements before the onset of the wind and wheel rotation, and after the stop of the wind and wheel rotation (red intervals in Figure 2.11(a)). Then the corrected signal (green line in Figure 2.11(b)) is obtained by subtracting αt from the recorded data (red line). The drift rate α depicted in Figure 2.11(b) is exaggerated. Indeed, the maximum drift force at the end of the measurements is no larger than 5% of the measured mean force.

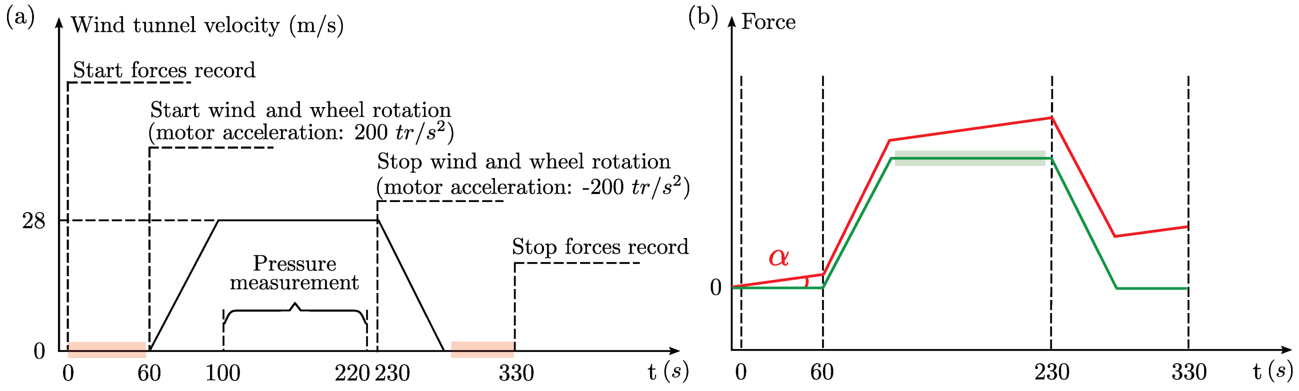

Figure 2.11: (a) The measurement procedure. The force measurements in red intervals are used for drift rate estimation; (b) An example of recorded force (red line) with drift rate α, and corrected force (green line) during one measurement. The time-averaged force coefficient is calculated from the data in green interval.

The acquisition is performed at $100Hz$. The corresponding time-averaged drag and lift coefficients are reckoned from the green interval shown in Figure 2.11(b):

$$Cx = \frac{\overline{Fx}}{\frac{1}{2}\rho V_0^2 s} \qquad Cz = \frac{\overline{Fz}}{\frac{1}{2}\rho V_0^2 s} \tag{2.2}$$

where ‘s’ is the total projected frontal area. Finally, the force coefficients are expressed in terms of SCx and SCz in full-scale where $S = (5/2)^2 * s = 2.12m^2$. The drag sensor has a range of $\pm 500N$ with a precision of $0.01N$, corresponding SCx of $1.3\times10^{-4}m^2$. The range of the three lift sensors is $\pm 20kN$ each with a precision of $0.02N$, corresponding SCz of $2.6\times10^{-4}m^2$.

2.1.6 PIV measurements in the vehicle wake

Two-component Particle Image Velocimetry (PIV) is applied to investigate the velocity fields in the near wake of the model. It is a non-intrusive, optical measurements technique used for the successive measurement of instantaneous velocity within a planar domain of interest. It is performed by seeding the flow with neutrally buoyant tracer particles, illuminating the particles in the plane of interest using laser sheets and capturing pairs of images with a small time shift. The velocity of the particles can be statistically determined by comparing the image pairs. Our PIV system comprises a dual pulse Nd:YAG laser and a Lavision Imager LX 16M camera with a resolution of 4920 × 3280 pixels. Three planes in the wake are investigated during the experiments, as depicted in Figure 2.12. They are the symmetrical plane $Y = 0mm$, horizontal plane $Z = 216mm = 0.54H$, and $Z = 48mm = 0.12H$ which is approximately at the half of the ground clearance at the diffuser exit. The time shift between the one pair of images is $60\mu s$ and each acquisition records 1000 image pairs at a rate of $4Hz$. Lavision software Davis 8.3.1 has been used to calculate the velocity fields. The vector calculation is done using double-pass, dual frame cross-correlation on constant window size. The interrogation window size is 64×64 pixels with a 50% overlap for the first pass and 32×32 pixels with a 50% overlap for the second, giving a spatial resolution of $5mm$. Considering an absolute displacement error of 0.1 pixel, the maximum uncertainty on the instantaneous velocity fields is estimated to be 0.26 ms^{-1}. In the following sections, the data from the PIV measurements will be normalized by H and V_0.

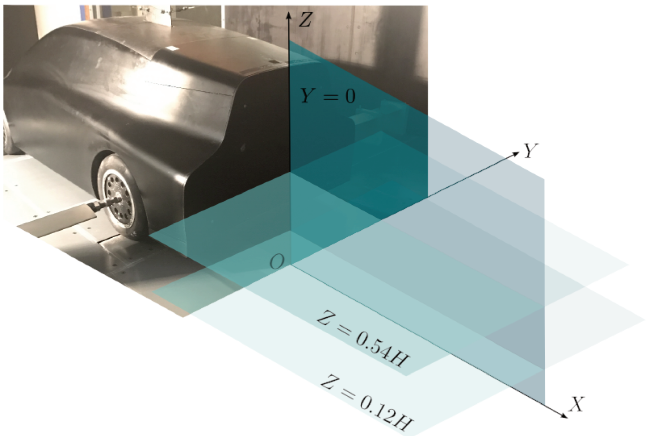

Figure 2.12: The position of the PIV measurement planes.

2.2 Numerical approach

CFD simulations utilizing commercial code LaBS, built on the Lattice Boltzmann Method, have been performed to support the experimental work. This solver has been developed within a consortium of industrial companies (Renault, Airbus, CS), academic laboratories (UPMC, ENS Lyon) and strong partnerships with others entities (Onera, Alstom, Paris Sud University, Gantha, Matelys) (Lucas *et al.*, 2017). The simulation of certain configurations in our study was directly run by Gantha engineer.

2.2.1 General introduction of the lattice Boltzmann solver

In recent years, the lattice Boltzmann method (LBM) has become a promising alternative numerical approach for simulating complex fluid flows. Unlike the conventional numerical schemes based on Navier-Stokes equations, the lattice Boltzmann method describes a fluid flow in terms of a discrete kinetic equation based on the particle density distribution functions f (Chen *et al.*, 1991):

$$f_i(\mathbf{x}+\mathbf{c}_i\Delta t, t+\Delta t) = f_i(\mathbf{x}, t) + \Omega_i(f(\mathbf{x}, t)), \qquad (i = 0, 1 \cdots, b) \tag{2.3}$$

In this equation, f_i represents the number of fluid particles along ith direction, according to a finite set of the discrete velocity vectors $\mathbf{c}_i$: $i = 0, ..., b$ on a regular square lattice. Therefore the velocity vectors are discretized both in direction and in magnitude with weight coefficient in different direction (some schemes for the discretisation are shown in Figure 2.13). $\mathbf{x}$ is the position in space. Δt is time increment. For convenience, we choose the convention $\Delta t = 1$ in the subsequent discussions. At the right-hand side of the equation is the collision term. It represents the change of f_i due to collision.

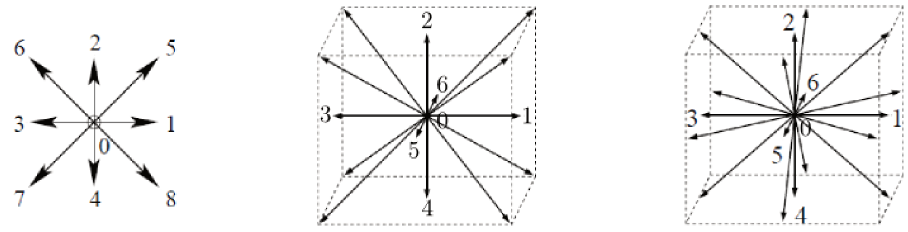

D2Q9 D3Q15 D3Q19

Figure 2.13: Examples of LBM discretisation of velocity space. The Lattice structure models are named DnQb, where D represents the dimension and Q for total number of the direction (Wagner, 2008).

The collision term may have different forms. The most popular collision form is the Bhatnagar–Gross–Krook (BGK) approximation (Krook *et al.*, 1954; Chen *et al.*, 1992; Qian & Orszag, 1993). They assumes that the main effect of collisions is to bring the distribution function closer to the equilibrium distribution, which is derived from the Maxwell-Boltzmann distribution. The simplest way of approximating the collision term is by using a single relaxation time τ (which is related to the macroscopic fluid viscosity): the local particle distribution relaxes to an equilibrium state f_i^{eq} at a single rate τ:

$$\Omega_i = -\frac{f_i - f_i^{eq}}{\tau} \tag{2.4}$$

Combining (2.3) and (2.4) the LBGK (lattice Boltzmann Bhatnagar–Gross–Krook) equation reads:

$$f_i(\mathbf{x}+\mathbf{c}_i, t+1) = f_i(\mathbf{x}, t) - \frac{f_i - f_i^{eq}}{\tau} \tag{2.5}$$

Separating (2.5) into the following two steps, we obtain the classical lattice Boltzmann formulation as:

$$\begin{aligned} &collision: \tilde{f}_i(\mathbf{x}, t) = f_i(\mathbf{x}, t) - \frac{f_i - f_i^{eq}}{\tau} \\ &streaming: f_i(\mathbf{x}+\mathbf{c}_i, t+1) = \tilde{f}_i(\mathbf{x}, t) \end{aligned} \tag{2.6}$$

The particles are first redistributed through the collision step when they interact and change their velocity directions; then each particle moves to the nearest lattice node in the direction of its velocity during the streaming step. So the general algorithm starts from the initial distribution functions, and then enters the collision-streaming loop for evolution, which can be stopped if certain condition is satisfied. The local computational nature of this explicit scheme allows for an efficient parallelization of the solver (Chen *et al.*, 1997).

The local equilibrium distribution function f_i^{eq} depends on local hydrodynamic properties for example density ρ and velocity $\rho\mathbf{u}$. And these quantities can be obtained through the velocity moments of the distribution function:

$$\rho = \sum_i f_i, \qquad \rho\mathbf{u} = \sum_i f_i\mathbf{c}_i \tag{2.7}$$

where $\sum_i \equiv \sum_{i=1,}^{b}$.

To recover macroscopic hydrodynamics, the local equilibrium distribution should obey the mass, momentum conservation laws at each lattice. Moreover the lattice structure have to be specified to achieve as high order of accuracy as possible with fixed number of discrete velocities (Chikatamarla, 2008; Peng, 2011). In the three-dimensional situation, one of the common choices is the D3Q19 model (Figure 2.13) (Qian & Orszag, 1993; Chen *et al.*, 1997), which is used in LaBS, where the equilibrium state f_i^{eq} takes the form:

$$f_i^{\mathrm{eq}} = \rho w_i[1 + 3\mathbf{c}_i \cdot \mathbf{u} + \frac{9}{2}(\mathbf{c}_i \cdot \mathbf{u})^2 - \frac{3}{2}u^2] \tag{2.8}$$

where w_i are weight coefficients: $w_0 = 1/3$, $w_{1-6} = 1/18$, and $w_{7-18} = 1/36$, with the direction numbers portrayed in Figure 2.13. Based on the Chapman–Enskog multiscaling expansion, which assumes the diffusion time scale being much slower than the convection time scale (Latt, 2007), with the Knudsen number as the expansion parameter (Chen & Doolen, 1998), the nonlinear incompressible Navier–Stokes equations can thus be recovered from (2.5) under the assumption that the Mach number remains small ($M \leq 0.4$). In contrast to the direct numerical simulation of the NS equations, where Poisson equation needed to be solved to obtain the pressure, in LBM, by the perfect gas law, the pressure p is calculated locally with a linear relation with density and temperature T (Peng, 2011),

$$p = \rho T \tag{2.9}$$

And T is the lattice temperature which is set to 1/3 for isothermal simulations. The relaxation time τ is related to the viscosity by the fluid viscosity ν through the relation (Chen *et al.*, 1991, 1992, 1997; Frisch *et al.*, 1986)

$$\nu = \left(\tau - \frac{1}{2}\right)T \tag{2.10}$$

Imposing boundary conditions accurately and stably is crucial for lattice Boltzmann method. The particle bounce back process is mostly applied to simulate no-slip boundary condition where the particle velocity direction are reversed on the solid boundary. While for free-slip boundary condition, the particle specular reflection process is often implemented that reverses the normal velocity components and maintains the tangential velocity directions (Li *et al.*, 2004). The two methods are sketched in Figure 2.14. However, this scheme fails to provide accurate and smooth results on curved geometries as it could only attain first order of accuracy (Chen *et al.*, 1997). For curved boundary, which is more realistic from the physical point of view, interpolation and extrapolation are needed to approximate the variables sitting on the boundary nodes away from the boundary wall in the Cartesian grid, in order to achieve second order of accuracy (Peng, 2011; Succi & Succi, 2001).

To achieve computation efficiency, variable resolution (VR) regions are used in LaBS. The hierarchical grid-refinement method (Filippova & Hänel, 1998) cascade inwards from coarse resolution region towards fine resolution region close to the surfaces. The mesh size differs by

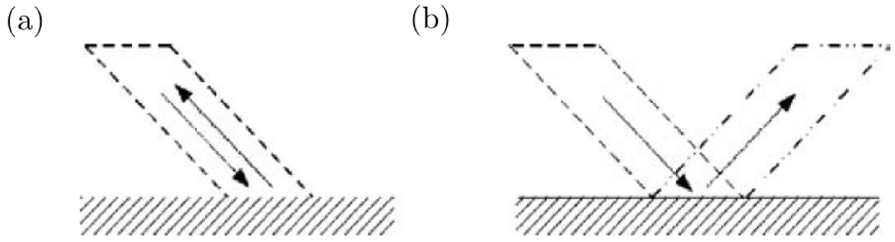

Figure 2.14: Implementation of boundary condition with (a) bounce back and (b) specular reflection in the LBM (Li *et al.*, 2004).

a factor of two between two adjacent VR regions. Such a treatment can conserve local mass and momentum and give continuous fluid density and velocity across VR boundaries (Li *et al.*, 2004).

Large eddy simulation (LES) is implemented in LaBS to model the turbulent flow. The subgrid-Scale turbulence effects were simulated through the Shear-Improved Smagorinsky Model (SISM) (Lévêque *et al.*, 2007; Lucas *et al.*, 2017). LaBS uses a wall law accounting for adverse pressure gradient (Afzal, 1996), curvature and roughness effects (Patel & Sotiropoulos, 1997).

2.2.2 Simulation case set-up

The model geometry is the same in the experiment. The inlet velocity is set to $U_0 = 28ms^{-1}$ same as in the wind tunnel leading to a Reynolds number $Re_{L_V} = 3.10^6$. The inflow is uniform without any turbulence injection. The outlet pressure condition is fixed to $p_0 = 101325Pa$. The extent of the computation domain is 44.8 m × 13.6 m × 7.15 m. As the vehicle in the wind-tunnel is mounted $500mm \approx 0.3L_V$ downstream of the leading-edge of the raised floor, to reproduce the boundary layer that impacts the model similar to the experiment, a no-slip condition is placed $500mm$ upstream of the model on the ground. Moreover, tire profiles under on-road conditions are applied in the CFD configuration.

Variable resolution regions are implemented using boxes and geometry offsets, as can be seen in Figure 2.15. 5 levels of resolution domains are employed from the smallest mesh size VR1 $1.5mm$ to VR5 $24mm$ with a factor of 2 between two adjacent VR regions. A total of 30 million nodes were used in the mesh.

The time step is $dt = 6 \times 10^{-6}s$. Time in non-dimensional unit is defined as $t^* = tU_0/L_r$. Computations are performed over a total $t^* = 50$ TU (time unit) corresponding to approximately 500 000 iterations. Integrated efforts over the whole geometry are recorded over time. They are used to monitor the convergence of the simulations as shown in Figure 2.16 for one configuration. From 15 TU the results are considered converged (corresponding to 150 000 iterations), and the flow is averaged until the end of the iteration, which corresponds to a total useful time unit $t^*_u = 35$. Simulations were carried out on a cluster of Intel(R) Xeon(R) E5-2680 v2 cores, with 3.2 Gb of RAM per core. The average computational time needed on 500 cores was nearly 14h for the simulations over $t^*_u = 50$.

In Figure 2.16(a) and (b) are respectively aerodynamics forces for the vehicle model with and without profiled support overhead. The simulations were initially carried out with the profiled support to better ensure the consistency with the experimental setup. The influence of the support on the vehicle has been discussed in Heft (2014). They reported a horseshoe vortex developing at the junction of the support and the vehicle, while only visible in the relevant locality. Moreover, it has little influence on the drag coefficients, which is estimated to be not larger than 3-5 counts. And no influence on the lift coefficient was found. However in our

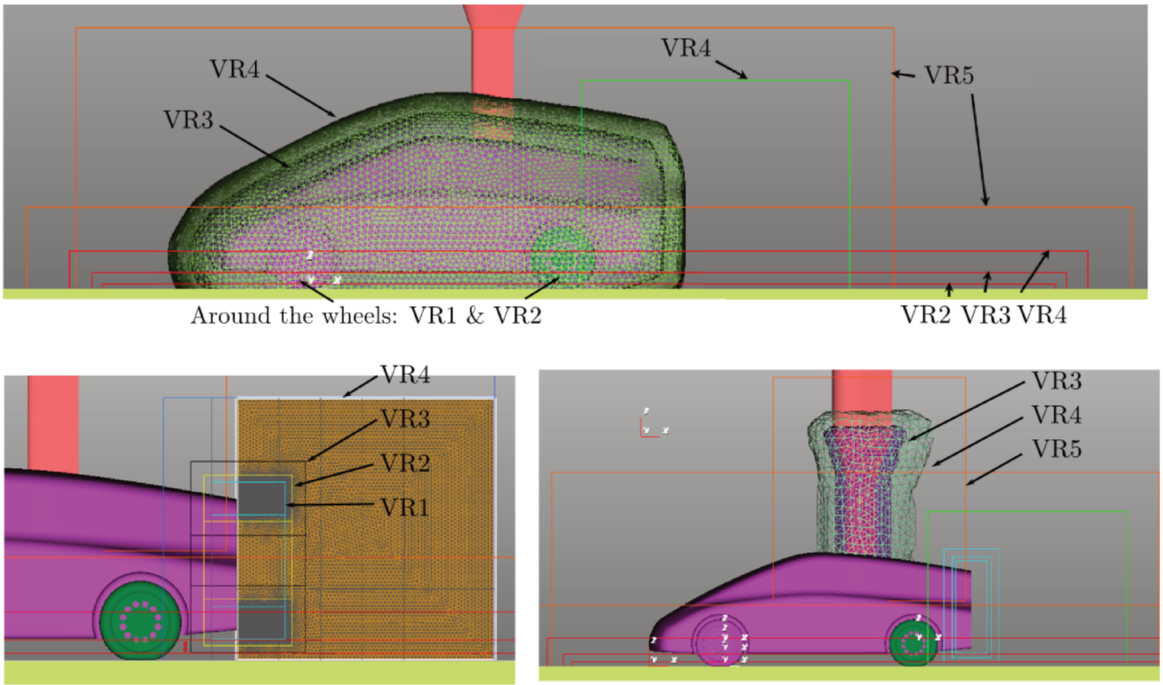

Figure 2.15: Variable resolution regions around the body. The mesh size for VR1 to VR5 is respectively $1.5mm$, $3mm$, $6mm$, $12mm$ and $24mm$.

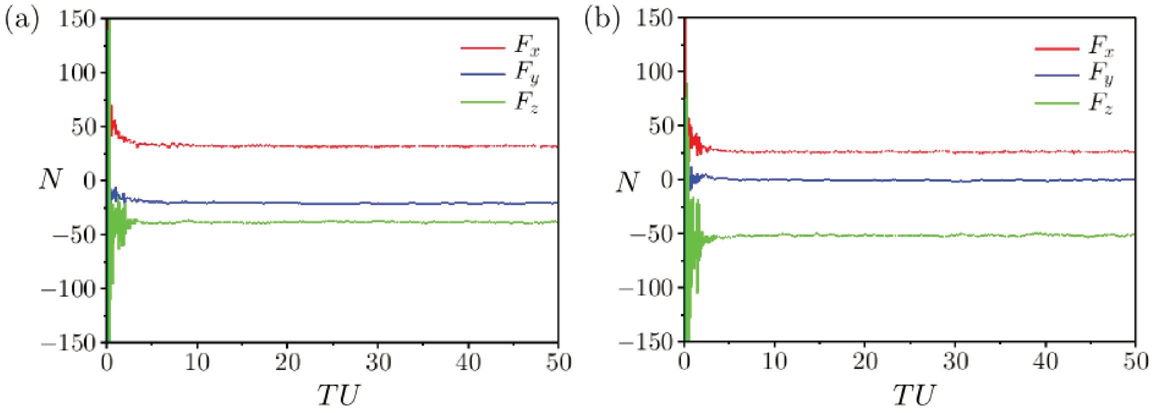

Figure 2.16: Time evolution of the aerodynamic drag F_x, side force F_y and lift F_z for one configuration with (a) and without (b) profiled support overhead.

simulation, important asymmetry were observed in the flow field, which could also be revealed by the non-negligible side force F_y after convergence in Figure 2.16(a). Attempts were made by mesh refinement in different areas to improve the symmetry but without success. Eventually simulations of several testing configurations without profiled support showed promising results. As can be seen in Figure 2.16(b), the stabilized side force F_y is close to zero. Therefore it was decided to perform all the simulations without the profiled support overhead of the vehicle in favor of the symmetry of the flow, although no clear idea could be provided on how the profiled support causes the flow asymmetry.

In the LaBS simulation the wheels have the same geometry with those used in experiment. The simulated tires are deformable as shown in Figure 2.17(a), with realistic wheel center height, contact patch area and side bulge of the 205/55 R16 tire under load in 2/5th-scale. As presented in Figure 2.17(b), the opening in the underside is due to the contact patch being immersed with the ground. The rotation of the wheels are achieved with the combination of the two methods Rotating Wall (RW) and Sliding Mesh (SM) (more details see Section 1.3.4). The rotating wall boundary condition are applied on the surface shown in Figure 2.17(c). The sliding mesh method is implemented around the part in Figure 2.17(d) to simulate more accurately the flow around the holes on the rim. While for rotating wheels with closed rim in Figure 2.17(e), only rotating wall boundary condition is employed.

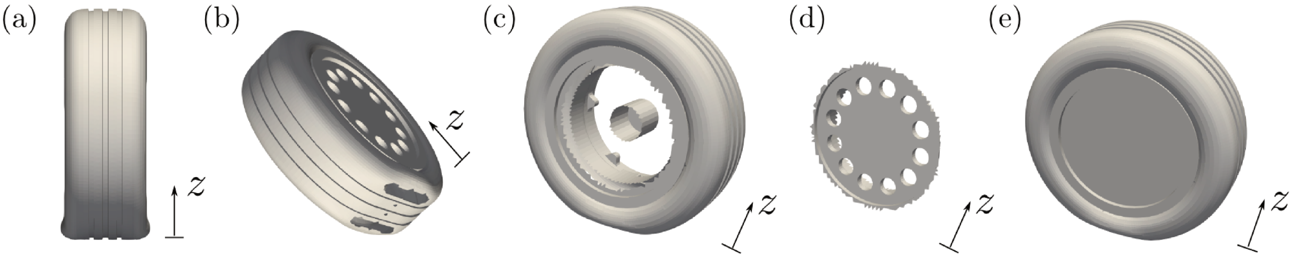

Figure 2.17: Wheel geometry and boundary setting in the LaBS simulation. (a) The realist tire deformation under load. (b) The contact patch on the ground. (c) The rotating part applied with Rotating Wall (RW) method. (d) The rotating part simulated with Sliding Mesh (SM) around. (e) Closed rim rotating wheel, only RW is employed.

Post-processing is achieved using standard visualization software Paraview.

As the geometry settings are not exactly the same with the experiment in terms of the tunnel blockage as well as the elimination of the profiled support, quantitative comparison of the forces and pressure level between the simulation and the experiment won't be of primary importance. The simulation results will be mainly used to complete the physical understanding of the flow field around the vehicle and the wheels.

Chapter 3

Smooth vehicle and underbody blockage modification

As introduced in the last chapter, the vehicle model is based on the Asmo model. Its geometry was modified so that when four rotating wheels are present, the front wheels are subject to reasonable yaw angle, and the model has a realistic wake balance. To throw light on the aerodynamic features around this modified geometry, the vehicle model without wheels and with polystyrene foam perfectly filling the wheelhouses (configuration noted N) has been first analyzed in Section 3.1. This configuration has an important downforce, a low drag, and a negative vertical pressure gradient in the base centreline, which is inverted compared to a typical passenger car in on-road condition.

The wheels in different states and with different tires can be regarded as underbody perturbations. In order to simplify these perturbations and investigate the impact of the underbody blockage, in Section 3.2, we applied a pair of profiled obstacles underneath the plugged rear wheelhouses, nothing being applied in the front underbody. Two regimes can be observed depending on the width of the obstacles. The first regime corresponds to configurations for which the wake of the obstacles closes, in a mean point of view, before the end of the underbody (obstacle of small width). In this regime, the underbody pressure decreases drastically when compared to configuration N. While the increase in obstacle size only has local effect on underbody and base pressure distributions, and does not modify the pressure on the symmetrical plane of the vehicle. In the second regime, the ‘unclosed’ obstacle wake ‘merged’ into the vehicle wake. This leads to a more global flow modification, manifested by a deepened suction on the entire base and an important pressure raise at the rear underbody. Whatever the regime, the vehicle wake organizations are not significantly modified.

Contents

3.1 The smooth vehicle model aerodynamic characterization

The experimental set-up is the same as described in Section 2.1. The wheels are removed, and the front and rear wheelhouses are plugged by polystyrene foam (Figure 3.1).

Figure 3.1: The smooth vehicle inside the working section of the wind tunnel.

To begin with, the $\overline{Cp}$ distribution on the body in the $y = 0$ plane together with the measurements on the body flank are displayed in Figure 3.2. The position of the profiled support is also indicated. The inward-pointing arrows represent positive $\overline{Cp}$ and outward ones are for negative $\overline{Cp}$. They outline the aerodynamic behavior around the model. The oncoming flow impinges at the model front nose, then bifurcates over the roof and below the underbody. Over the roof, the flow accelerates up to the summit ($x \approx 1$), with $\overline{Cp}$ decreasing from one to zero and then continues decreasing down to $\overline{Cp_{min}} \approx -0.75$. Afterwards, there is a flow deceleration along with a pressure recovery until the blunt trailing edge. Below the underbody, important suction occurs on the front radius ($\overline{Cp} \approx -1.05$), followed with a steep pressure rise ($\overline{Cp} > -0.5$) roughly at $x = -0.65$. Again the flow is mildly accelerated due to the slightly decreased passage area between the underbody and the ground. From then on the underbody surface is flat until the diffuser ($-0.25 < x < 2.5$), where the flow undergoes a deceleration then an acceleration. Eventually, the pressure raises in the diffuser ($2.5 < x < 3.25$). The fixed rear separations on the roof and at the diffuser exit set the prerequisites for the base pressure level around $\overline{Cp} = -0.14$. On the body flank, the pressure is approximately constant at around $\overline{Cp} = -0.25$.

This global $\overline{Cp}$ distribution also enables us to clarify the origin of the aerodynamic forces: the pressure contribution of the underbody mainly directs towards the negative z-axis; the pressure contribution of the base points in the positive x-direction; for the roof, it has one component along positive z-axis and another along positive x-axis. Table 3.1 presents the aerodynamic forces acting on the model and the different contributions to the pressure forces obtained from the experiment. The integrated underbody pressure and base pressure are denoted respectively by SCp_{U} and SCp_{B}. Note that on the roof there is only one line of pressure taps in the plane $y = 0$, no estimated contribution is provided from these measurements due to the lack of precision. All these values are expressed in full scale, i.e. multiplied by $(5/2)^2$. The smooth vehicle N has a negative lift coefficient and small drag coefficient. Comparing with the lift and drag coefficients of the Asmo model obtained in Aljure *et al.* (2014), which are respectively around -0.030 and 0.153, our results give -0.063 in Cz and 0.146 in Cx. Being consistent with the order of magnitude, the smaller lift and drag is then ascribed to the differences in the

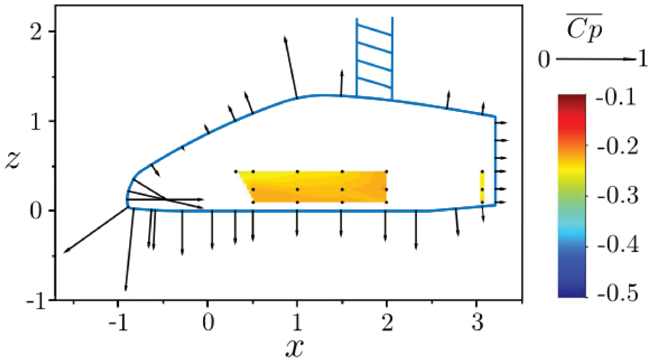

Figure 3.2: The distribution of time-averaged $\overline{Cp}$ in the $y = 0$ plane and on the body flank. Arrows locate the pressure taps in the $y = 0$ plane, with the inward-pointing arrows representing positive $\overline{Cp}$ and outward ones for negative $\overline{Cp}$; $\overline{Cp}$ equal to unit one is shown at the top right. The coordinate system conforms to that in Figure 2.3(b), with the coordinates normalized by the vehicle base height.

	$SCz(m^2)$	$SCx(m^2)$	$SCp_U(m^2)$	$SCp_B(m^2)$
N	-0.441	0.310	-2.907	-0.182

Table 3.1: Aerodynamic forces and integrated underbody and base pressure obtained from the experiment. All the values are expressed in full scale, i.e. multiplied by $(5/2)^2$.

model geometry and also the absence of the wheel-like obstacles in the underbody, as will be shown and discussed in the next sections.

Next we will delve into more details the surface pressure distributions and the related flow behavior. The numerical results will be equally presented for complementary information. In Figure 3.3(a) and (b) the experimental and numerical underbody pressure distributions of the smooth model are depicted. On first inspection, the simulation successfully captured the evolution of the underbody pressure, despite some discrepancy in absolute values. Figure 3.3(c) is the interpolated underbody pressure standard deviation obtained in the experiment. The underbody exhibits low pressure fluctuation, except a locally high Cp' occurs at the front part of the underbody. It brings to evidence a boundary layer detachment due to the adverse pressure gradient imposed by the geometry at the entry of the underbody. To get an idea of the increased and then decreased underbody pressure after the reattachment, a focus on the flow field beneath the underbody seems necessary. Thanks to the numerical simulation, the time-averaged field of the horizontal plane $5mm$ beneath the underbody surface (the ground clearance being $65mm$) is presented in Figure 3.3(d). It is colored by the time-averaged spanwise velocity $\overline{v}$ (in y direction) overlaid with 2D streamlines. Apparently, the velocity is outward at the front part of the underbody, then becomes almost parallel in the middle, and subsequently goes inward. The divergence followed by the convergence of the streamlines is amenable to the increase and then decrease of the underbody pressure evolution upstream of the diffuser. This reflects the three-dimensionality of the underbody flow.

Now, we turn our attention to the base pressure distribution. Figure 3.4(a) and (b) are respectively the experimental and numerical base pressure distributions. The numerical base pressure is significantly higher. In order to highlight the $\overline{Cp}$ variation, the colorbar ranges are chosen differently. It appears that the numerical result recovers the prominent characters of the base pressure distribution, which is a negative vertical pressure gradient in the middle line, and lower pressure at the two sides ($y \approx \pm 0.6$) below the indentation areas where the height of the base is reduced. The vertical pressure gradient in the middle line is defined as the slope of the linear regression of the base centerline pressure measurements, which is $d\overline{Cp}/dz = -0.044$ for

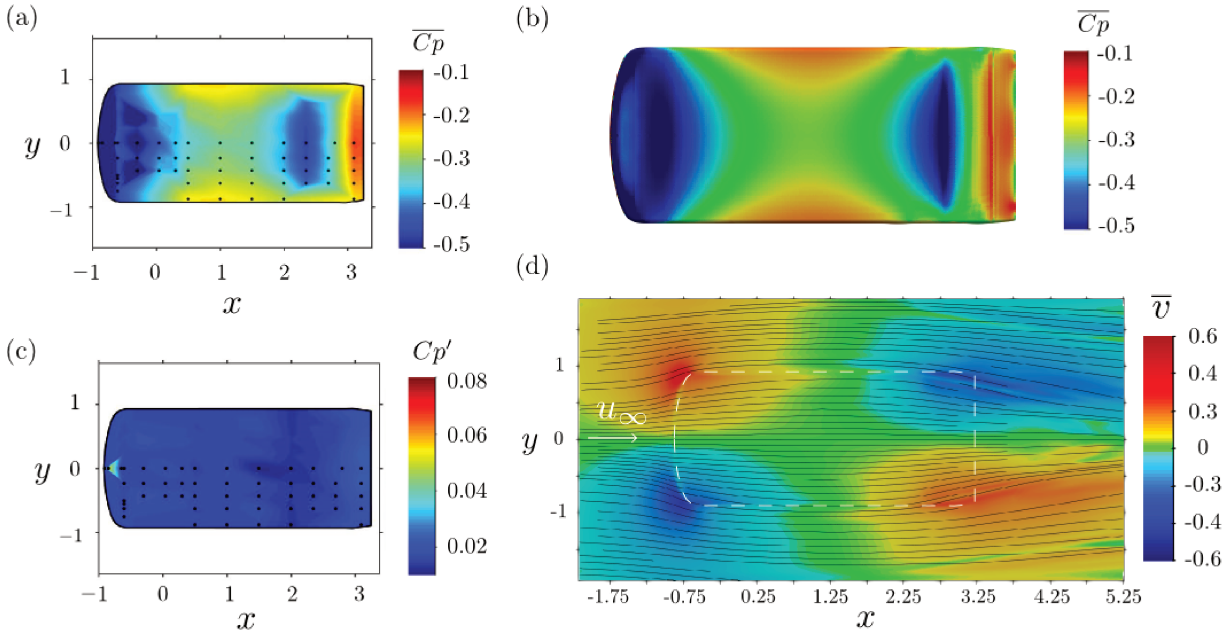

Figure 3.3: (a) Experimental results of the underbody $\overline{Cp}$ distribution; (b) Numerical results of the underbody $\overline{Cp}$ distribution; (c) The distribution of the standard deviation of the pressure coefficient Cp' on the underbody surface; (d) The numerical results of the time-averaged spanwise velocity $\overline{v}$ (in y direction) overlaid with streamlines in the horizontal plane $5mm$ beneath the underbody surface.

the experiment and $d\overline{Cp}/dz = -0.022$ for the simulation. This difference is expected since there is almost a factor 2 in the absolute $\overline{Cp}$ values shown in Figure 3.4(a) and (b). In Figure 3.4(c), the base pressure standard deviation measured in the experiment is provided, which makes high pressure fluctuations identified at the bottom-center of the base. The time-averaged trace lines on the base surface obtained from the simulation in Figure 3.4(d) shows a unstable node UN_{B} at the bottom-center. This time-averaged unstable node is associated to the base stagnation point. On the one hand it accounts for the higher pressure level as shown in Figure 3.4(a) and (b); on the other hand, the impingement position of the wake reversed flow may not be fixed in the lower region due to the unsteadiness and entails the strong fluctuation seen in Figure 3.4(c).

To determine the position of the base stagnation point, let us now consider the flow picture in the symmetry plane, $y = 0$, in Figure 3.5. Figure 3.5(a) and (b) are respectively PIV and numerical results. The time-averaged streamwise velocity $\overline{u}$ in Figure 3.5(a) illustrates the extension of the wake recirculation domain where reversed flow with negative streamwise velocity is discernible. It can be quantified by the recirculation length L_r, defined as the maximum streamwise position of the contour line $\overline{u} = 0$, i.e.

$$L_r = \max_x(\overline{u}(x) = 0) \tag{3.1}$$

For the vehicle model, the recirculation length measured by PIV is $L_r = 1.36$. The time-averaged vertical velocity $\overline{w}$ additionally displays an asymmetry of the wake. The large downward motion of the entrained flow (negative $\overline{w}$) along the upper shear layer and the upward flow that dominates the base surface form a sizable clockwise mean recirculating structure (see streamlines in Figure 3.5(a)). Meanwhile a smaller counter clockwise mean structure is formed with the less pronounced entrained flow (upward positive $\overline{w}$) along the lower shear layer and the downward flow at the bottom part of the base. It can also be noted that the reversed flow that impinges the base is tilted downwards, resulting a stagnation point situated at the lower part of the base ($z \approx 0.5$ corresponding $z \approx 0.34$ in Figure 3.4), which is coherent with the

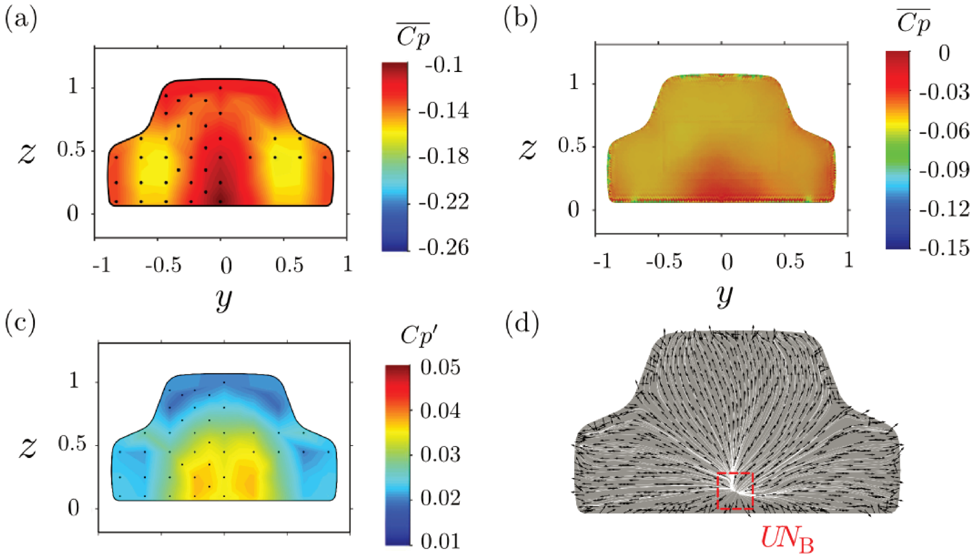

Figure 3.4: (a) Experimental results of the underbody $\overline{Cp}$ distribution; (b) Numerical results of the underbody $\overline{Cp}$ distribution; (c) The distribution of the standard deviation of the pressure coefficient Cp' on the underbody surface; (d) The numerical results of the time-averaged trace lines on the base.

observations in Figure 3.4. The reason for the asymmetry of the wake in this plane is twofold: the first is the ground proximity; the second is the roof boat tail angle (10°) being larger than the diffuser angle (5°), which promotes the downwash from the top trailing edge. It will be seen shortly in the next chapter that this mean wake wall-normal balance is inverted compared to the baseline configuration with four rotating wheels.

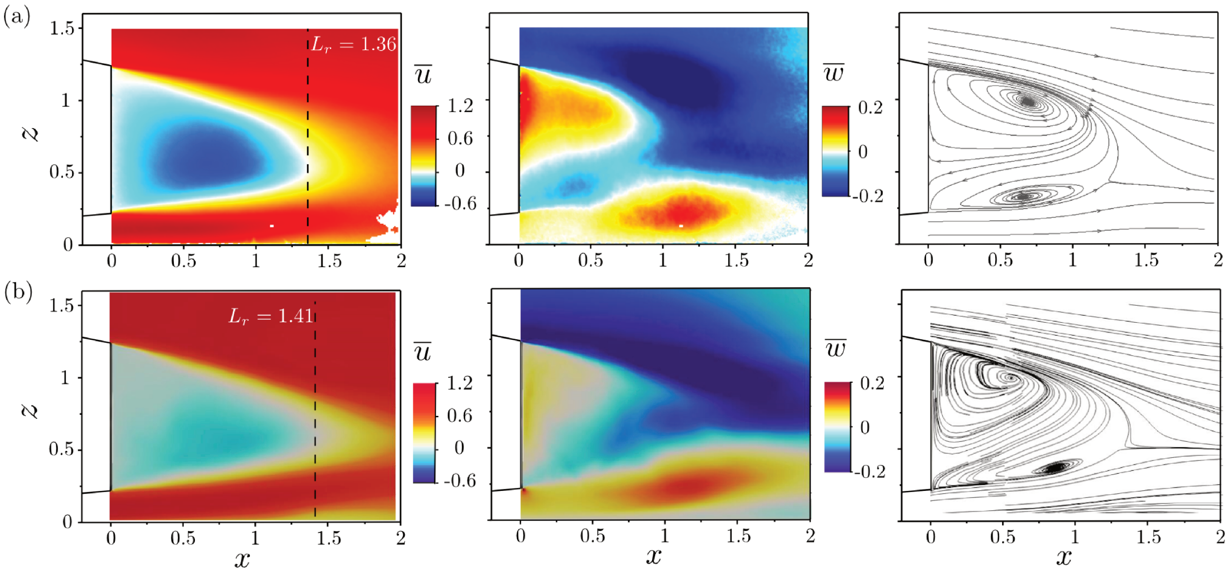

Figure 3.5: PIV measurements (a) and numerical results (b) of the time-averaged streamwise velocity $\overline{u}$, vertical velocity $\overline{w}$ and 2D streamlines in the symmetrical plane $y = 0$. The origin of the coordinate system is translated to the point on the flat plate at the mid-span and rear end of the model (Figure 2.3(b)). The coordinates are normalized by the vehicle base height.

The numerical results are depicted in Figure 3.5(b). Several discrepancies can be noted when confronted to the experimental results. Firstly, the reversed flow inside the recirculation wake has smaller velocity magnitude. It brings to evidence a decrease of entrained flow inside the wake, which is the reason for the elongated recirculation length ($L_r = 1.41$ in the simulation). And it is consistent with the higher base pressure as shown in Figure 3.4(b). Secondly, the upper clockwise recirculating structure is closer to the base than the lower one, which may be related to the absence of the profiled support in the simulation (see Section 2.2.2). Lastly, the streamlines leave the saddle point horizontally rather than slightly deflected towards the ground as seen in Figure 3.5(a). In spite of the disparities, the asymmetry of the wake in this symmetrical plane is globally recovered by the simulation.

The time-averaged Reynolds stresses $\overline{u'w'}$, $\overline{u'u'}$ and $\overline{w'w'}$ derived from the PIV measurements in this symmetrical plane are given in Figure 3.6. The dynamics of the shear layers can therefore be observed. The velocity fluctuations are practically concentrated along the upper and lower shear layers. And they are all the more important along the lower shear layer when we look at the $\overline{u'w'}$ and $\overline{u'u'}$ distributions, which confirms the z-asymmetry of the mean wake flow discussed in the last paragraphs. When analyzing the normal stresses $\overline{w'w'}$, high values of $\overline{w'w'}$ at around $x > 1.4$ can be related to the strong vertical flow movements at the closure of the main bubble.

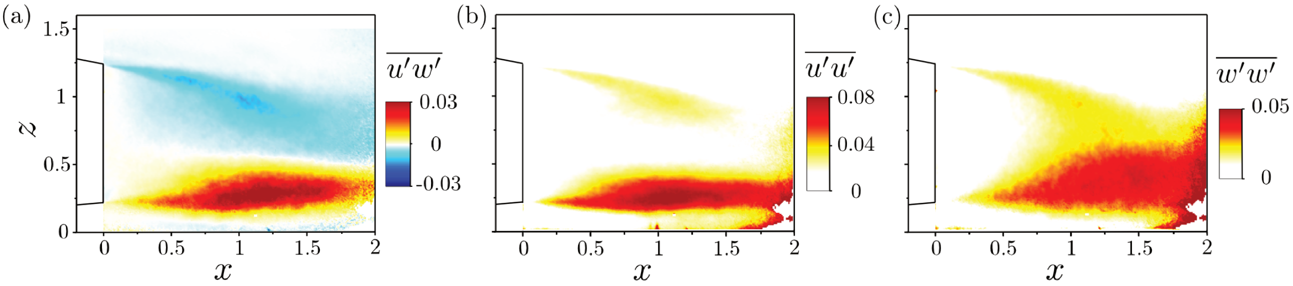

Figure 3.6: PIV measurements of the time-averaged Reynolds stresses $\overline{u'w'}$ (a), $\overline{u'u'}$ (b) and $\overline{w'w'}$ (c) in the symmetrical plane $y = 0$.

To investigate the low base pressure regions at the two sides ($y \approx \pm 0.6$) below the indentation areas, the horizontal PIV data is acquired at $z = 0.54$ in the wake, as shown in Figure 3.7(a) together with the numerical results in the same plane. Inside the recirculation zone, two large mean recirculating structures are pressed against the base and they are closer to the base than those in the $y = 0$ plane (Figure 3.5(a)), therefore induce lower pressure on the afterbody at $y \approx \pm 0.6$. The numerical result assumes similar distribution of the streamwise velocity albeit an underestimation of the reversed flow velocity magnitude close to the base.

Based on the underbody and afterbody pressure distributions, the flow field in the symmetrical $y = 0$ plane and in the horizontal $z = 0.54$ plane, the simulation shows acceptable agreement with the experimental results. Hence additional flow visualization will be carried out using the simulation results to further explore the wake structure, where no experimental measurements are available.

The streamwise velocity distribution in the crossflow plane at $x = 1$ is extracted from the numerical results in Figure 3.7(b). From the recirculation region we can roughly discern the shape of the base. It seems that at the left and right sides, the development of the mixing layers is symmetric. While in the middle plane $y = 0$, the downwash is more important than the underbody upwash. Moreover the bottom boundary of the recirculation region assumes a 'M' shape where two pairs of counter-rotating vortices can be observed through the 2D streamlines above the two vertex of 'M' ($y \approx \pm 0.5$). This 'M' shape is also observable at the lower boundary of the iso-contour of $\overline{Cp_{tot}} = 0$ in Figure 3.7(c). The iso-contour of $\overline{Cp_{tot}} = 0$ identifies the recirculation region by its low total pressure. At the two vertex of 'M', local upwash is more pronounced as can be seen from the positive vertical velocity $\overline{w}$. The mean numerical 3D streamlines in Figure 3.7(d) unfolds a strong three-dimensinality of the wake flow, similar to that of the Asmo car model (Aljure *et al.*, 2014). The two pairs of counter-rotating vortices remain identifiable with the 2D streamlines at the rearmost crossflow plane. A tentative

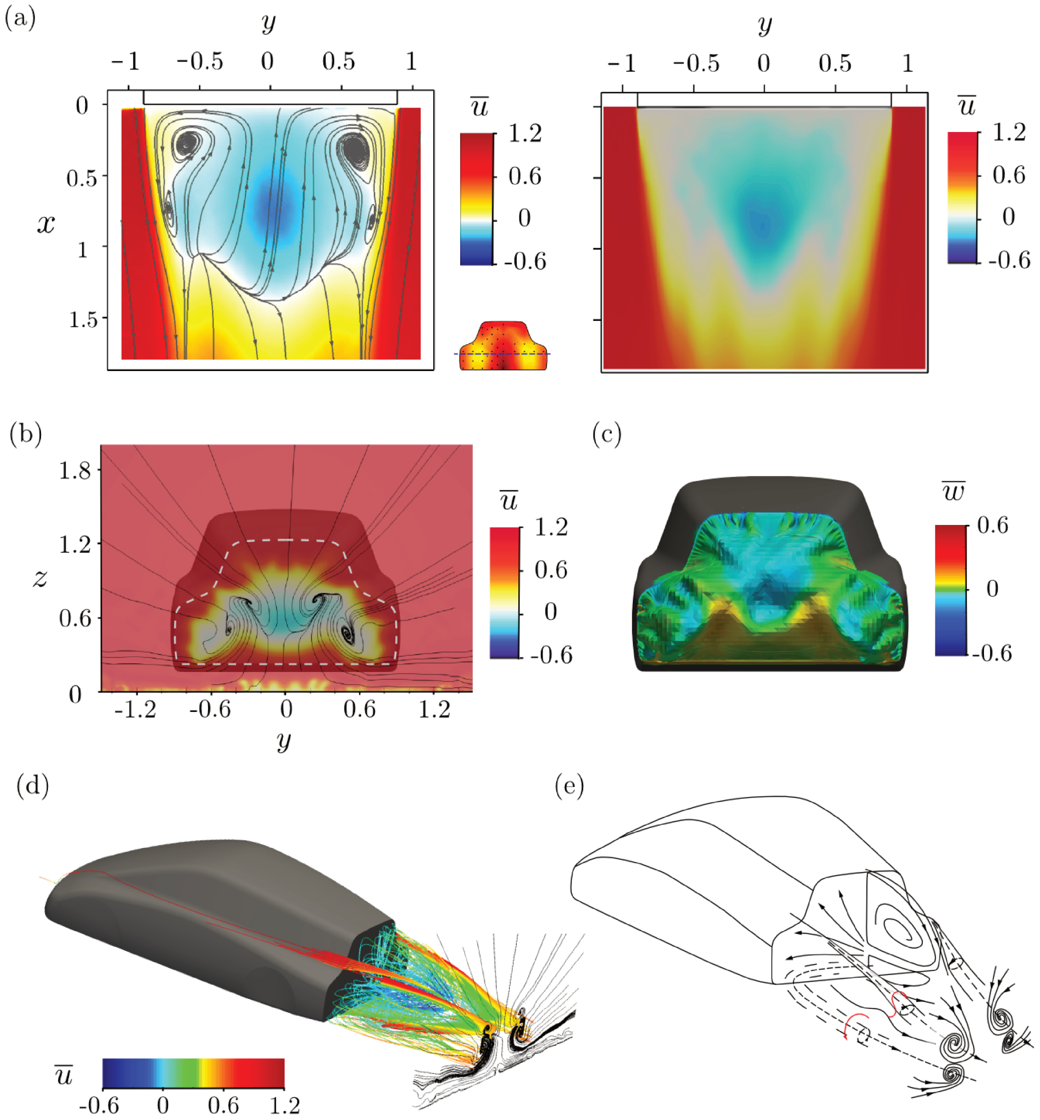

Figure 3.7: (a) PIV measurements and numerical results of the time-averaged streamwise velocity $\overline{u}$ in the horizontal plane $z = 0.54$ with its vertical position indicated by the dashed line on the base; (b) Time-averaged streamwise velocity $\overline{u}$ in the crossflow plane $x = 1$ overlaid with 2D streamlines from the simulation. The dashed line figures the base shape; (c) Iso-contour of $\overline{Cp_{tot}} = 0$ ($\overline{Cp_{tot}} = \overline{Cp} + \boldsymbol{u}^2$) colored by time-averaged vertical velocity $\overline{w}$. (d) Mean numerical streamlines in the wake colored by time-averaged longitudinal velocity $\overline{u}$; (d) Schematic model of the flow structure in the wake.

attempt to specify the wake topology is shown in Figure 3.7(e) based on the 3D streamlines in Figure 3.7(d). From the numerical streamlines we can observe that the high speed flow separating at the indentation area moves downwards and also towards the mid plane. Then it meets the more pronounced upward underbody flow which gives rise to a swirling motion, creating two longitudinal vortices, similarly in Aljure *et al.* (2014), which is the inner pair of counter-rotating vortices in Figure 3.7(b) and (d). The outer pair of longitudinal vortices is not observed in Aljure *et al.* (2014). However, it is in good agreement with the existence of the horseshoe vortex shown in Perry *et al.* (2016), which develops at the higher pressure side of the rectangular base of a Windsor body equipped with adjustable rear tapers. And probably they are captured by the horizontal plane $z = 0.54$ in Figure 3.7(a) as the smaller recirculating structures at $x \approx 0.8$ and $y \approx \pm 0.75$. In addition, the local upwash at the exit of the underbody feeds the two pairs of longitudinal vortices as indicated by the red lines in Figure 3.7(e).

Summary In this section, the smooth vehicle model without wheelhouses nor wheels is investigated. It is considered to be the first step if its interaction with the wheels want to be further studied, especially when not much information about the fluid dynamics around the model is available in the literature.

In terms of aerodynamic forces, the experimental results show a negative lift coefficient and a small drag coefficient. The simulation has been proven to be capable of reproducing the main features of the surface pressure distributions and the mean wake flow. The underbody flow exhibits a three-dimensionality with outward then inward flow motions, which will be possibly modified if obstacles are present at the two sides of the underbody. The wake flow also displays highly 3D features due to the base geometry. Two pairs of longitudinal vortices are detectable in the near wake. The negative vertical pressure gradient in the base centerline is coherent with $z-$asymmetry in the wake symmetrical plane $y = 0$. It is due to the ground proximity and also the vehicle geometry.

3.2 Modification of the underbody blockage rate

3.2.1 Experimental set-up

The experimental set-up is the same as described in Section 2.1 (Figure 3.8(a)). We maintain the smooth vehicle model with plugged wheelhouses and without wheels. Then we mount a pair of obstacles with the height of the ground clearance beneath the two plugged rear wheelhouses to simulate the rear wheels, since it has been established in the literature the dominance effect of the rear wheels on vehicle drag (Elofsson & Bannister, 2002; Koitrand & Rehnberg, 2013). A parametric study is thereupon carried out by varying the width of the obstacle pair to achieve different aerodynamic blockage in the underbody. As shown in Figure 3.8(b), the obstacles are half-elliptical (divided along the minor axis) base cylinders with a blunt trailing edge. When installed, their major axis are parallel to the oncoming flow. They are fixed on the ground by screws to keep aligned with the wind and they are in contact with the vehicle. We define the geometric blockage rate as the ratio between the total width of the obstacle pair (which is two times of the elliptical minor axis) and the vehicle width, denoted as τ. Parametric study is carried out with $\tau = \{10, 15, 20, 25, 30, 35, 40\}\%$. The end of the obstacles are tangential to the rear wheelhouse end and their outboard sides are tangential to the sides of the vehicle. The location of the obstacles is depicted in Figure 3.9. In the underbody no pressure measurement can be acquired on the underside of the plugged wheelhouses. Hence the interpolated underbody pressure there will be lack of precision. In addition, for high blockage rates ($\tau = 30, 35, 40\%$), certain underbody pressure taps are sheltered. Thus the sheltered pressure taps are excluded from the interpolation. In this configuration, no aerodynamic forces are recorded by the balance inside the vehicle due to the contact with the obstacles fixed on the ground.

The semi-elliptical base cylinders are chosen as we expect the flow to be attached on the obstacles surface until the blunt trailing edge so that the width of the obstacle wake at the separation equals to the obstacle width. To ascertain this point, the interpolated underbody pressure standard deviation is depicted in Figure 3.10. With the available pressure sensors, it can be perceived that, important fluctuation indicated by high Cp' presents only at the downstream of the lower front edge radius, and behind the obstacles. The former is related to the small separation bubble. The latter seems to confirm that the flow is practically attached on the obstacle surface before separation.

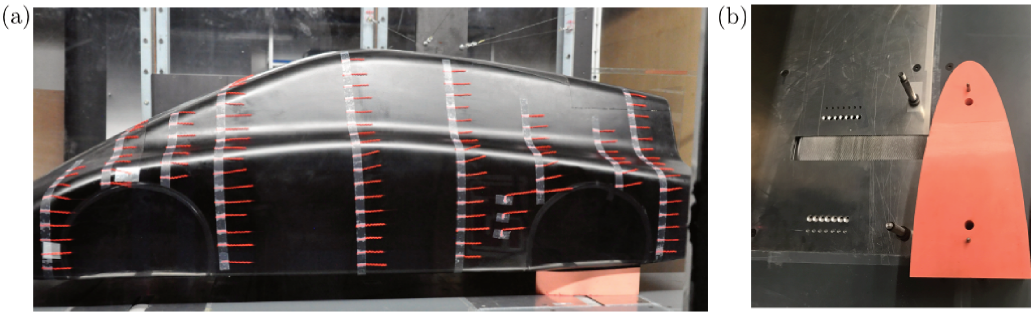

Figure 3.8: (a) The smooth vehicle with obstacles beneath the two plugged rear wheelhouses in the wind tunnel. (b) The half-elliptical (divided along the minor axis) base cylinders and their installation with screws on the floor.

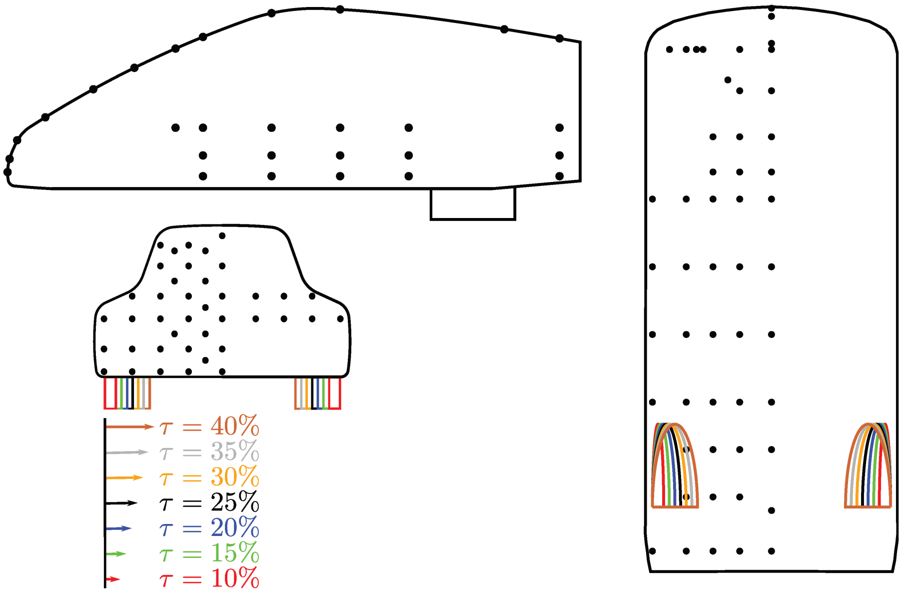

Figure 3.9: A sketch of the location of the obstacles underneath the vehicle model with the black dots indicating the pressure taps on the model surface.

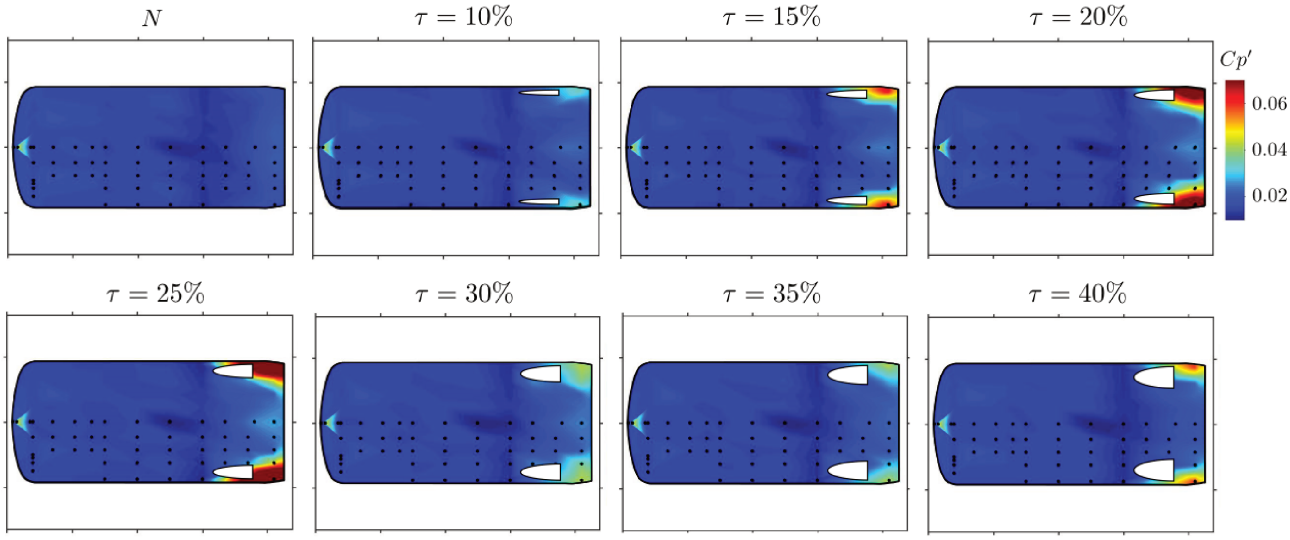

Figure 3.10: The distribution of the standard deviation of the pressure coefficient Cp' on the underbody surface.

3.2.2 Mean properties of the surface pressure

To begin with, an approximate estimation of the base pressure level will be given for different τ configurations, assuming that the underbody flow takes the form of 2D classical channel flow as schematized in Figure 3.11. However, the objective of the subsequent deduction is to disprove the 2D channel flow assumption.

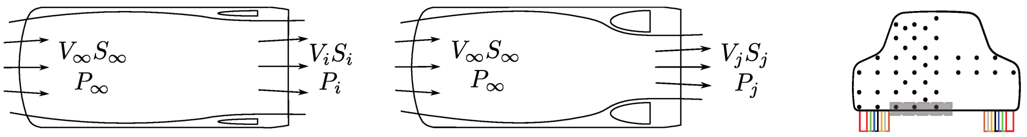

Figure 3.11: A sketch of the underbody flow configuration under the assumption of 2D channel flow. The pressure at the exit of the underbody will be estimated by the average of the 3 pressure measurements in the grey box.

Considering a streamline from the entrance of the underbody to the exit, neglecting gravity, we apply Bernoulli's equation:

$$P_\infty + \frac{1}{2}\rho V_\infty^2 = P_i + \frac{1}{2}\rho V_i^2 \qquad P_\infty + \frac{1}{2}\rho V_\infty^2 = P_j + \frac{1}{2}\rho V_j^2 \tag{3.2}$$

Introducing the static pressure coefficient, we obtain:

$$Cp_i = 1 - \left(\frac{V_i^2}{V_\infty^2}\right) \qquad Cp_j = 1 - \left(\frac{V_j^2}{V_\infty^2}\right) \tag{3.3}$$

Combining the two in (3.3), it can be written:

$$\frac{1 - Cp_i}{1 - Cp_j} = \frac{V_i^2}{V_j^2} \tag{3.4}$$

Supposing that the fluid velocity is constant at the entrance section S_∞ and exit section S_i and S_j, for configuration i and j respectively; we also assume the conservation of mass between the entrance and the exit, then we have

$$V_\infty S_\infty = V_i S_i \qquad V_\infty S_\infty = V_j S_j \tag{3.5}$$

The pressure coefficient Cp_j at the underbody exit of configuration j can therefore be expressed as:

$$Cp_j = 1 - \left(\frac{S_i}{S_j}\right)^2 (1 - Cp_i) \tag{3.6}$$

where S_i/S_j can be approximately taken as $(1-\tau_i)/(1-\tau_j)$, we get:

$$Cp_j = 1 - \left(\frac{1-\tau_i}{1-\tau_j}\right)^2 (1 - Cp_i) \tag{3.7}$$

The idea is to estimate the base pressure Cp_j from (3.7) with the measurement of $\tau = 10\%$ as the reference Cp_i, and then the estimated values will be compared to the experimental measurements. Taking the average of the 3 pressure measurements in the grey box in Figure 3.11 as the pressure at the exit section, the comparison is then displayed in Figure 3.12. The choice of $\tau = 10\%$ and the three pressure taps are arbitrary, yet it has been checked that same conclusion can be drawn if other choices are made.

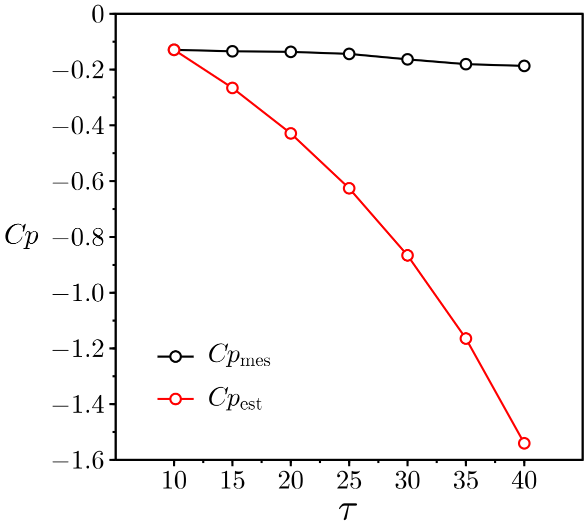

Figure 3.12: Comparison between the estimated pressure at the underbody exit and the measured ones.

According to Figure 3.12, the estimated pressure is not in accordance at all with the measured ones. With increasing τ, the disparity is widening. It suggests a significant underestimation of the pressure level which arises from the over prediction of the exit velocity V_j obtained from (3.5). Indeed, the entering flow exits the underbody not only through the passage between the obstacles but also from their outer sides, which is duly not akin to a classical channel flow.

In the following, the global impact of the blockage rate will be provided by plotting integrated underbody pressure and integrated base pressure as a function of τ. In Figure 3.13, the longitudinal axis is the blockage rate, left vertical axis is the integrated underbody pressure, and right vertical axis is the integrated base pressure. For comparison, the smooth vehicle configuration N is also presented. For the underbody pressure, from N to $\tau = 10\%$, there is a sudden drop when the obstacles are applied and then it bounces back with two slopes, with a larger slope when $\tau > 25\%$. For the base pressure, from N to $\tau = 40\%$ it continues reducing, also with a more negative slope when $\tau > 25\%$.

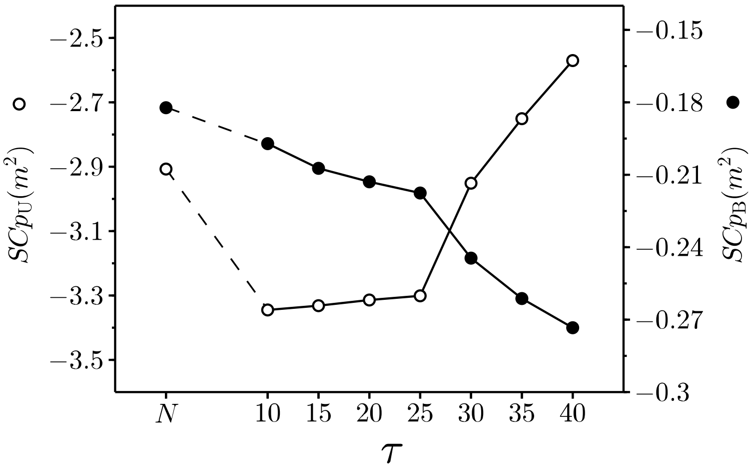

Figure 3.13: The integrated underbody pressure (left axis) and integrated base pressure (right axis) for N and all the blockage rates.

To better visualize the pressure variation on different parts of the vehicle, the distributions of $\overline{Cp}$ in the $y = 0$ plane are presented in Figure 3.14. Among all the configurations, the time averaged wall pressure on the roof seems to be weakly dependent of τ. For smaller τ values the curves nearly overlap (Figure 3.14(a)), and for higher τ the difference is only noticeable close to the rear end (Figure 3.14(b)). This demonstrates the limited influence of τ on the flow over the model roof.

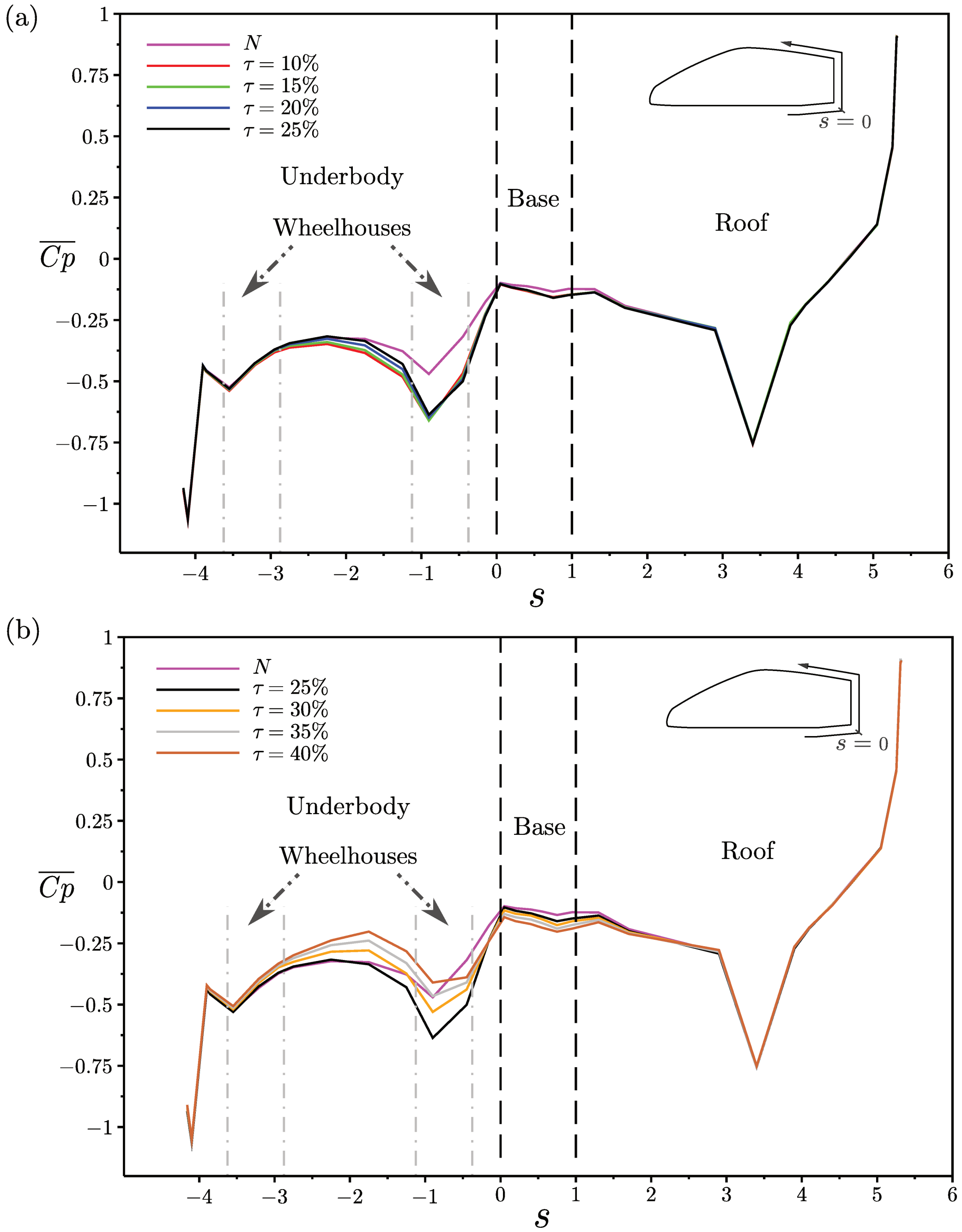

Figure 3.14: The distribution of $\overline{Cp}$ in the $y = 0$ plane on the curvilinear abscissa s (normalized by the height of the base) with the origin at the underbody rear end for (a) N, $\tau = 10, 15, 20, 25\%$; (b) N, $\tau = 25, 30, 35, 40\%$

In the underbody, when analyzing Figure 3.14(a), different behaviors are observed between N and the smaller blockage configurations. At the streamwise position of the rear wheelhouses (around $s = -1$), the suction is more notable when small blockage obstacles are mounted. This yields the drastic drop of the integrated underbody pressure from N to $\tau = 10\%$ in Figure 3.13. From 10% to 25%, their pressure at the rear part of the underbody are nearly superposed ($-1 < s < 0$). The difference between the small blockage rate configurations is only discernible at the upstream of the obstacles $-3 < s < -1$, the pressure increases mildly with increasing blockage rate, which accounts for the slowly augmented integrated underbody pressure from 10% to 25% in Figure 3.13. As for larger obstacles given in Figure 3.14(b), the underbody pressure between the obstacles are no longer the same. The large raise of the underbody pressure due to the increasing blockage rate extends from $s = -3.5$ to $s = -0.15$, which results in the steep increment of the integrated underbody pressure at $\tau > 25\%$ in Figure 3.13.

The base pressure on the $y = 0$ centerline for lower blockage rates is nearly superposed. They drop slightly at the upper part of the base when compared to the smooth model N (Figure 3.14(a)). While for larger τ the increase in size results in a gradual loss of the centerline pressure (Figure 3.14(b)). The mean centerline pressure is equally displayed in Figure 3.15(a). After a pressure descent when the obstacles are applied, a plateau presents at low blockage rate until $\tau = 25\%$, and further enlargement in obstacle size results in a $\langle \overline{Cp_C} \rangle$ decline. However, the integrated base pressure is decreasing with increasing τ (Figure 3.13). Therefore it can be deduced that, at small τ values, despite the insensitivity of the centerline pressure to the change of the underbody blockage rate, pressure modification due to τ variation can be measured at the two sides of the base. This can be corroborated from the horizontal $\overline{Cp}$ evolution at the left side of the base in Figure 3.15(b): the pressure level is decreasing with increasing τ.

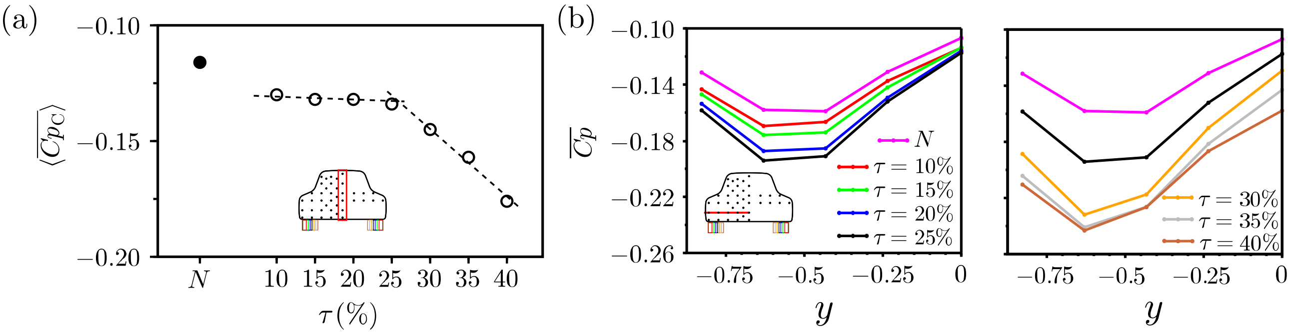

Figure 3.15: (a) The area-averaged base pressure coefficient on the centerline (in the red box) – $\langle \overline{Cp_C} \rangle$ for N and all the blockage rate; (b) Profiles of $\overline{Cp}$ at the horizontal line on the left side of the base (indicated by the red line).

After the overview of the surface pressure variation, it is worth mentioning that according to Figure 3.13, 3.14 and 3.15, two regimes with a separation at $\tau = 25\%$, can be easily distinguished. To sum up, when $\tau \leq 25\%$, enlarging the obstacles width only increases marginally the underbody pressure upstream the obstacles. The centerline pressure between the obstacles, downstream in the diffuser and in the base are practically not affected. Alongside, a gradual drop of the pressure at the two sides of the base is detectable. However at higher blockage rate $\tau > 25\%$, the pressure in the centerline and at the two sides of the base are both influenced by the underbody blockage change. The two regimes are to be discussed in more details in the following subsections.

3.2.3 Small underbody blockage

Looking back to Figure 3.14(a), the striking difference between N and small blockage configurations at the rear part of the underbody needs to be understood. From their underbody pressure distributions in Figure 3.16(a), the more significant suction compared to N can be clearly observed at the rear underbody surface. Effectively, it has been established in the previous section the 3D feature of the underbody flow of the smooth vehicle model. The underbody flow comes outwards and inwards as illustrated in Figure 3.3(d). However, once the obstacles are employed at the two sides, they prevent the outside high pressure flow penetrating the low pressure region and channel the flow pass through between them. Accordingly the pressure between the obstacles is much decreased. This is reminiscent of the side plates or skirts that once used in race cars to improve downforce in the late 1970s (Katz, 1995). Thereby we speculate that if we continue reducing the obstacles size towards two thin plates, the blockage rate in the underbody decreases to zero, and the curve will superimpose with those of the small blockage rates (at least at $-1 < s < 0$), rather than behaves as N which has no blockage in the underbody. In such scenario, the effect of the obstacles can be deemed as a guidance of the underbody flow.

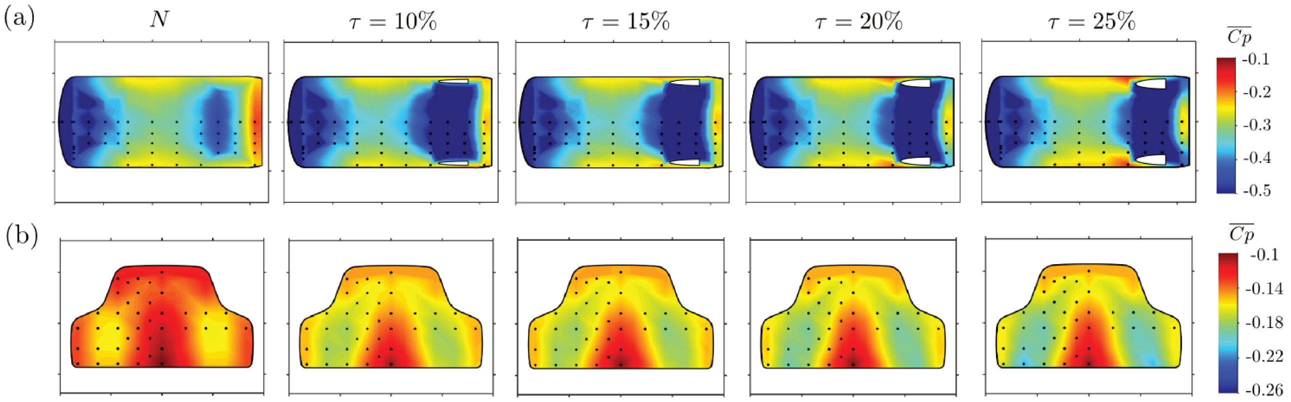

Figure 3.16: The underbody pressure distribution (a) and the base pressure distribution (b) for N and $\tau = 10, 15, 20, 25\%$.

For small blockage rates, the influence of the obstacle width remains local. First, it can be discerned in Figure 3.16(a), upstream of the obstacles in the underbody, the enlarging size gradually increases the pressure in their stagnation zones. Second, with increasing τ, the pressure at the two sides of the base decreases, which has be seen in Figure 3.15(b) and also can be observed in their base pressure distributions in Figure 3.16(b). This is owing to greater displacement of the flow by wider obstacles, thus the flow contouring the profiled obstacles gains a higher velocity, and a lower pressure. To confirm this point, the streamwise pressure evolution close to the profiled obstacles is provided in Figure 3.17: the local velocity increase by enlarging obstacles is thus brought to evidence. Consequently, different pressure level is set at the rear separation of the obstacles. The near wakes of the profiled obstacles then interact with the wake of the vehicle and different pressure condition on the vehicle base is imposed. Nevertheless, the underbody central flow is practically unaffected, as evidenced by the superposition of the curves at $-1 < s < 0$ in Figure 3.14(a). Thereby the base centerline pressure remains the same (Figure 3.15(a)) as a result of an identical separation condition at the central exit of the underbody diffuser.

To better visualize the obstacle wake, the horizontal PIV data acquired at the half of the ground clearance is given in Figure 3.18. The wakes of the obstacles are looming up with increasing τ from the streamwise velocity $\overline{u}$ distributions (Figure 3.18(a)). The intensity of the planar turbulent kinetic energy $k = 0.5 \times (\overline{u'u'} + \overline{v'v'})$ in the obstacle wake also increases (Figure 3.18(b)). When compared to N, higher velocity deficit (Figure 3.18(a)) can be noticed downstream in the middle ($x > 1$), which can be related to the more remarkable fluctuation (Figure 3.18(b)) in the same region. This indicates an enhanced interaction of the vehicle wake with the ground when profiled obstacles are employed. We can therefore infer that the vehicle wake develops closer to the ground so the z-asymmetry is more pronounced.

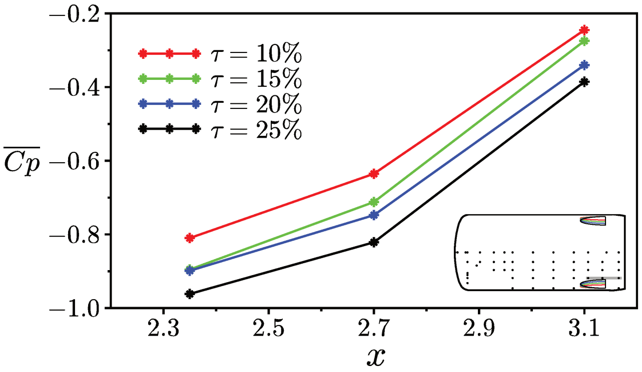

Figure 3.17: The $\overline{Cp}$ evolution on the measurement line close to the obstacles (indicated in gray line) for $\tau = 10, 15, 20, 25\%$.

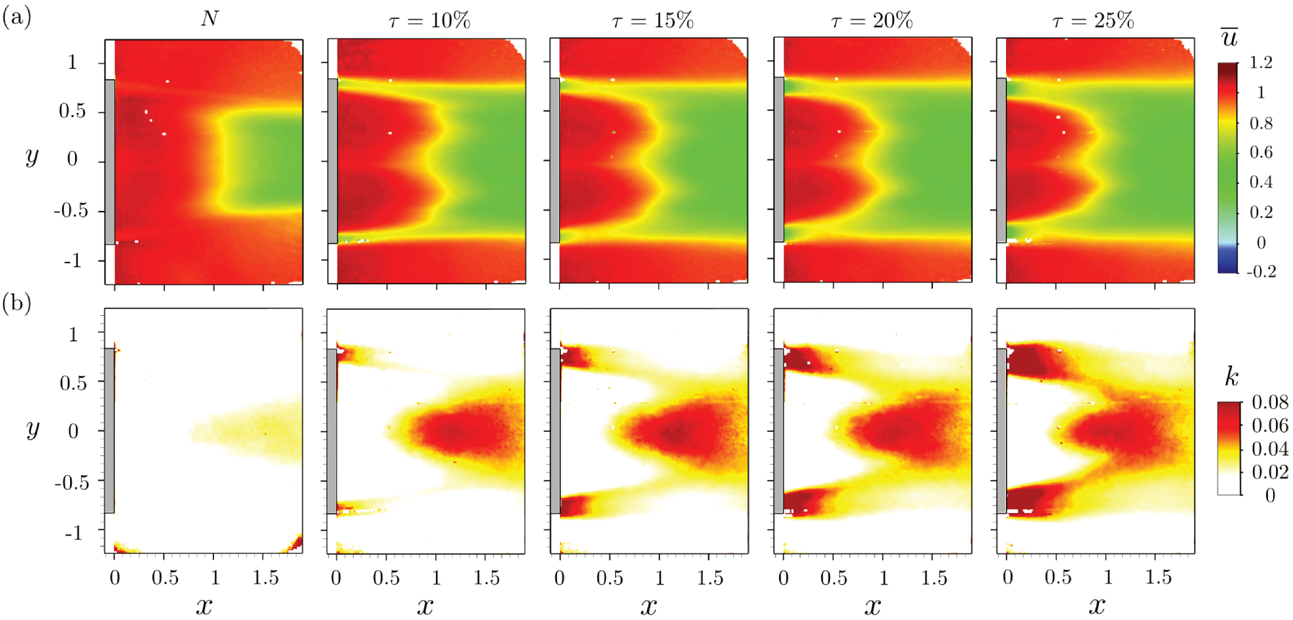

Figure 3.18: The time-averaged streamwise velocity $\overline{u}$ (a) and the planar turbulent kinetic energy $k = 0.5 \times (\overline{u'u'} + \overline{v'v'})$ (b) in the horizontal PIV plane at the half of the ground clearance for N and $\tau = 10, 15, 20, 25\%$. The vertical position of this horizontal plane is indicated in dashed line in Figure 3.19(b).

To ascertain this point, the PIV measurements in the symmetrical plane $y = 0$ are reported in Figure 3.19. For each configuration, a large clockwise mean recirculating structure and a smaller counter clockwise mean structure can be identified with the 2D streamlines in Figure 3.19(a). However, when obstacles are mounted, the recirculation region becomes less elongated, and the counter clockwise structure shrinks in size. Inside the recirculation region, the direction of the reversed flow impinging the base is tilted more downwards. The saddle point tends to descent in z direction and the streamlines leaving the saddle point are deflected more towards the ground.

Moreover, in the planar turbulent kinetic energy $k = 0.5 \times (\overline{u'u'} + \overline{w'w'})$ distributions in Figure 3.19(b), an enhancement of the lower shear layer turbulent dynamics is evident when compared to N. Accordingly, the recirculating bubble tends to close earlier, as evidenced in Table 3.2. This more pronounced z-asymmetry also agrees well with the reduced vertical pressure gradient in the base centerline $d\overline{Cp}/dz$ reported in Table 3.2. Comparisons within different blockage rates show that with increasing τ there is a subtle amplification of k in both upper and lower shear layers. As a result, the wake top / bottom equilibrium remains identical,

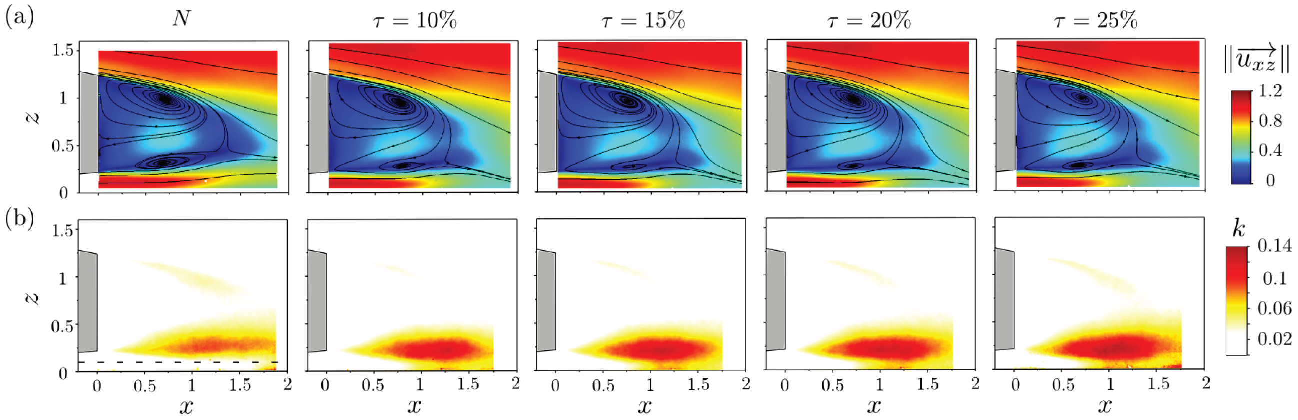

Figure 3.19: The time-averaged velocity magnitude (a) and the planar turbulent kinetic energy $k = 0.5 \times (\overline{u'u'} + \overline{w'w'})$ (b) in the symmetrical PIV plane for N and $\tau = 10, 15, 20, 25\%$. The dashed line indicates the vertical position of the horizontal PIV plane in Figure 3.18.

	N	$\tau = 10\%$	$\tau = 15\%$	$\tau = 20\%$	$\tau = 25\%$
$SCp_{\mathrm{B}}(m^2)$	-0.182	-0.197	-0.207	-0.213	-0.218
L_r	1.36	1.34	1.30	1.28	1.27
$d\overline{Cp}/dz$	-0.044	-0.066	-0.074	-0.074	-0.072

Table 3.2: The integrated base pressure SCp_{B}, recirculation length L_r in the $y = 0$ plane and the vertical pressure gradient $d\overline{Cp}/dz$ at the base centerline for N and $\tau = 10, 15, 20, 25\%$.

which can be reflected by their similar $d\overline{Cp}/dz$ values. Furthermore, the increasing upper and lower turbulent kinetic energy is coherent with the reducing mean wake length L_r. And according to Roshko (1993), longer mean wake length is associated with higher base pressure, which is duly observed in their integrated base pressure SCp_{B} in Table 3.2.

3.2.4 Large underbody blockage and the separation

We turn now our attention to larger underbody blockage rates, $\tau > 25\%$. To begin with, the pressure maps in the underbody and on the base are depicted in Figure 3.20, with $\tau = 25\%$ as a reference. When τ augments, a pressure rise at the rear part of the underbody is salient in Figure 3.20(a), not merely between the obstacles but also upstream of them. While on the base (Figure 3.20(b)), there is a gradually broad suction with increasing blockage rate. As opposed to $\tau \leq 25\%$ where the obstacles have only a local effect downstream on the vehicle base, and the pressure in the symmetrical $y = 0$ plane is scarcely influenced, the increasing size at $\tau > 25\%$ entails a more important modification of the surface pressure distribution. These surface pressure distributions also corroborate the mean pressure evolution in Figure 3.13.

To further elaborate the different behavior between small and large blockage rates, a closer look of the surface pressure modification is provided in Figure 3.21. Figure 3.21(a) delineates the pressure evolution in the underbody between the obstacle pairs. A clear layered distributions can be seen for larger blockage rates. The last two pressure measurements in the streamwise direction lie in the underbody diffuser. The slope between them reveals a progressively reduced diffuser efficiency at $\tau > 25\%$, which seems logic as the increasing width of the profiled obstacles will certainly diminish the passage area between them, which counteracts the effect of the diffuser. Figure 3.21(b) embodies the mean pressure around the base boundary as a function of τ, from which we can observe a more deepened suction on the top and at the side of the vehicle from $\tau = 25\%$ onwards. It reflects that the increase in size at $\tau > 25\%$ leads to a more

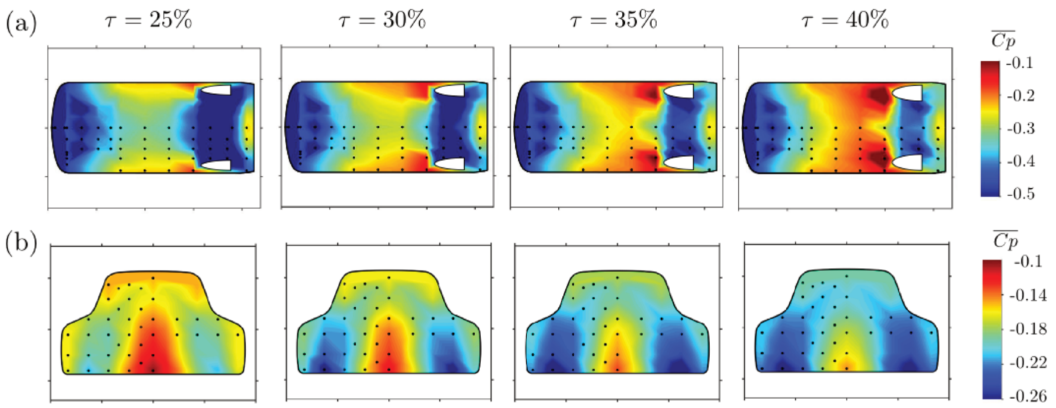

Figure 3.20: The underbody pressure distribution (a) and the base pressure distribution (b) for $\tau = 25, 30, 35, 40\%$.

important modification all around the base on the upper part of the vehicle body.

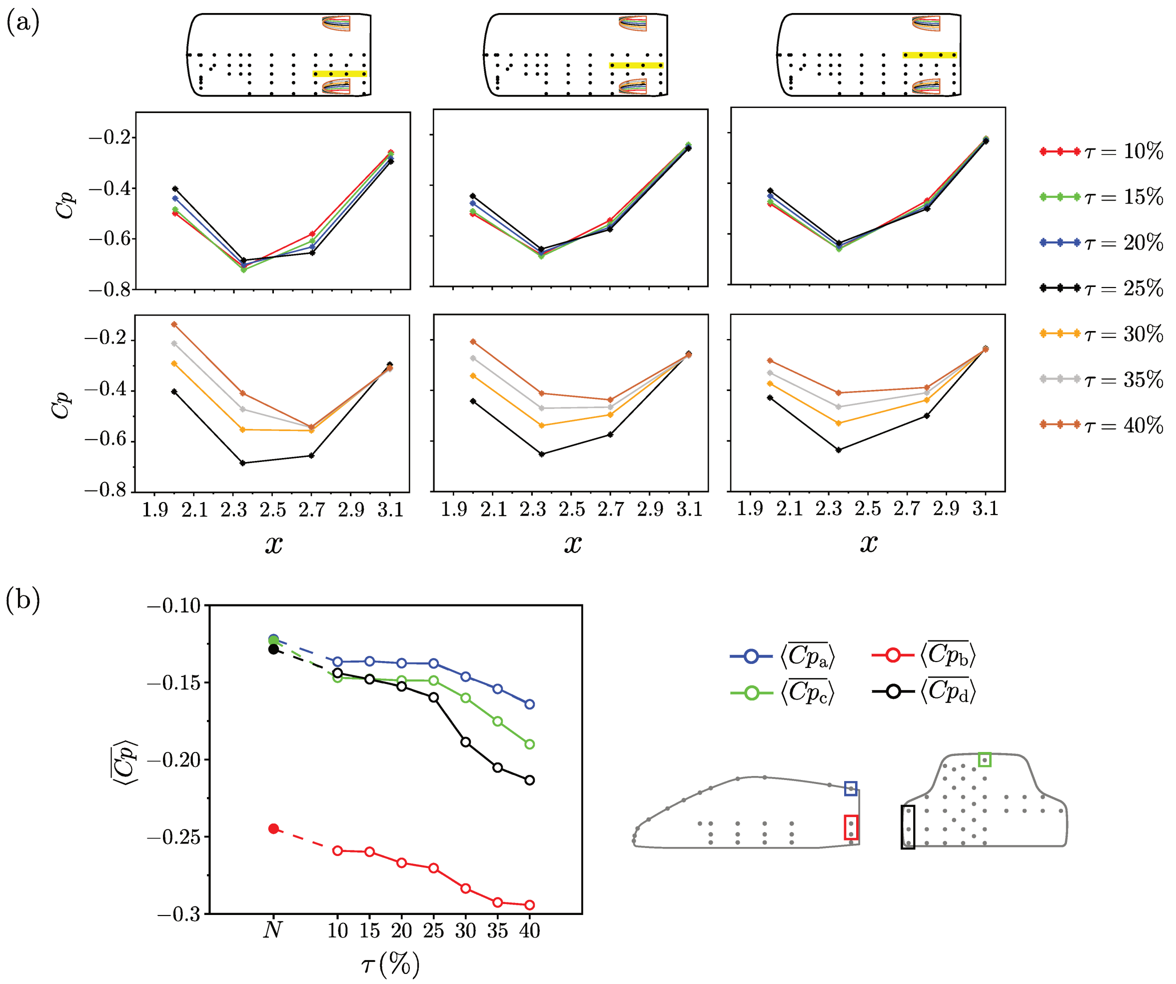

Figure 3.21: (a) Zoom of the pressure evolution at the rear part of the underbody for all the blockage rates; (b) Mean pressure around the base boundary as a function of τ.

All these observations lead to the questions of how this separation between ‘small’ and ‘large’ at $\tau = 25\%$ comes about and whether the separation in underbody and base pressure are related to one another. To answer this, further investigations are carried out on the obstacle wakes in the horizontal PIV plane at the half of the ground clearance. When analyzing Figure 3.22, we come across that reversed flow (blue region of negative velocity) can be captured in the wakes of configurations with higher blockage rates than 25%. This can be further visualized by the profiles of $\overline{u}$ at $x = 0.01$ in Figure 3.22(c). $\tau = 25\%$ has two gaussian-like wake profiles. However for larger obstacles, at this streamwise position, their mean wakes are not yet closed. From the distribution of $k = 0.5 \times (\overline{u'u'} + \overline{v'v'})$ in Figure 3.22(b), same conclusion can be drawn. For $\tau > 25\%$, the concentration of velocity fluctuations along the detaching shear-layers is particularly clear. While for $\tau = 25\%$ the significant fluctuation is attributed to the interaction of the opposed shear layers.

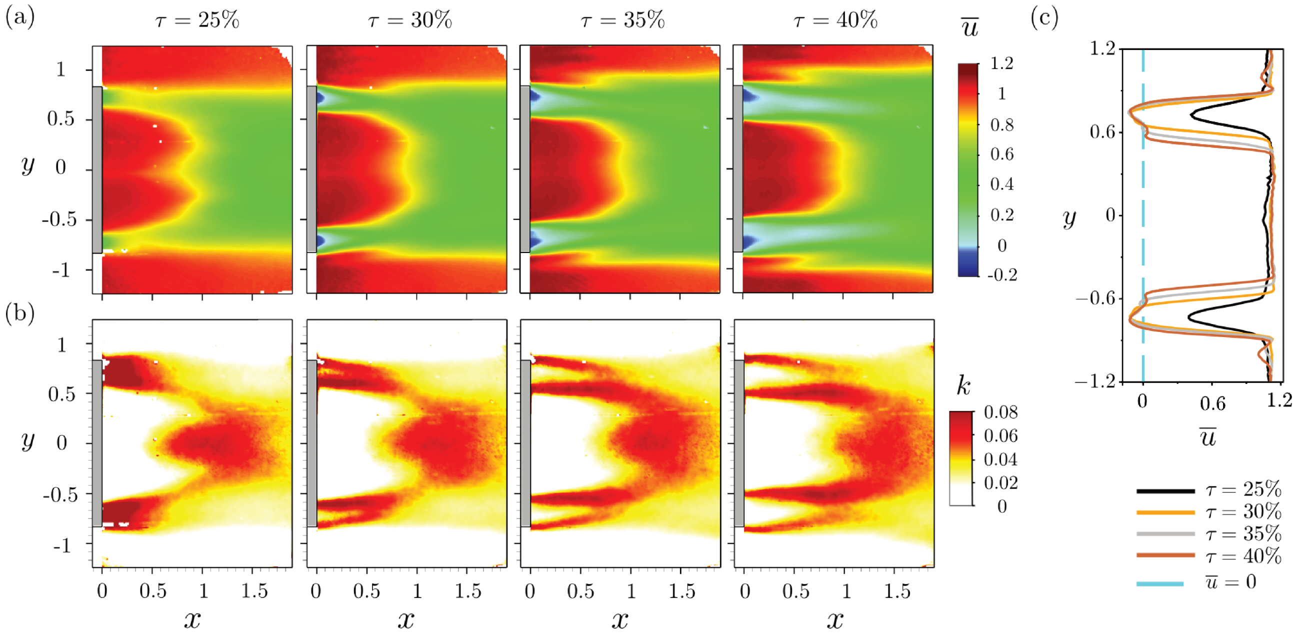

Figure 3.22: The time-averaged velocity magnitude (a) and the planar turbulent kinetic energy $k = 0.5 \times (\overline{u'u'} + \overline{w'w'})$ (b) in the horizontal PIV plane at the half of the ground clearance, for $\tau = 25, 30, 35, 40\%$. (c) Profiles of $\overline{u}$ at $x = 0.01$. $\overline{u} = 0$ is indicated in blue dash line.

Enlightened by this point, we conjecture that with the 'unclosed' obstacle wakes (in a time-averaged point of view) exposed to the vehicle wake, strong interaction between them will ultimately lead to a drastic pressure drop in the vehicle base.

Circumstantial evidence can be gained from the wake flow investigation of a 2D circular cylinder in Balachandar *et al.* (1997). The Reynolds number is around 300 based on the diameter. It is reported that the pressure in the mean wake reaches a minimum upstream of the reattachement point and gradually recovers to upstream value downstream the closure of the mean bubble (Figure 3.23(a)). This pressure evolution is also true for other bluff bodies at higher Reynolds numbers. For instance, Figure 3.23(b) depicts the pressure contours in the wake of an Ahmed geometry at ground proximity, with $Re \approx 9.2 \times 10^4$ based on model height (Grandemange *et al.*, 2013*b*). The pressure minimum in the wake is reported inside the recirculation region, corresponding to the center of the time-averaged recirculation structures. Further downstream, the pressure coefficient increases to reach positive values after the recirculation closure. Thereupon, the remarkable drop of SCp_{B} for larger obstacles $\tau > 25\%$ can be interpreted as a much lower pressure condition being imposed on the vehicle base by the unclosed mean wakes of the obstacles.

This upheaval in vehicle wake at $\tau > 25\%$ is possibly propagated upstream so that the underbody flow is also influenced, which is reminiscent of the *Diffuser pumping* phenomenon investigated by Cooper *et al.* (1998, 2000). They revealed that the exit pressure of an automo-

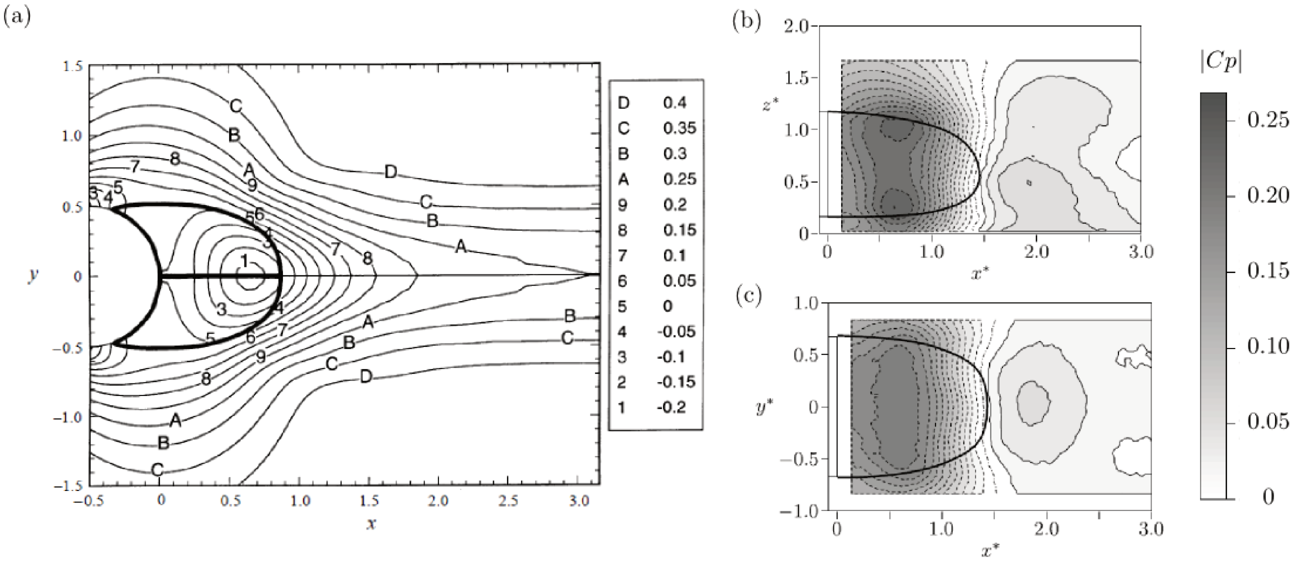

Figure 3.23: Static pressure coefficient in the wake of a circular cylinder at a Reynolds number of 300 (Balachandar *et al.*, 1997) (a). Contours of static pressure in the wake of an Ahmed geometry at ground proximity, with $Re \approx 9.2 \times 10^4$, in symmetrical plane $y^* = 0$ (b) and vertical plane $z^* = 0.67$ (c); the continuous and dashed lines are respectively positive and negative values; The thick black line locates the separatrix of the mean flow (Grandemange *et al.*, 2013*b*).

tive diffuser is more or less fixed by the vehicle base. As the diffuser recovers pressure along its length, the fixing of the outlet pressure effectively reduces the diffuser inlet pressure and it is said to have *pumped down* the pressure at the diffuser inlet. Hence it is the diffuser that controls how much (depending on the diffuser angle or length etc.) the pressure is 'pumped down' from the diffuser exit to the diffuser inlet. Within our context, it is possible that for larger obstacles, with lower pressure at the exit of the vehicle diffuser, as well as decreased passage area between the obstacle pair, the pressure at the diffuser inlet is much less 'pumped down' (meaning that the pressure at the diffuser inlet is increased).

Aside from the half-elliptical base cylinders, circular cylinders with same blockage rates τ are also tested, with additionally one cylinder pair of $\tau = 27.5\%$. Their installation is the same to the half-elliptical base cylinders. The end of the circular cylinders is tangential to the rear wheelhouse end and their outboard sides are tangential to the sides of the vehicle.

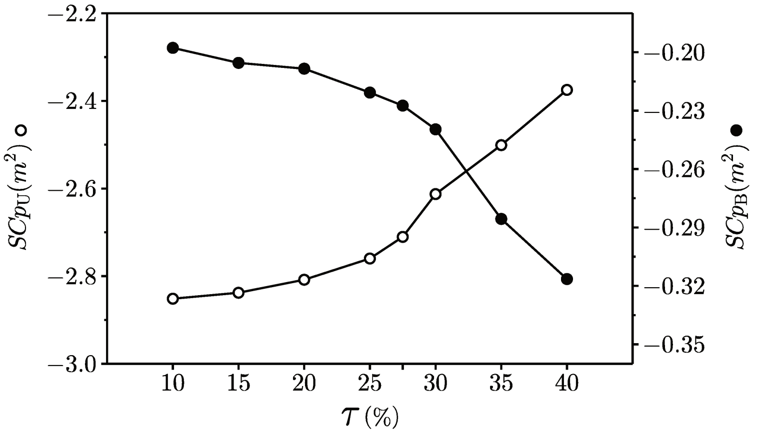

Figure 3.24: The integrated underbody pressure (left axis) and integrated base pressure (right axis) for circular cylinders with $\tau = \{10, 15, 20, 25, 27.5, 30, 35, 40\}\%$.

In Figure 3.24, the integrated underbody and base pressure as a function of τ evolve in a similar fashion to Figure 3.13 with a separation at around $\tau = 27.5\%$. However the curves have a less sharp change in slope (even if the measurement at $\tau = 27.5\%$ is disposed of). This is presumably related to the non-fixed separation point on the circular cylinders as opposed to half-elliptical base cylinders.

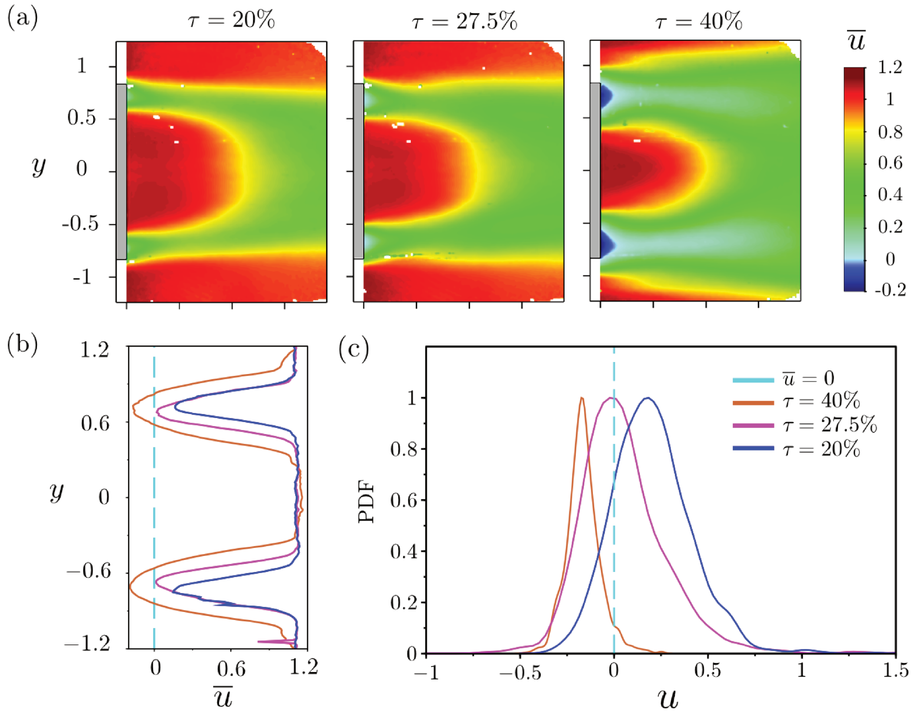

Figure 3.25: (a) The time-averaged streamwise velocity $\overline{u}$ distribution in the horizontal PIV plane at the half of the ground clearance for circular cylinders of $\tau = 20, 27.5, 40\%$; (b) Profiles of $\overline{u}$ at $x = 0.01$, with $\overline{u} = 0$ indicated in blue dash lines; (c) Probability density functions (PDF) of the maximum deficit at $x = 0.01$. The maximum deficit is taken at $y_m = \text{argmin}_{y>0}\,\overline{u}(y)$ for each configuration. The PDF distributions are normalized for easier comparison.

In matters of the cylinder wakes, only three measurements are available, which are $\tau = 20\%, 27.5\%$ and 40% (Figure 3.25). In the wakes of small blockage rate configuration $\tau = 20\%$, the streamwise velocity is all positive, pointing out that their mean wakes in this horizontal plane are already closed upstream the exit of the diffuser. On the contrary, in the mean wakes of large blockage rate $\tau = 40\%$, considerable reversed flow can be observed. In between, for $\tau = 27.5\%$ the maximum deficit at the exit of the underbody is approximately zero, as can be perceived from the profiles of the streamwise velocity $\overline{u}$ at $x = 0.01$ in Figure 3.25(b). Thus in a 2D point of view, the closure of their wakes locates approximately at the exit of the underbody. Notwithstanding, it should be pointed out that this mean wake length for a circular cylinder is much longer than in a 2D flow in Balachandar *et al.* (1997). Taking the recirculating length as the distance between the cylinder end and the vehicle base plus one radius, and normalizing by its diameter leads to $L_r \approx 2.16$ (at $Re_D = 2.04 \times 10^5$). While in Balachandar *et al.* (1997) this value is around 1.21 at $Re_D = 300$ and 1.10 at $Re_D = 1.4 \times 10^5$, which emphasizes an important disparity of the flow around a circular cylinder of a low aspect ratio ($H/D \approx 0.71$) bounded by the underbody and the ground, from a typical 2D flow. Furthermore, insight into the velocity statistics at this streamwise position ($x = 0.01$) can be gained from the PDF distributions of the maximum deficit (taken at $y_m = \text{argmin}_{y>0}\,\overline{u}(y)$ for each configuration). As shown in the Figure 3.25(c), with increasing blockage rate, the proportion of negative component is thereby increasing. Lastly it is noteworthy that even for the smallest circular cylinder, the integrated underbody pressure ($SCp_{\mathrm{U}} = -2.852m^2$) is higher than that of the smooth vehicle configuration N ($SCp_{\mathrm{U}} = -2.907m^2$), revealing that the circular cylinder is devoid of flow guidance effect.

If for 'large' blockage rates the drastic raise in underbody pressure and base suction compared to 'small' ones comes down to the 'merging' of the 'unclosed' obstacles wakes with the vehicle wake, it is then anticipated that with one obstacle pair gradually distanced from the base, whose mean wakes will close more and more upstream, it could be equivalent to reducing the width of the obstacle in our experiments. While in this scenario, the underbody blockage is not changed. In order to achieve this confirmation, a small experiment is carried out.

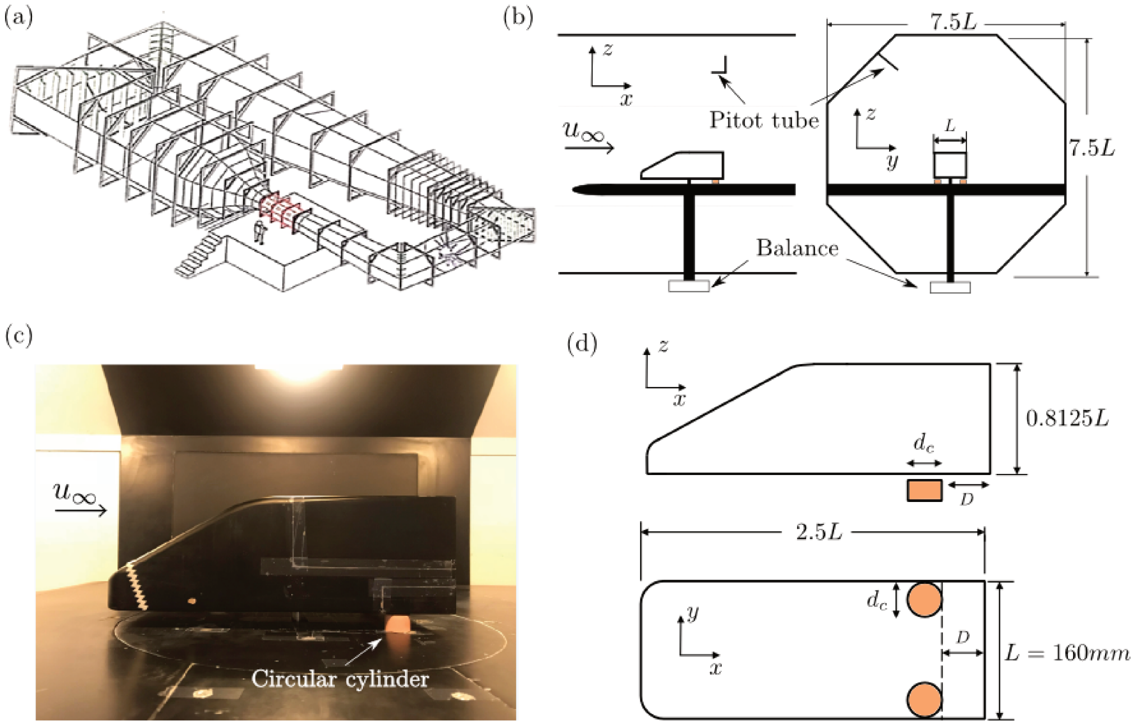

Figure 3.26: Verification experiment: (a) Schematic of the wind tunnel S120 in Pprime Institute; (b)(c) The model inside the regular octagonal working section; (d) The geometry of the tested model; two pairs of circular cylinders with blockage rates of $\tau = 2d_c/L = 25\%$ and 35% tested in the underbody.

This a posteriori verification test is conducted in a more reduced-scale wind tunnel, S120 in Pprime Institute, with a regular octagonal working section of $1.2m^2$ (Figure 3.26(a)). It is a closed-loop wind tunnel, with a contraction ratio of $20:1$. The maximum free-stream velocity is about $90m/s$ with a turbulence intensity of approximately 0.2%. Shown in Figure 3.26(b) and (c) is the simplified Windsor-type model inside the working section. It does not have underbody diffuser, and its geometrical parameters are given in Figure 3.26(d). The experiments are conducted at a free stream velocity of $40m/s$, corresponding to a Reynolds number $Re \approx 3.85 \times 10^5$ based on the square root of the model's frontal area. For the obstacle pair that are tested in various streamwise positions in the underbody, we are using circular cylinders to avoid incorrect alignment with the wind. They are fixed on the tunnel floor by double faced adhesive tape. Two cylinder diameters $d_c = 20mm$ and $28mm$ are tested, corresponding respectively blockage rates of $\tau = 2d_c/L = 25\%$ and 35%. The ground clearance is set at $22mm$. Leaving a small gap of $2mm$ between the obstacle pair and the model allows the measurements of the aerodynamic lift and drag of the model (without obstacles), which are acquired by the six-component balance shown in Figure 3.26(b).

The results are provided in Figure 3.27, with the lift (Cz) and drag (Cx) coefficients as a

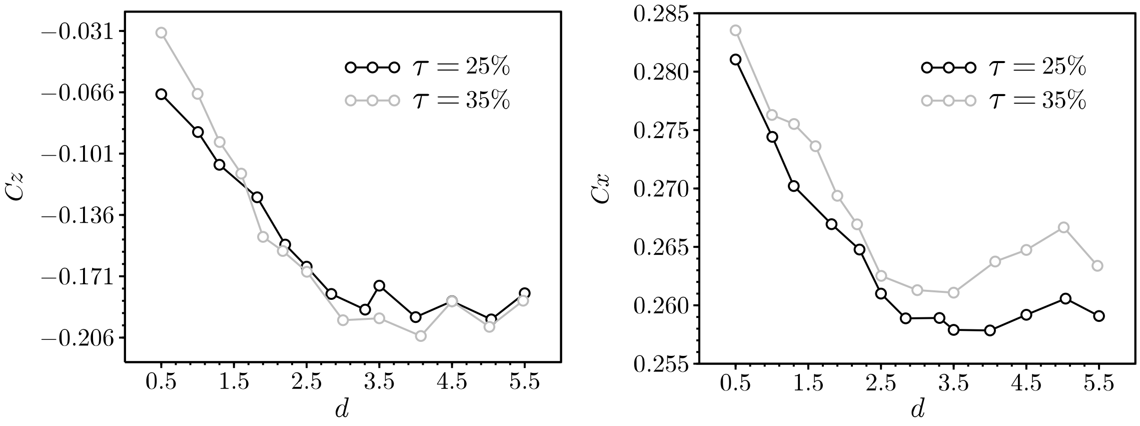

Figure 3.27: The lift (Cz) and drag (Cx) coefficients as a function of normalized distance $d = D/d_c$+0.5 (see Figure 3.26(d) for notations) for the tested two pairs of circular cylinders.

function of normalized distance $d = D/d_c + 0.5$. Here +0.5 tries to take into account the flow separation position on a circular cylinder, which is roughly at $0.5d_c$ in the streamwise direction. For instance, when the end of the cylinders is tangential to the model base, $D = 0$ and $d = 0.5$. At around $d < 3$, the measured lift and drag coefficients exhibit a strong sensitivity towards the distance of the obstacles to the base. We can have sight of a rapid descent of the lift (increasing downforce) and drag coefficients when the obstacle pair is moved away from the base. While from $d \approx 3$ onwards, the curves change slope. The lift coefficients seem to fluctuate around constant values. And the drag coefficients decrease mildly then followed by an increase and finally a decrease. The final raise and drop of the drag coefficient at $d > 4$ is not of primary concern as the obstacle pair is already very far away from the base, which might bring about other phenomenons. However, the continuous reduce of Cz and Cx with increasing d, and the change in slope at nearly same normalized distance $d \approx 3$ consolidate the idea that the two coefficients are both tightly related to the streamwise development of the obstacles mean wakes. Furthermore, from the drag evolution, it can be said that at equal normalized distance to the base, smaller obstacle entails smaller vehicle drag.

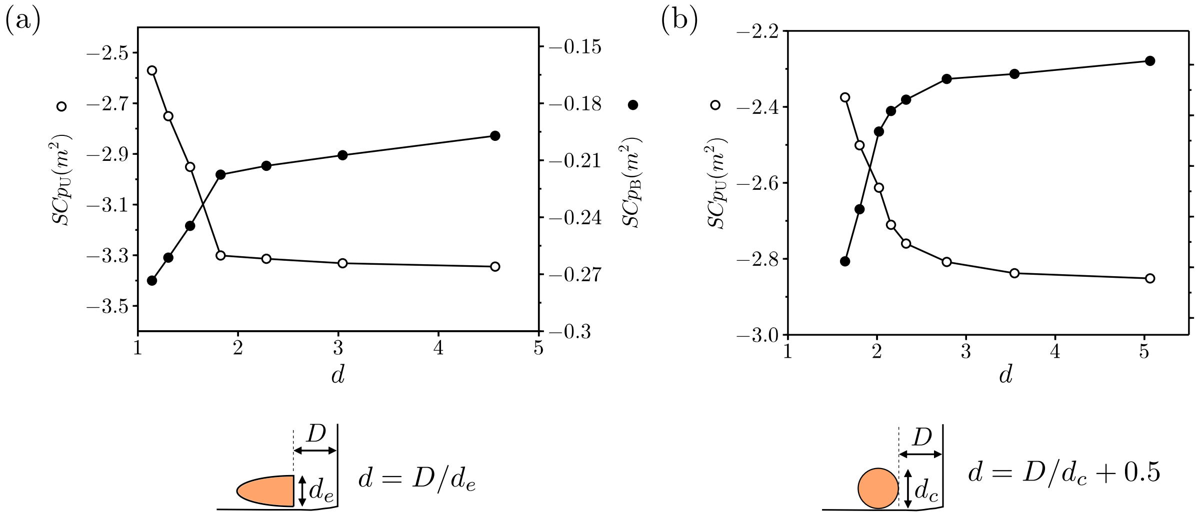

Figure 3.28: The integrated underbody pressure (left axis) and integrated base pressure (right axis) for half-elliptical base cylinders (a) and circular cylinders (b) tested in the wind tunnel S620, as a function of normalized distance.

Similarly, the results in Figure 3.13 and Figure 3.24 are plotted anew as a function of the normalized distance from the base in Figure 3.28. The ‘large’ and ‘small’ blockage rates can

	$\tau = 25\%$	$\tau = 30\%$	$\tau = 35\%$	$\tau = 40\%$
$SCp_{\mathrm{B}}(m^2)$	-0.218	-0.245	-0.261	-0.273
L_r	1.27	1.23	1.21	1.20
$d\overline{Cp}/dz$	-0.072	-0.071	-0.072	-0.076

Table 3.3: The integrated base pressure SCp_{B}, recirculation length L_r in the $y = 0$ plane and the vertical pressure gradient $d\overline{Cp}/dz$ at the base centerline for $\tau = 25, 30, 35, 40\%$

analogously be referred to as ‘close to’ and ‘far away from’ the vehicle base for one particular blockage rate. In addition, the measured aerodynamic coefficients of the reduced model bear a stronger resemblance to the results in Figure 3.28(b), with a smoother transition from ‘large’ to ‘small’, as both of them use circular cylinders. Finally, the results with various streamwise position highlights the potential of reducing the model drag by decreasing the underbody blockage as well as shifting obstacles away from the base. In a real life scenario, the rear wheels are preferred to be installed at a rearmost position to achieve better stability. Nonetheless it is possible that an optimum position can be achieved considering both factors.

Back to ‘large’ blockage rate half-elliptical base cylinders, their impact on the time-averaged flow field in the symmetrical plane $y = 0$ is provided in Figure 3.29. Except the shortening bubble with increasing blockage rate in Figure 3.29(a), no significant modification of the wake topology is observed. As summarized in Table 3.3, the decreasing base pressure is in agreement with the reducing recirculation length and larger curvature of mean streamlines at separation. While their vertical pressure gradients of the base centerline measurements remain close. From the planar turbulent kinetic energy $k = 0.5 \times (\overline{u'u'} + \overline{w'w'})$ distributions in Figure 3.29(b), we can observe a slightly increasing dominance of unsteadiness along the lower shear flow.

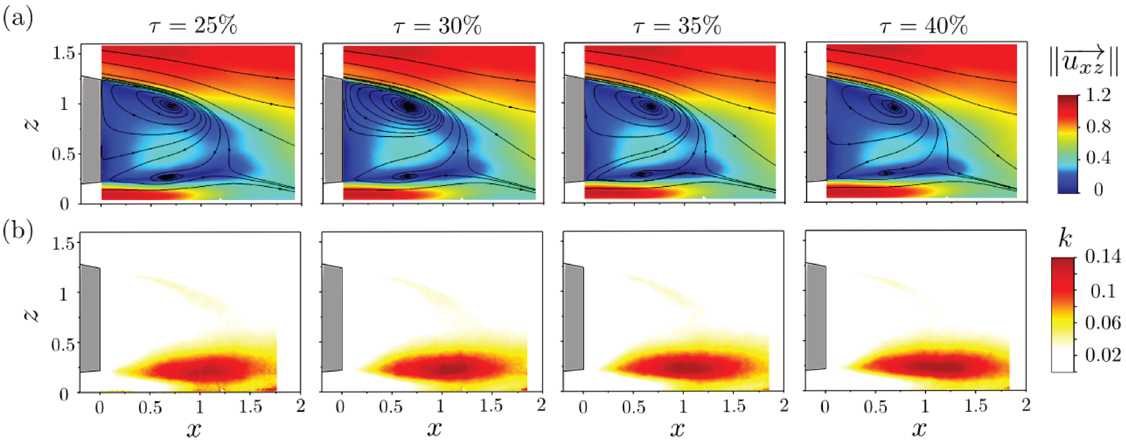

Figure 3.29: The time-averaged velocity magnitude (a) and the planar turbulent kinetic energy $k = 0.5 \times (\overline{u'u'} + \overline{w'w'})$ (b) in the symmetrical PIV plane for $\tau = 25, 30, 35, 40\%$.

Summary In this section, 7 pairs of profiled obstacles are tested whose blockage rate in the underbody increases from 10% to 40%. With increasing obstacle width, the surface pressure distributions bring to light two regimes with a separation at $\tau = 25\%$.

For small blockage rates ($\tau \leq 25\%$), when compared to the smooth vehicle model N, an effect of flow guidance can be corroborated which manifests as a drastic drop of the underbody pressure at the rear part between the obstacle pair and therefore a drop in the integrated underbody pressure. This effect arises from the prevention of the outside flow penetrating the low pressure regions, which will be the same if two thin plates are mounted instead of the obstacle pair. Besides, in this blockage range, the enlarging width only has a local impact on the surface pressure of the vehicle. It raises the pressure upstream of the obstacles in the underbody. And it decreases locally the pressure downstream on the vehicle base as decreased pressure condition is set at the rear separation of the obstacle and imposed on the vehicle base. The pressure in the symmetrical plane $y = 0$ is nearly unaffected.

For larger blockage rates where $\tau > 25\%$, the enlarging size entails a more important modification in terms of the pressure distribution on the vehicle surface. In the underbody, an important pressure augmentation extends from upstream to downstream of the obstacle pair. The diffuser efficiency decreases. In the middle of the underbody the exit flow is affected, and the base centerline pressure drops concomitantly. On the upper part of the vehicle body, the decreasing pressure all around the base boundary reflects that the whole vehicle wake is contaminated by the enlarging obstacles in the underbody, therefore creates a broad suction on the base surface. To sum up, the increase in underbody blockage rate increases slowly the base suction and underbody pressure in the small blockage range while much more rapidly at larger blockage rates.

The separation of 'small' and 'large' blockage rates at $\tau = 25\%$ is believed to be associated with the streamwise development of the obstacle wakes in the underbody. In the horizontal planar PIV measurements at the half of the ground clearance, for 'small' blockage rate obstacles ($\tau \leqslant 25\%$), no reversed flow is captured in their wakes at $x > 0$. Whereas for 'large' blockage rate obstacles ($\tau > 25\%$), their mean wakes are not yet closed at the exit of the underbody. The 'merging' of their unclosed mean wakes with the vehicle wake is deemed to account for the important increase in underbody pressure and base suction.

The experiment with circular cylinders of different blockage rates beneath the same geometry also provides strong evidence of the correspondence between their mean wake closure and the vehicle's surface pressure level. An additional experiment with reduced scale model is carried out, aiming at reproducing this separation in lift and drag coefficients, with same underbody blockage rate but at various distance to the base. The results suggest that with one obstacle pair gradually distanced from the model base, we can discern two regimes, 'close to' and 'far away from' the base. The two regimes differ greatly in their sensitivity of the global aerodynamic coefficients towards this distance, and they can be analogously referred to as 'large' and 'small' blockage rates situations. Hence it is sufficient to remark that, although the experiments in the two wind tunnels differ from one another to a large extent (one is testing different underbody blockage, the other changes the obstacle position in the underbody; the geometry involved are quite different, one has diffuser, the other not, etc.), the results seems to be universal. And both support the hypothesis that the unclosed mean wakes of the underbody obstacle yields much stronger interaction with the vehicle wake and thus more important influence on the vehicle surface pressure distribution.

Eventually, the wake measurements in the symmetrical plane demonstrate that, for all the tested profiled obstacles, the vehicle mean wakes seem to have similar topology, with a large clockwise mean recirculating structure and a smaller counter clockwise mean structure. While compared with N, their wakes exhibit more pronounced z-asymmetry which develop closer to the ground. This is in accordance with their vertical pressure gradient of the base centerline measurements. As summarized in Figure 3.30(a), their $d\overline{Cp}/dz$ values are similar but smaller than that of N. In large blockage regime, the degree of wake asymmetry is very likely to saturate, even though a decreasing diffuser efficiency is observed with increasing obstacle width. In addition, there is a clear reduction of the recirculation length with increasing underbody blockage rate (Figure 3.30(b)), indicating an increasing curvature of mean streamlines at

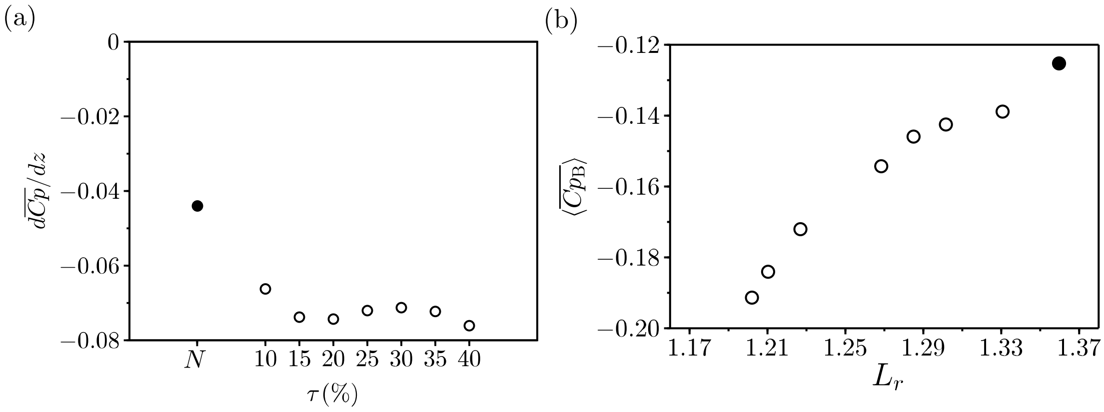

Figure 3.30: (a) The vertical pressure gradient at the base centerline $d\overline{Cp}/dz$ as a function of the blockage rate. N is also presented for comparison in black dot. (b) Mean base $\overline{Cp_{\mathrm{B}}}$ level as a function of the recirculation length for decreasing blockage rate from left to right. N is also presented for comparison in black dot.

separations.

Chapter 4

The wheel-vehicle interaction

In this chapter, the profiled obstacles are firstly substituted by rear rotating wheels (Section 4.1). The configuration is denoted with *XR*. Compared to N, decreased pressure is observed at the rear underbody and the suction increases on the base (Section 4.1.2). For rotating or stationary rear wheels, no modification has been remarked in terms of mean wake topology compared to N (Section 4.1.3). The effect of the rear wheels alone can therefore be viewed, at first order, as a blockage effect. The rotation or not of the wheels varies the blockage rate in the underbody, with stationary wheels generating wider wakes hence higher blockage.

In Section 4.2, front rotating wheels are additionally included. This baseline configuration, denoted with *RR*, is investigated compared to *XR*. Its underbody flow momentum is significantly reduced due to the presence of the front wheels. The well-balanced vehicle wake in the symmetrical plane is thus recovered. The wakes of the rear wheels are larger than those of *XR*, revealing an enhanced interaction between the wheel wakes and the vehicle wake. However, the locally decreased base pressure downstream the rear wheels is compensated by the pressure recovery at the base upper region, due to the wake balance inversion. Therefore, the mean base pressure (and drag) remain unchanged compared to *XR*.

At last in Section 4.3, different wheel states are tested at the front and rear axle in comparison with the baseline configuration *RR*. When the front wheel rotation is stopped, the front stationary wheels create larger wakes and lower pressure in their wakes, leading to lower lift coefficient. While the vehicle wake balance is slightly affected. When the rear wheel rotation is stopped, the diffuser accentuates the higher blockage effect created by rear stationary wheel. There is an increase in pressure between the rear wheels, leading to higher lift. The reduced underbody flow momentum ultimately results in a downward deflection of the vehicle wake.

Contents

With the fillings in the wheelhouses being unplugged, the pressure measurements inside the front and rear wheelhouses exhibit non-negligible (positive or negative) contribution to the vehicle drag. Nevertheless, their contribution is not the concern of this chapter, as it does not affect the following analysis based on vehicle drag and base pressure. Their influence will be evaluated in Section 5.2.

4.1 Effect of the rear wheels for two wheels configuration

In this section, the study will be further expanded to substitute the profiled obstacles by rear wheels with the reference tire (three longitudinal grooves) as a more realistic approach. The results of this study will be presented in three sections. Section 4.1.1 gives a detailed description of the large scale flow structures around the rear rotating wheels gleaned from the numerical results. Section 4.1.2 investigates the impact of the rear rotating wheels on the flow features around the vehicle model, in comparison with the smooth vehicle configuration N. In Section 4.1.3, the rotation of the rear wheels will be stopped. The effect of the wheel state will be explored. XR and XS denote respectively the configuration without front wheels and with rear Rotating wheels, and rear Stationary wheels.

The experimental set-up is the same as described in Section 2.1. The front wheelhouses are still plugged by polystyrene foam. The fillings in the rear wheelhouses are removed and the rear wheels are mounted with the standard rear axle track (Figure 4.1). The geometric blockage rate of the wheels is $\tau = 24.6\%$.

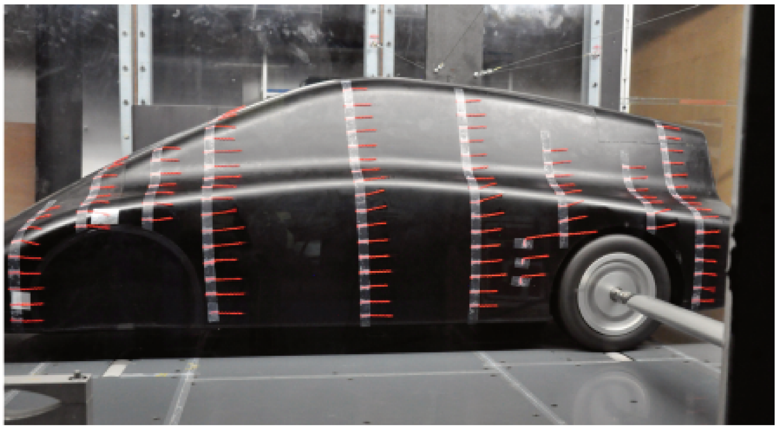

Figure 4.1: Installation of configuration with two rear wheels in the wind tunnel.

4.1.1 Flow field around rear rotating wheels

The flow around a wheel inside the wheelhouse is complex and highly three-dimensional. To visualize the development of the wake of the rear rotating wheel, several important quantities obtained from the simulation results are presented in Figure 4.2.

From Figure 4.2(a), the positive pressure peak ($Cp > 1$) in front of the contact patch can be observed. It is attributed to the converging boundary layers on the moving tire and the ground, transmitting energy to the flow in front of the contact patch through the shear stresses. A *jetting* phenomenon is therefore produced as the flow is pumped out from the front of the contact patch and then deflected by the oncoming flow in the streamwise direction. The jetting vortex can be discernible in Figure 4.2(a) by its low pressure and high velocity in the core, and

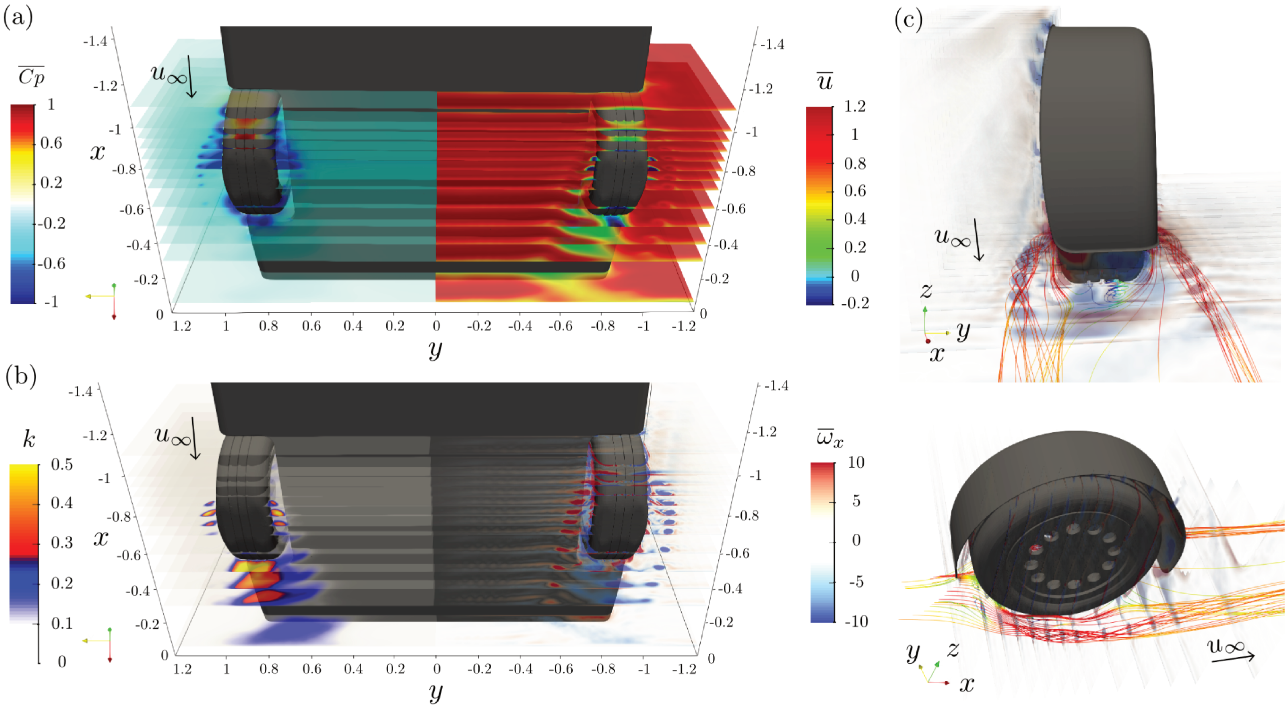

Figure 4.2: Bottom views of the rear wheels: (a) The evolution of $\overline{Cp}$ on the left and time-averaged streamwise velocity $\overline{u}$ on the right in parallel streamwise slices from upstream to downstream of the rear wheels; (b) The evolution of turbulent kinetic energy k on the left and streamwise vorticity $\overline{\omega_x}$ on the right in parallel streamwise slices from upstream to downstream of the rear wheels. (c) The time-averaged streamlines colored by $\overline{u}$ at the lower part of the rear left wheel, with the slices colored by $\overline{\omega_x}$, in rear view and outboard view.

also by the intense longitudinal vorticity in Figure 4.2(b). The time-averaged streamlines in Figure 4.2(c) also reflect the swirling motion of the jetting vortex. Furthermore, as illustrated from the mean turbulent kinetic energy k distribution in Figure 4.2(b), in the swirling core it is devoid of high turbulent kinetic energy. Thus it brings to evidence the spatial stability of the jetting vortex.

The high fluctuation zones at the two sides of the contact patch ($-0.85 < x < -0.7$) are recirculation zones where the flow can not stay attached to the wheel surface. They can also be seen by their low pressure and mean negative velocity in Figure 4.2(a) at the same location ($-0.85 < x < -0.7$). However in most of the numerical studies (McManus & Zhang, 2006; Regert & Lajos, 2007) the jetting vortex are often merged with the separation zones where iso-surfaces of Q or vorticity are applied to highlight the lower wheel wake as shown in Figure 4.3(a) (marked as N) and (b) (marked as L and R). In our simulation results the two recirculation zones are rather small (marked as N in Figure 4.3(c)(d)), and the side flow (marked as P) remains well attached to the wheel side surface. We propose that at the inner side of the wheels, the high momentum flow in the underbody accelerates when traveling between the two rear wheels, and promotes an earlier attachment when compared to Figure 4.3(a) which is an isolated rotating wheel and Figure 4.3(b) where only one front wheel is simulated; at the outer side, the potential flow tends to deflect inward and will also limit the size of the recirculation area.

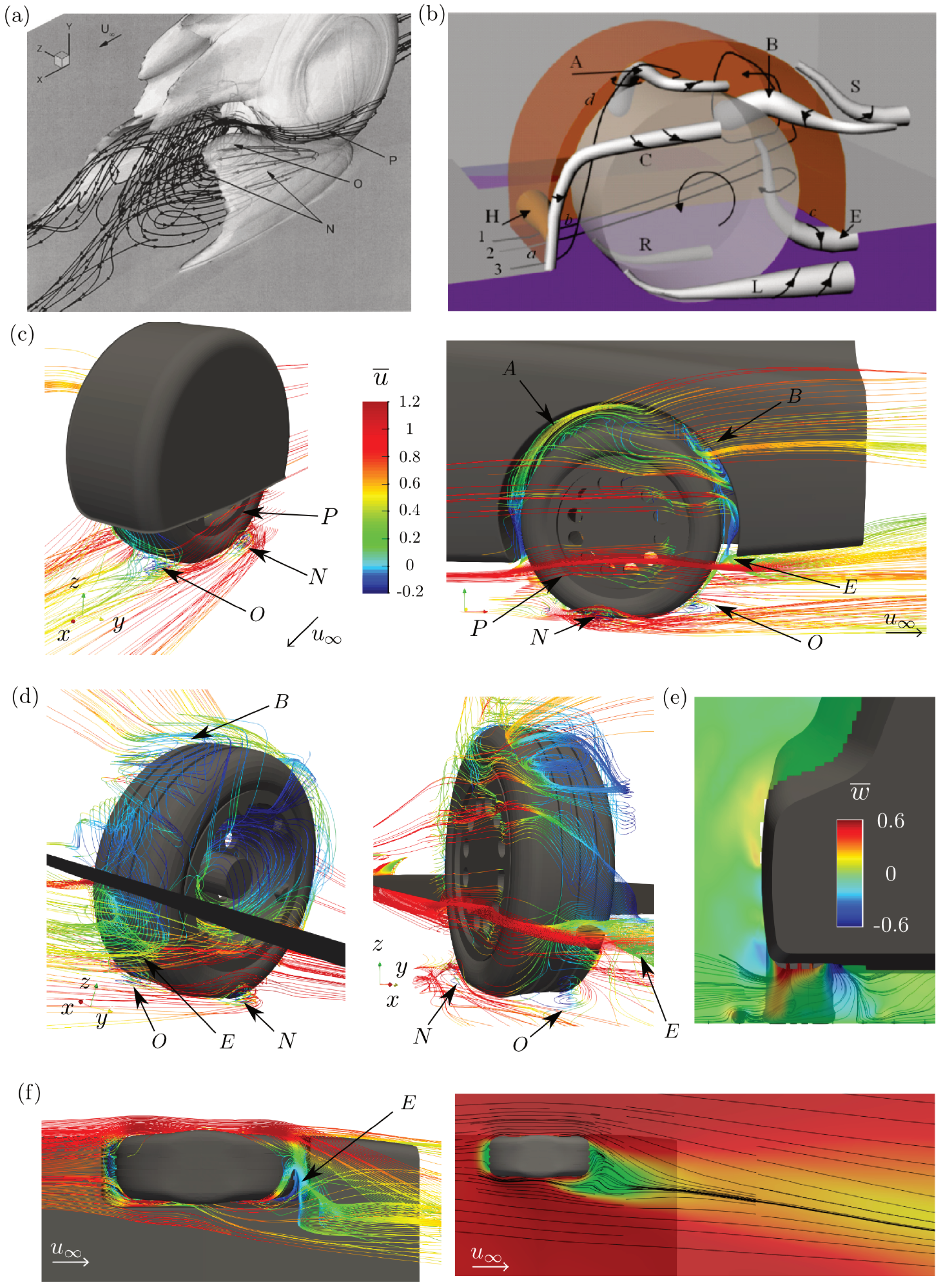

Figure 4.3: (a) Isosurface of vorticity magnitude $\Omega d/U_\infty = 3.5$ and streamlines in the lower near wake of an isolated rotating wheel (McManus & Zhang, 2006); (b) Vortex skeleton model of the wheelhouse flow field with vortices detected by $Q-$Criterion (Regert & Lajos, 2007); (c) Simulation results of the time-averaged streamlines around the rear left rotating wheel, colored by the time-averaged streamwise velocity $\overline{u}$, in inboard rear view and side view; (d) Inner views of time-averaged streamlines colored by $\overline{u}$ (the vehicle upper surface and the rear wheelhouse are removed for better visualization); (e) Iso-x plane slightly upstream the end of the wheel ($x = -0.45$), colored by the time-averaged vertical velocity $\overline{w}$; (f) Bottom view of the flow around the rear left rotating wheel: at left, the time-averaged 3D streamlines colored by $\overline{u}$; at right, the horizontal slice colored by $\overline{u}$ at the half of the ground clearance, overlaid with 2D streamlines.

Another region with high unsteadiness is behind the wheel, as seen in Figure 4.2(b). For one thing, it is characterized by the important suction ($Cp < -1$) immediately behind the contact patch due to the diverging surface, which has been proposed by Fackrell & Harvey (1975) albeit not observed, and afterwards has been validated by Mears *et al.* (2004); McManus & Zhang (2006); Heyder-Bruckner (2011). For another, an area of reversed flow can be found behind the wheel in Figure 4.2(a) with negative streamwise velocity, and in Figure 4.3 marked as O. This recirculation region also interacts with the flow entrained upwards by the lower wheel running surface, and the flow descending from the downstream part of the wheelhouse, marked as E in Figure 4.3(c), hence gives rise to significant fluctuations.

In addition, the time-averaged streamlines of the simulation results shown in Figure 4.3(c) globally agree well with the general schematic of the flow put forth by Regert & Lajos (2007) in Figure 4.3(b). The interaction of the up-flow entering the wheelhouse and the running surface of the wheel moving in the opposite direction results in boundary layer separation over the upper part of the wheel, which gives rise to the formation of vortex A. It leaves the wheelhouse from the front upper part. Vortex B mainly results from the flow entering the wheelhouse from its front leading edge or from the outboard side, getting entrained by the wheel rotation, recirculating inside the wheelhouse and the wheel hub cavity and eventually leaving the wheelhouse from the rear upper part. An inner view of B is given in Figure 4.3(d).

Besides, there are also several disparities when compared to the results of Regert & Lajos (2007). Firstly, inside the wheelhouse behind the leading edge, the boundary layer separation is less pronounced and so does vortex H. It can be attributed to the smaller gap between the wheel and wheel arch in our simulation. Secondly, there is no evident existence of C and S arising from the separation on the upstream and downstream edge of the wheel arch. In fact, for the simulated front wheel in Regert & Lajos (2007), the outside flow and the wheel-approaching flow have small yaw angle (pointing outboard) that promotes the separation. While in our simulation, the boat-tail shape of the vehicle at its rear part diminishes the massive separation on the wheel arch. At last, the vortex E not only originates from the flow entering at the front of the wheelhouse between the wheel and the inner wall. It could also be the outside potential flow that is inhaled inside, as shown in Figure 4.3(c), impinges on the downstream part of the wheel arch and then stretched downwards to the underbody.

From Figure 4.3(d) we can have sight of an upward flow entrained by the wheel running surface at its lower bottom that interacts with the flow descending from the wheelhouse and gives rise to vortex E. An iso-x plane slightly upstream the end of the wheel ($x = -0.45$) is extracted from the simulation in Figure 4.3(e), colored by the time-averaged vertical velocity $\overline{w}$. It highlights the upward (red) motion of the flow entrained by the lower part of the wheel and the downward (blue) flow exiting the wheelhouse. The bottom view of E is given in Figure 4.3(f). At right is the horizontal slice at the half of the ground clearance colored by the streamwise velocity $\overline{u}$ obtained from the simulation. The low velocity flow leaving the wheelhouse from the inner side and the rear bottom is captured as the green region at the rear part of the wheel. From the 2D streamlines we can observe that the low velocity region is diverted inward by the outside flow. And its size is much reduced in the streamwise direction by the high momentum flow at the inner side, before exiting the underbody.

4.1.2 Effect of the rear rotating wheels

The full scale aerodynamic lift and drag coefficients and the integrated underbody and base pressure of the configuration with rear rotating wheels *XR* are provided in the Table 4.1, together with the smooth vehicle configuration N. On the one hand, the presence of the rear rotating wheels increases the lift by 15.8% which is attributed to the raise of 4.8% in the integrated underbody pressure; and on the other, it increases the drag by 25.8% which can be related to the reduction of 27.5% in the integrated base pressure.

	$SCz(m^2)$	$SCx(m^2)$	$SCp_{\mathrm{U}}(m^2)$	$SCp_{\mathrm{B}}(m^2)$
N	-0.450	0.310	-2.907	-0.182
XR	-0.379	0.390	-2.768	-0.232

Table 4.1: Full scale lift and drag coefficients of the vehicle, integrated underbody and base pressure for smooth vehicle configuration N and the configuration with rear rotating wheels XR.

The comparison of the time averaged surface pressure $\overline{Cp}$ distributions in the $y = 0$ plane for the two cases are presented in Figure 4.4(a). When rear rotating wheels are employed, we can perceive a subtle increase at the front part of the underbody ($s < -3$), suggesting that the flow velocity is marginally reduced from the entrance of the underbody. Between the front and rear wheelhouses, the pressure raise is more noticeable, which is due to the stagnation zones in front of the rear wheels that can be observed in their underbody pressure distributions in Figure 4.4(b). The drop of the pressure at the rear part of the underbody for XR conjures up the comparison between N and small blockage rate configurations in Section 3.2 (Figure 3.14(a)). However the pressure drop is not as tremendous as small blockage rates configurations. In contrast to the rear wheels, the profiled obstacles completely seal the gap between the vehicle body and the ground. This reminds us of the work in Katz (1995) demonstrating the effect of the side skirt gap on the downforce of a race car. They pointed out that, leaving even a small gap between the ground and the side plate will allow the air from outside to penetrate into the underbody low pressure region and yield a reduced downforce.

In the base, their centerline pressure distributions exhibit different levels yet nearly the same vertical pressure gradient ($d\overline{Cp}/dz = -0.044$ for N and XR). Actually the rear wheels create a broad suction on the base, which is discernible on the base pressure distributions and their difference in Figure 4.4(c). Moreover, the base pressure drop is more important at the two sides ($y \approx \pm 0.63$).

In addition, there is a good continuity in their pressure distributions from the left side (in the underbody) and from the right side (on the roof) of the base. Except the pressure tap close the base, the other pressure measurements on the roof almost superimpose for the two cases. It demonstrates that only at the rear part of the roof is the pressure affected by the wake modification.

In the following, the modification of the mean flow field around the vehicle by the presence of the rear rotating wheels will be investigated to further understand the base pressure variation using PIV measurements where available and simulation results for additional information.

As described in Section 4.1.1, the diverging surface behind the contact patch, the flow reversal region O behind the wheel and its interaction with the flow leaving the wheelhouse E (Figure 4.3(c)) are sources of the low pressure, and they prone to decrease the pressure level downstream. This can be visualized in Figure 4.5(a), which are numerical results of the pressure distributions for the two configurations N and XR in the horizontal plane at the half of the ground clearance. The pressure evolution in this horizontal plane is in accordance with their underbody pressure distributions (Figure 4.4(b)). It can be remarked that the rear wheels generate flow stagnation areas upstream, suction zones at the front and rear tire shoulders and two low pressure regions in the wheel wakes that extend further downstream into the vehicle wake.

Not only the pressure is reduced by the rear rotating wheels but also the velocity is decreased behind them, as displayed in Figure 4.5(b). The time-averaged streamwise velocity $\overline{u}$

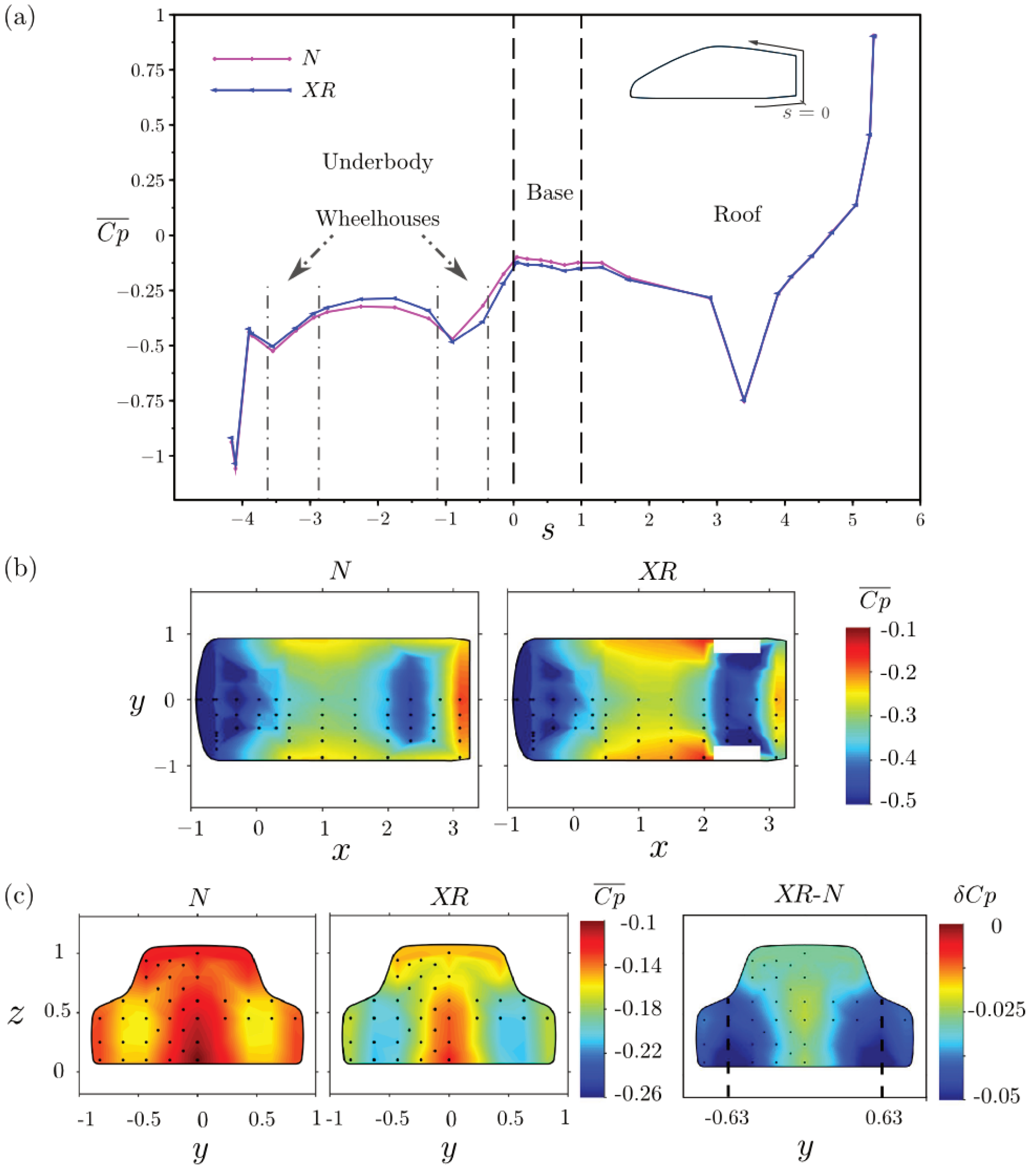

Figure 4.4: Comparison between N and XR. (a) The distribution of $\overline{Cp}$ in the $y = 0$ plane on the curvilinear abscissa s (normalized by the height of the base) with the origin at the underbody rear end; (b) The distribution of $\overline{Cp}$ on the underbody surface; (c) The time-averaged base pressure distribution and their base pressure difference.

distributions in this horizontal plane at the half of the ground clearance captured by the PIV measurements bring to evidence the velocity deficit downstream the wheels.

Furthermore, Figure 4.5(c) presents the iso-contour of $\overline{Cp_{tot}} = 0$ for XR from the simulation results, which underlines the 'dead areas' with low pressure as well as low velocity. It reveals the interaction between the wheel wakes and the vehicle wake, where the previous originate from the rear part of the wheel, diverted more inward by the outside flow and connect with the latter one at $y \approx \pm 0.6$. These effects are deemed to induce the important pressure reduction at the two sides in the base (Figure 4.4(c)).

Intense turbulent fluctuations have been reported behind the rear wheels in Figure 4.2(b). They are convected further downstream as can be observed from the distribution of the planar turbulent kinetic energy $k = 0.5 \times (\overline{u'u'} + \overline{v'v'})$ obtained by PIV measurements at the half of the ground clearance, in Figure 4.6(a). The wheel wake regions contain high turbulent kinetic energy, in contrast to the smooth vehicle model, whose underbody mass flow has only marginal

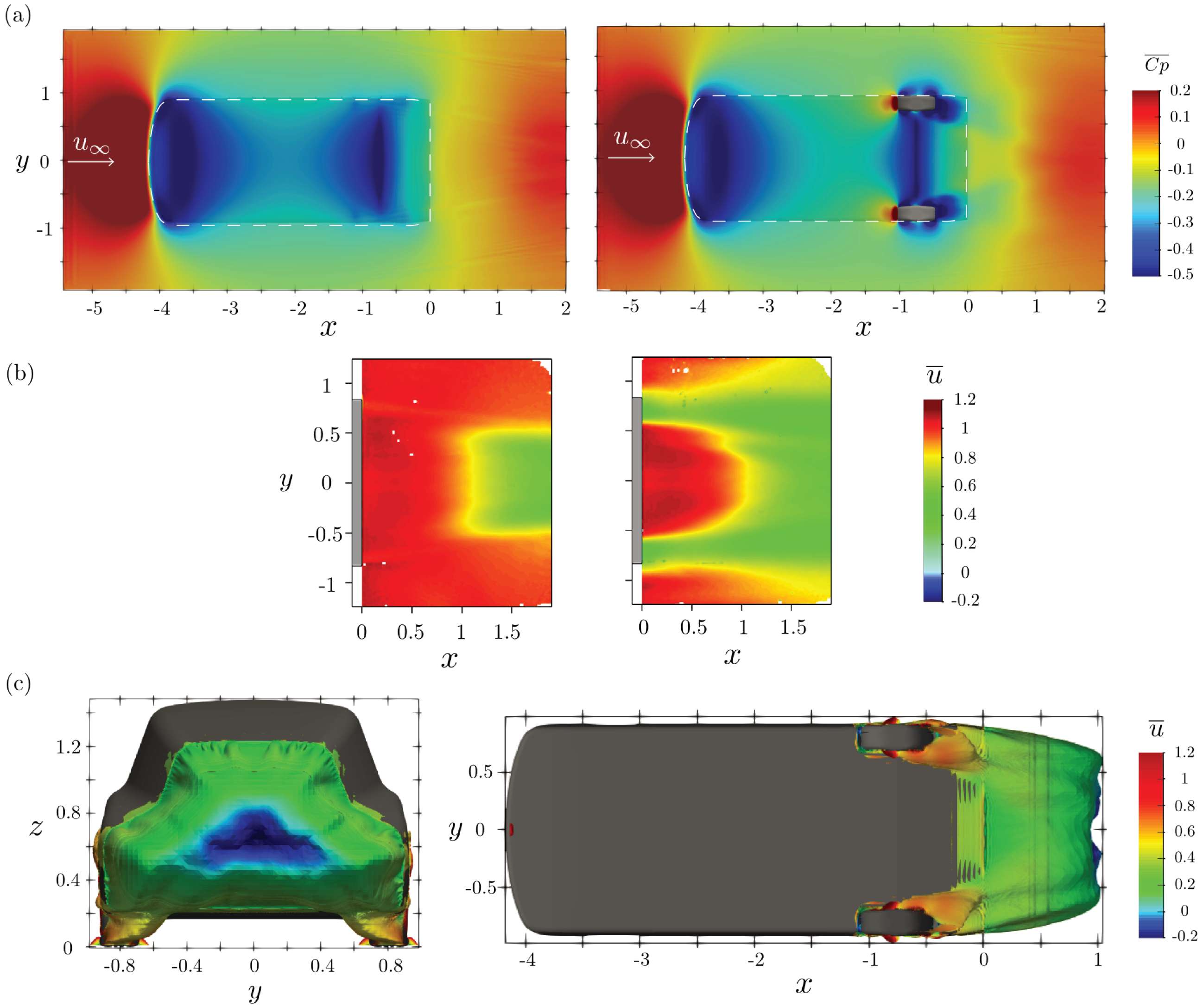

Figure 4.5: (a) Pressure distribution in the horizontal plane at the half of the ground clearance for N on the left and XR on the right from the numerical results; (b) PIV measurements of the time-averaged streamwise velocity $\overline{u}$ in the horizontal plane at the half of the ground clearance for N on the left and XR on the right; (c) Iso-contour of $\overline{Cp_{tot}} = 0$ ($\overline{Cp_{tot}} = \overline{Cp} + \boldsymbol{u}^2$) colored by time-averaged streamwise velocity $\overline{u}$ for XR.

turbulence intensity at $x > 0.8$ in the middle. In addition, Figure 4.6(b) reports the distribution of the turbulent kinetic energy $k = 0.5 \times (\overline{u'u'} + \overline{w'w'})$ in the symmetrical PIV plane $y = 0$. It highlights the concentration of k in the upper and lower shear layer regions resulting from the velocity fluctuations. The evolution of the shear layers leads to an increase of k along the streamwise direction. Specifically, the fluctuations are more remarkable in the lower shear layer and all the more important for XR. The non-balance vehicle wake in this symmetrical plane is retained.

From Figure 4.6(a) and (b) we conjecture that the rear wheels act as perturbations, creating high fluctuations immediately behind them, at the two sides of the underbody, and will eventually influence the exit flow in the middle more downstream. This development can be ascertained from the evolution of the turbulent kinetic energy $k = 0.5 \times (\overline{u'u'} + \overline{v'v'} + \overline{w'w'})$ obtained from the numerical simulation for XR presented in Figure 4.6(c) at various streamwise planes. The two high fluctuation regions behind the wheels are convected downstream and inboard with reducing intensity and enlarging size, and they completely merge at $x > 1.5$. It is worthy of notice that at $x = 0$, high fluctuation is also detectable downstream of the wheelhouses on the vehicle's flank, which is associated with the flow exiting the wheelhouses (A and B in Figure 4.3(c)). This will also modify the shear layer dynamics at the two sides of the vehicle.

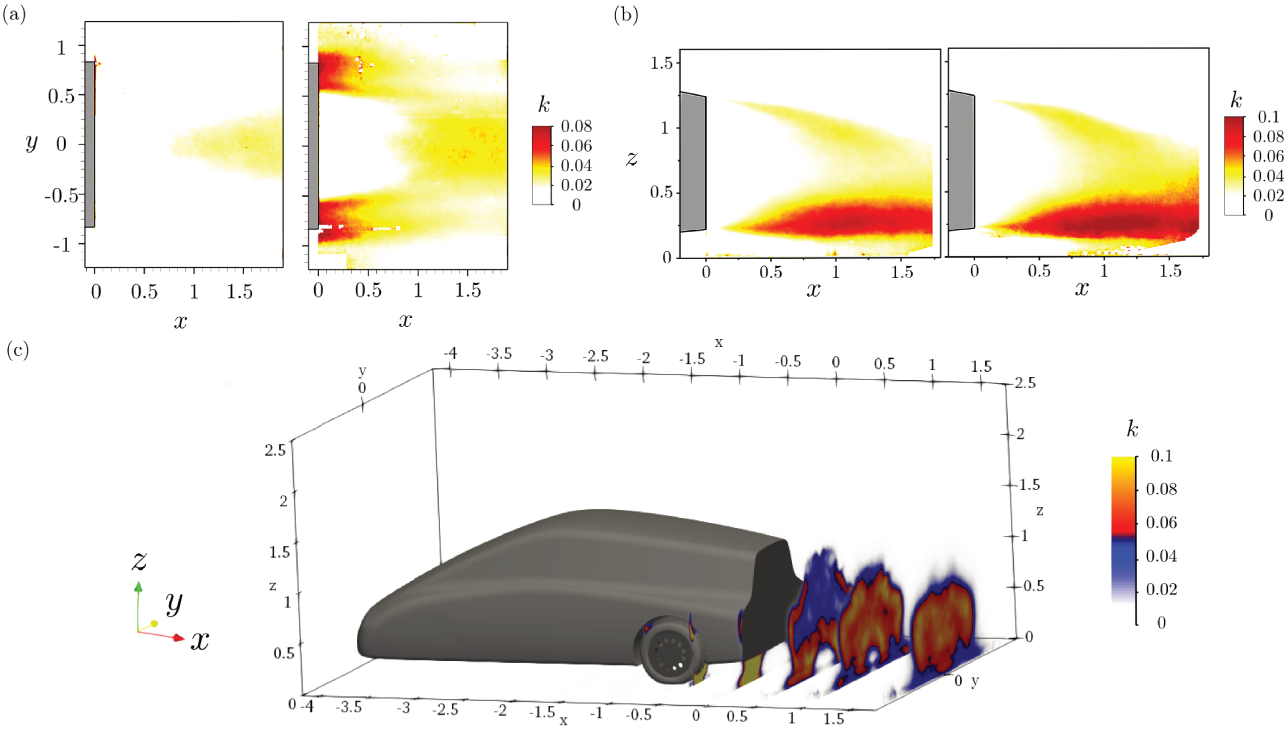

Figure 4.6: (a) PIV measurements of the planar turbulent kinetic energy $k = 0.5 \times (\overline{u'u'} + \overline{v'v'})$ at the half of the ground clearance for N on the left and XR on the right; (b) PIV measurements of the planar turbulent kinetic energy $k = 0.5 \times (\overline{u'u'} + \overline{w'w'})$ in the symmetrical plane $y = 0$ for N on the left and XR on the right; (c) Turbulent kinetic energy $k = 0.5 \times (\overline{u'u'} + \overline{v'v'} + \overline{w'w'})$ at $x = 0, 0.5, 1, 1.5$ from the numerical results for XR

The increase of the fluctuations by the rear rotating wheels is likely to enhance the wake entrainment and yields a reduced wake length. This point can be confirmed by Figure 4.7(a), which shows the velocity magnitude with 2D streamlines for both configurations in the $y = 0$ PIV plane. A shortening in recirculation length in this symmetrical plane is evident: this downstream distance falls from $L_r = 1.36$ in the smooth body case to $L_r = 1.26$ when rear rotating wheels are employed. This variation is consistent with the reduced pressure level in the centerline in Figure 4.4(c) (XR-N). Notwithstanding, their wakes exhibit similar topology. The upper vortex is more extended than the lower one and the reversed flow is titled downwards, which conforms to their similar vertical pressure gradient in the base centerline in Figure 4.4(a) and (c). The two effects can be further demonstrated in their iso-contours lines at $\overline{u} \in \{-0.25, 0.25, 0.65\}$ in Figure 4.7(b). The wake is shorter for XR and the reversed flow highlighted by $\overline{u} = -0.25$ moves closer to the base, yet without remarkable variation in the vertical position.

4.1.3 Effect of the rear wheel state

In the following, the impact of the wheel rotation will be investigated.

The comparisons between XR and XS in terms of the aerodynamic lift and drag coefficients, integrated underbody and base pressure are given in Table 4.2. The augmentation of the lift and drag for rear stationary wheels configuration corresponds with the increase in underbody

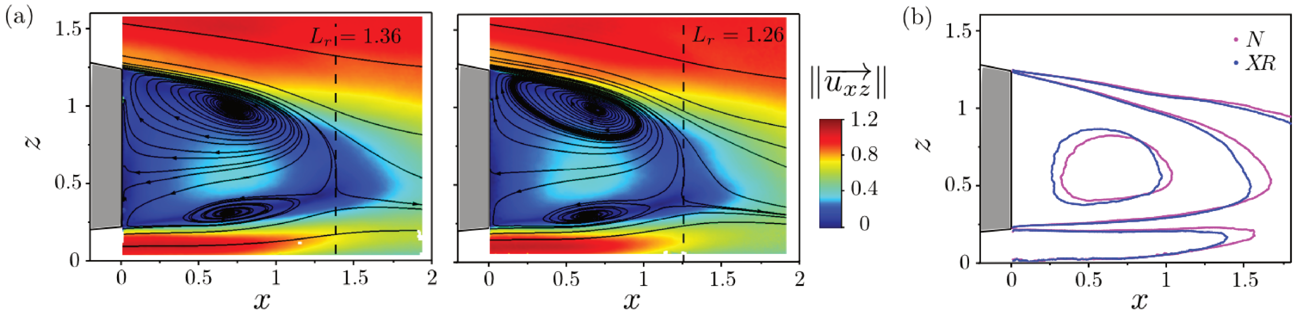

Figure 4.7: (a) PIV measurements of the velocity magnitude overlaid with 2D streamlines in the $y = 0$ plane for N on the left and XR on the right; (b) Iso-contour lines at $\overline{u} \in \{-0.25, 0.25, 0.65\}$ in the $y = 0$ PIV plane.

pressure and base suction. As the physical blockage rate of the wheels is 24.6%, close to the profiled obstacle pair of $\tau = 25\%$, thereupon, the integrated surface pressure coefficients are equally tabulated for $\tau = 25\%$. The larger blockage case $\tau = 30\%$ is also presented, as it has higher underbody pressure and base suction than $\tau = 25\%$, similar to the stop of the wheel rotation from XR to XS.

	$SCz(m^2)$	$SCx(m^2)$	$SCp_{\mathrm{U}}(m^2)$	$SCp_{\mathrm{B}}(m^2)$
XR	-0.379	0.390	-2.768	-0.232
XS	-0.225	0.445	-2.662	-0.260
$\tau = 25\%$	-	-	-3.301	- 0.218
$\tau = 30\%$	-	-	-2.951	- 0.245

Table 4.2: Full scale lift and drag coefficients, integrated underbody and base pressure for the configuration with rear rotating wheels XR and rear stationary wheel XS. The integrated underbody and base pressure for the configuration with profiled obstacles $\tau = 25\%$ and $\tau = 30\%$ are equally presented.

Above all, it is noted that the two wheels configurations have higher SCp_{U} values than $\tau = 25\%$ and $\tau = 30\%$. Secondly, despite the smallest physical blockage rate of the wheels (24.6%), XR is subject to higher base suction than $\tau = 25\%$ but less than $\tau = 30\%$. The base pressure of XS is even lower than that of $\tau = 30\%$. Moreover, the augmentation of the underbody blockage rate from $\tau = 25\%$ to $\tau = 30\%$ accounts for 10.6% increase in SCp_{U} and 12.4% decrease in SCp_{B}. And for configurations with rear wheels, the stop of the rotation results in 3.8% increase in SCp_{U} and 12.0% decrease in SCp_{B}.

Figure 4.8 provides the $\overline{Cp}$ distributions in the $y = 0$ plane for the 4 configurations. In the underbody, the curves for $\tau = 25\%$ and $\tau = 30\%$ are below those of XR and XS, specifically at the rear part, which agrees well with their lower SCp_{U} values. This can be attributed to the effect of guidance created by obstacle pairs that seal the gap between the vehicle underbody and the ground (Section 3.2). In the base, XR is lower than $\tau = 25\%$ at the bottom but the two lines are almost superposed at the upper base portion. Similarly, XS lies below that of $\tau = 30\%$ while gradually recovers to the same level on the upper part. This trend is consistent with their integrated base pressure.

Now if we compare within the two groups, $\tau = 25\%$ with $\tau = 30\%$ and XR with XS, it turns out that they have something in common. In the underbody, the curve for XR is below that of XS, in particular at the rear portion, which is the same case between $\tau = 25\%$ and $\tau = 30\%$. While in the base, XR is above XS, and $\tau = 25\%$ is likewise above $\tau = 30\%$. The similarity between the two groups can also be noticed in their surface pressure distributions in Figure 4.9. In Figure 4.9(a), from 25% to 30%, there is a pressure recovery upstream of the

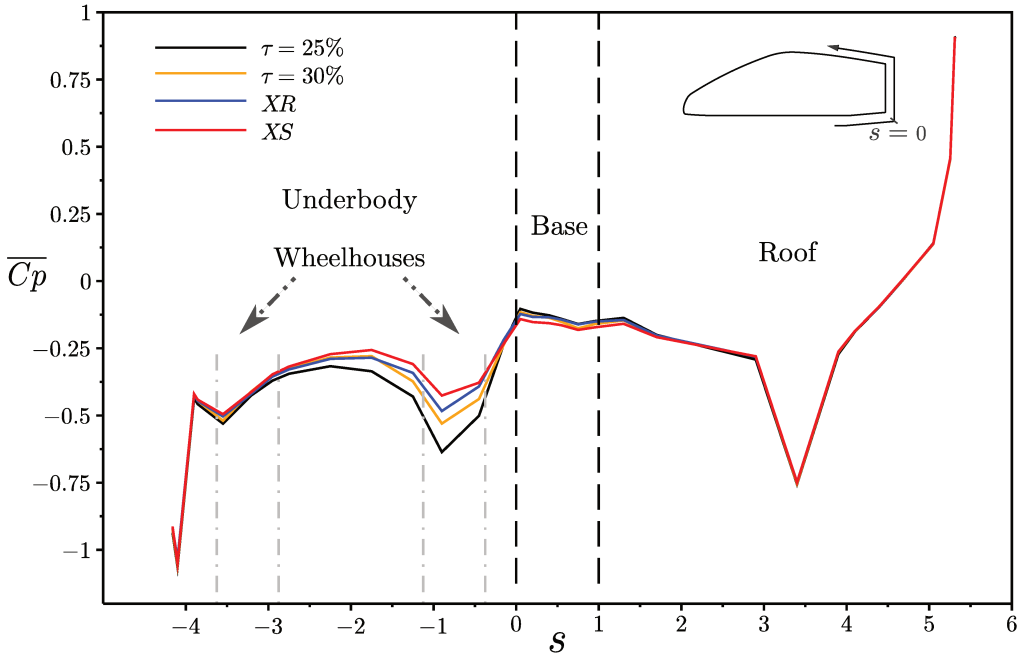

Figure 4.8: The distribution of $\overline{Cp}$ in the $y = 0$ plane on the curvilinear abscissa s (normalized by the height of the base) with the origin at the underbody rear end for $\tau = 25, 30\%$, *XR* and *XS*.

obstacles, and the suction between them is reduced. Identically, from *XR* to *XS*, not only the pressure raises in front of the rear wheelhouses, but there is also a pressure increase between the rear wheels. A zoom in the rear part of the underbody in Figure 4.9(b) assumes a reduced diffuser efficiency from *XR* to *XS*, which is the same with regard to an increase in the blockage from 25% to 30%. As for the base pressure in Figure 4.9(c), when τ augments, the pressure drops; and from rotating to stationary, we can also have sight of a pressure reduction over the entire base surface.

From the preceding results, one may speculate that, for wheels half shielded inside the wheelhouses and half exposed to the underbody flow, the stop of their rotation amounts to an increase in the underbody blockage rate. To ascertain the idea, the horizontal PIV plane at the half of the ground clearance will be given, where the wakes of the obstacles and wheels can be observed. Figure 4.10(a) presents the time-averaged streamwise velocity fields in this PIV plane. On first sight, the 30% case has a higher deficit in the wakes than the 25%, and the rear stationary wheels also have larger wakes than the rotating ones.

Indeed, the wake size reduction by rotation has been established for isolated wheel (Fackrell & Harvey, 1975; McManus & Zhang, 2006; Heyder-Bruckner, 2011; Diasinos *et al.*, 2015). Although the wakes captured in this PIV plane result from the wheels as well as the wheelhouses, *XS* still exhibits higher deficit. The attempt to unravel the larger wake for stationary wheel inside the wheelhouse will be tackled in Section 4.3.1 where numerical simulations are available for configuration having four stationary wheels.

As established in Section 3.2.4, the respectable gap in base pressure between $\tau = 30\%$ and $\tau = 25\%$ can be attributed to the 'merging' of the non-closed mean wakes of the larger obstacles ($\tau = 30\%$) with the vehicle wake. The relative decrease in SCp_{B} from *XR* to *XS* (12.0%) is close to that from $\tau = 25\%$ to $\tau = 30\%$ (12.4%). While in contrast to $\tau = 30\%$, in this horizontal plane, no reversed flow is observed in the mean wakes of the stationary wheels. It can be further visualized by the profiles of $\overline{u}$ at $x = 0.01$ in Figure 4.10(b). To gain more insight into the velocity statistics at this streamwise position, the PDF distributions of the maximum deficit (taken at $y_m = \mathrm{argmin}_{y>0}\, \overline{u}(y)$ for each configuration) are shown in the Figure 4.10(c). The PDF

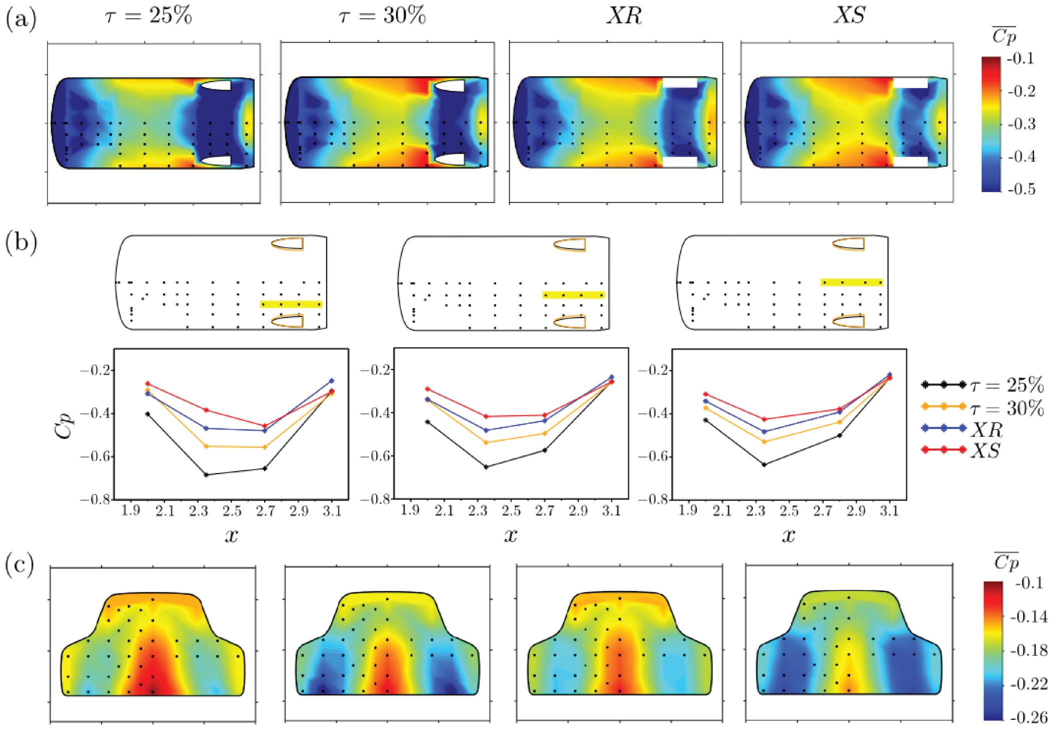

Figure 4.9: The underbody pressure distribution (a), zoom of the pressure evolution at the rear part of the underbody (b), and the base pressure distribution (c) for $\tau = 25, 30\%$, XR and XS.

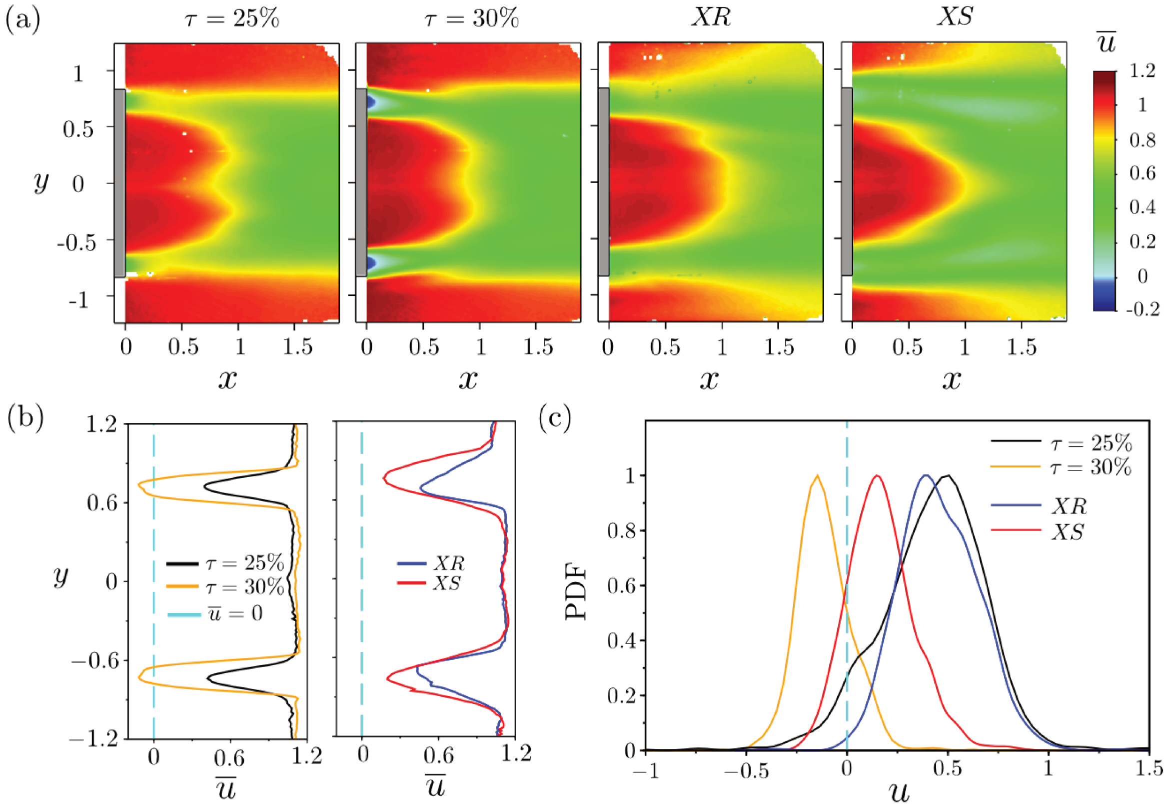

Figure 4.10: (a) The time-averaged streamwise velocity $\overline{u}$ distribution in the horizontal PIV plane at the half of the ground clearance for $\tau = 25, 30\%$, XR and XS; (b) Profiles of $\overline{u}$ at $x = 0.01$, with $\overline{u} = 0$ indicated in blue dash lines; (c) Probability density functions (PDF) of the maximum deficit at $x = 0.01$. The maximum deficit is taken at $y_m = \text{argmin}_{y>0}\,\overline{u}(y)$ for each configuration. The PDF distributions are normalized for easier comparison.

for the stationary wheel features more important negative component than the rotating wheel, which possibly entails the base pressure decrease. However, if we compare *XS* to $\tau = 30\%$, their PDF distributions do not seem to tally with their base pressure levels, since *XS* has much more base suction. Thereupon, several possible explanations are proposed below.

First, the wake profiles of stationary wheels at $x = 0.01$ seems to be larger but less elongated than those of $\tau = 30\%$. This is probably attributed to the different flow separation mechanisms. According to Figure 4.3(d), it can be said that the velocity deficit in the wakes of *XR* and *XS* at $x > 0$ originates from the wheels as well as the wheelhouses. Whereas for the profiled obstacles beneath the plugged wheelhouses, their base is tangential to the rear wheelhouse end and the flow separation is fixed at their rear sharp edges. Making a analogy with Figure 3.27(b), *XS* might be interpreted as a larger obstacle with a more upstream separation d situated in the 'far away from base' regime, while $\tau = 30\%$ is in the 'close to base' regime while with lower drag (base suction). Second, due to the highly 3D features of the wheel wakes, one would also expect reversed flow in the wakes of *XS* at higher vertical position, which is not captured in the 2D PIV measurement at the half of the ground clearance. Third, at the outer sides ($y = \pm 1.2$) the velocity for wheels exhibit lower values (Figure 4.10(b)), indicating that they may have additional penalty on the base pressure which not only arises from the underbody region.

The distributions of the planar turbulent kinetic energy $k = 0.5 \times (\overline{u'u'} + \overline{v'v'})$ for the 4 configurations are shown in Figure 4.11. For configurations with rear wheels, the lower fluctuation downstream in the middle ($x > 0.75$) reflects attenuated interaction of the vehicle wake with the ground, as opposed to configurations with obstacles. And their outer shear layers extend more outboard, implying possibly enhanced interaction with the flow at the two sides of the vehicle. The comparison between *XR* and *XS* demonstrates a more important fluctuation for stationary wheels especially in the inner shear layers.

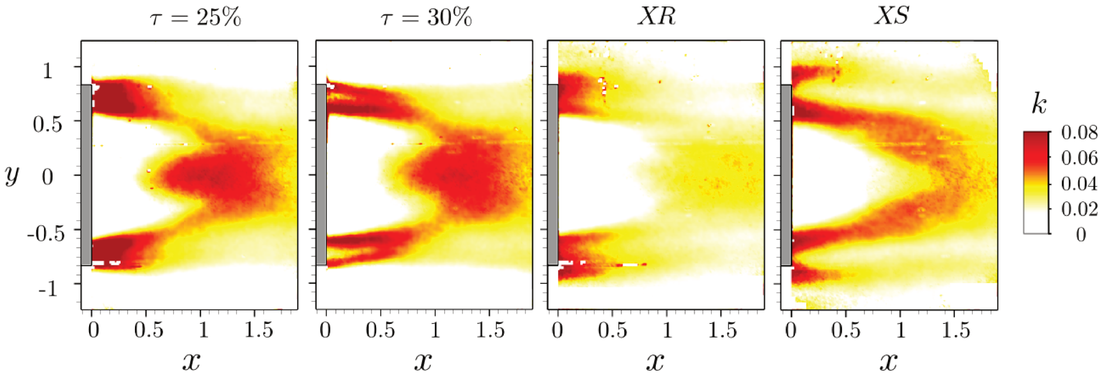

Figure 4.11: The time-averaged planar turbulent kinetic energy $k = 0.5 \times (\overline{u'u'} + \overline{v'v'})$ in the horizontal PIV plane at the half of the ground clearance for $\tau = 25, 30\%$, *XR* and *XS*.

The interaction of the underbody obstacles with the vehicle can be described by the velocity magnitude field $\|\overrightarrow{u_{xz}}\|$ in the symmetrical plane of the vehicle wake. In Figure 4.12, their wake organizations by 2D streamlines for the 4 configurations all suggest a larger clockwise-rotating structure in the upper part, in agreement with the location of the lower base pressure region (Figure 4.9(c)). However, as can be noted in Table 4.3, the higher saddle points in z for *XR* and *XS* suggest that their wakes have lower degree of z-asymmetry, and are less oriented towards the ground. It corresponds well with the observations in the previous horizontal PIV plane (Figure 4.11). Moreover, it can also be confirmed by their higher vertical pressure gradient in the base centerline in Table 4.3.

The bubble length variation within the two groups conforms to their base pressure level. The increase in underbody blockage rate from $\tau = 25\%$ to $\tau = 30\%$ decreases the bubble length, and so does the halt of the rotation from XR to XS. Besides the bubble length L_r, an additional way to quantify the global curvature of the near wake flow is to plot the velocity angles of streamlines emerging from the upper and lower separations. In Figure 4.13, the velocity angles of streamlines originated from $(x, z) = (0.07, 1.3)$ and $(x, z) = (0.07, 0.21)$ are depicted. Within the two groups, similar trends can also be observed. Between $\tau = 25\%$ and $\tau = 30\%$, XR and XS, their initial angles are nearly equal. Whereas lower deviations appear further downstream along the top ($x \in [0.4, 1.2]$) and bottom ($x \in [0.1, 0.9]$) streamlines for $\tau = 25\%$ and XR, which is consistent with more downstream closure of the recirculation bubble. This time mean scenario differs from mechanisms such as imposing separation angle by flaps or tappers (Grandemange *et al.*, 2013*c*; Perry *et al.*, 2016), or pulsing high-frequency jet at the trailing-edges to create fluidic boat-tailing effect (Barros *et al.*, 2016; Li, 2017), where the bubble length change is strongly associated to the modification of the initial streamline angle at the separation. Here, the blockage variation and the wheel state change at the two sides of the vehicle underbody barely modify the flow separation conditions in the symmetrical plane, while their influence on the mean flow curvature can be seen more downstream. The drop of the bottom streamline angles at around $x > 0.9$ is related to the streamlines leaving the saddle points being deflected towards the ground.

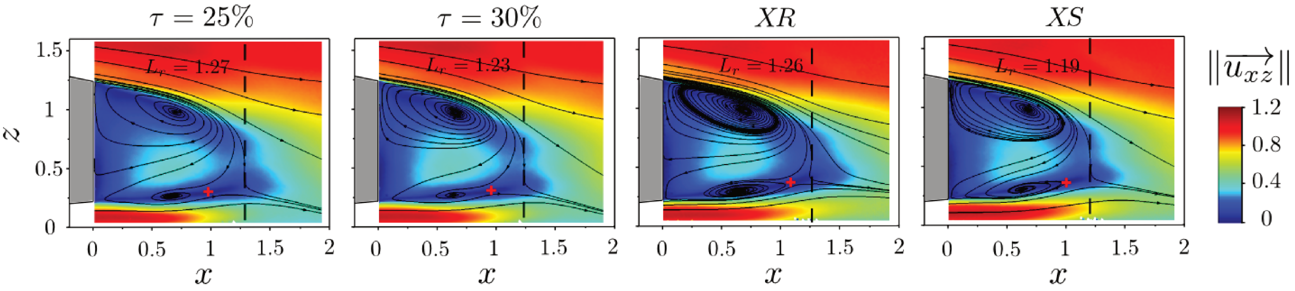

Figure 4.12: 2D streamlines overlaid on the contour maps of the time-averaged velocity magnitude, for $\tau = 25, 30\%$, XR and XS, in the symmetrical PIV plane. L_r indicates the bubble length and is highlighted by the dashed line. Red crosses are saddle points. Their positions are reported in Table 4.3.

	$\tau = 25\%$	$\tau = 30\%$	XR	XS
x_S	0.95	0.91	1.09	0.98
z_S	0.30	0.31	0.38	0.37
$d\overline{Cp}/dz$	-0.072	-0.071	-0.044	-0.047

Table 4.3: Saddle point positions (x_S, z_S) and vertical pressure gradient in the base centerline ($d\overline{Cp}/dz$) for $\tau = 25, 30\%$, XR and XS.

In order to quantify their wake dynamics, following the analyses in Barros *et al.* (2016) and Li (2017), the streamwise evolution of the integral of the turbulent kinetic energy $\mathcal{K}$ and averaged kinetic energy $\mathcal{E}$ inside the recirculation domain $\Omega_{(\overline{u}<0)}$ are computed. They are defined as follows:

$$\mathcal{K}(x) = \int_{\Omega_{(\overline{u}<0)}} k(x, y) dy, \tag{4.1}$$

$$\mathcal{E}(x) = \underbrace{\int_{\Omega_{(\overline{u}<0)}} \frac{\overline{u}^2(x, y)}{2} dy}_{\mathcal{U}(x)} + \underbrace{\int_{\Omega_{(\overline{u}<0)}} \frac{\overline{w}^2(x, y)}{2} dy}_{\mathcal{W}(x)} . \tag{4.2}$$

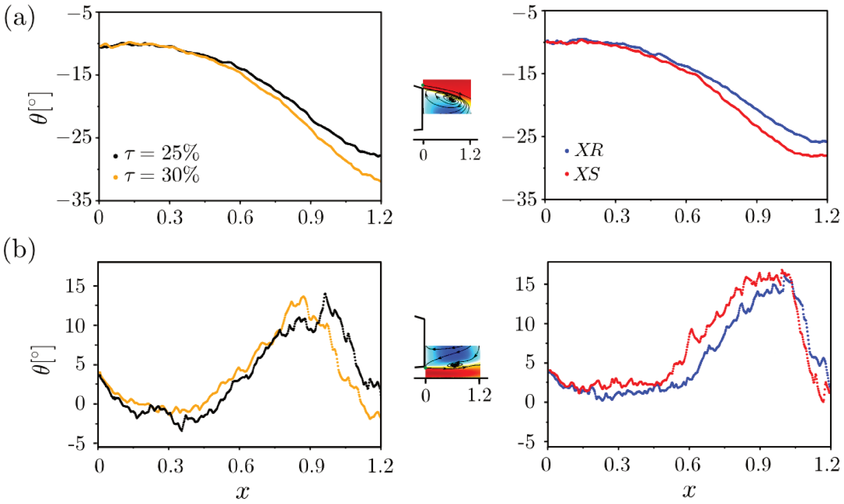

Figure 4.13: Streamwise evolution of the velocity angle $\theta = arctan(\overline{w}/\overline{u})$ of the streamlines issuing from the top $(x, z) = (0.07, 1.3)$ (a) and the bottom $(x, z) = (0.07, 0.21)$ (b) separation points for $\tau = 25, 30\%$, *XR* and *XS*.

The results are reported in Figure 4.14, with the longitudinal axis normalized by the recirulation length L_r of each configuration. From these plots the similarity within the two groups can be reinforced. There is an overall increase of $\mathcal{K}$ for $\tau = 30\%$ and *XS* in comparison with $\tau = 25\%$ and *XR*, pointing out an amplification of the velocity fluctuations in their wakes. The augmentation of $\mathcal{E}$ for $\tau = 30\%$ and *XS* brings to evidence an enhancement of the reversed flow kinetic energy. Slight differences lie in the contribution of the cross-stream velocity $\mathcal{W}(x)$ to $\mathcal{E}(x)$. A more noticeable increase of $\mathcal{W}$ for $\tau = 30\%$ at $x/L_r < 0.1$ indicates a more energetic cross-stream flow adjacent to the base, while in the range $x/Lr \in [0.3, 0.75]$, $\mathcal{W}$ debilitates. However the amplitude remains very small.

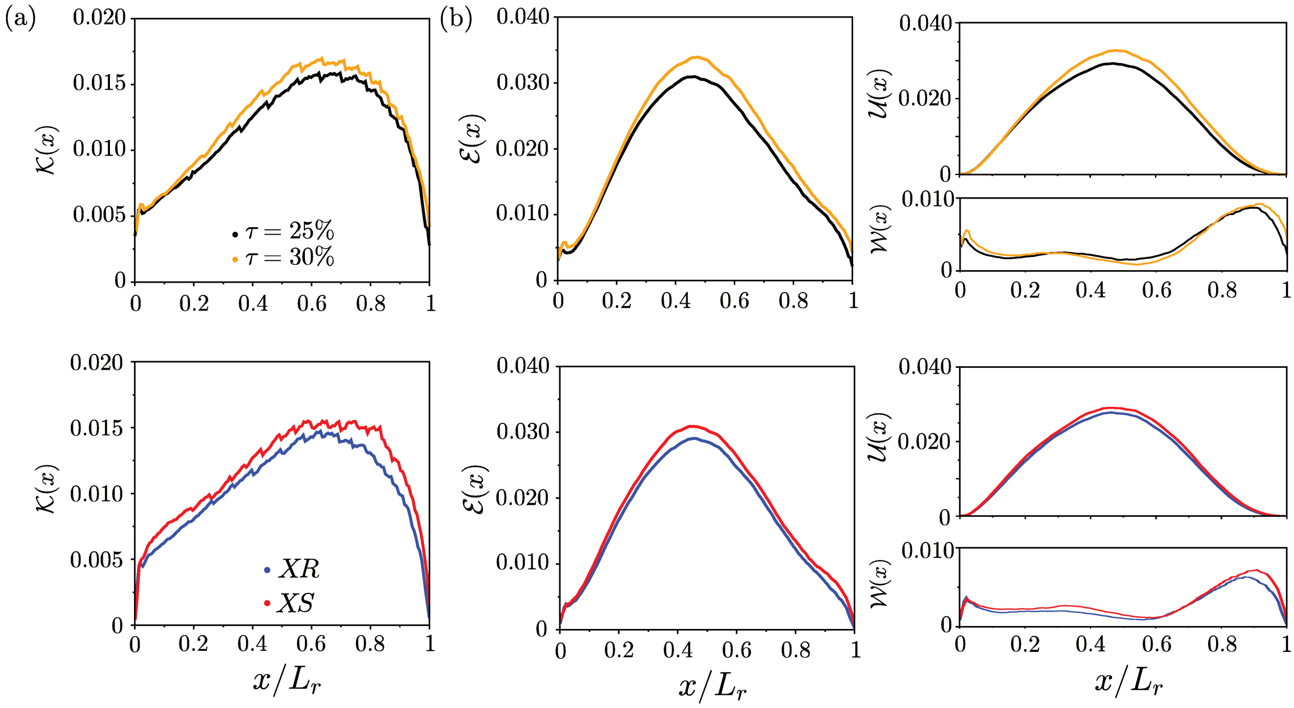

Figure 4.14: Streamwise evolution of the integrated turbulent kinetic energy $\mathcal{K}$ (see Eq.4.1) and averaged kinetic energy $\mathcal{E}$ (see Eq.4.2) inside the recirculation region for $\tau = 25, 30\%$, *XR* and *XS*.

Summary In this section, we first briefly outlined the flow structures around the rear rotating wheels gleaned from the numerical results. Permanent existing features of the rotating wheels, such as the *jetting* phenomenon, the positive pressure peak ($Cp > 1$) in front of the contact patch and the important suction ($Cp < -1$) immediately behind the contact patch, are recovered by the simulation, no matter the wheel is isolated or inside a wheelhouse. The comparison with the wheelhouse flow field in Regert & Lajos (2007) highlights the difference in front and rear wheelhouses. Nonetheless, the general schematic of the flow agrees well with their work.

Next, we explored how the inclusion of the rear rotating wheels interact with the flow around the vehicle. Its comparison with the smooth vehicle configuration N is conducted. The rear rotating wheels decrease the underbody pressure between them as they partially inhibit the outside flow from entering this low pressure region, similar to the small blockage obstacles in Section 3.2. However they marginally increase the pressure at the entrance of the underbody and vastly increase the pressure in front of them, which in total increase the integrated underbody pressure and therefore the lift coefficient, compared to N. The rear rotating wheels together with the wheelhouses create low pressure regions in their wakes and extend further downstream into the vehicle wake, consequently decreasing the pressure on the base regions behind them, at $y \approx \pm 0.6$ in Figure 4.4(c). The global drop of the base pressure is associated with the reduced recirculation length. High fluctuations arising from the rear wheels eventually increase the unsteadiness of the central part of the underbody flow more downstream. Hence the entrainment inside the vehicle wake is increased. However the wake balance in the symmetrical plane is not changed compared to N. The reduction of the base pressure results ultimately in the drag increase of the vehicle model.

The last emphasis is placed on the effect of the wheel state on the aerodynamic of the vehicle. The rear wheels are retained stationary to compare with the rotating ones. We managed to establish a link between the stop of the rotation and the increase of the underbody blockage rate, notably from $\tau = 25\%$ to $\tau = 30\%$, as they share a lot of common ground. It has been demonstrated in Section 3.2 that in large underbody blockage range, the raise in blockage increases the underbody pressure especially at the rear part and decreases globally the base pressure. Similarly, the rear stationary wheels have higher deficit in their wake (although no reversed flow is captured in the PIV plane at the half of the ground clearance) compared to the rear rotating wheels. They increase the underbody pressure, as underbody flow momentum is reduced, and increase the base suction, as lower pressure condition is imposed on the base surface. Thus the lift and drag augment. Similarities also lie in modifications in the vehicle wake. Higher fluctuation in the recirculation bubble is responsible for the shortening of the bubble length, for larger blockage rate $\tau = 30\%$ and rear stationary wheels. This comparison also demonstrates that, without knowing the complex flow structure created by wheels, at first order, we can reproduce this wheel–vehicle aerodynamic interactions by passive obstacles, and one of the important parameters to characterize the interaction is the wake width.

4.2 Baseline configuration analysis

In this section, the study will be undertook in the most realist situation where four rotating wheels are employed. This baseline configuration is denoted with *RR*. The experimental set-up is the same as described in Section 2.1. In Section 4.2.1 the description of the flow around front rotating wheel inside the wheelhouse will first be addressed. Then a short review of the flow inside the rear wheelhouse will be given, with special regard to the difference of the rear wheelhouse flow between the two configurations *XR* and *RR*. These results are based on numerical simulations. Next, in Section 4.2.2 the impact of including front wheels on the aerodynamics around the vehicle will be investigated.

4.2.1 Mean flow around the wheels

In Figure 4.15, the mean velocity fields at the half of the ground clearance are illustrated for *RR* and *XR* from the simulation results. A general view of the flow modification by employing front wheels can therefore be gained. From this general picture, three main aspects can be noted. First, the 2D streamlines highlight the different yaw angles of the wheel-approaching flow, for the front and rear wheels in configuration *RR* and the rear wheels in configuration *XR*. Second, the front wheels of *RR* have relatively small deficit in their wakes. Third, the rear wheels of *RR* have larger wakes than those of *XR*. In the following, additional information from the simulation will be provided to get a clearer view of these aspects.

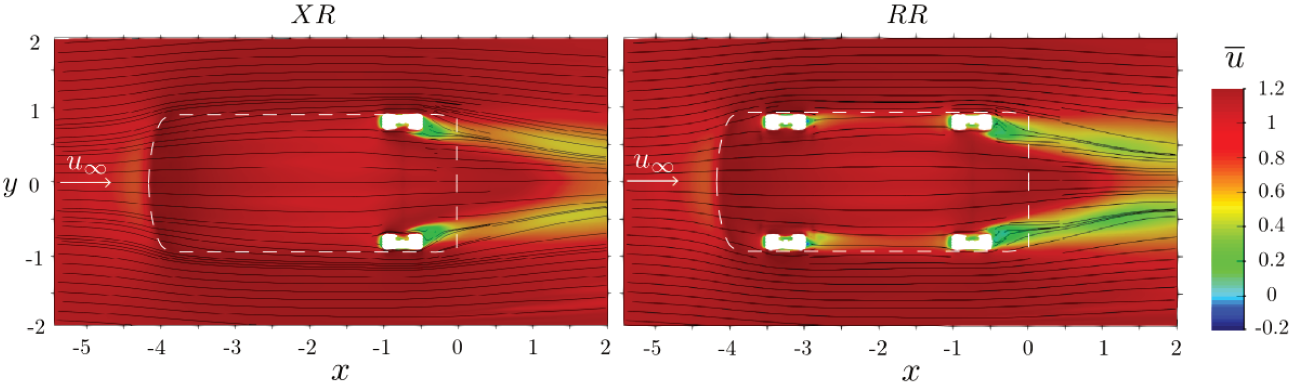

Figure 4.15: Comparison between *XR* and *RR*: the numerical results of $\overline{u}$ distribution in the horizontal plane at the half of the ground clearance, overlaid with 2D streamlines.

In Figure 4.16(a), the 3D streamlines around the front wheels in bottom view exhibit a yaw angle α of around 12°. This value shows good accordance with the front wheel yaw angle of $10° - 15°$ that is often encountered by the passenger vehicles (Pfadenhauer *et al.*, 1996). After all, the yaw angle is one of the important parameters that the modification of the Asmo model geometry was targeting by Michelin and ACE. The high angle of attack yields considerable flow asymmetry. The outboard lower wake N has a larger size than the inboard one. Moreover, the vortex E in Figure 4.3(c)–(f) that leaves the wheelhouse from its rear bottom is less evident here. It is sufficient to remark from the streamlines in Figure 4.16(b) that, at the rear bottom of the wheel, the side flow is vectored inward to attach on the wheel shoulder and then entrained upwards. At the inner side, this upward flow and the wheel-approaching flow with high yaw angle tend to hamper the outflow from leaving the wheelhouse at its rear bottom. Hence, the wake regions behind the front wheels captured by the horizontal plane at the half of the ground clearance in Figure 4.15 are relatively small. Instead, the low velocity flow leaves the lower part of the wheelhouse mainly from the outboard side. Then it separates at the side edge of the wheel arch, which conforms to the vortex S observed by Regert & Lajos (2007) in Figure 4.3(b). However it was not discernible at the rear wheelhouse of *XR*, which demonstrates that the wheelhouse flow is substantially influenced by the aerodynamic around the vehicle. Figure 4.16(d) gives an inner view of S and its origin (the wheel arch is removed). Before leaving the wheelhouse, it is entrained upwards by the running rear surface of the wheel.

There is a significant recirculation region between the wheel and the inner surface of the wheelhouse, where the flow can be clearly seen entrained by the wheel rotation. It also feeds the vortex B which leaves the front wheelhouse from the upper part (Figure 4.16(c)). The bigger yaw angle together with the larger wheelhouse depth are amenable to larger vortex B than that of the rear wheelhouse, tallying with the observation of Regert & Lajos (2007). The

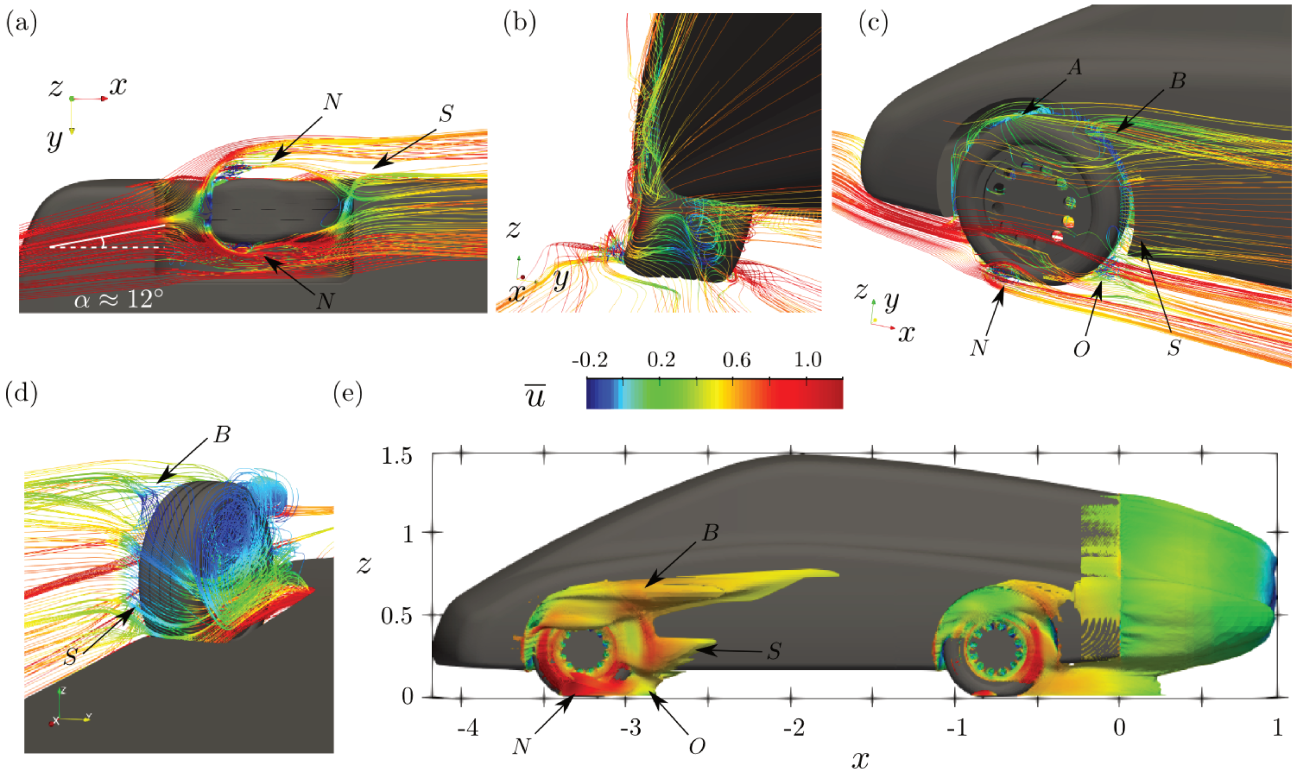

Figure 4.16: Numerical results for four rotating wheels configuration: Time-averaged 3D streamlines around the front left rotating wheel colored by $\overline{u}$, in bottom view (a), rear view (b), side view (c), and inboard view (the vehicle upper surface and the front wheelhouse are removed for better visualization) (d); (e) Iso-contour of $\overline{Cp_{tot}} = 0$ ($\overline{Cp_{tot}} = \overline{Cp} + \boldsymbol{u}^2$), colored by time-averaged streamwise velocity $\overline{u}$.

size variation of the vortex B for front and rear wheelhouses can be easily corroborated from the iso-contour of the $\overline{Cp_{tot}} = 0$ in Figure 4.16(e). Besides, for the front wheel/wheelhouse, the important outboard lower wake N and the separation bubble S can also be detected. The iso-contour also highlights the important total pressure loss at the rear bottom of the rear wheel. In order to shed more light into this point, the flow field around the rear wheel for *RR* will be analyzed and be compared to that of *XR*.

In Figure 4.17(a), the 3D streamlines around the rear wheels in bottom view are displayed for *RR* and *XR*. They seem to resemble each other in general.

Situated in the far wake of the front wheel, the yaw angle of the rear wheel approaching flow of *RR* is approximately 0°. Whereas for *XR*, $\alpha \approx 2°$. In essence, the distance between the vehicle front face and the wheel significantly dictates the angle of attack of the wheel in the vicinity of the underbody (Hucho & Sovran, 1993; Fabijanic, 1996; Wiedemann, 1996). The further the wheelhouse is located to the front face of the vehicle, the smaller is the angle. The front wheels of *RR* correspond well with the 1D fore-body length configuration reported in Regert & Lajos (2007) with $\alpha \approx 9.18°$, where the distance between the fore-body and the front wheelhouse equals approximately to one diameter of the wheelhouse. For *XR*, it is in a similar fashion to the infinite fore-body length configuration with $\alpha \approx 2.78°$ in Regert & Lajos (2007), whose body in front of the wheel is infinite long.

Unlike the front wheel of *RR* in Figure 4.16(a), for *RR* and *XR*, sizable outflow E can be discernible leaving the rear wheelhouse from the rear bottom. Still, we can remark that in the case of *RR* the outflow E has lower streamwise velocity and larger size. For better visualization, a 2D longitudinal section (indicated in white dot line) of the wheel wake cutting through the vortex E is depicted in Figure 4.17(b), colored by velocity magnitude accompanied with in-

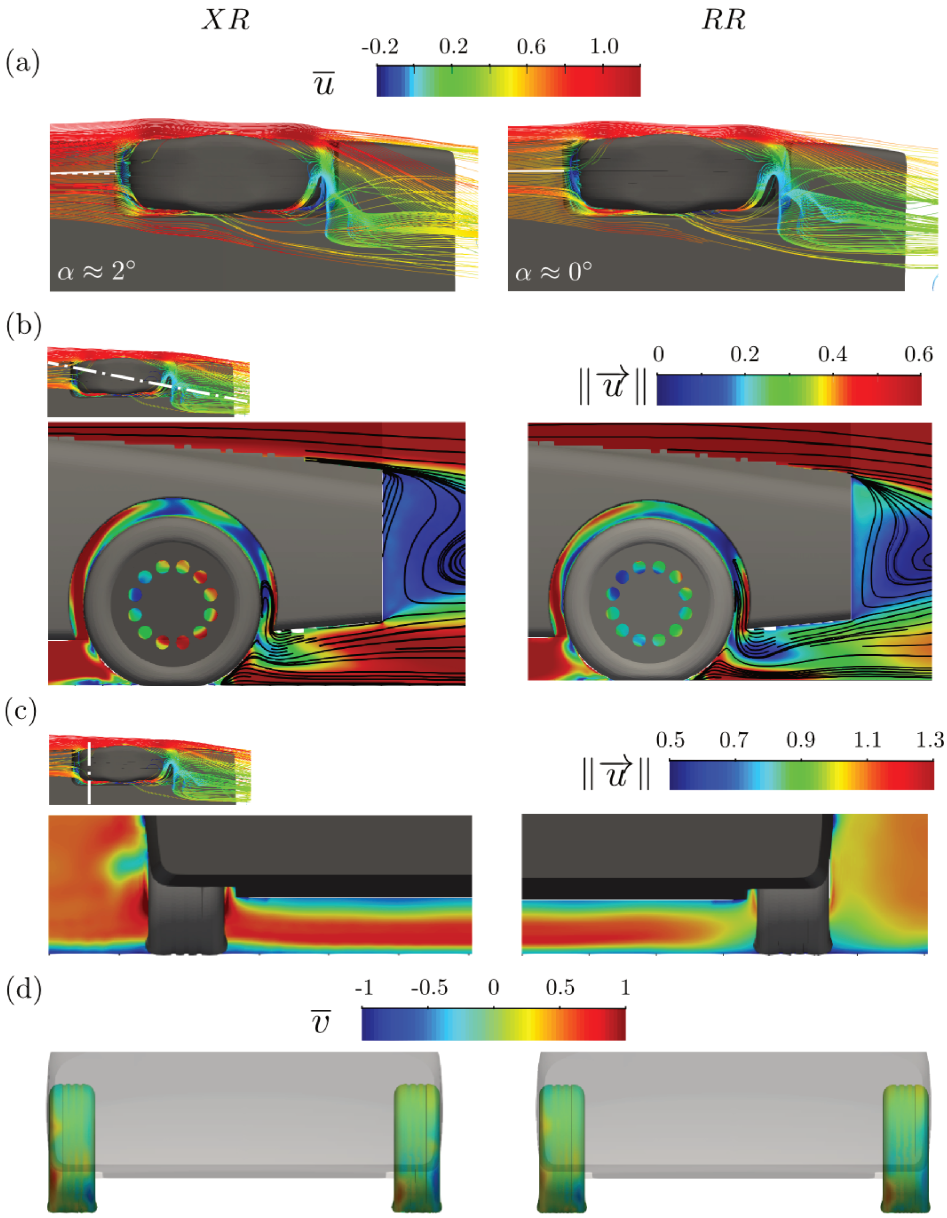

Figure 4.17: Comparison of flow fields around the rear wheels between *XR* and *RR* from simulations. (a) Time-averaged 3D streamlines around the rear left rotating wheels colored by $\overline{u}$, in bottom view; (b) 2D longitudinal section of the wheel wake, colored by velocity magnitude, overlaid with in-plane streamlines. Its position is indicated in white dot line; (c) Vertical cross section at $x = -1$, indicated in white dot line, colored by velocity magnitude; (d) Time-averaged cross-flow velocity $\overline{v}$ on the rear wheels surface (at the first mesh) in rear view.

plane streamlines. It can be perceived that the flow leaves the wheelhouse at the rear bottom opening, but it does not extend to the ground, while it is turned by the outer flow. However for *RR*, the flow exiting the wheelhouse spreads more downward and the velocity deficit behind the wheel is more important.

A cross section ($x = -1$, indicated in white dot line) upstream of the rear wheel center ($x = -0.75$) is shown for the two configurations in Figure 4.17(c). At this streamwise location, the velocity magnitude is reasonably lower for *RR* owing to the presence of the front wheel. Therefore, it can be argued that as the rear wheel approaching flow of *XR* has higher momentum, it is more capable of vectoring the outflow from the wheelhouse rear bottom and moving it closer to the underbody surface. The velocity deficit behind the rear wheel is thus reduced.

Finally in Figure 4.17(d), the distribution of the time-averaged cross-flow velocity $\overline{v}$ on the rear wheels surface is considered. The surface velocity is the velocity at the first mesh. On the rear tire shoulders below the underbody, non-zero cross-flow velocity $\overline{v}$ can be noticed, which can draw the outer flow inward. Meanwhile for *XR* the magnitude of $\overline{v}$ is higher, indicating that the vectoring of the cross flow is stronger and accordingly the wheel wake width is reduced.

4.2.2 Mean flow around the vehicle

Having examined the local modification of the flow field by the employ of the front wheels, this section is devoted to investigate its impact on the global aerodynamic forces, the pressure distribution of the vehicle surface as well as the vehicle wake. The full scale aerodynamic lift and drag coefficients and the integrated underbody and base pressure of the baseline configuration *RR* are given in Table 4.4, together with *XR* for comparison. First of all, we can observe a tremendous raise in lift coefficient with a change of sign, when front wheels are present. This is on account of the increase in the integrated underbody pressure. Secondly, the slight increase in drag coefficient is consistent with the marginal raise in base suction.

	$SCz(m^2)$	$SCx(m^2)$	$SCp_{\mathrm{U}}(m^2)$	$SCp_{\mathrm{B}}(m^2)$
XR	-0.379	0.390	-2.768	-0.232
RR	0.020	0.393	-2.274	-0.234

Table 4.4: Full scale lift and drag coefficients, integrated underbody and base pressure for the configurations with two rear rotating wheels *XR* and four rotating wheels *RR*.

It has been established in Section 3.2 that the increase in underbody blockage rate results in base pressure drop. Nevertheless, from Figure 4.15 in previous section, the intensified deficit behind the rear wheels of *RR* does not increase dramatically the base suction as well as the drag coefficient when compared to *XR*. Therefore more research on the surface pressure variation is required.

To begin with, the comparison of the time averaged $\overline{Cp}$ distributions in the $y = 0$ plane for *XR* and *RR* are provided in Figure 4.18(a). A zoom of the measurements inside the gray box, as well as the 2 front pressure taps, denoted with i, ii, iii, iv, are presented in Figure 4.18(b). By careful look at these measurements, we infer that the position of the front stagnation point is different for the two configurations. The deepened suction at iii, iv for *XR* around the lower radius of the front face suggests that its front stagnation point is displaced upwards compared to *RR*. While its measurement at i is not lower than at ii, thus the stagnation point probably locates between the two pressure taps. As for *RR*, the stagnation point is below the tap ii and above the negative measurement at iii. The lowering of the front stagnation point for *RR* is in accordance with its reduced downforce reported in Table 4.4, which is directly associated with the significantly reduced underbody flow momentum. As for *RR*, there is a clear increase of pressure at $s < -3$ in the underbody segment, suggesting that the underbody flow is notably slowed down from the entrance of the underbody. Besides, at the rear part especially between the rear wheels, the pressure is also higher for *RR*. The two curves increase with different slopes in the diffuser. They cross and eventually recover to the base pressure level. The smaller slope of *RR* indicates a reduced diffuser efficiency. And at the bottom of the base, its pressure is lower. However in the base segment, the two curves intersect again. For *RR*, its vertical pressure gradient $d\overline{Cp}/dz$ in the centerline is much higher: 0.065 compared to -0.044 for *XR*. On the roof, the measurement of the pressure tap closest to the base maintains a good continuity with

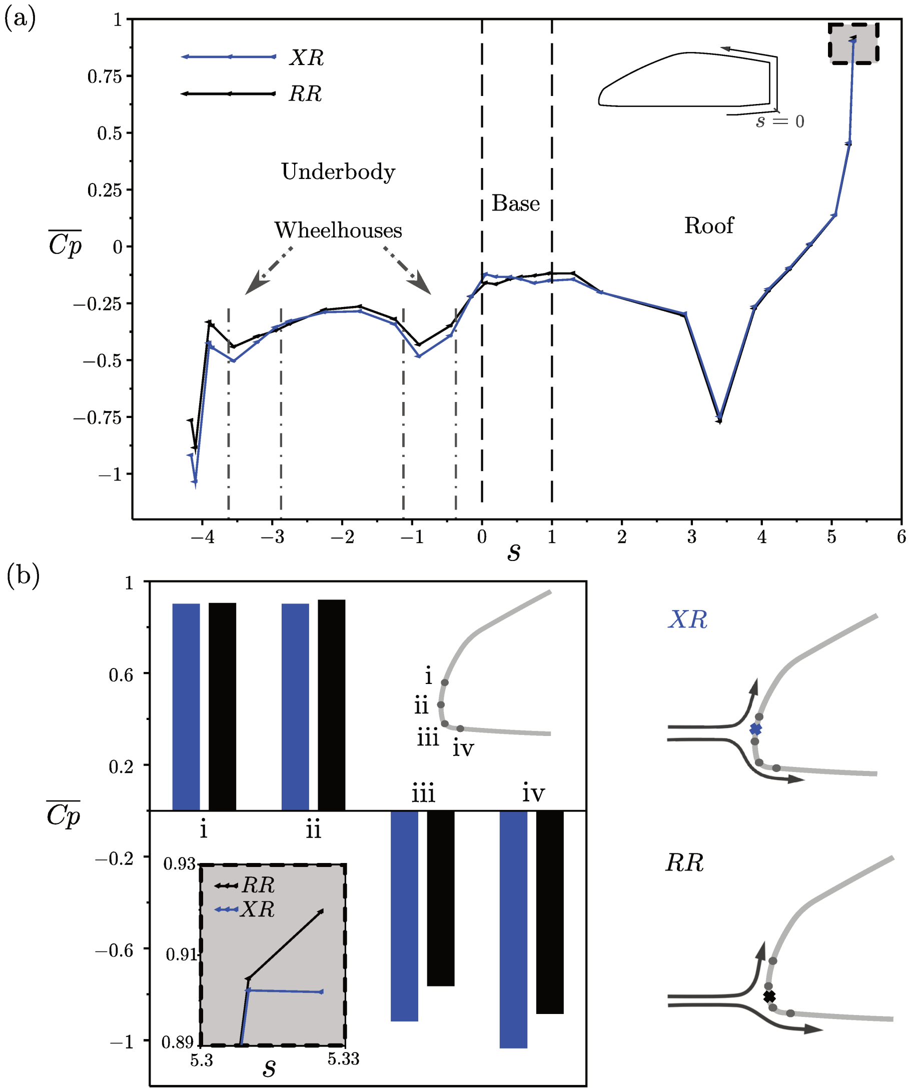

Figure 4.18: (a) The distribution of $\overline{Cp}$ in the $y = 0$ plane on the curvilinear abscissa s (normalized by the height of the base) with the origin at the underbody rear end, for *XR* and *RR*. The last two pressure taps inside the gray box are zoomed in (b); (b) Zoom of the measurements at the four front pressure taps, denoted by *i*, *ii*, *iii* and *iv*, and a sketch of their front stagnation point positions with respect to the four pressure taps.

the base pressure level. Apart from that, distinct pressure levels is only discernible at the forehead of the roof (inside the gray box).

The comparison of their pressure maps in the underbody is given in Figure 4.19(a). Conforming to the line plot in Figure 4.18(a), we note an increase in $\overline{Cp}$ for *RR* at the front and rear part of the underbody surface. Locally behind the front wheelhouses, the low pressure brings to evidence the wakes of the front wheels. In total, the integrated underbody pressure is much higher.

The change in vertical pressure gradient of the base centerline can be clearly seen in their base pressure maps in Figure 4.19(b). For *XR*, higher pressure region appears at the bottom part of the base in the middle line. While for *RR*, we can have sight of a higher pressure (red) region in an inverted triangle shape at the upper part of the base surface. Their base pressure difference also enables the two maps to be compared easily. Considering the similarity of the integrated base pressure, and the drag for the two configurations, it can be said that while *RR* assumes a deepened suction in the lower regions, which is plausible due to the increased deficit

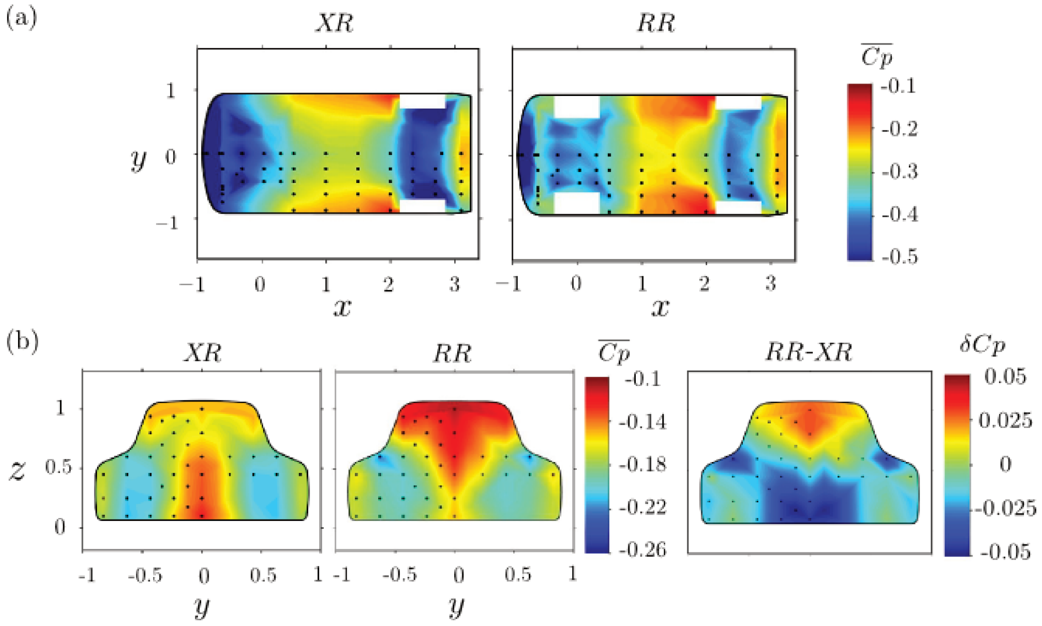

Figure 4.19: (a) The distribution of $\overline{Cp}$ on the underbody surface for *XR* and *RR*; (b) The time-averaged base pressure distribution and their base pressure difference.

in the wheel wakes (Figure 4.15), this is counteracted by a pressure recovery over the upper region of the base, effectively resulting in close drag values. Accordingly, it is indicative of a different flow structure impinging on the base, and will be seen shortly.

The PIV measurements of the vehicle wake in the symmetrical plane $y = 0$ are reported in Figure 4.20. In Figure 4.20(a), the map of the time-averaged velocity magnitude $\|\overrightarrow{u_{xz}}\|$ overlaid with 2D streamlines are depicted. On first inspection, the global orientation of the vehicle wake in this symmetrical plane is apparently altered when front wheels are introduced. The downwash does not prevail over the upwash, as the potent upwash creates a larger recirculation region in the lower wake, which correlates well with the decreased pressure at the bottom of the base. And as expected, the direction of the flow impinging the base is modified: for *XR* it is tilted downwards, while for *RR* it is markedly upwards, leading to higher pressure on the upper part of the base.

The distinct orientation of the wake is highlighted in Figure 4.20(b) by the velocity angle $\theta = arctan(\overline{w}/\overline{u})$ of the streamlines issuing from the top $(x, z) = (0.07, 1.3)$ and the bottom $(x, z) = (0.07, 0.21)$ separation points. For *RR*, the higher angle along the top and bottom streamlines is in reasonable agreement with the upward deflection of the mean wake. Furthermore, it should be pointed out that the velocity angles are different since $x = 0$ at the trailing edge. For *RR*, the velocity angle magnitude at the upper separation is smaller than the roof angle (10°). Whereas for *XR*, the velocity angle at the lower separation is smaller than the diffuser angle (5°).

Figure 4.20(c) gives the distribution of time-averaged planar turbulent kinetic energy $k = 0.5 \times (\overline{u'u'} + \overline{w'w'})$ for the two configurations. When compared to *XR*, the mean wake of the baseline configuration *RR* appears well-balanced as the distribution is more symmetric in z-direction. The increased upwash is accompanied by substantially attenuated TKE in the lower shear layer and enhanced level on the opposite side.

This well-balanced mean wake is often seen for typical passenger cars in on-road condition, where the important upwash from the underbody is generally acknowledged to be induced by the combined action of the diffuser and wheels (Marklund & Lofdahl, 2012; Aljure *et al.*, 2014; Pavia & Passmore, 2017; Avadiar *et al.*, 2018). Our study supplements the necessary conditions

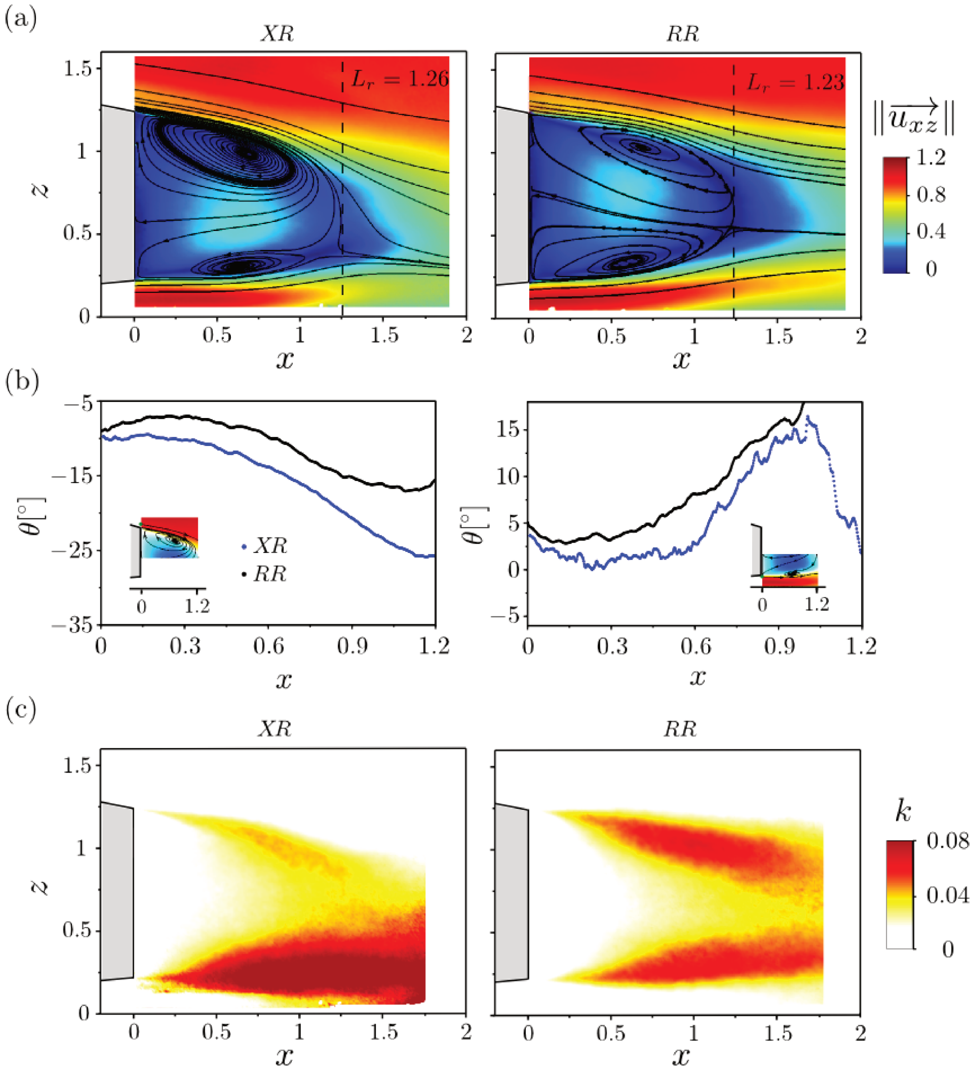

Figure 4.20: Comparison of the PIV measurements in the symmetrical plane $y = 0$ between *XR* and *RR*. (a) The velocity magnitude overlaid with 2D streamlines; (b) Streamwise evolution of the velocity angle $\theta = arctan(\overline{w}/\overline{u})$ of the streamlines issuing from the top $(x, z) = (0.07, 1.3)$ and the bottom $(x, z) = (0.07, 0.21)$ separation points; (c) Planar turbulent kinetic energy distributions.

for the generation of upwash: the presence of the front wheels is also of necessity. As for the configuration N, which has a diffuser, and *XR*, where there is a diffuser plus two rotating rear wheels, they both assume more important downwash in the near wake. Summarizing the observations above, when compared to two rear wheels configuration, the employ of the front wheels decreases vastly the underbody flow momentum, accompanied by a lowering of the front stagnation point (Figure 4.18). With the larger expansion of the rear wheel wakes in the underbody for the four wheels configuration (Figure 4.15), the diffuser efficiency is much reduced (Figure 4.18(a)). The pressure at the diffuser exit is thus recovered to lower level, while the exit flow in the symmetrical plane is vectored to higher velocity angle (Figure 4.20(b)). Ultimately, the upwash from the underbody is enhanced and the wake wall-normal balance is inverted.

The intensified upwash for the baseline configuration is also believed to be associated with more converged rear wheel wakes (at the inner side) compared to two rear wheels configuration, as can be discernible from their time-averaged $\overline{u}$ maps obtained from the planar PIV measurements at the half of the ground clearance in Figure 4.21(a).

Presented in Figure 4.21(b) are the profiles of the streamwise velocity $\overline{u}$ at two streamwise locations $x_1 = 0.05$ and $x_2 = 0.5$ for the two configurations. We can roughly apply the con-

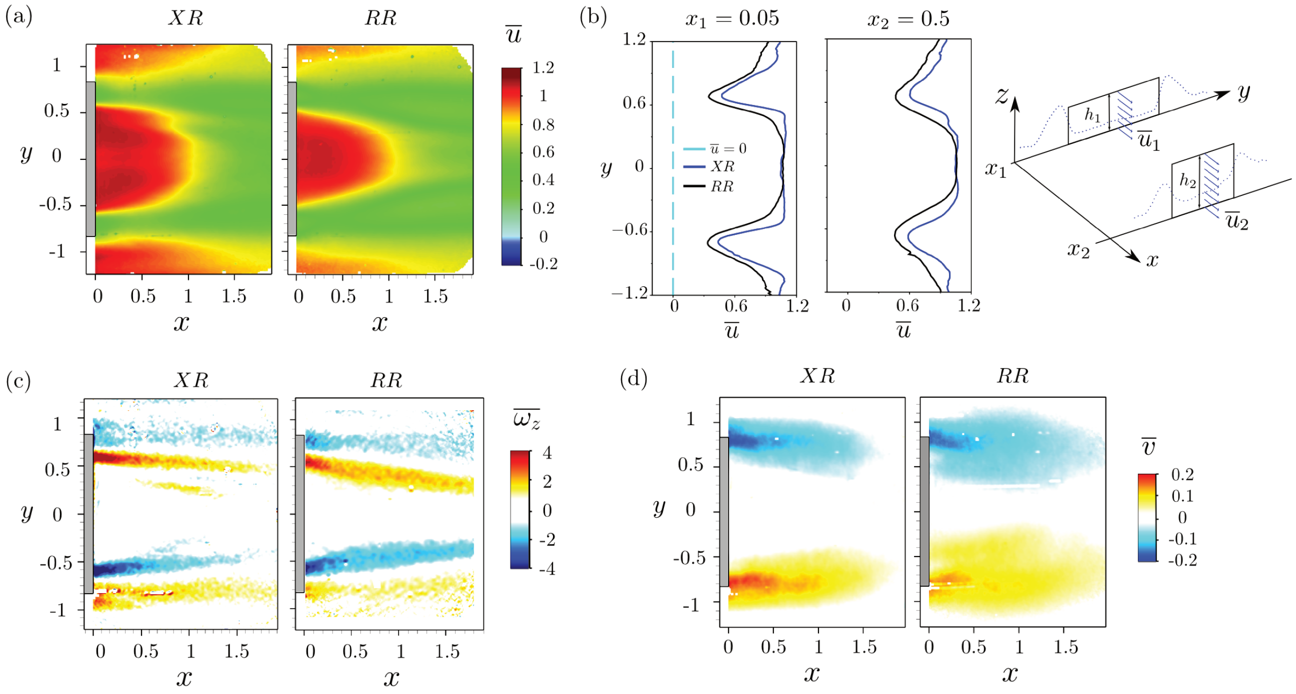

Figure 4.21: Comparison of the planar PIV measurements at the half of the ground clearance between *XR* and *RR*. (a) Distribution of time-averaged streamwise velocity $\overline{u}$; (b) Profiles of $\overline{u}$ at two streamwise locations $x_1 = 0.05$ and $x_2 = 0.5$; the two boxes in the schema at right roughly indicate the underbody potential flow region at the two streamwise positions; Distribution of time-averaged vorticity $\overline{\omega_z}$ (c) and spanwise velocity $\overline{v}$ (d).

tinuity equation to estimate how much the underbody potential flow goes upward from x_1 to x_2 for the two configurations. This is done by integrating the profile of $\overline{u}$ in their potential flow segment (loosely taken as the segment between two inner vorticity extremums) at x_1 and x_2, neglecting the loss by viscosity and considering a uniform profile of $\overline{u}$ in vertical direction, and considering the conservation of flow rate from x_1 to x_2, as delineated in the sketch in Figure 4.21(b). h_1 being approximately the same for the two configurations, and this leads to $h_{2XR} \sim 1.03h_1$ and $h_{2RR} \sim 1.08h_1$. Despite of the rough approximations, this seems to agree well with the more upward motion of the underbody flow for four wheels configuration. The more converged wheel wakes for the baseline configuration can be additionally perceived in Figure 4.21(c) where the shear layers at the two sides of the wheels are highlighted by the vorticity $\overline{\omega_z}$, and in Figure 4.21(d) where higher cross-flow velocity $\|\overline{v}\|$ is observed in the middle for *RR*.

The modification of the entire wake by the introduction of the front wheels will be analyzed with the aid of the numerical results. Before that, their numerical base pressure distributions are provided in Figure 4.22. It appears that the two maps recover the prominent characteristics when compared to corresponding maps in Figure 4.19(b) obtained from the experimental measurements. Hence the corresponding wake topology will be deemed reasonable. Nonetheless, the pressure values do not exhibit similar levels. So the data presented in the following will mainly give a quantitative impression of the vehicle wake rather than for any precise quantitative interpretation.

In Figure 4.23, velocity maps in various parallel streamwise planes in the vehicle wake are extracted from the simulations. At $x = 0$, higher deficit can be seen behind the wheels for four wheels configuration. At more downstream position ($x = 0.25, 0.5$), the distributions of $\overline{u}$ preserve roughly the shape of the base and the wheels. While for *RR*, it is sufficient to remark

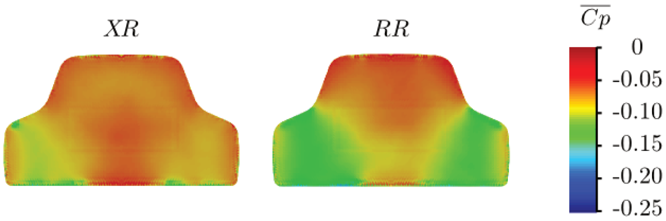

Figure 4.22: The time-averaged base pressure distributions of *XR* and *RR* obtained from the numerical simulations.

a gradual reduced section of the underbody flow bounded by wheel wakes, with increasing upsweep of the underbody central flow, from $x = 0.25$ to $x = 1.75$.

The comparison of their iso-contour of $\overline{Cp_{tot}} = 0$ in Figure 4.24(a) also brings to evidence this higher degree of upwash from the center of the underbody. It seems that the lower wake ($z < 0.6$) develops into two symmetric lobes that are separated by the higher-speed fluid from the bottom. The mean numerical streamlines are depicted for the two configurations in Figure 4.24(b). The wake topology of *XR* is akin to that of *N* presented in Figure 3.7(d) in Section 3.1. While for *RR*, the counter-rotating vortice pair created by the upwash, which has the same sense of rotation with the lower pair in the wake of *XR*, almost dominates the entire wake region. And the other pair of longitudinal vortices, which tallies with the upper pair in rotation direction in the wake of *XR*, fed by the downwash, is weakened and squeezed outboard.

The last point is about the pressure measurements below the indentation areas on the base. As illustrated in Figure 4.19(b), apart from the gradient change at the center of the base, there is a deepened suction at these measuring points when front rotating wheels are introduced. This arises from the larger streamline curvature of the local separating flow. As displayed in the 2D longitudinal section in Figure 4.17(b) from the numerical results, the upper shear layer that forms off the indentation area dives into the wake with higher angle. Additionally, the velocity plots at various streamwise positions in the wake in Figure 4.23 and the iso-contour of $\overline{Cp_{tot}} = 0$ in Figure 4.24 also bring to evidence the high-speed fluid deflecting towards the wake center issuing from the indentation areas, which, together with the underbody upwash, squeeze the wake region. Figure 4.25 shows the cross-correlation without time lag of surface-pressure fluctuations with the measurement below the left indentation area, for four rotating wheels configuration. The positive correlation with the measurement at the bottom of the base reveals that this flow separation from the indentation area is strongly connected to the underbody upwash. With its increased downward motion (pressure decreases as a result of an increased flow curvature), the upwash from the underbody is enhanced (pressure decreases). Alongside, the downwash from roof is reduced, leading to the negative correlation shown on the upper part of the base (pressure increases).

This last observation could possibly be related to the difference in upstream conditions between *XR* and *RR*. From Figure 4.26, it is noted that as opposed to *XR*, the unsteadiness arising from the outflow of the front wheelhouse (*A* and *B* in Figure 4.16(c) and (e)) convects all the way downstream and eventually modifies the shear layer dynamics above the indentation areas. And this is a spin-off of the particularity of the vehicle geometry.

Summary In this section, the baseline configuration – the vehicle model with four rotating wheels *RR* is analyzed and compared to two rear rotating wheels configuration *XR*. The presence of the front rotating wheel reduces the underbody flow momentum from the underbody entrance compared to *XR*. A lowered front stagnation point is observed, in accordance with the considerable increase in lift coefficient from downforce to positive lift. The presence of the front rotating wheels also decreases the momentum of the rear approaching flow, in contrast to *XR*

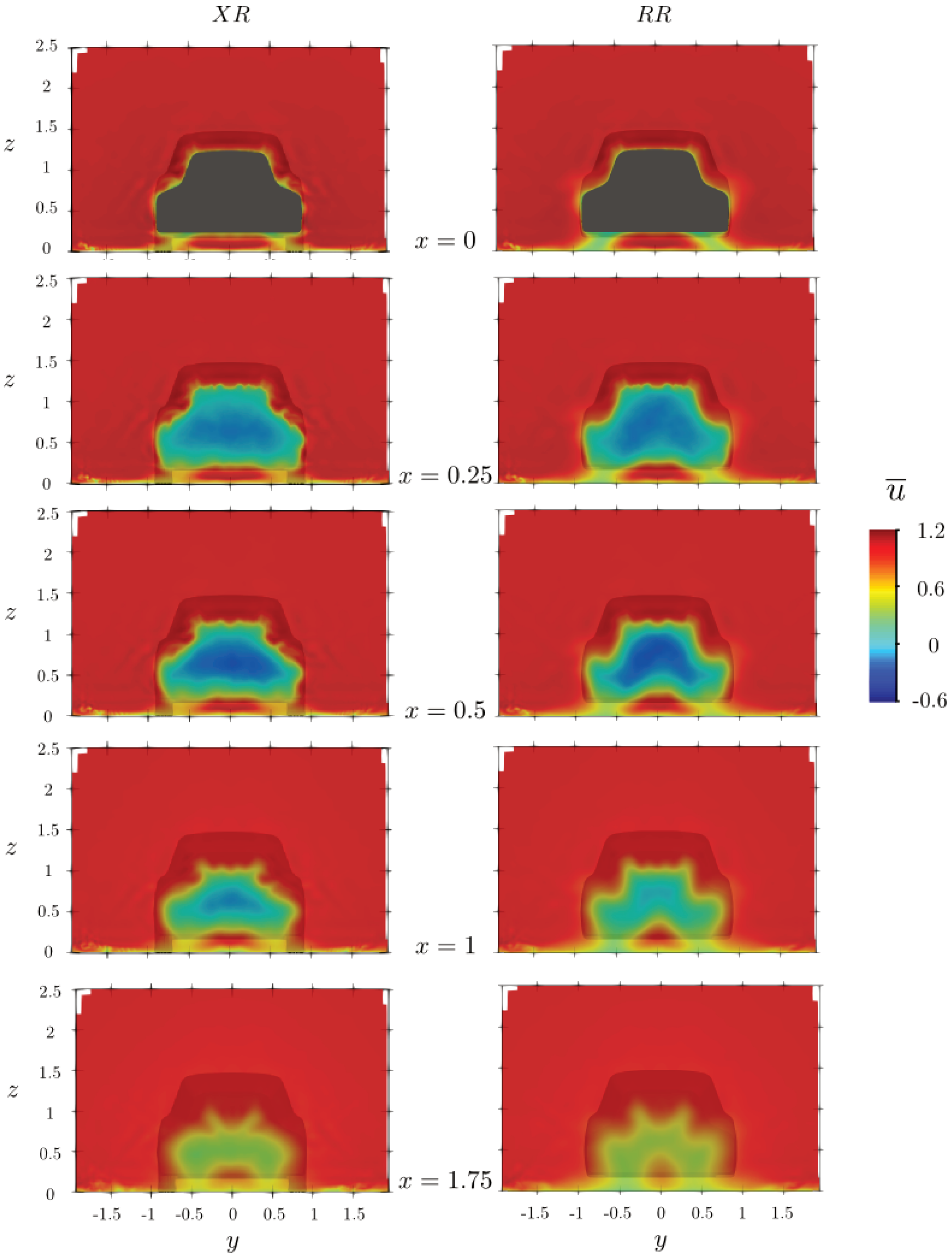

Figure 4.23: Time averaged streamwise velocity distributions at various streamwise positions in the vehicle wake for *XR* and *RR* obtained from the numerical simulations.

where the rear wheels are directly subject to high velocity underbody flow, therefore resulting larger and more inward deflected rear wheel/wheelhouse wakes. It is likely that this larger expansion of the rear wheel wakes decreases the underbody diffuser efficiency, which is in favor of the upwash from the underbody. The wake wall-normal equilibrium is completely altered, and a well-balanced wake is recovered. The enhanced upwash feeds the lower recirculation zone, increasing its size compared to the upper vortex. Accordingly, the direction of the flow impinging the base is tilted upwards. Although the higher deficit behind the rear wheels reduces the base pressure at the lower part, it is counteracted by the important pressure recovery at the upper part. Ultimately the integrated base pressure for the two configurations are close, and so do their drag coefficients. At last, the important yaw angle of the front wheel approaching

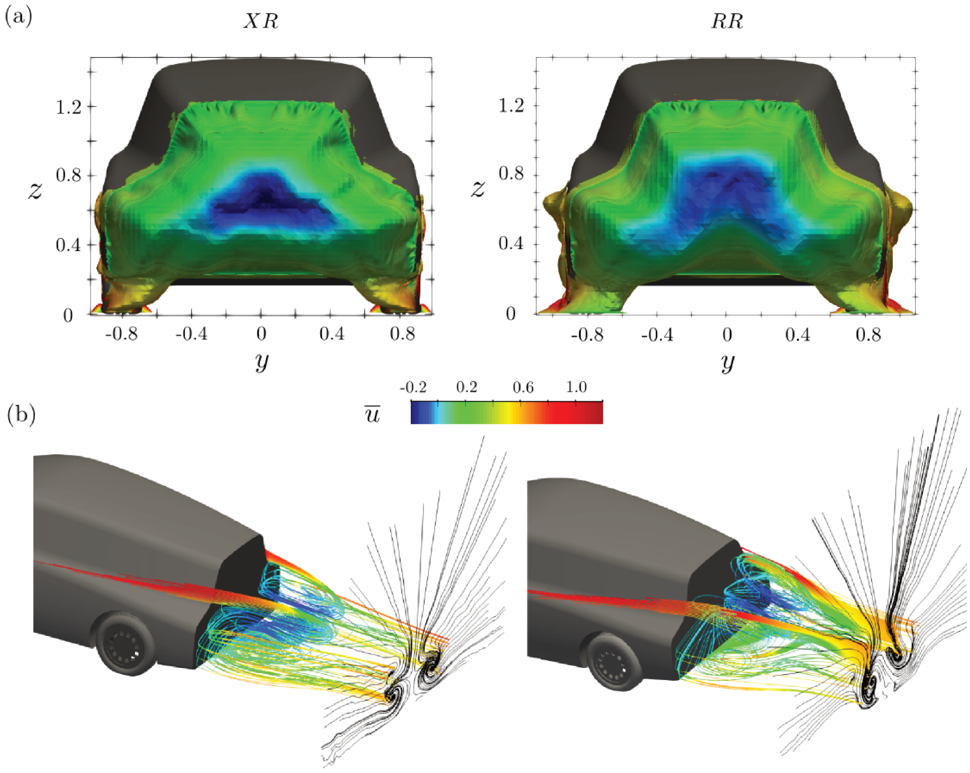

Figure 4.24: Numerical results for *XR* and *RR*. (a) Iso-contour of $\overline{Cp_{tot}} = 0$ ($\overline{Cp_{tot}} = \overline{Cp} + \boldsymbol{u}^2$), colored by time-averaged longitudinal velocity $\overline{u}$; (b) Mean numerical streamlines in the wake colored by time-averaged longitudinal velocity $\overline{u}$.

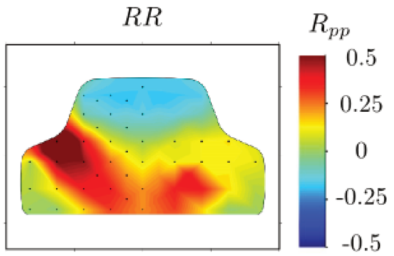

Figure 4.25: Pressure cross-correlation at zero time delay with pressure measurement below the left indentation area.

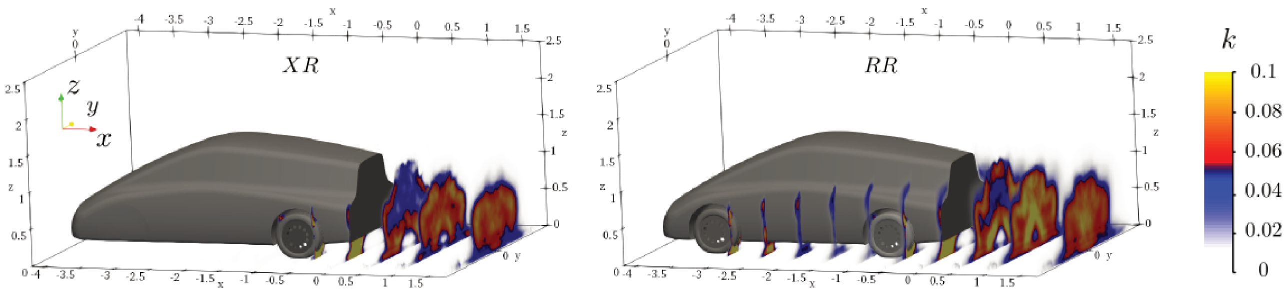

Figure 4.26: Turbulent kinetic energy $k = 0.5 \times (\overline{u'u'} + \overline{v'v'} + \overline{w'w'})$ at $x = 0, 0.5, 1, 1.5$ from the numerical results for *XR* and *RR*.

flow yields large amount of outflow from the upper part of the wheel arch. Its unsteadiness will convect all the way downstream and eventually modifies the shear layer dynamics at the trailing edge above the indentation areas. It is observed that the shear layer forms off this area plunges into the vehicle wake with higher angle, hence inducing local pressure drop on the base.

4.3 Effect of the wheel state for four wheels configurations

In this section, the effect of the wheel state for four wheels configurations will be considered. The experimental set-up is the same as described in Section 2.1. With the simulation results, insight into flow around front and rear stationary wheel shielded in wheelhouse, and their links to flow around isolated wheel are given in Section 4.3.1. Although a vehicle with stationary wheels is not often representative of a real life scenario, except in circumstances where the wheels are locked under braking, it is still of interest as it sheds light on the effect of the wheel rotation. Thereupon in Section 4.3.2, comparisons among four combinations of front and rear wheel states are addressed, which are vehicle with four *R*otating wheels (*RR*), vehicle with front *S*tationary, rear *R*otating wheels (*SR*), vehicle with front *R*otating, rear *S*tationary wheels (*RS*) and four *S*tationary wheels (*SS*). The results are mainly from experimental measurements. At last, in Section 4.3.3, an approach to investigate the wheel state, certainly out of step with the reality, consists in turning the four wheels in the opposite direction. This configuration is denoted by (RR^{-1}). Its influence on the vehicle surface pressure distribution as well as the mean vehicle wake will also be analyzed.

4.3.1 Mean flow structure around stationary wheels

A global comparison of the flow fields between four rotating wheels configuration and four stationary wheels configuration can be outlined in Figure 4.27, with the help of the simulation results. A quick look of the iso-contour of $\overline{Cp_{tot}} = 0$ in Figure 4.27(a) reveals similar trend for front and rear wheelhouse/wheel between the two configurations. At the upper part of the front and rear wheelhouses, the total pressure loss regions shrink in size for *SS*; whereas at the bottom part of the wheel, the iso-contour extends larger and further. The mean velocity fields at the half of the ground clearance in Figure 4.27(b) bring to evidence the enhanced wake deficit behind the stationary wheels when compared to the rotating ones. More detailed flow fields around the front and rear stationary wheels inside the wheelhouse will be described to better comprehend the difference with rotating wheels.

The time-averaged flow field around the front stationary wheel can be generally understood from the numerical results presented in Figure 4.28. The iso-contour of $\overline{Cp_{tot}} = 0$ on the upper part of the wheelhouse in Figure 4.27(a) corresponds the outflow in the same position depicted in Figure 4.28(a). An inner view of the 3D streamlines in Figure 4.28(b) and (c) indicates that this outflow mainly arises from the up-flow entering the wheelhouse, partly separating on the upper tire tread and leaving the wheelhouse, which resembles the structure A in rotating wheel situation. However this separation occurs more downstream compared to a rotating wheel. For rotating front wheel, large amount of flow leaves the wheelhouse (in vortex A and B) from the upper part as a consequence of the rotation. Here the outflow from the upper part of the wheel arch is much reduced. Instead the flow inside the wheelhouse mainly leaves the volume from the bottom rear opening, as can be clearly observed from Figure 4.28(b) and (c). At the rear part of the wheel, the outboard main streamwise flow and inboard recirculating flow is drawn to attach on the rear tire tread and directed downwards. Further more, there is no upwards entrained flow at the rear bottom of the wheel as the wheel is not rotating. Hence, the important downward flow leaving the wheelhouse spreads all the way to the ground and rolls up, forming a counter rotating vortice pair, which greatly enlarges the front wheel wake

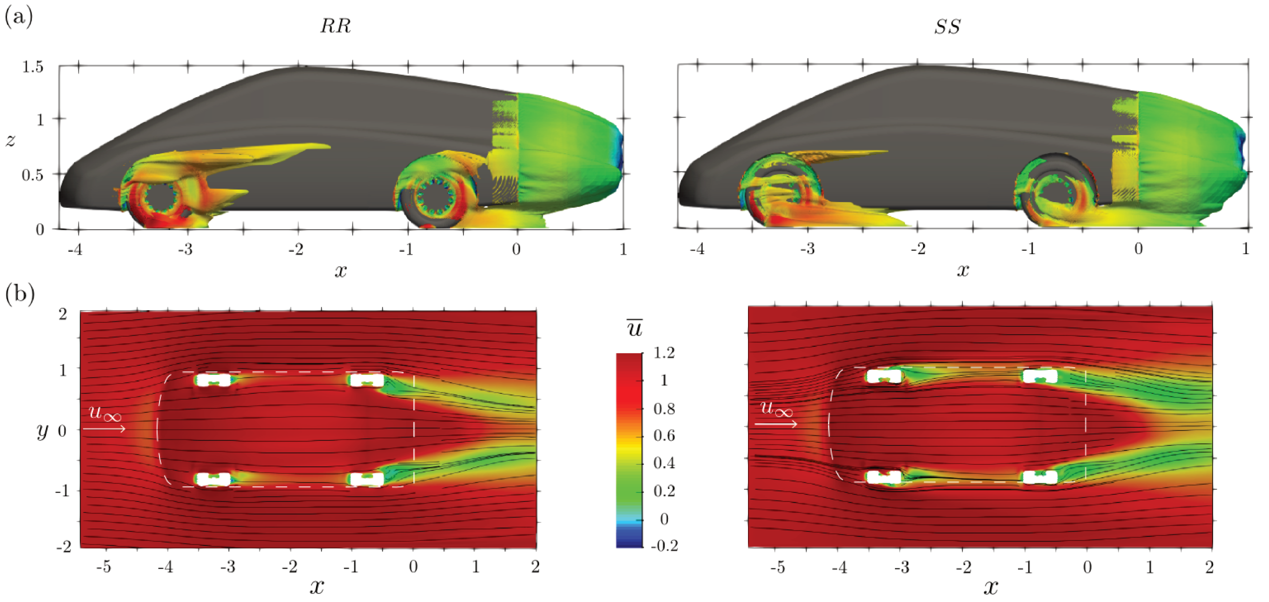

Figure 4.27: Comparison between four rotating wheel and four stationary wheel configurations: (a) Iso-contour of $\overline{Cp_{tot}} = 0$ ($\overline{Cp_{tot}} = \overline{Cp} + \boldsymbol{u}^2$), colored by time-averaged streamwise velocity $\overline{u}$; (b) Maps of $\overline{u}$ in the horizontal plane at the half of the ground clearance, overlaid with 2D streamlines. The results are gleaned from numerical simulations.

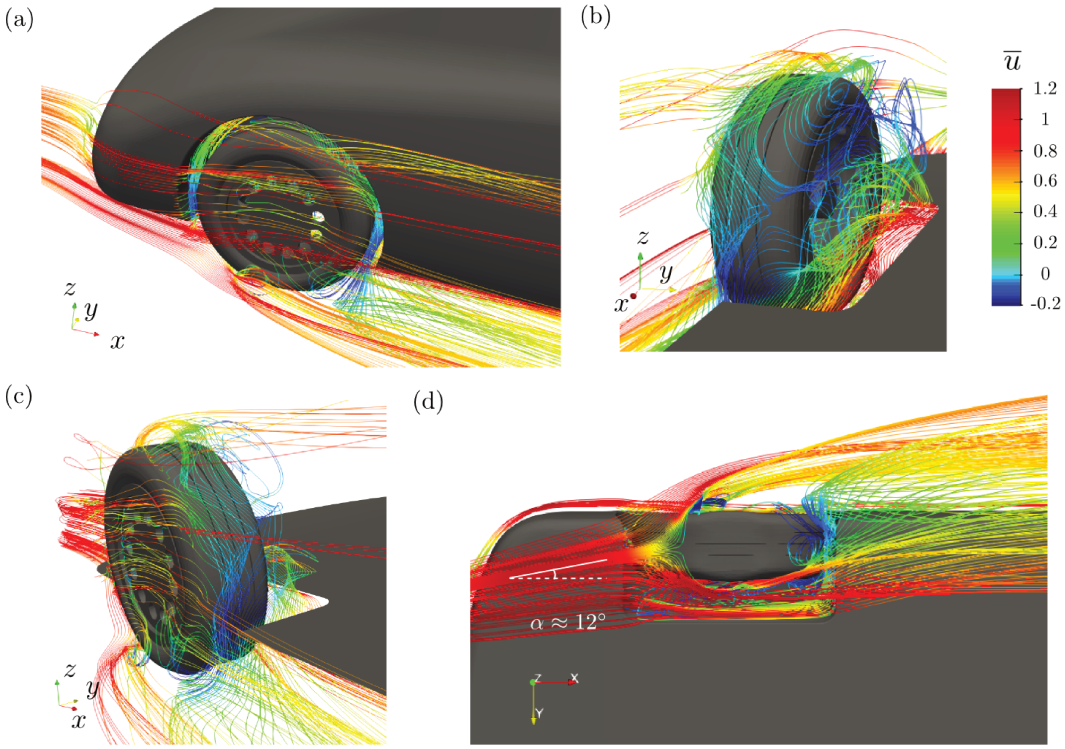

Figure 4.28: Time-averaged 3D streamlines around the front left stationary wheel colored by $\overline{u}$, in side view (a), inboard top view (b), outboard rear view (c) and bottom view (d). The vehicle upper surface and the front wheelhouse are removed in (b) and (c) for better visualization.

compared to rotating wheel. The vortice also extends upstream to the rear surface of the wheel as can be observed in Figure 4.28(c).

It can also be noted that the counter rotating vortex pair is not symmetric. The downward flow moves from right to left (for the left front wheel) and the outboard vortex is larger than the inboard one. This is owing to the large yaw angle of the wheel-approaching flow. In the bottom view in Figure 4.28(d), the yaw angle is estimated to be 12°, equal to that of the front rotating wheel. It can thereby be concluded that the yaw angle is independent of the wheel state. Apart from the large counter rotating vortices, from Figure 4.27(a), important total pressure loss can be detectable on the wheel hub. This is due to the cross flow that goes through the stationary openings on the wheel hub from the inner recirculating zone, identifiable in Figure 4.28(a) and (c).

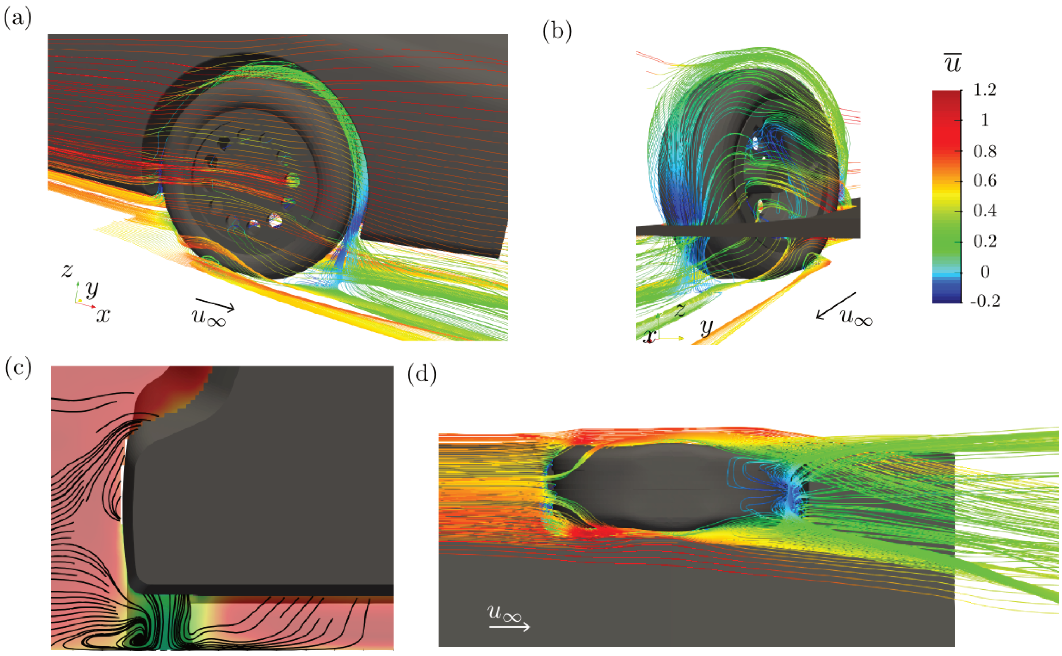

Figure 4.29: Time-averaged 3D streamlines around the rear left stationary wheel colored by $\overline{u}$, in side view (a), inboard rear view (b), and bottom view (d). The vehicle upper surface and the front wheelhouse are removed in (b); (c) The vertical plane $x = -0.4$ downstream of the rear wheel, colored by $\overline{u}$, accompanied with 2D streamlines.

Similar flow topology presents in the rear wheelhouse (Figure 4.29). The iso-contour of $\overline{Cp_{tot}} = 0$ (Figure 4.27(a)) and the side view of the 3D streamlines around the rear wheelhouse (Figure 4.29(a)) provide no evidence of outflow from the upper wheel arch. The inner view of the streamlines (Figure 4.29(b)) shows that the flow contours the wheel circumference and leaves the wheelhouse from its rear bottom. It is swept down towards the ground, finally induces counter rotating vortices, and increases the wheel wake compared to *RR*. This vortice pair is also evidenced by the 2D streamlines in the vertical plane $x = -0.4$ downstream of the rear wheel (Figure 4.29(c)). In addition, it appears symmetric from the bottom view in Figure 4.29(d). The angle of the wheel-approaching flow is approximately zero, akin to the configuration *RR* (Figure 4.17(a)). Above the vortice pair, the wake region is diverted slightly inward by the outside potential flow.

Hitherto, detailed pictures of the flow around rotating and stationary wheels inside front and rear wheelhouses are delineated. It is time to take stock of their similarity and difference with isolated situations in the literature. A retrospective analysis of flow structures around an isolated stationary and rotating wheel is given in Figure 4.30, which are results from DES model by Heyder-Bruckner (2011). The later separation on the upper surface of stationary wheel, compared to rotating one, that causes more downwash on the rear tire tread is also reported by Fackrell & Harvey (1975); McManus & Zhang (2006); Diasinos *et al.* (2015) in their study on isolated wheels. As a consequence, more flow is directed down towards the ground and fuels the counter rotating ground vortices.

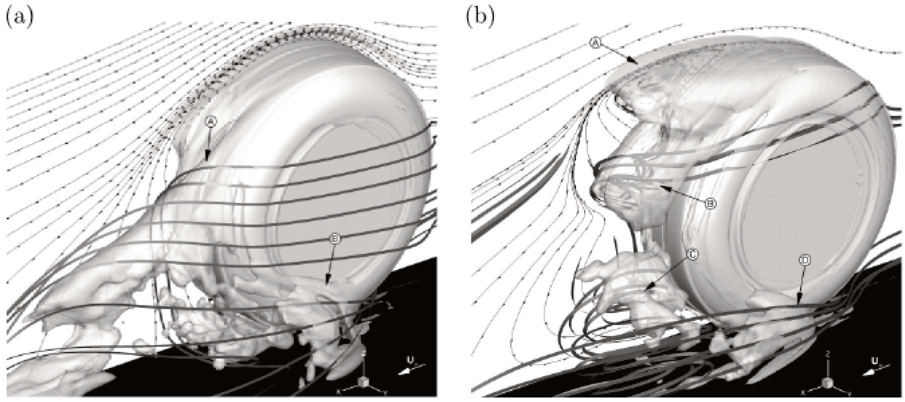

Figure 4.30: DES results by Heyder-Bruckner (2011) around an isolated stationary and rotating wheel, with iso-surface of the Q-criterion ($Q = 100000$), streamlines in the $y = 0$ plane and ribbons showing various flow structures.

For wheel half shielded inside the wheelhouse, the upper part of the wheel is no longer exposed to freestream flow. Nevertheless, as air enters the wheelhouse from the front leading edge and contours the front tire tread, different separation position can still be observed for different wheel state. For stationary wheels, the flow patterns are almost identical regardless of the presence or not of the wheelhouse: there is strong downwash directly behind the tire that entrains the side flow and feeds the counter rotating vortex pair forming on the ground. However, for a stationary wheel inside a wheelhouse, the flow upon the wheel is limited by the wheelhouse volume, and with the presence of the underbody, the vortex pair formed behind the wheel probably has less intensity and smaller size than that of an isolated stationary wheel with the same dimension.

For an isolated rotating wheel, Figure 4.30 highlights the earlier separation on the top wheel tread. An arch shaped vortex is thereby formed in the upper rear separation zone. Consequently, the wheel wake is higher than that of the stationary case. At the lower bottom, the rotation of the wheel induces a recirculation region (marked as C in this figure, which corresponds the vortex O in Figure 4.3(c)(d) and Figure 4.16(c)(e)). The entrained side flow and the earlier separated flow that eventually convects downwards and upstream will interact with this recirculation region and enhance the circulation in the wake. This wake region is also deemed as counter rotating ground vortex pair yet with much less intensity as opposed to the stationary wheel wake. However when rotating wheel is shielded inside the wheelhouse, a great deal of the flow entering the wheelhouse leaves the volume from the upper part of the wheel. Only few amount exits the wheelhouse from the rear bottom opening, where it collides head-on with the upward flow entrained by the wheel running surface, so that its momentum is partly canceled out. In this circumstance, no counter rotating vortices are produced. Furthermore, if the yaw angle is important as for a front rotating wheel, the outflow leaves the lower part of the wheelhouse mainly from the outboard side (S in Figure 4.16(c)(e)), and the amount of flow exiting the rear bottom will be further reduced.

4.3.2 Aerodynamics around the vehicle

Now we turn our attention to the comparison among the four configurations: *RR*, *SR*, *RS* and *SS*. The experimental measurements of the vehicle drag and lift coefficients as well as the integrated underbody and base pressure are reported in Table 4.5.

	$SCz(m^2)$	$SCx(m^2)$	$SCp_{\mathrm{U}}(m^2)$	$SCp_{\mathrm{B}}(m^2)$
RR	0.020	0.393	-2.274	-0.234
SR	-0.068	0.406	-2.342	-0.239
RS	0.148	0.447	-2.177	-0.259
SS	0.083	0.448	-2.256	-0.263

Table 4.5: Experimental results of the aerodynamic lift and drag coefficients and time-averaged underbody and base pressure for configurations with front/rear rotating/stationary wheels.

With different wheel states, distinct lift coefficients are observed, from which we speculate that for the same rear wheel state, the rotation of the front wheel increases the lift ($SCz_{RS} > SCz_{SS}$, $SCz_{RR} > SCz_{SR}$), while for the same front wheel state, the rotation of the rear wheel decreases the lift ($SCz_{SR} < SCz_{SS}$, $SCz_{RR} < SCz_{RS}$). As far as the drag coefficient is concerned, the four rotating wheels configuration has the smallest drag. The stop of the front wheel rotation raises slightly the vehicle drag, while the stop of the rear wheel rotation has a higher penalty on the vehicle drag. When the rotation of the front wheel and rear wheel is inhibited at the same time, the drag further increases. While in general, it is the rear wheel state that dominates the drag level. In addition, there is a good correlation between the lift coefficient and integrated underbody pressure, as well as between the drag coefficient and integrated base pressure.

The analysis of the pressure variation related to different wheel state is primarily undertook in the median plane $y = 0$ (Figure 4.31(a)). Ostensibly, at the front part of the underbody ($s < -2$), the pressure levels are close for configurations with same front wheel state; and at the rear part of the vehicle ($-1.5 < s < 2$), including the rear underbody, the base and the downstream portion of the roof, the curves can be grouped by their rear wheel state. And their underbody and base pressure maps in Figure 4.31(b) and (c) conform to the line plot in the $y = 0$ plane.

In Figure 4.31(b), considering configurations with same rear wheel state, behind front stationary wheels (*SR* and *SS*), the pressure appears to be much lower. While if same front wheel states are preserved, we can discern an important pressure drop between rear rotating wheels (*RR* and *SR*). These two types of pressure reduction arise from different mechanisms. The first one is linked to the wheel wake, the latter is associated with the underbody flow momentum. According to Section 4.3.1, the significant pressure recovery behind the front rotating wheels is achieved by the elimination of the counter-rotating ground vortex pair. That is why for the same rear wheel state configurations, the rotation of the front wheels augments the lift coefficient ($SCz_{RS} > SCz_{SS}$, $SCz_{RR} > SCz_{SR}$) owing to their higher pressure imprint on the underbody. Meanwhile, if we compare the configurations with same front wheel states, the important suction due to rear wheel rotation indicates that the flow velocity is increased, which accounts for the drop of the lift coefficient ($SCz_{SR} < SCz_{SS}$, $SCz_{RR} < SCz_{RS}$). Moreover, a decreased diffuser efficiency is discernible in the line plot in Figure 4.31(a) for rear stationary wheels configurations. Similar results have been reported in Section 4.1.3 between *XS* and *XR*, where the effect of the rear wheel state was demonstrated, at first order, to be a blockage effect.

The pressure distributions on the body flank also make the wheel wakes identified (Figure 4.31(d)). For front stationary wheels configurations (*SR* and *SS*), the low pressure region downstream the wheelhouse reaches a minimum at the lowest pressure tap. Yet for front rotating wheels (*RR* and *RS*), the most important suction is measured at the higher pressure tap. On the basis of the wheelhouse outflow description in Section 4.3.1 and 4.2.1, the former is associated with the counter rotating vortex developed on the ground, and the latter is connected to the outflow from the side of the wheel arch. Besides, downstream rear stationary wheels (*RS* and *SS*), the pressure is mildly lower.

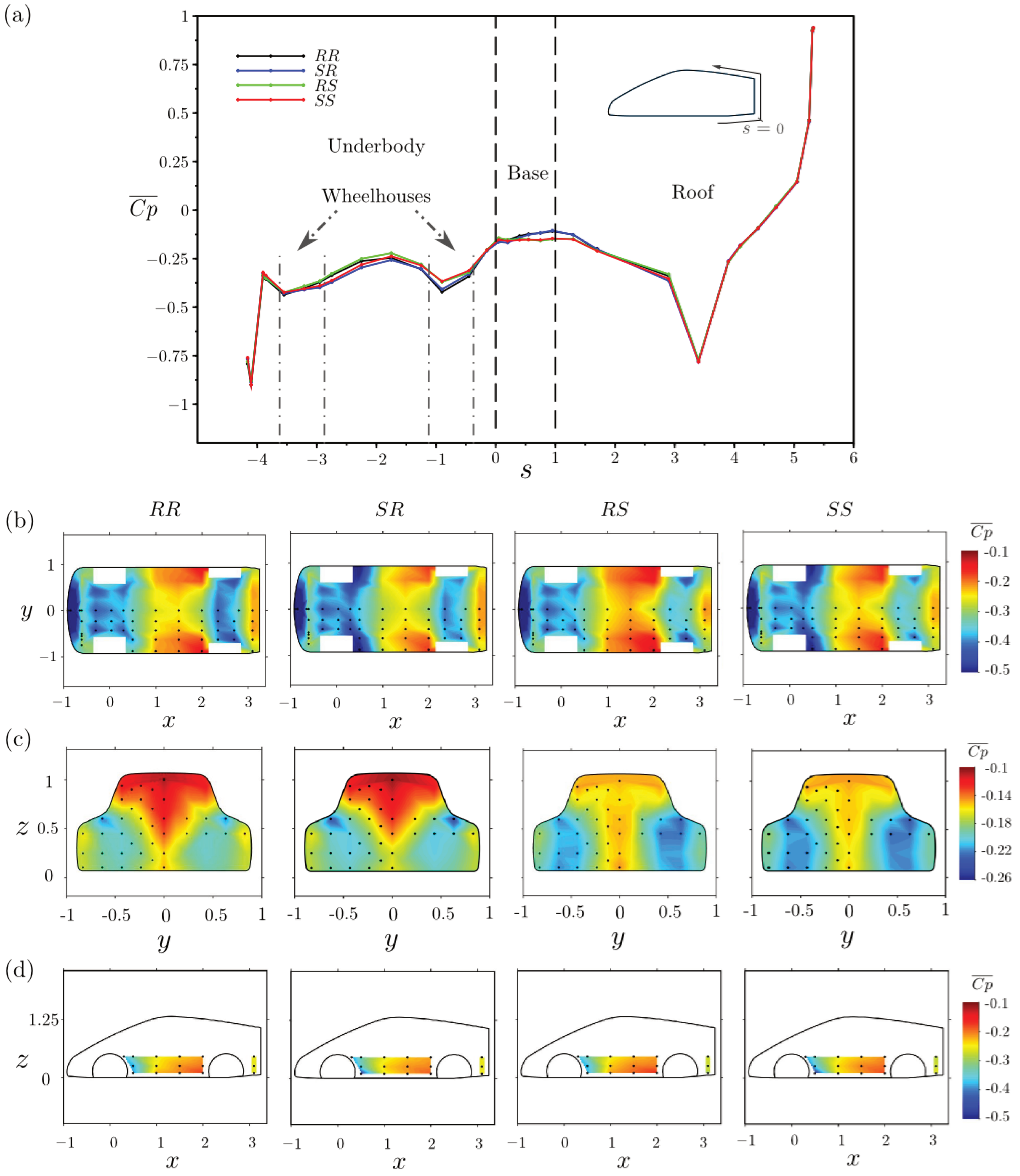

Figure 4.31: (a) The distribution of $\overline{Cp}$ in the $y = 0$ plane on the curvilinear abscissa s (normalized by the height of the base) with the origin at the underbody rear end, for *RR*, *SR*, *RS* and *SS*; Their underbody (b), base (c) and lateral (d) pressure distributions.

The standard deviation of the underbody and side body pressure Cp' additionally illustrate regions strongly disturbed by wheels (Figure 4.32). The intensified fluctuation behind stationary wheels extends more downstream in the underbody (Figure 4.32(a)) and exhibits closer to the ground on the body flank (Figure 4.32(b)), highlighting the existence of the counter rotating ground vortices. We can also remark an enhanced unsteadiness at the inner side of the rear rotating wheels in Figure 4.32(a) (*RR* and *SR*). This corresponds with the flow inside the inner wheel hub cavity got entrained by the wheel rotation and interacting with the underbody flow, as delineated in Figure 4.3(d)(f).

The base pressure distributions in Figure 4.31(c) assume to be highly dependent of the rear

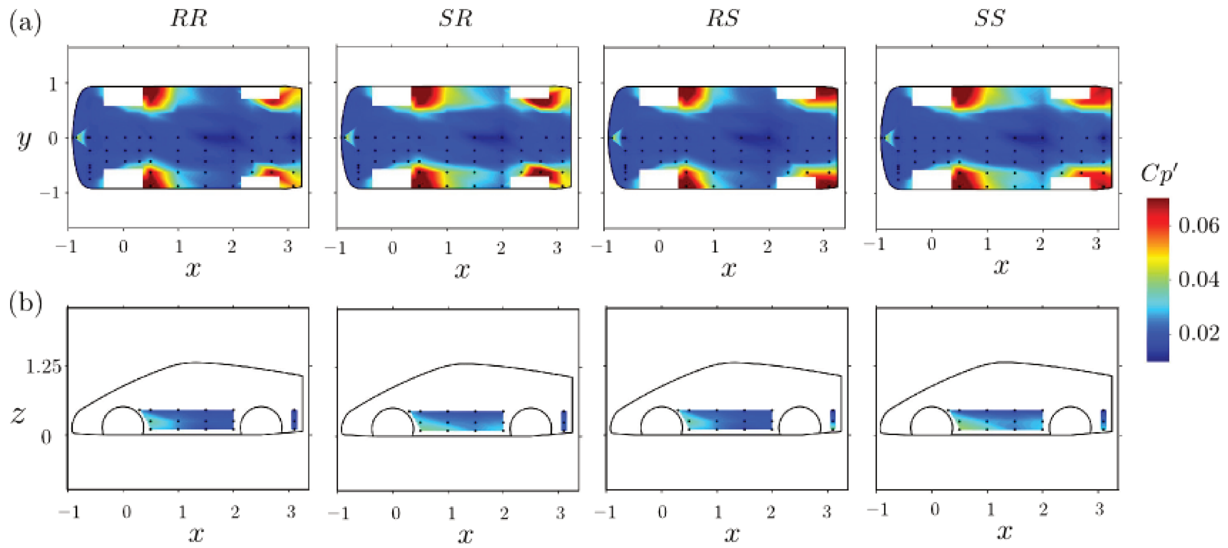

Figure 4.32: The distributions of pressure standard deviation Cp' in the underbody (a) and on the side body (b), for *RR*, *SR*, *RS* and *SS*.

wheel state. For rear stationary wheel configurations, the base pressure has lower level and nearly zero vertical pressure gradient at the centerline ($d\overline{Cp}/dz = -0.009$ and 0.008 for *RS* and *SS*). For rear rotating wheel configurations, there is remarkable base pressure recovery, with positive vertical pressure gradient ($d\overline{Cp}/dz = 0.065$ and 0.085 for *RR* and *SR*). Hence, the drag level is dominated by the rear wheel state. The standard deviation of the base pressure Cp' is equally presented for the four configurations (Figure 4.33). The rear stationary configurations (*RS* and *SS*) have almost identical distributions. While the rotation of the rear wheels (*RR* and *SR*) seems to move upwards the high Cp' region on the base surface, as the fluctuation at the bottom of the base is reduced. It is then envisaged that the variations in $\overline{Cp}$ and Cp' distributions, mainly depending on rear wheel state, are tightly coupled with the wake topology modifications. To illustrate this, the PIV measurements in the wake symmetrical plane $y = 0$ are displayed in Figure 4.34.

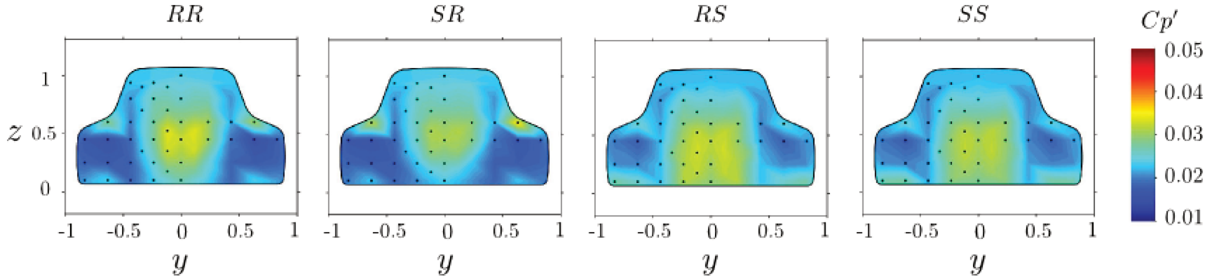

Figure 4.33: The distributions of base pressure standard deviation Cp', for *RR*, *SR*, *RS* and *SS*.

From the 2D mean streamlines in Figure 4.34(a) we can perceive that the configurations with same rear wheel state possess similar wake topology. For *RR* and *SR*, predominant upwash displays in the wake and leads to upward deflecting reversed flow inside the mean recirculation bubble. Therefore the upper vortex structure is pushed more downstream, which results in a significant pressure recovery at the upper part of the base and a positive vertical pressure gradient in the base centerline. In addition, their recirculation lengths L_r in the $y = 0$ plane are larger, consistent with their higher base pressure. For *RS* and *SS*, the upper and lower recirculation structures develop at equal distance away from the base surface. The mean backward flow is more or less horizontal, leading to nearly zero vertical pressure gradient in the base centerline. The base stagnation point of the reversed flow can be related to the high pressure fluctuation already seen in Figure 4.33. In Figure 4.34(b), their downward vertical velocity $\overline{w}$ at the upper region above the mean circulation bubble is more important compared to rear rotating wheel configurations. In addition, their reduced upwash below the mean circulation bubble seems to be consistent with the decreased underbody flow momentum evidenced by Figure 4.31(a) and (b). This can be supported by the work of Grandemange *et al.* (2013*c*), wherein a downward deflection of the bottom flap at the rear of a squareback model reduces not only the underbody upsweep, but also the lift coefficient, which is primarily attributed to the reduced underbody flow momentum. Nevertheless, it is worthwhile mentioning that the distinct wake topology for different rear wheel state for four wheels configurations was not observed in Section 4.1.3 for two rear wheels configurations. It can thus be inferred that for two rear wheels configurations, as the vehicle wake is dominated by downwash, this wake organization is more robust to underbody flow momentum modification.

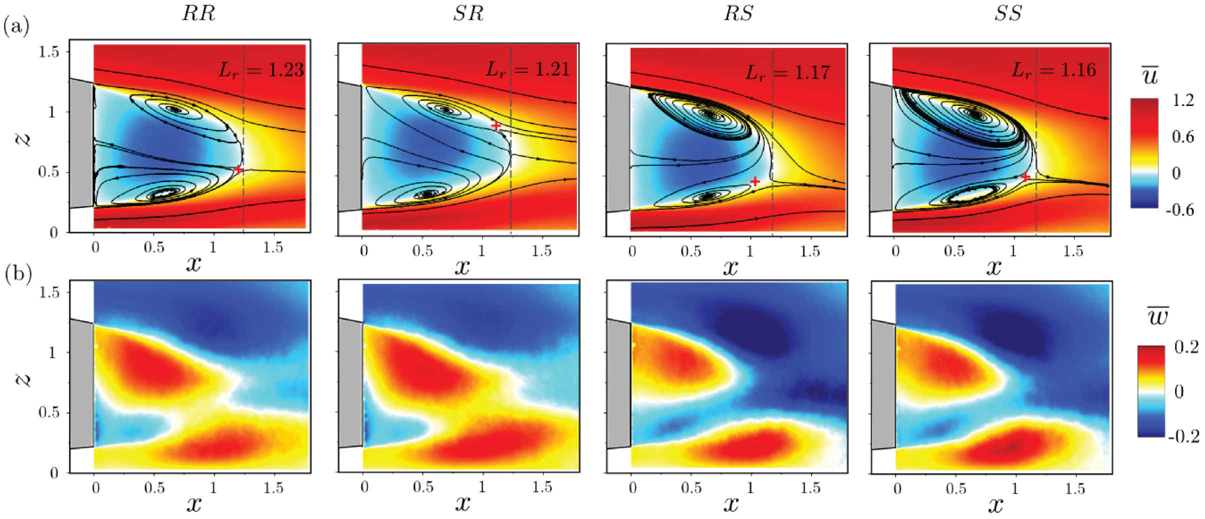

Figure 4.34: PIV measurements in the symmetrical plane $y = 0$ in the wake for *RR*, *SR*, *RS* and *SS*: (a) Time-averaged streamwise velocity $\overline{u}$ maps overlaid with 2D streamlines, L_r (see Eq. 3.1) indicates the bubble length highlighted by the dashed line, and red crosses are saddle points whose positions are presented in Table 4.6; (b) Time-averaged cross-stream velocity field $\overline{w}$.

Furthermore, it should be pointed out from Figure 4.34 that, apart from the primary impact of the rear wheel state, the front wheel state also exhibits a secondary effect on the wake topology. Comparing the configurations with same rear wheel state, the rotation of the front wheel seems to diminish the upward vertical velocity $\overline{w}$ below the mean circulation bubble. Consequently, the vertical positions of the saddle points at the end of the recirculation bubble (marked as red cross in Figure 4.34(a)) are shifted downwards, as summarized in Table 4.6.

	x_S	z_S
RR	1.206	0.557
SR	1.110	0.876
RS	1.023	0.433
SS	1.074	0.495

Table 4.6: Saddle point position (see Figure 4.34(a)) in the $y = 0$ plane of the wake.

The velocity angle $\theta = \arctan(\overline{w}/\overline{u})$ of the streamlines issuing from the top and the bottom separation points in this PIV plane are presented in Figure 4.35. At $x > 0$, the evolution of the top streamline angles in Figure 4.35(a) highlights the dominant effect of the rear wheel state, with higher angles indicating a more upward deflected wake for rear rotating wheel configurations. Within the two groups having same rear wheel state, for front stationary cases, the angle raises marginally at more downstream locations. In Figure 4.35(b), the evolution of the bottom streamline angle reflects the positions of the saddle points where the curves begin to drop (except for *SR*). For rear rotating wheels, in contrast to rear stationary cases, their saddle points lie more downstream. While comparing *RS* to *SS*, its saddle point is likely to be lower. In opposition to the comparison between *XR* and *RR* (Figure 4.20(b)), where the two configurations have different vertical pressure gradient in the base centerline and with different velocity angles at the separations, here less apparent angle variation is discernible at $x = 0$ for both top and bottom shear layers.

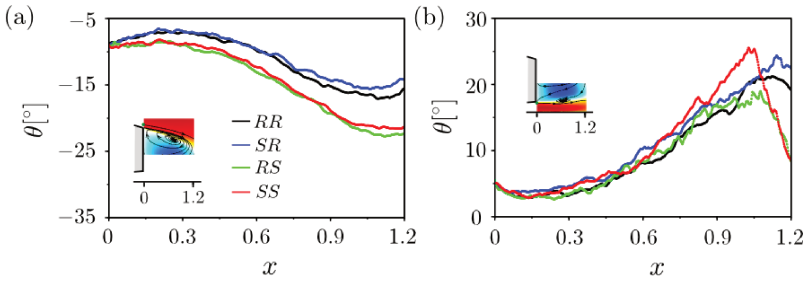

Figure 4.35: Streamwise evolution of the velocity angle $\theta = arctan(\overline{w}/\overline{u})$ of the streamlines issuing from the top $(x, z) = (0.07, 1.3)$ (a) and the bottom $(x, z) = (0.07, 0.21)$ (b) separation points, for *RR*, *SR*, *RS* and *SS*.

The wake dynamics can be further analyzed by the mean turbulent kinetic energy $k = 0.5 \times (\overline{u'u'} + \overline{w'w'})$ maps in Figure 4.36. From the fluctuation point of view, the baseline configuration indeed exhibits the most upper/lower balanced distribution. Furthermore, it is apparently the rear wheel state that dictates the global distribution of k in this symmetrical plane. For rear stationary configurations (*RS* and *SS*), the fluctuation of the bottom mixing layers is considerably stronger. Whereas the front wheel state plays a less important role in the upper/lower shear layer balance. Comparing identical rear wheel state configurations, the front rotation is prone to slightly increase the bottom fluctuations while mildly damps the top turbulent kinetic energy.

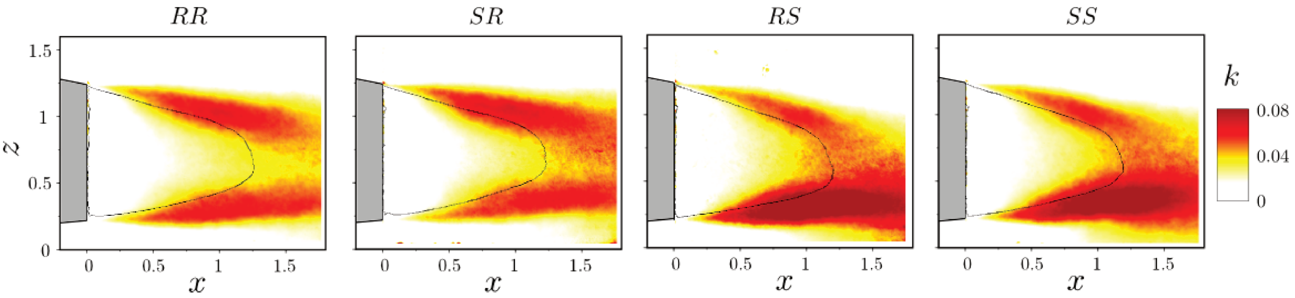

Figure 4.36: Planar turbulent kinetic energy distributions in the $y = 0$ PIV plane, for *RR*, *SR*, *RS* and *SS*.

In the following, we will be interested in the measurements of the rear wheels wakes. The PIV measurements of the streamwise velocity at the half of the ground clearance are given in Figure 4.37. It can be noticed that there is a conspicuous resemblance between configurations with same rear wheel state. The enlargement of the wheel wakes by stationary rear wheels is in common with the numerical results presented in Figure 4.27(b). The profiles of the streamwise velocity $\overline{u}$ at the exit of the underbody $(x = 0.05)$ are extracted in Figure 4.37(b). The inner segment of the velocity profiles $(y \in [-0.6, 0.6])$ of the four configurations nearly collapse. While the maximum velocity deficit is evidently increased for rear stationary wheel configurations, although no negative velocity is measured at this vertical plane. At the outer side, the velocity profiles recovers to two different levels which is dictated by the front wheel state, with higher level for front rotational configurations. In Figure 4.37(c), their PDF distributions of the maximum deficit (taken at $y_m = \text{argmin}_{y>0}\,\overline{u}(y)$ for each configuration) at this streamwise location are shown in the Figure 4.10(c). Similar to the comparison between *XR* and *XS*, the PDF for the stationary rear wheel configurations features more important negative component, tallying with their lower base pressure. Moreover, for same rear wheel state configurations, front wheel rotation seems to shift marginally the curves towards positive u direction.

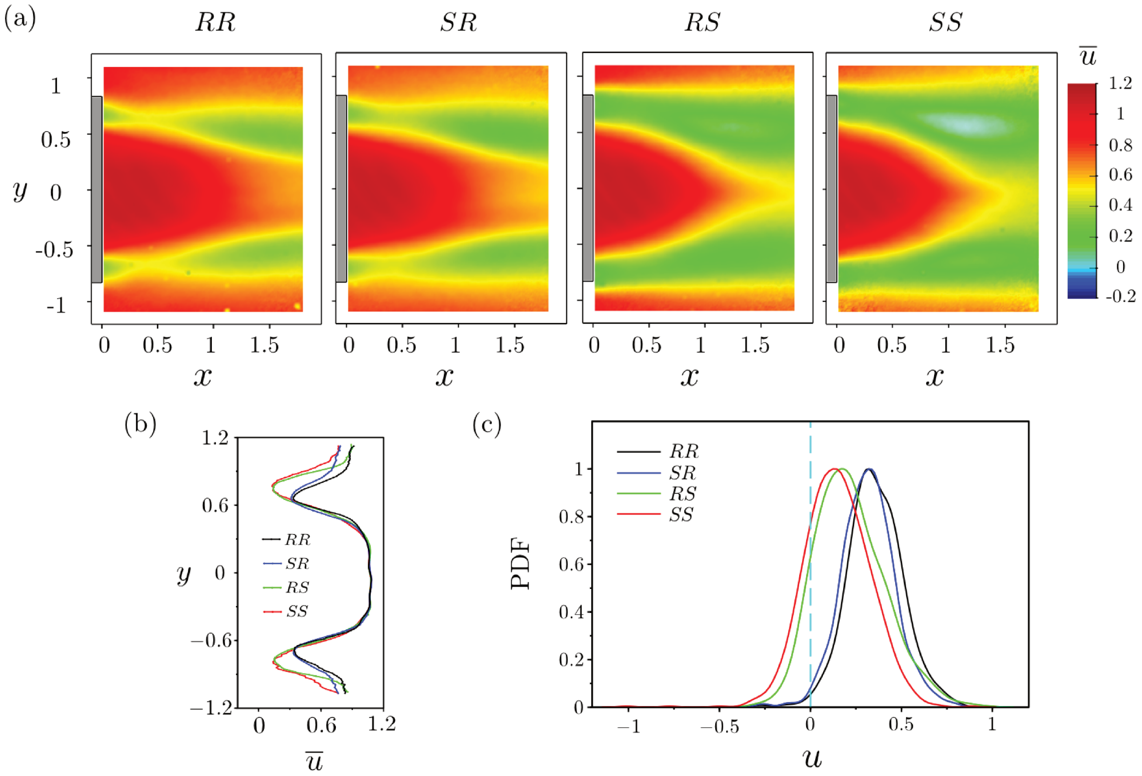

Figure 4.37: Comparison of the planar PIV measurements at the half of the ground clearance among *RR*, *SR*, *RS* and *SS*. (a) Distribution of time-averaged streamwise velocity $\overline{u}$; (b) Profiles of $\overline{u}$ at the exit of the underbody $x = 0.05$; (c) Probability density functions (PDF) of the maximum deficit at $x = 0.05$. The maximum deficit is taken at $y_m = \text{argmin}_{y>0}\,\overline{u}(y)$ for each configuration. The PDF distributions are normalized for easier comparison.

With the numerical results, we can have access to the velocity distribution at the whole trailing edge plane $x = 0$, to shed light on the rear wheel wake development (Figure 4.38(a)). For *SS*, a small region of $\overline{u}$ close to zero can be observed. If the reversed flow can yield important pressure drop at the vehicle base, it is then worthwhile to take into account the velocity fluctuation around the mean value of the streamwise velocity. To do so, we first assume that at any spatial point, the velocity follows a normal distribution with an average of $\overline{u}$ and a standard deviation of u' (the PDFs presented in Figure 4.37(c) are close to normal distributions). Then we plot the distribution of $\overline{u} - u'$ for *RR* and *SS* at plane $x = 0$, to highlight the possible region that could give rise to important wheel-vehicle wake interaction (Figure 4.38(b)). Indeed, the distribution for *SS* seems to indicate higher probability of reversed flow in this plane, as negative $\overline{u} - u'$ spreads over larger area.

The distributions of the planar turbulent kinetic energy at the half of the ground clearance measured by PIV are given in Figure 4.39(a). They are quite noisy due to the limited number of

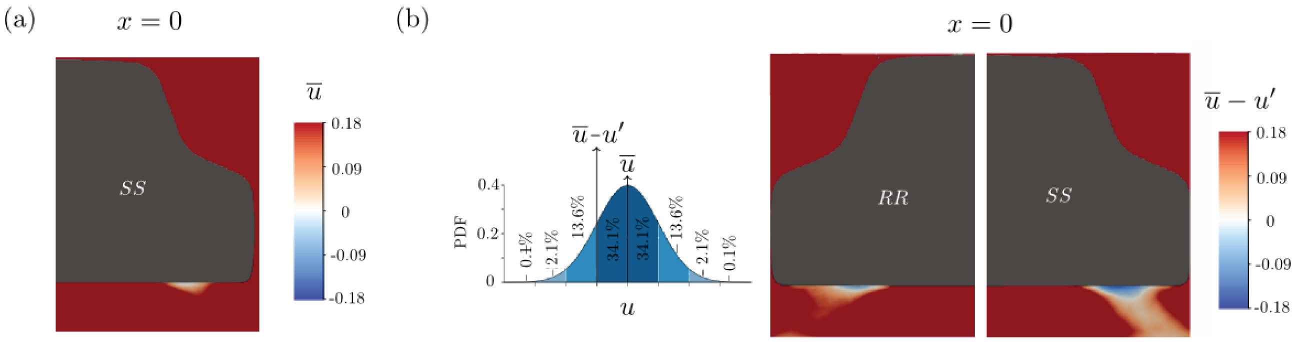

Figure 4.38: (a) The distribution of the streamwise velocity at the trailing edge plane $x = 0$ for *SS*, extracted from the numerical results; (b) The distribution of $\overline{u} - u'$ at $x = 0$ extracted from the numerical results, for *RR* and *SS*. The PDF of the streamwise velocity is delineated assuming that at any spatial point the velocity follows a normal distribution with an average of $\overline{u}$ and a standard deviation of u'.

images which do not provide a good convergence for the second order statistics. Nevertheless, we can still have sight of enhanced fluctuation in the inner shear layers of the stationary rear wheels. Similar observations are reported for comparison between *XR* and *XS* (Figure 4.11).

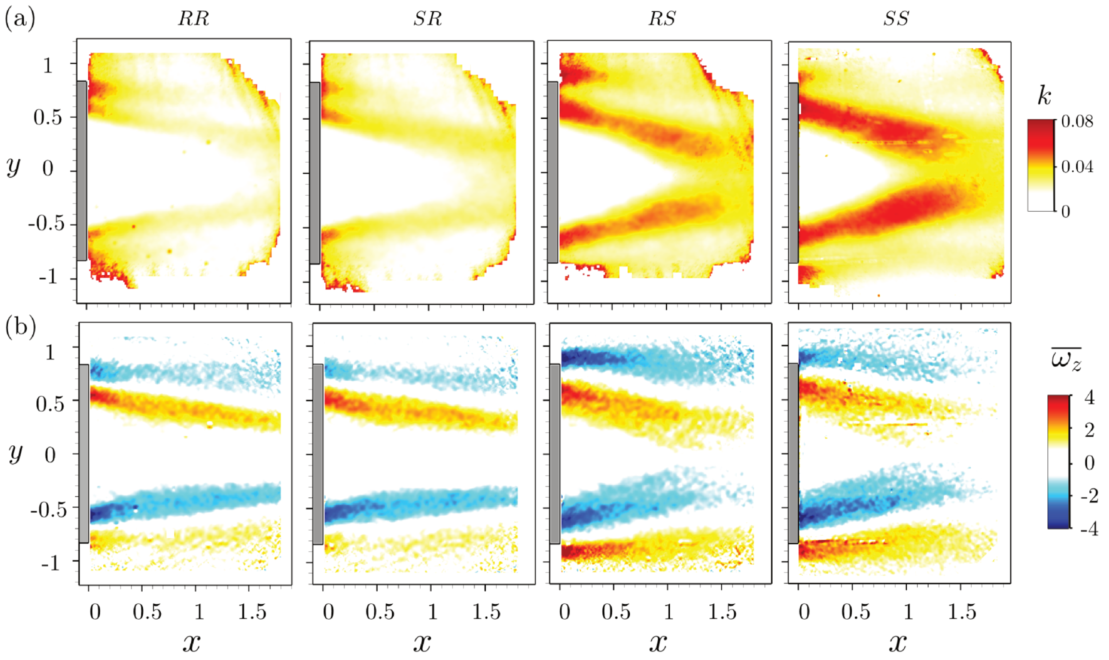

Figure 4.39: PIV measurements of planar turbulent kinetic energy k (a) and the time-averaged vorticity $\overline{\omega_z}$ (b) at the half of the ground clearance, for *RR*, *SR*, *RS* and *SS*.

Finally, the time-averaged 2D vorticity fields in Figure 4.39(b) also make the shear layers discernible. At $x = 0$ in Figure 4.39(b), the inner shear layers of front stationary configurations depart slightly more inward than their counterparts. It is probably attributed to the higher deficit created downstream front stationary wheels, which makes subordinate contribution to the development of the rear wheel/wheelhouse wake. Analogous to comparison between *XR* and *RR* shown in Figure 4.17(c) and Figure 4.21(c), the lower momentum of the rear wheel approaching flow yields to more inward deflecting wakes. This can presumably be associated with their slightly upward lifted mean recirculation bubble as illustrated in Figure 4.34.

4.3.3 Forward? Backward?

The four wheels are now forced to turn in the opposite direction with the rated rotational speed. This configuration is denoted with RR^{-1}. If the study of vehicle with stationary wheels can be considered compatible with a real life scenario only in situations where the wheels are locked under braking, whereas turning the wheels in the opposite direction seems completely disconnected from reality. However it is still of interest to reinforce the links between underbody blockage with the vehicle aerodynamics.

For wheel shielded inside the wheelhouses, the mechanism of downsizing the wheel wake by rotation lies in the suppression of the counter rotating ground vortice, as established in Section 4.3.1. Although neither numerical simulation nor PIV measurements of the wakes are available for RR^{-1}, it is anticipated that the opposite rotation of the wheel will be in favor of the downwash behind the rear tire tread and culminate in even more sizable counter rotating ground vortices than the stationary case, and thus an even higher underbody blockage. To confirm this, the configuration RR^{-1} will be compared to *RR* and *SS*. Their lift, drag coefficients, and integrated underbody and base pressure coefficients are firstly tabulated.

	$SCz(m^2)$	$SCx(m^2)$	$SCp_{\mathrm{U}}(m^2)$	$SCp_{\mathrm{B}}(m^2)$
RR	0.020	0.393	-2.274	-0.234
SS	0.083	0.448	-2.256	-0.263
RR^{-1}	0.153	0.494	-2.145	-0.276

Table 4.7: Experimental results of the aerodynamic lift and drag coefficients and time-averaged underbody and base pressure for *RR*, *SS* and RR^{-1}.

According to Table 4.7, from the most realistic configuration to the least, the lift and drag coefficients both increase, which is rather reassuring. Moreover, the evolution of the aerodynamic coefficients are in reasonable agreement with the integrated underbody and base pressure. The comparison of their surface pressure distributions are then given in Figure 4.40.

Their time averaged $\overline{Cp}$ distributions in the $y = 0$ plane are depicted in Figure 4.40(a). From *RR* to *SS* and to RR^{-1}, a gradual raise of the underbody centerline pressure can be discernible except a small portion in the middle ($-3 < s < -2.25$). The increase of the underbody pressure at its front ($s < -3$) and rear part ($s > -2.5$) indicates a good agreement with the reduced underbody flow momentum by enlargement of the wheel wakes. The progressive reduced diffuser efficiency is also brought to light. In the base, the curves are layered with gradual deepened suction. The vertical pressure gradient of RR^{-1} is reckoned to be $d\overline{Cp}/dz = -0.008$. At the rear roof, a good continuity of pressure measurements is maintained with the base pressure level.

From the underbody pressure maps in Figure 4.40(b), for RR^{-1} the important suction zones behind the front wheels move more inwards than those of *SS*. Meanwhile, the lowest pressure tap downstream the front wheelhouse on the vehicle flank (Figure 4.40(c)) exhibits a slight pressure recovery. It can thus be inferred that the opposite rotation strongly entrains the flow inside the large front wheelhouse cavity that fuels the counter rotating ground vortices at the inner side. Their pressure standard deviation distributions in Figure 4.41 reveal a much more enhanced fluctuation of RR^{-1} downstream the front and rear wheelhouses, and at the inboard side of rear wheelhouses. In the underbody, the regions with enhanced fluctuation gain in size, which supports the enlargement of wheel wakes. Therefore it is believed that the enlarged rear wheel wakes strongly interact with the vehicle wake, and yield the broad suction on the entire base surface (Figure 4.40(d)).

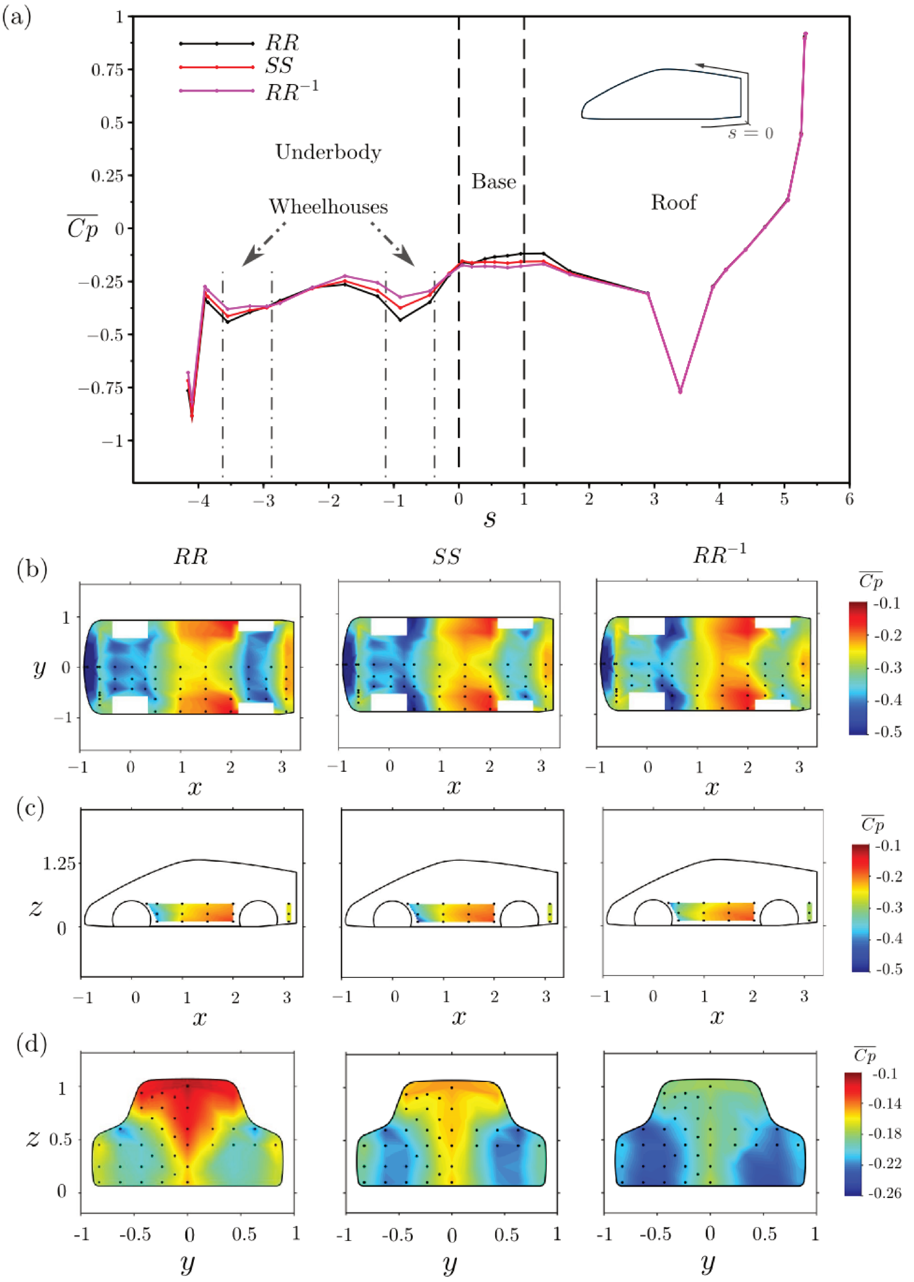

Figure 4.40: (a) The distribution of $\overline{Cp}$ in the $y = 0$ plane on the curvilinear abscissa s (normalized by the height of the base) with the origin at the underbody rear end, for *RR*, *SS* and RR^{-1}; Their underbody (b), lateral (c) and base (d) pressure distributions.

The mean wake in the symmetrical $y = 0$ plane for RR^{-1} is measured and presented in Figure 4.42 along with *RR* and *SS*. Its further drop of the base pressure reasonably agrees with the shortening of the mean recirculation length. The saddle point moves upstream and downwards. It also suggests that the wake is diverted more towards the ground, which is in good consistent with the reduced underbody momentum.

Summary In this section, the flow field around front and rear stationary wheels inside the wheelhouses are primarily portrayed with the results from numerical simulation. In common with isolated stationary wheels, the strong downwash behind the rear tire tread that feeds the counter rotating vortex pair is always discernible. On the flip side, no counter rotating vortex is generated behind rotating wheel shielded in wheelhouse, which is dissimilar to isolated rotating

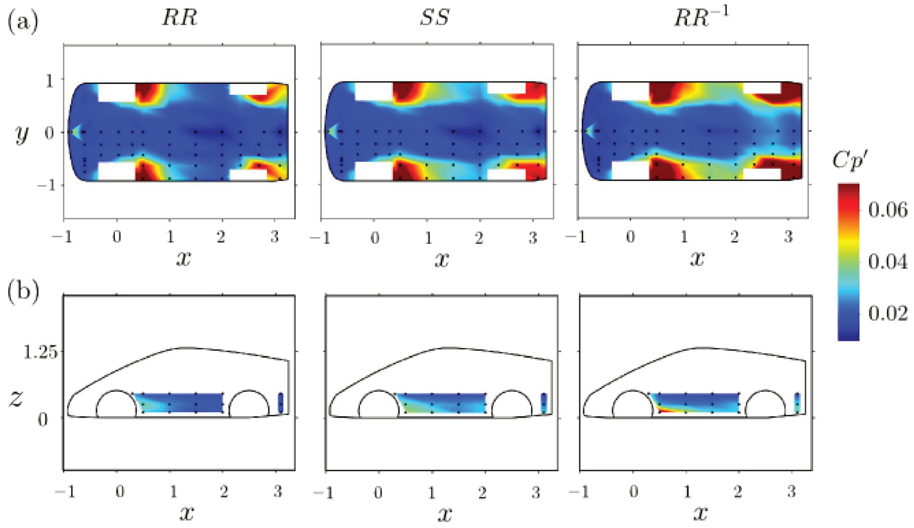

Figure 4.41: The distributions of pressure standard deviation Cp' in the underbody (a) and on the side body (b), for RR, SS and RR^{-1}.

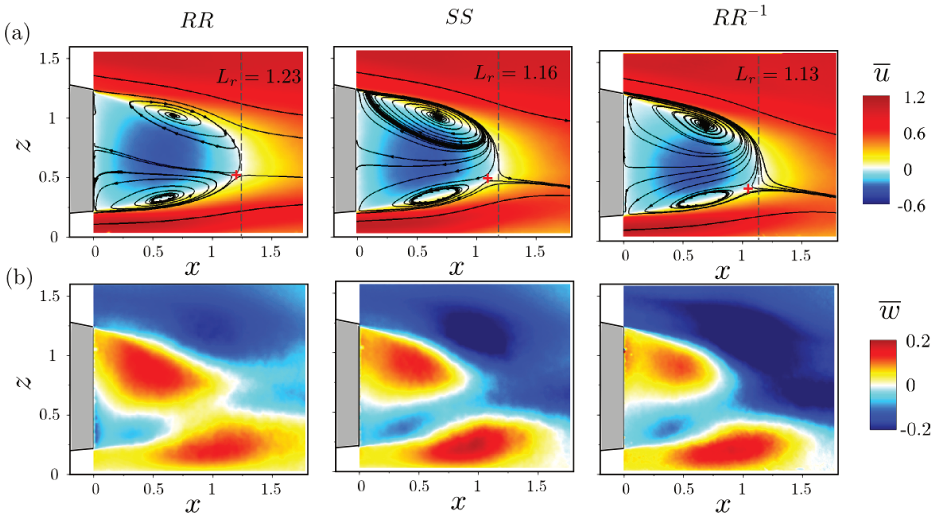

Figure 4.42: PIV measurements in the symmetrical plane $y = 0$ in the wake for RR, SS and RR^{-1}: (a) Time-averaged streamwise velocity $\overline{u}$ maps overlaid with 2D streamlines, L_r indicates the bubble length highlighted by the dashed line, red crosses are saddle points. The saddle point of RR^{-1} locates at $x = 1.008, z = 0.448$; the other two see Table 4.6; (b) Time-averaged cross-stream velocity field $\overline{w}$.

wheels. Consequently, the stationary wheels create larger wakes behind.

The underbody and side body surface pressure distributions make the different wheel states identifiable. Particularly behind stationary wheels, low pressure and high fluctuation exhibit close to the ground. Their larger wakes also amount to an increase in underbody blockage. Therefore the underbody flow momentum between the stationary wheel pair decreases, and it is all the more important at the rear underbody where situates the diffuser. Moreover for configurations with rear stationary wheels, their base is subject to higher suction due to the stronger interaction between the wheel wakes and the vehicle wake. The upwash from the underbody is reduced as a result of the enhanced fluctuation and the diminished underbody flow momentum. Consequently the vehicle wake in the symmetrical plane is diverted closer to the ground, and the vertical pressure gradient in the base centerline drops nearly to zero. From the fluctuation point of view, the wake is no longer well-balanced as an enhanced bottom fluctuation is observed. Furthermore, apart from the primary impact of the rear wheel state, the front wheel state also has a secondary effect on the mean wake topology in the symmetrical plane. Comparing same rear state configurations, with front rotating wheels, the saddle point in the mean wake is displaced more downwards. While their base pressure and drag level mildly precede those with stationary front wheels.

The most unrealistic configuration with four wheels turning in the opposite direction is equally measured in order to further validate the aforementioned link between wheel wake size, underbody blockage and base pressure level. Although neither numerical simulation nor PIV measurements of the wakes are available for this configuration, it can be expected that the opposite rotation of the wheel is in favor of the downwash behind the rear tire tread therefore additionally increases the wheel wakes. This is corroborated by the increased pressure between the wheel pair in the underbody and the decreased pressure in the base.

At last, it is important to emphasize the higher sensibility of the well-balanced wake (the baseline configuration) towards rear wheel state variation (rotating/stationary/turning in opposite direction), as the modification of wake wall-normal equilibrium was not observed in previous section for two rear wheels configurations (Section 4.1.3).

Chapter 5

Vehicle geometry and tire influence

In this chapter, we first add an additional bottom at the rear underbody to eliminate the vehicle diffuser. An increase in pressure is observed on the underbody, particularly on the rear part. This decrease in underbody flow momentum causes the mean wake completely being diverted downward. This global effect leads to an insensitivity of the aerodynamic coefficients towards underbody disturbances (presence of wheels, state of the wheels, ...). In other words, the presence of a diffuser accentuates the global, local and wake balance effects introduced by rear underbody modifications.

The second part investigates effects of two different tires. One has carborundum powder glued on the flank, aiming at representing tire sidewall marking; the other is a slick tire without grooves. It is shown that the change of tire (front or rear) may be interpreted as a change in the wheel blockage rate (wheel more or less wide) with the same consequences on the pressure distributions at the base and underbody as those analyzed in previous chapters (but with a smaller effect). It has also been observed that the rear tire change can, in some configurations, have a significant effect on the wake balance. In addition, we present the pressure distributions inside the front and rear wheelhouses. Local pressure modifications inside of them are equally observed for different tires at different states. The contribution of the wheelhouses to the vehicle drag are evaluated to be roughly 20%.

Contents

5.1 The impact of the vehicle geometry on wheel-vehicle interaction

Figure 5.1 displays the modified geometry with flat underbody. The roof boat tail angle remains at 10° and the bottom angle decreases from 5° to 0°. This modified geometry with four rotating wheels will be denoted by $\underline{RR}$. To start with, the aerodynamic coefficients of $\underline{RR}$ compared to RR are tabulated (Table 5.1).

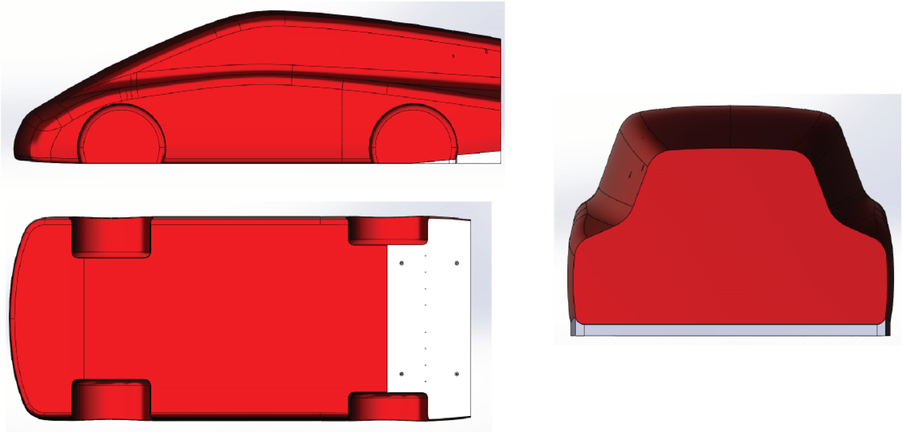

Figure 5.1: Elimination of the vehicle diffuser: vehicle model with additional bottom screwed at the rear underbody.

	$SCz(m^2)$	$SCx(m^2)$	$SCp_{\mathrm{U}}(m^2)$	$SCp_{\mathrm{B}}(m^2)$	$d\overline{Cp}/dz$
RR	0.020	0.393	-2.274	-0.234	0.065
$\underline{RR}$	0.339	0.437	-1.937	-0.306	-0.074

Table 5.1: Full scale lift and drag coefficients, integrated underbody and base pressure for RR and $\underline{RR}$.

All the integrated aerodynamic parameters exhibit important variations, which suggests a significant flow modification generated by the elimination of the underbody diffuser. The lift coefficient SCz is strongly increased, associated with a raise in integrated underbody pressure SCp_{U}. Their underbody pressure distributions in Figure 5.2(a) highlight an important pressure increase downstream the front wheelhouses. This is aligned to the past investigations on the vehicle diffuser, where the diminution of diffuser angle increases the underbody pressure and thus increases the lift (Cooper *et al.*, 1998, 2000; Jowsey, 2013). The elimination of the underbody diffuser can be analogous to modifying flap or tapper angle at the blunt trailing edge of a vehicle model (Littlewood & Passmore, 2010; Grandemange *et al.*, 2013*c*; Perry *et al.*, 2016). As a consequence, the vehicle wake is oriented differently. The reversed sign of the vertical pressure gradient at the base centerline ($d\overline{Cp}/dz$) provides strong evidence of the wake wall-normal equilibrium alteration. Moreover, proposed by Grandemange *et al.* (2013*c*), the model drag is a second order polynomial containing a coupling term between the top and bottom flap orientation angles, wherein the contributions of the wake size, of the lift induced drag and of the local drag induced by the inclination of the flaps are identified. According to their findings, here the drag rise by reducing the diffuser angle from 5° to 0° can be primarily ascribed to the increase in wake size as the height of the separated region is augmented. Alongside, the integrated base pressure SCp_{B} is lowered. As depicted in Figure 5.2(b), an increased suction at the two sides of the base surface can be perceived, accompanied by a vertical pressure gradient inversion.

The global modification of the wake height and wake balance can be clearly observed from the mean wake measurements in the symmetrical plane (Figure 5.3). It is worth mentioning that for $\underline{RR}$, the sizable clockwise recirculating structure and the negative $d\overline{Cp}/dz$ value remind the mean wake flow of two wheels configurations (Figure 4.12). However, the lift coefficients of the flat underbody configuration and two wheels configurations have completely opposite sign. In fact, it can be seen that for $\underline{RR}$, there is much decreased momentum in the underbody in this PIV plane. The streamlines leave the saddle point with a larger angle deflected towards the ground. At the end of the mean bubble at $x = L_r = 1.22$, the non zero velocity magnitude

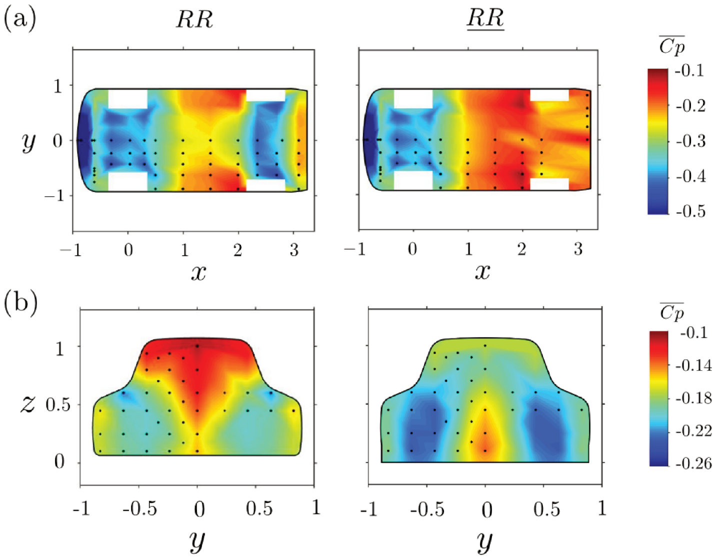

Figure 5.2: The underbody (a) and base (b) pressure distribution for RR and $\underline{RR}$.

is indicative of an important downward vertical velocity. Besides, the smaller counter clockwise vortex seen in this time averaged plot may simply be a feature of the averaging of the random shed structures of the instantaneous flow.

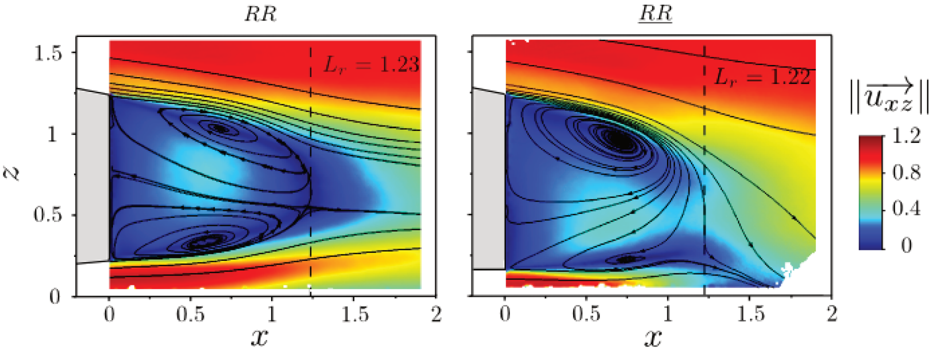

Figure 5.3: 2D streamlines overlaid on the contour maps of the time-averaged velocity magnitude, for RR and $\underline{RR}$, in the symmetrical PIV plane. L_r indicates the bubble length and is highlighted by the dashed line.

The numerical simulation of the configuration $\underline{RR}$ broadens the wake flow investigations. The time averaged streamlines depicted in Figure 5.4(a) reveal a pair of intense counter-rotating vortices in the vehicle near wake. These structures are reminiscent of those observed in the wake of an Ahmed body with a slant angle larger than 25° (Ahmed *et al.*, 1984), especially with rounded rear pillar (Fuller & Passmore, 2014; Rossitto *et al.*, 2016), and also in the wakes of real vehicles as sedan and fastback cars (Hucho & Sovran, 1993). Their formation is strongly associated with the higher underbody pressure (Figure 5.2(a)). The significant central downwash measured in Figure 5.3 is thus induced by the strong trailing vortices. The iso-contour of $\overline{Cp_{tot}} = 0$ in Figure 5.4(b) also highlights the recirculation region dominated by downwash and the two longitudinal structures developing at the two sides.

In addition, it is worth noting that the iso-contour demonstrates almost identical pattern at the front wheel when compared to RR (Figure 4.16(e)), illustrating that the underbody flow at the front region is scarcely impacted by the diffuser. It is consistent with their similar underbody pressure distribution at $x > 1$ reported in Figure 5.2(a). However, when compared to RR at the rear wheel, the outflow at the upper wheel arch creates a larger low total pressure region, while the lower wheel wake shrinks in size.

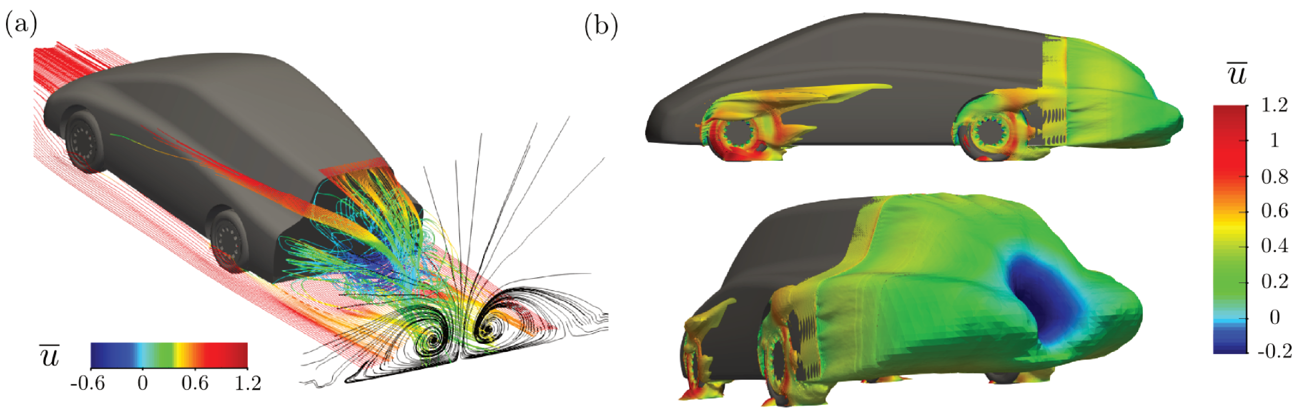

Figure 5.4: (a) Time averaged 3D streamlines around the vehicle for $\underline{\mathit{RR}}$; (b) Iso-contour of $\overline{Cp_{tot}} = 0$ ($\overline{Cp_{tot}} = \overline{Cp} + \boldsymbol{u}^2$), colored by time-averaged longitudinal velocity $\overline{u}$. The results are obtained from the numerical simulation.

In order to elaborate this local rear wheel wake modification, we display the 3D streamlines around the rear wheel in bottom view in Figure 5.5(a), obtained from the simulation. When compared to the streamlines in same view for RR (Figure 4.17(a)), the wheel wake and the outflow from the wheelhouse rear bottom is no longer deflected inward by the outside flow but rather parallel to the x-axis. This may be attributed to the larger low total pressure region at the upper rear wheel arch and the smaller wheel wake at the bottom of the rear wheel depicted in Figure 5.5(b), when compared to the rear wheel of the baseline configuration (Figure 4.16(e)). This wake development can also be seen from the horizontal plane (still at $z = 0.12$, but no more at the half of the ground clearance for the flat underbody geometry) extracted from the numerical results in Figure 5.5(b). When confronted to the PIV measurement at the same position in Figure 5.5(c), the numerical result appears to recover the main characteristic of the underbody flow. In addition, the velocity deficit downstream in the middle ($x > 1$) in Figure 5.5(c) can be related to the closure of the mean bubble and the onset of the large scale rotation.

Given these changes in vehicle wake topology and wheel wake development, we may interpret that the energetic downwash impinges the ground and separates the underbody flow apart from the middle. Thereupon, at the inner side of the rear wheels, the underbody flow tends to divert the wheel wake outwards, counteracting the outside flow prone to vector the wheel wake inwards. This emphasizes that the wheel wake development is indissociable from the vehicle wake evolution. While the latter highly depends on the vehicle geometry.

The profile of the streamwise velocity $\overline{u}$ at the exit of the underbody ($x = 0.05$) is depicted in Figure 5.5(d) together with that of RR. In spite of the noisy profile at this location for the flat underbody configuration, it can be noted that its maximum deficit is higher than that of RR. In order to evaluate the degree of local wheel-vehicle wake interaction as put forth in § 4.3, the spatial distribution of $\overline{u} - u'$ at $x = 0$ is reckoned from the numerical results for the two configurations, shown in Figure 5.6. There is no negative $\overline{u} - u'$ for $\underline{\mathit{RR}}$ at $x = 0$, indicating that at this section, more than 84% ($Pr\{u > \overline{u} - u'\}$ deduced from the normal distribution) of the velocity population has positive streamwise velocity values. In other words, the reversed flow accounts for very small proportion. Therefore we assume that the interaction of the rear wheel wakes with the vehicle wake is weakened for flat underbody configuration. More precisely, it is estimated that, the variation in base pressure (or drag) from the smooth vehicle configuration N to RR would exceed that from the smooth vehicle with flat underbody (denoted by $\underline{N}$, but not measured in this study) to $\underline{\mathit{RR}}$.

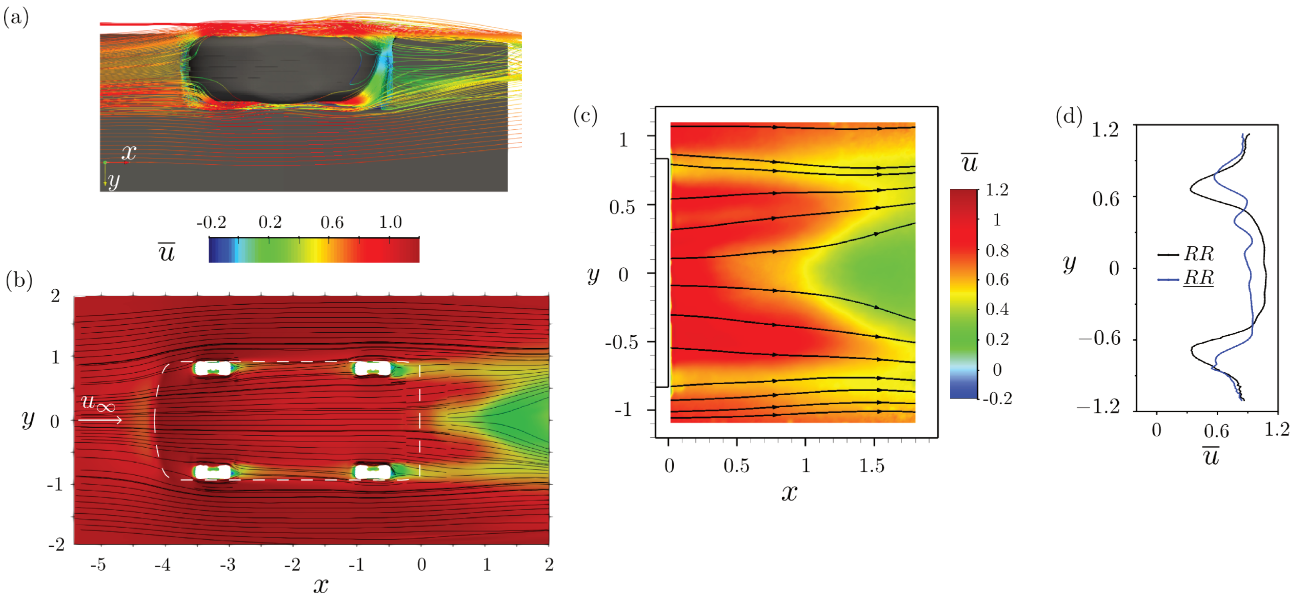

Figure 5.5: (a) Time-averaged 3D streamlines around the rear left wheel colored by $\overline{u}$, in bottom view, from the numerical results for $\underline{RR}$; (b) Numerical results of $\overline{u}$ distribution in the horizontal plane at $z = 0.12$, overlaid with 2D streamlines, for $\underline{RR}$; (c) PIV measurement of $\overline{u}$ distribution in the horizontal plane at $z = 0.12$, overlaid with 2D streamlines, for $\underline{RR}$; (d) Streamwise velocity profiles extracted from the horizontal PIV measurements at $x = 0.05$ for *RR* and $\underline{RR}$.

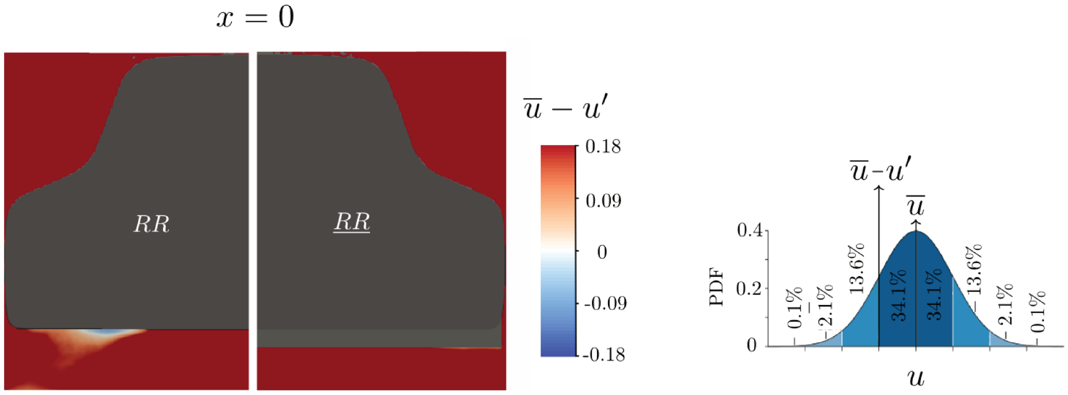

Figure 5.6: The distribution of $\overline{u} - u'$ at $x = 0$ extracted from the numerical results, for *RR* and $\underline{RR}$. At right, the PDF of the streamwise velocity is delineated assuming that at any spatial point the velocity follows a normal distribution with an average of $\overline{u}$ and a standard deviation of u'.

To further confirm the weakened interaction between the wheels and the vehicle owing to the geometry modification, the wheel state change will be considered. Table 5.2 compares the aerodynamic coefficients of four rotating and four stationary wheels configurations for both vehicle geometries, with and without diffuser. The stop of the wheel rotation results in a higher increase in drag (14.0%) and base suction (12.4%) for vehicle with diffuser, whereas it causes 11.2% of increase in drag and 6.9% in base suction for flat underbody geometry.

	$SCz(m^2)$	$SCx(m^2)$	$SCp_{\mathrm{U}}(m^2)$	$SCp_{\mathrm{B}}(m^2)$	dCp/dz
RR	0.020	0.393	-2.274	-0.234	0.065
SS	0.083	0.448	-2.256	-0.263	0.008
$\underline{RR}$	0.339	0.437	-1.937	-0.306	-0.074
$\underline{SS}$	0.291	0.486	-2.045	-0.327	-0.067

Table 5.2: Full scale lift and drag coefficients, integrated underbody and base pressure for *RR*, *SS*, $\underline{RR}$ and $\underline{SS}$.

Figure 5.7 provides the $\overline{Cp}$ distributions in the $y = 0$ plane for the 4 configurations. In the underbody, the curves for $\underline{SS}$ and $\underline{RR}$ are above those of *RR* and *SS*, which agrees well with their larger lift coefficient and integrated underbody pressure, indicating a much reduced underbody flow. In the base, a clear pressure drop is discernible at the upper part for configurations with flat underbody, which is indicative of the wake balance change compared to configurations with diffuser. Another interesting finding is that the curves for $\underline{RR}$ and $\underline{SS}$ are more or less superposed, contrary to *RR* and *SS*. This reminds of the nearly unaffected pressure at the vehicle symmetrical plane within smaller blockage rate range investigated in Section 3.2.3.

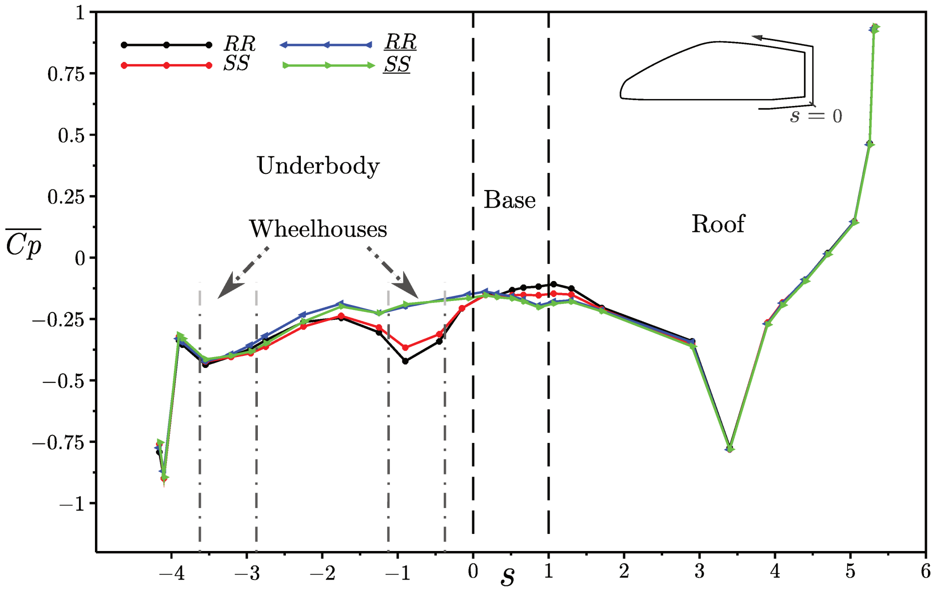

Figure 5.7: The distribution of $\overline{Cp}$ in the $y = 0$ plane on the curvilinear abscissa s (normalized by the height of the base) with the origin at the underbody rear end for *RR*, *SS*, $\underline{RR}$ and $\underline{SS}$.

To shed more light into the surface pressure variation, the pressure difference between configurations with stationary and rotating wheels is depicted in Figure 5.8 for both vehicle geometries. In the side body, the two groups exhibit similar variations. In the underbody, the deepened suction downstream front stationary wheels is both observed. While between the rear wheelhouses, the pressure augmentation is less significant for configuration without diffuser. Therefore the integrated underbody pressure is smaller for $\underline{SS}$ compared to $\underline{RR}$, which is not the case between *SS* and *RR*. At last, in the case of the flat underbody configurations, the stationary wheels decrease the base pressure level to a lesser extent. They decreases more locally the pressure downstream on the vehicle base, analogous to an enlargement of the profiled obstacles in the underbody at smaller blockage rates (Section 3.2.3). At the center, the pressure drop is more subtle, with a slightly increased vertical pressure gradient $d\overline{Cp}/dz$. The 6.9% of decrease in base pressure is comparable to an enlargement of the elliptical base cylinders from 10% to 20%, which leads to 8.0% of the base pressure drop.

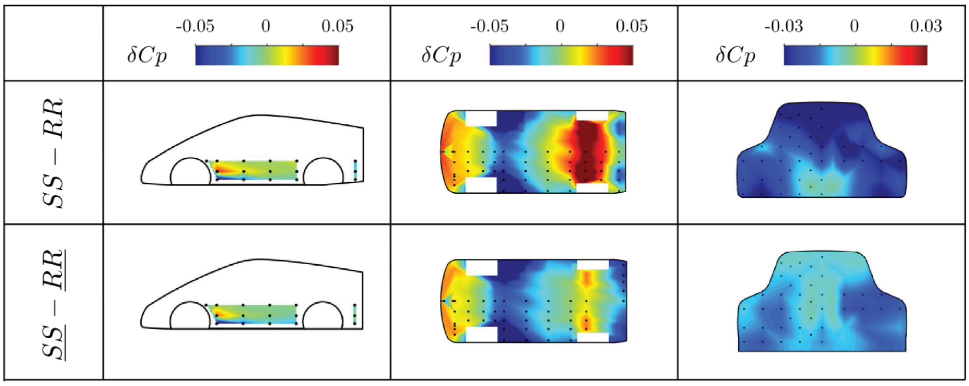

Figure 5.8: The surface pressure difference of configurations with different wheel states for the two vehicle geometries, with and without diffuser.

The PIV measurements of the streamwise velocity at $z = 0.12$ are presented in Figure 5.9(a). Overall, the stationary wheels create larger wakes than the rotating ones. Furthermore for the flat underbody cases, the wake width of the wheels is reduced relative to the wheels in the same state for vehicle with underbody diffuser. Although no simulation are launched for $\underline{SS}$, its velocity map in this horizontal plane, its base pressure difference compared to $\underline{RR}$, its similar wake topology (not shown here) in plane $y = 0$ to that of $\underline{RR}$ and its positive lift coefficient, all provide strong evidence of the intense counter-rotating vortice pair in the vehicle near wake. The wheel wakes are therefore limited by the diverged underbody flow at the inner side and the inward deflecting flow at the outer side. The distributions of $\overline{u} - u'$ in this plane (Figure 5.9(b)) corroborate the weakened interaction between the wheel and vehicle wakes from SS to $\underline{SS}$, as no negative $\overline{u} - u'$ can be detectable at the underbody exit for $\underline{SS}$, as opposed to SS.

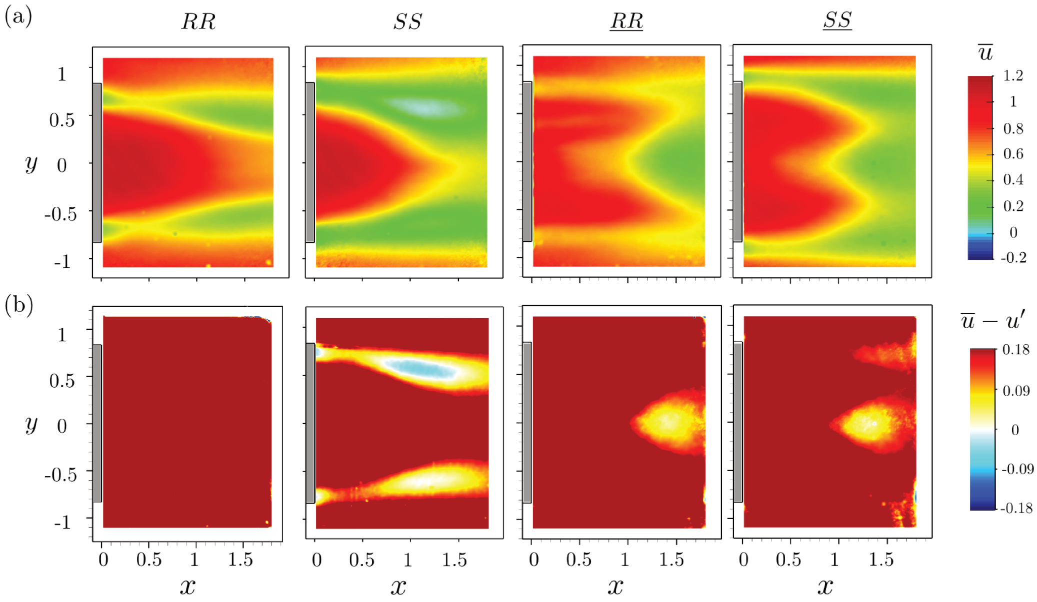

Figure 5.9: PIV measurement of $\overline{u}$ (a) and $\overline{u} - u'$ (b) distribution in the horizontal plane at $z = 0.12$, forRR, SS, $\underline{RR}$ and $\underline{SS}$.

Summary We demonstrated in this section that the wheel-vehicle interaction is closely related to the vehicle geometry. Although the inherent distinction in wake features is observable for different wheel states or different tires (see next section) regardless of the vehicle geometry, their impact on the vehicle drag and base pressure is not always the same.

The elimination of the diffuser reduces considerably the underbody flow momentum, leading to an important raise in lift coefficient. A significant top-bottom asymmetry thus exhibits in the vehicle wake, dominated by strong downwash, alongside with an intense trailing counter-rotating vortice pair. The divergent underbody flow is deemed to be highly associated with this global flow motion around the model. Consequently, rear wheel wakes are subject to the outward-deflecting underbody flow at the inner side, and the inward-deflecting freestream flow at the outer side, resulting a nearly streamwise development. The wake size is therefore limited. Contrary to configurations with underbody diffuser and with same wheel states, the proportion of the reversed flow in the wheel wakes at the exit of the underbody is considerably reduced. Therefore, the reduction of the base pressure by the wheels is limited.

In addition, for flat underbody configurations, from rotating to stationary, the surface pressure modification manifests like an enlargement of the underbody blockage within small blockage rate range established in Section 3.2.3, without modification of the mean wake organization. While for the baseline configuration, the underbody diffuser accentuates the underbody blockage effect by the stop of the wheel rotation. The local wheel-vehicle wake interaction is much more enhanced, and the mean wake balance is easily modified.

5.2 Effect of the tire

In this section, two other types of tires, apart from the tire with three longitudinal grooves, are considered, which are displayed in Figure 5.10. The first one is the reference tire used in all the preceding chapters and sections. The second one is on the basis of the first one, additionally having carborundum powder glued on the flank, aiming at representing tire sidewall marking. Configurations with this type of tire will be identified by a c subscript. The last one is referred to as a 'slick tire' without grooves, which is similar to a race car tire. A subscript with s stands for configurations with this smooth tread tire. All the three are reduced scale Michelin tires having realistic deflected shape of a 205/55 R16 tire. Their aerodynamic influence on the vehicle will been investigated with the experimental measurements.

Figure 5.10: Three types of tires investigated in the study. From left to right: the reference tire having three longitudinal grooves; the reference tire with additional carborundum powder glued on the flank; the slick tire.

5.2.1 Influence of the tire sidewall 'marking'

Comparisons among configurations with reference tire and the tire with glued carborundum powder are listed in the following for stationary (Table 5.3) and rotating (Table 5.4) situations.

	$SCz(m^2)$	δ/SCz	$SCx(m^2)$	δ/SCx	$SCp_{\mathrm{U}}(m^2)$	δ/SCp_{U}	$SCp_{\mathrm{B}}(m^2)$	δ/SCp_{B}
XS	-0.225	-	0.445	-	-2.662	-	-0.260	-
XS_c	0.002	-100.9%	0.492	10.6%	-2.430	-8.7%	-0.308	18.2%
SS	0.083	-	0.448	-	-2.256	-	-0.263	-
S_cS_c	0.132	59.0%	0.454	1.3%	-2.220	-1.6%	-0.273	3.8%
$\underline{SS}$	0.291	-	0.486	-	-2.045	-	-0.327	-
$\underline{S_cS_c}$	0.302	3.8%	0.484	-0.4%	-2.021	-1.2%	-0.338	3.4%

Table 5.3: Full scale lift and drag coefficients, integrated underbody and base pressure for stationary wheels with the reference tire and the tire with sidewall carborundum powder. The relative differences are equally given with respect to the reference tire configurations (XS, SS and $\underline{SS}$).

	$SCz(m^2)$	δ/SCz	$SCx(m^2)$	δ/SCx	$SCp_{\mathrm{U}}(m^2)$	δ/SCp_{U}	$SCp_{\mathrm{B}}(m^2)$	δ/SCp_{B}
XR	-0.379	-	0.390	-	-2.768	-	-0.232	-
XR_c	-0.320	-15.6%	0.394	1.0%	-2.700	-2.5%	- 0.248	6.8%
RR	0.020	-	0.393	-	-2.274	-	- 0.234	-
R_cR	-0.009	-145.0%	0.386	-1.8%	-	-	- 0.236	0.8%
RR_c	0.062	60.0%	0.394	0.3%	-2.243	-1.4%	- 0.236	0.8%
R_cR_c	0.079	295.0%	0.386	-1.8%	-2.244	-1.3%	- 0.237	1.3%
$\underline{RR}$	0.339	-	0.437	-	-1.937	-	-0.306	-
$\underline{R_cR_c}$	0.283	-16.5%	0.428	-2.1%	-1.955	0.9%	-0.308	0.7%

Table 5.4: Full scale lift and drag coefficients, integrated underbody and base pressure for rotating wheels with the reference tire and the tire with sidewall 'marking' (glued carborundum powder). The relative differences are equally given with respect to the reference tire configurations (XR, RR and $\underline{RR}$). For instance, the configuration RR_c stands for vehicle equipped with four rotating wheels, with reference tires in front and sidewall 'marking' tires at the rear.

From these measurements above, it is noted that the relative differences in lift coefficients often exhibit important values. It can be referred to the lift coefficients of the reference configurations being close to zero, or the reverse in sign of SCz between the counterparts. In addition, except for comparison between XS and XS_c, the relative differences of drag and base pressure seem to be much lower. In order to better visualize the small variations especially in the base, the surface pressure differences will be presented with respect to the reference configurations.

Figure 5.11 is comprised of the surface pressure difference for stationary wheels configurations. For two wheels configurations, the stationary wheels with sidewall markings eminently increase the underbody pressure (except immediately downstream the rear wheels) and the base suction, which is amount to an increase in the underbody blockage rate. In essence, for XS_c, the PIV measurements at the half of the ground clearance (Figure 5.12(a)) assume reversed flow in the wheel wakes, as opposed to XS. According to Section 3.2.4, the drastic drop of base pressure is thus an illustration of the strong interaction of the unclosed wheel wakes with the vehicle wake. It is worthwhile mentioning that the physical size of the glued carborundum powder is no larger than $2mm$, which at most increases the physical blockage rate from 24.6% of a reference wheel pair to 25.2%. The relative decrease in base pressure is 18.2% (Table 5.3) compared to the baseline configuration XS. It is practically comparable to an enlargement of the elliptical base cylinders from 25% to 35%, which leads to 20.1% of the base pressure drop. It is thus inferred that the glued carborundum powder on the wheel sidewall importantly enhances the intensity of the ground counter rotating vortex pair fed by the entrained side flow.

For four wheels configurations, in the vicinity of the front wheelhouses, the distributions

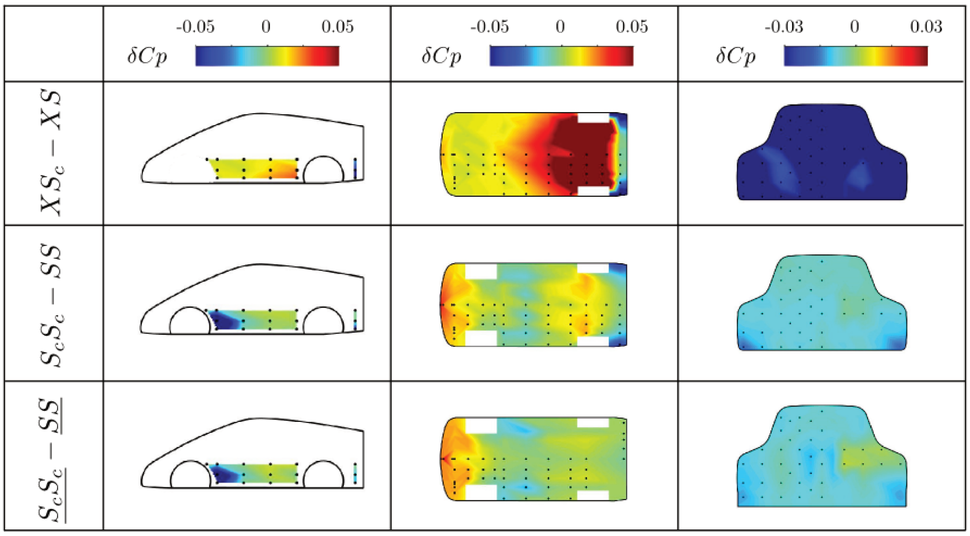

Figure 5.11: The surface pressure difference for stationary wheels configurations between reference tire and tire with glued carborundum powder on the sidewall.

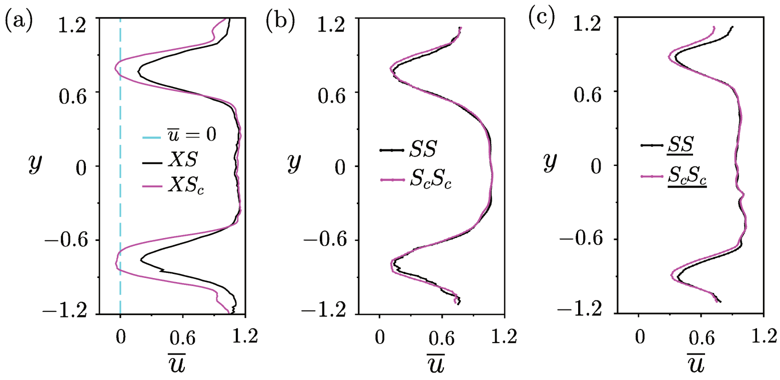

Figure 5.12: Profiles of the streamwise velocity $\overline{u}$ at the exit of the underbody ($x = 0.05$) extracted from the planar PIV measurements at half ground clearance, for XS and XS_c (a), SS and S_cS_c (b), $\underline{SS}$ and $\underline{S_cS_c}$ (c).

show similar variations which are independent of the presence or not of the diffuser. The underbody flow is slightly slowed down at the entry as a result of an increase in underbody blockage, evidenced by preceding comparison between XS and XS_c. However downstream the front wheels, the deepened suction in the underbody is subtle but more importantly on the vehicle flank. Supplementary pressure measurements in the wheelhouses are available for several four wheels configurations. As depicted in Figure 5.13, at the rear part inside the front wheelhouses, the front stationary wheel with side ‘marking’ tire decreases the pressure more importantly at the outboard side, while it leads to a small pressure recovery at the inner side (Figure 5.13(e), (f)). This is coherent with the greater pressure drop on the vehicle flank than in the underbody downstream the front wheelhouses. Based on the flow field around front stationary wheel from the numerical results (Section 4.3.1), it is conjectured that with the important yaw angle of the front wheel approaching flow, there is a more significant enhancement of the ground counter rotating vortex pair at the outer side.

Between the rear wheel pair, the increase of pressure by tires with sidewall ‘marking’ becomes less apparent, notably for configurations without diffuser. It can therefore be said that with the same variation in ‘blockage’ at identical streamwise position in the underbody, higher velocity of the on-coming flow yields higher pressure variation between the wheel pair. What is more, when compared to two wheels configurations, the maximum velocity deficit is lessened

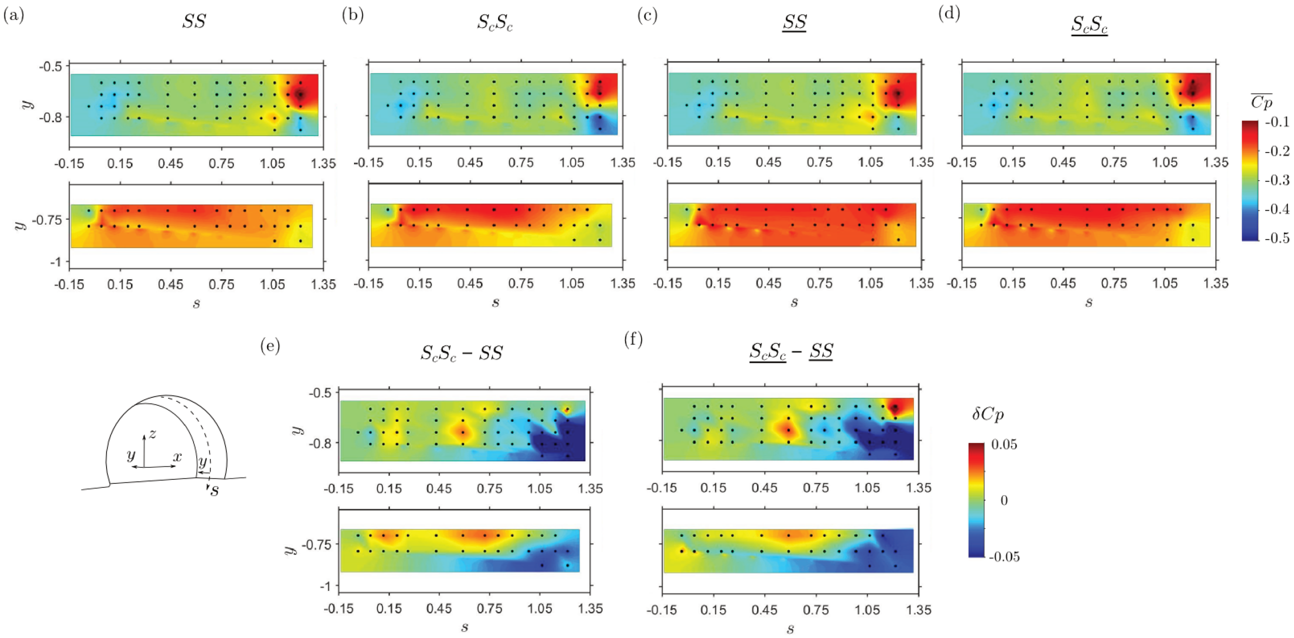

Figure 5.13: Pressure distribution inside the front and rear wheelhouses for SS (a), S_cS_c (b), $\underline{SS}$ (c) and $\underline{S_cS_c}$ (d). Wheelhouses pressure difference of $S_cS_c - SS$ (e) and $\underline{S_cS_c} - \underline{SS}$ (f).

for both tires, as can be observed in their velocity profiles at the exit of the underbody in the horizontal plane at the half of the ground clearance (Figure 5.12(b) and (c)). It is thus inferred that with diminished velocity of the rear wheel approaching flow due to the presence of the front wheels, the intensity of the ground counter rotating vortex pair fed by the downwash behind the rear tire tread and the entrained side flow is ultimately reduced. The mean recirculation wakes of the larger 'blockage' tire close more upstream than in two wheels configuration. No reversed flow is detectable in this plane. While the wheel wakes of rear S_c are slightly larger than those of rear S, thus leading to a base pressure drop to a much lesser extent. Inside the rear wheelhouses (Figure 5.13), a decrease in $\overline{Cp}$ is also discernible at the downstream part for wheels with sidewall 'marking' tires.

In Figure 5.14, comparisons are carried out for rotating wheels. For two wheels configurations, we also observed increased pressure at the rear part of the underbody (except locally behind the rear wheels) and decreased pressure on the base, which is consistent with the higher deficit in the wakes of the rotating wheels with sidewall 'marking' tire (Figure 5.15(a)). Still, when compared to XR, XR_c does not decrease the base pressure as much as a stationary wheel with reference tire (6.8% for XR_c compared to XR, as opposed to 12.0% for XS), suggesting that the impact of wheel state on the vehicle base pressure outweights that of the change in tire. In Figure 5.15(a), their streamwise velocity profiles at the exit of the underbody are extracted from the horizontal PIV plane. The velocity profile for XS is equally presented for comparison. The curves are not very symmetric with respect to $y = 0$. Nevertheless, it can still be perceived that the stationary wheels with reference tires have larger wakes and higher deficit than XR_c, which agrees with their base pressure levels.

The second line of Figure 5.14 involves configuration R_cR, which has front rotating wheels with sidewall 'marking' tires and rear rotating wheels with reference tires. Although no measurements are available for this configuration at the vehicle flank and in the underbody, the subtle base pressure difference with respect to RR confirms the secondary effect of the front wheel on the vehicle wake flow. The marginally decreased pressure at the bottom of the base centerline is reminiscent of the configuration SR. Concretely, the front rotating wheels with

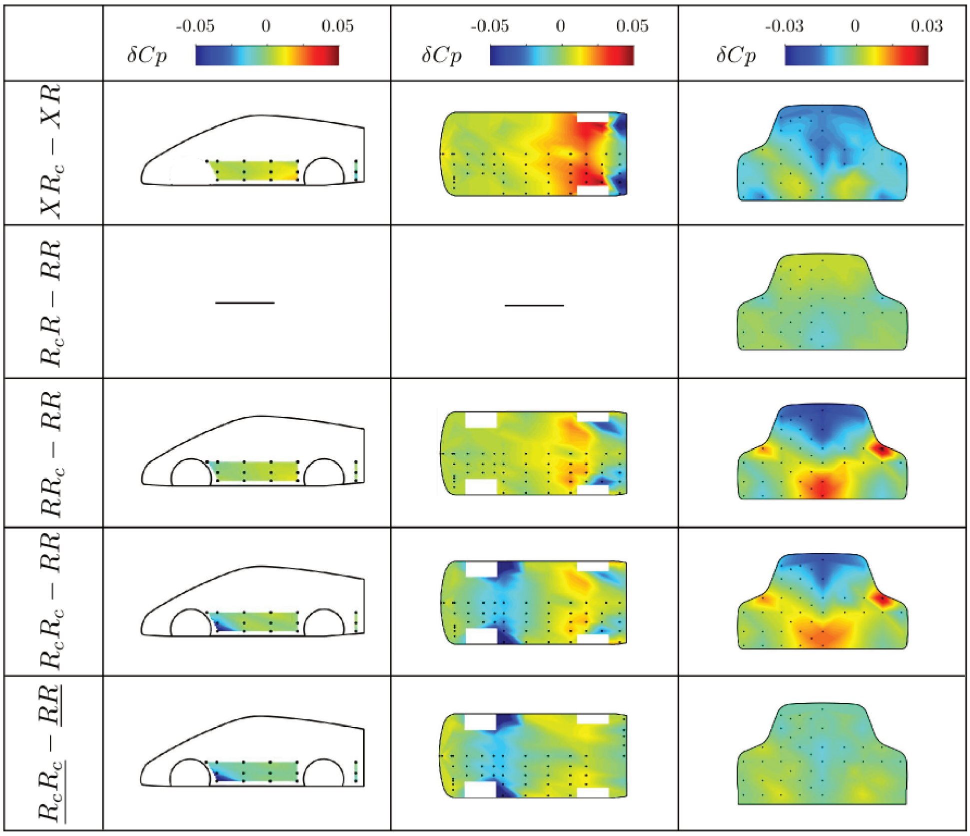

Figure 5.14: The surface pressure difference for rotating wheels configurations between reference tire and tire with glued carborundum powder on the sidewall.

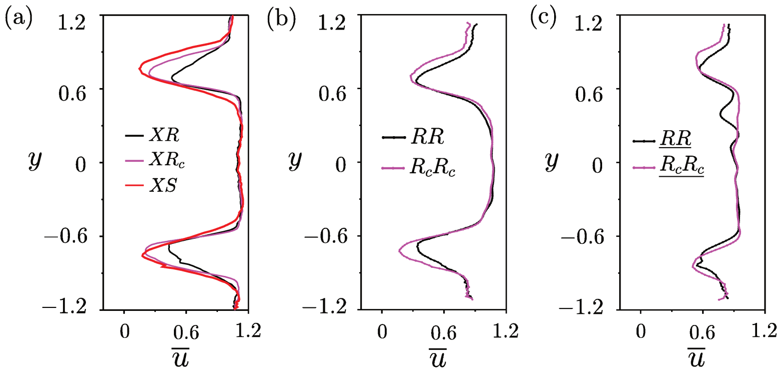

Figure 5.15: Profiles of the streamwise velocity $\overline{u}$ at the exit of the underbody ($x = 0.05$) extracted from the planar PIV measurements at half ground clearance, for XR, XR_c and XS(a), RR and R_cR_c (b), $\underline{RR}$ and $\underline{R_cR_c}$ (c).

sidewall 'making' tires increase mildly the vertical pressure gradient at the base centerline (from $dCp/dz_{RR} = 0.065$ to 0.077), yet less than that of SR ($dCp/dz_{SR} = 0.085$); and they decrease marginally the base pressure (0.8%), lower than that of SR, which decreases the base pressure by 2.1% (Table 4.5). The higher impact of the wheel state is once again justified.

Insight into the local influence of the front R_c can be gained from the comparison between RR and R_cR_c, and also between $\underline{RR}$ and $\underline{R_cR_c}$. It is noticed that the front R_c creates higher suction downstream the front wheelhouses, observable on the vehicle flank and in the underbody. This suction in the underbody has a negative contribution to the lift coefficient. Inside the front wheelhouses in Figure 5.16, the pressure at the rear part exhibits lower level for front R_c relative to front R, which tallies with the side body and underbody pressure distributions.

When applying sidewall 'marking' tire at the rear wheel (RR_c, R_cR_c and $\underline{R_cR_c}$), gradually

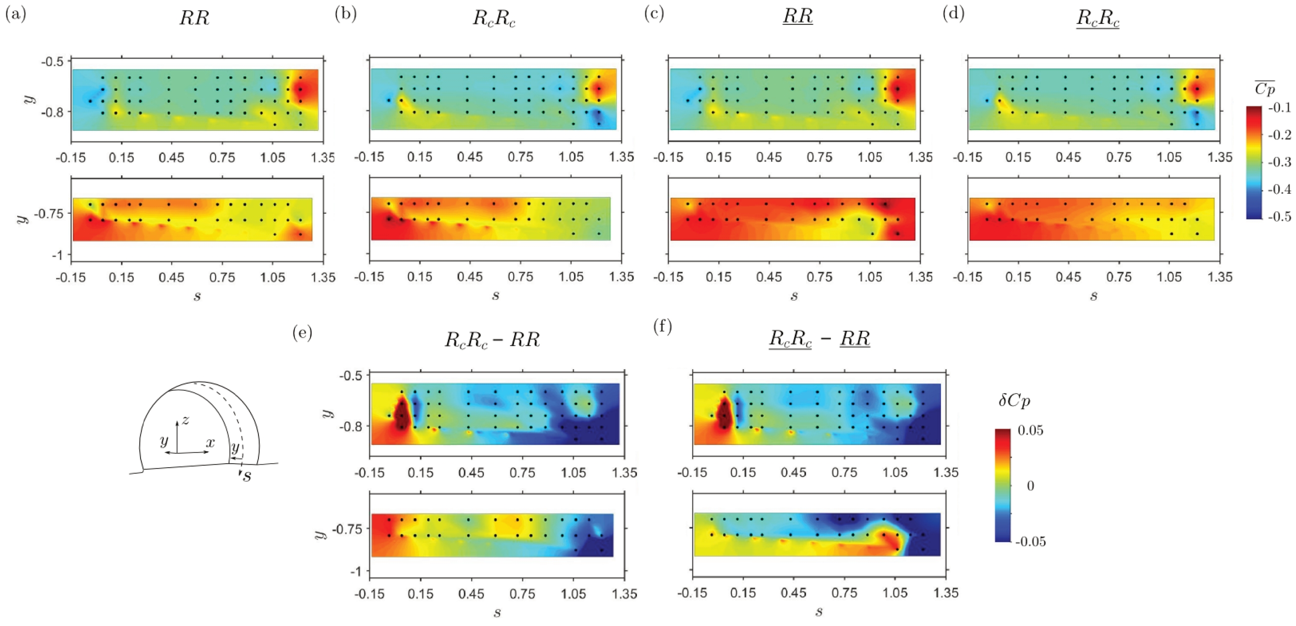

Figure 5.16: Pressure distribution inside the front and rear wheelhouses for RR (a), R_cR_c (b), $\underline{RR}$ (c) and $\underline{R_cR_c}$ (d). Wheelhouses pressure difference of $R_cR_c - RR$ (e) and $\underline{R_cR_c} - \underline{RR}$ (f).

reduced pressure raise is observed between the rear wheel pair, especially compared to two wheels configurations. This could also be attributed to the reduced velocity of the rear wheel approaching flow as mentioned previously for stationary wheels.

For vehicle with diffuser, the rear R_c markedly reduces the vertical pressure gradient on the base centerline. For RR_c and R_cR_c, their vertical pressure gradient are respectively $dCp/dz = -0.003$ and $dCp/dz = 0.005$. Correspondingly the wake wall-normal equilibrium in the symmetrical plane is modified, as reported in Figure 5.17. In spite of the nearly equal recirculation length, the upwash from the underbody appears to be weakened for RR_c and R_cR_c. The relative base pressure distributions of R_cR, RR_c and R_cR_c with respect to the baseline configuration RR emphasize the high dependence of the wake wall-normal equilibrium on the rear tire.

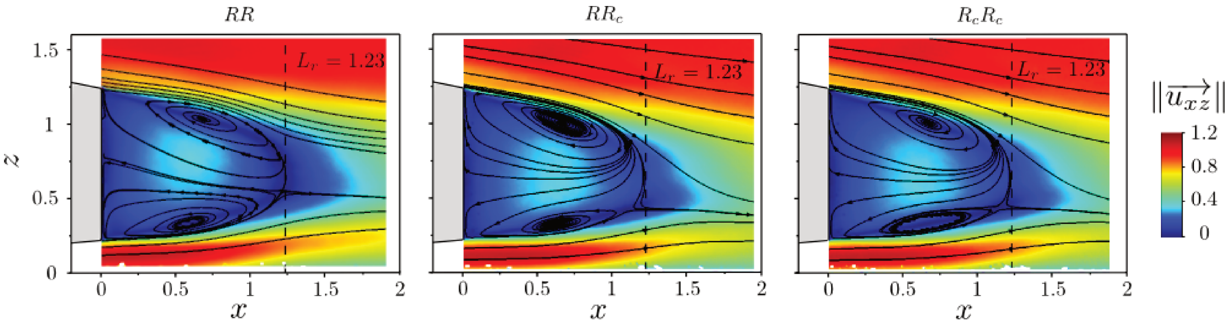

Figure 5.17: The PIV measurements of the velocity magnitude overlaid with 2D streamlines in the symmetrical plane of mean vehicle wake, for RR, RR_c and R_cR_c.

With regard to the reduced upwash by rear R_c, it is probably associated to their less inward convected wheel wakes, as will be elaborated below. In Figure 5.15(b), the profiles of the streamwise velocity at the exit of the underbody are shown for configuration RR and R_cR_c. For R_cR_c, the maximum deficit of the two wheel wakes is reached at more outward spanwise positions. Besides, in Figure 5.18(a) their vorticity $\overline{\omega_z}$ distributions in this horizontale PIV plane are given. An increased vorticity by the sidewall 'marking' can be observed. Additionally, the contours of maximum $|\overline{\omega_z}|$ along each shear layer are plotted in Figure 5.18(b) for the two configurations. The location of the maximum $|\overline{\omega_z}|$ in the shear layers of R_cR_c also provides evidence of a less convergent development of their wake flow. Furthermore, as shown in Figure 5.16(a), (b) and (e) inside the rear wheelhouses, a more important pressure drop is measured in the rear part at the outboard side for R_cR_c ($s \approx 1.22$, $y \approx -0.88$), indicating a smaller inward-pointing pressure gradient in the vicinity of the wheel's rear bottom. This may result in a less inward defection of the wheel wake.

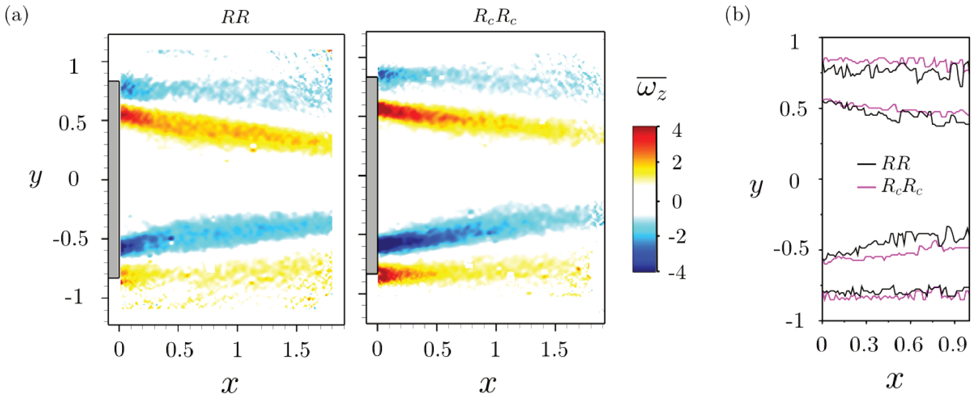

Figure 5.18: The planar PIV measurements at the half ground clearance for RR and R_cR_c: (a) Vorticity $\overline{\omega_z}$ distributions; (b) The contours of maximum vorticity magnitude along each shear layer.

For vehicle without diffuser, the rear R_c does not alter the vertical pressure gradient on the base centerline. This is ascribed to the predominance of the downwash in the vehicle wake of both configurations, as established in last section (Section 5.1) for vehicle model with flat underbody. The smaller reduction of SCp_{B} relative to configurations with underbody diffuser is also in good consistent with previous findings, where this unbalanced vehicle wake is subject to weakened wheel-vehicle wake interaction. It should also be mentioned that for the flat underbody configurations, the variation in drag and base pressure induced by the tire change (from $\underline{RR}$ to $\underline{R_cR_c}$) is about one order of magnitude smaller than the modification of wheel state (from $\underline{RR}$ to $\underline{SS}$ in last section).

It is worth noting that from $\underline{RR}$ to $\underline{R_cR_c}$ the drag variation does not consistent with the base pressure change (2.1% reduction in drag but 0.7% raise in base suction). The same is true for R_cR and R_cR_c. Meanwhile, local effect of side 'marking' tire inside the wheelhouses has been detected, which may also contribute to the drag variation. And it will be thoroughly investigated in Section 5.2.3.

5.2.2 Influence of the tire grooves

In the following, the wheel with slick tire will be analyzed. Apparently the slick tire will block completely the contact patch, contrary to the reference wheel with three longitudinal grooves on the tire tread, where the flow can pass through the grooves at the contact patch. The grooves in the 'full wet' tires used in motorsport today are known to displace 65 liters of water every second at top speed (PIRELLI, 2018). Thus in drier conditions, air will follow these paths and significantly change the flow field. Figure 5.19 gives the velocity magnitude distribution in two vertical sections for four rotating wheels configuration RR obtained from the numerical simulation, with one cutting through the longitudinal groove (indicated as y_1) and the other not (y_2). A local high speed region (inside the dashed red box) with velocity magnitude up to $\|\overrightarrow{u}\| \approx 0.6$ is identifiable immediately downstream the contact patch at y_1, which resembles a jet, but less eminent at y_2. The wheel wakes measured in the horizontal PIV plane will be presented at first to offer insight into the impact of this jet-like flow through the grooves. The wheel wake measurements in the horizontal plane are only available for two wheels configurations. Their streamwise velocity profiles at the exit of the underbody are extracted in Figure 5.20, from which it can be seen that the wheels with slick tires exhibit very slightly enlarged wakes in both stationary and rotating states.

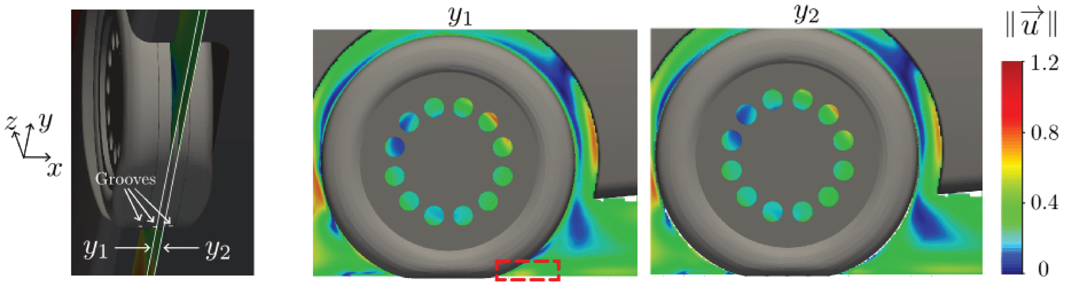

Figure 5.19: The velocity magnitude distribution in two vertical sections y_1 and y_2 for four rotating wheels configuration *RR* obtained from the numerical simulation. y_1 passes through the longitudinal groove and y_2 passes through a wheel section contacting with the ground.

According to research on steady or quasi-steady jet at the base of blunt body geometries (Roumeas *et al.*, 2009; Wassen *et al.*, 2010; Krentel *et al.*, 2010; Littlewood & Passmore, 2012; Barros *et al.*, 2016), when the jet blowing is directed toward the interior of the body wake, a *fluidic boat-tailing* effect can be achieved, ultimately results in base pressure raise and drag reduction. In our scenario, it is thus inferred that the flow passes through the grooves, acting as quasi-steady jets blowing into the wheel wake region. The wheel wake therefore shrinks slightly in size, even measurable at the spanwise direction. However in the simulation results for stationary wheels, this groove jet phenomenon is not observed. It is probably attributed to the ground boundary layer, estimated to be $14mm$ from the simulation, based on 99% of the free-stream velocity, at 1/2 diameter upstream the wheel center. This value is more than 4-fold than the groove size ($\sim 3mm$). Therefore, the mildly increased velocity deficit for stationary wheel with slick tire may related to other mechanisms, for example enhanced ground counter rotating vortex.

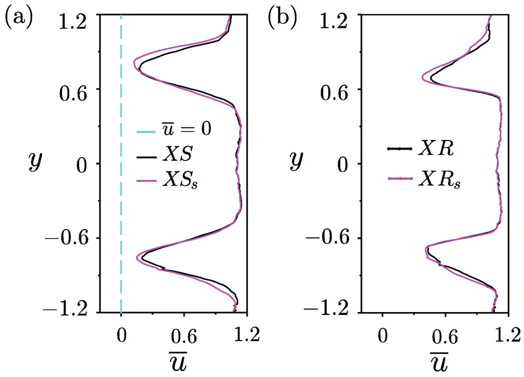

Figure 5.20: Profiles of the streamwise velocity $\overline{u}$ at the exit of the underbody ($x = 0.05$) extracted from the planar PIV measurements at half ground clearance, for XS and XS_s (a), XR and XR_s (b).

Given the changes in wheel wakes, one would expect marginally increased underbody blockage due to the slick tire. Thereupon the induced surface pressure modifications are depicted in Figure 5.21 and 5.22. The ensuing pressure raise between the wheel pair is duly observed. Even so, as opposed to sidewall 'marking' tire in the last section, here the pressure change due to the slick tire tread is more local, mainly surrounding the wheelhouses, and generally has smaller value. Another interesting finding is that for four wheels configuration, R_sR_s also diminishes the vertical pressure gradient at the base centerline, from $dCp/dz_{RR} = 0.065$ to

0.029, while it is nearly half of the reduction by R_cR_c. This is supported by the vehicle mean wake measurement in the symmetrical plane (Figure 5.23), where the reversed flow inside the mean bubble is titled slightly downwards relative to RR. Furthermore, as can be seen from the pressure difference distribution inside the rear wheelhouse (Figure 5.22), the reduced inward-pointing pressure gradient in the vicinity of the wheel's rear bottom seems to indicate a good agreement with the vehicle wake balance modification, as a moderately inward defection of the wheel wake is expected.

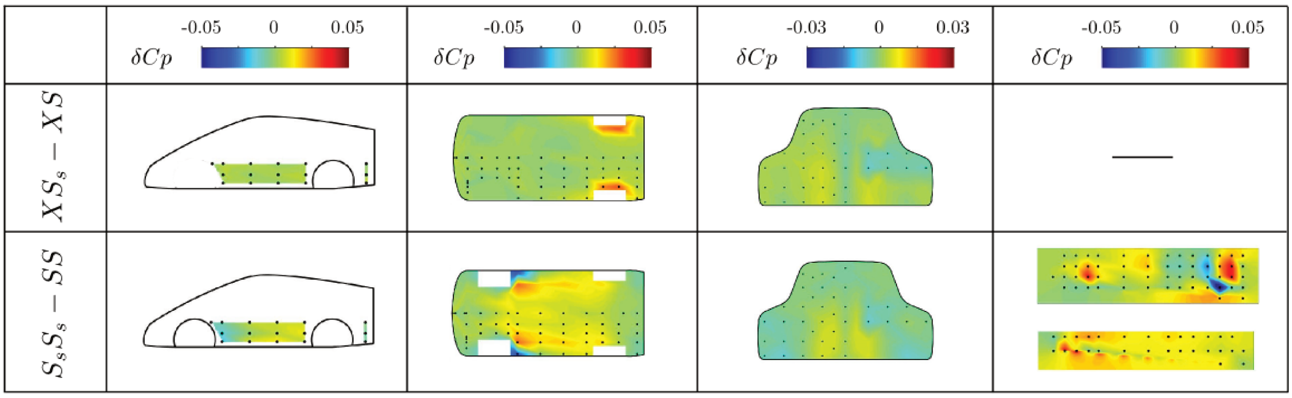

Figure 5.21: The surface pressure difference for stationary wheels configurations between reference tire and slick tire.

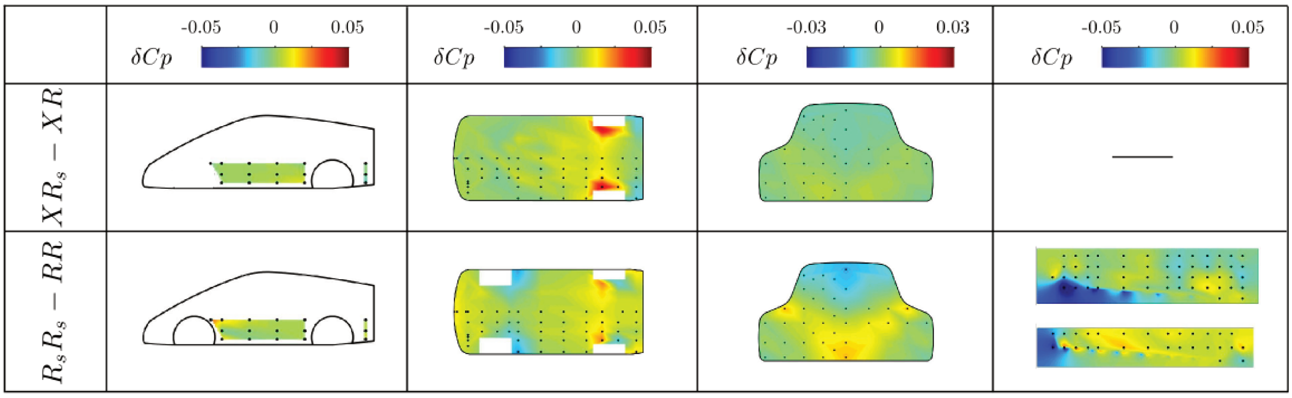

Figure 5.22: The surface pressure difference for rotating wheels configurations between reference tire and slick tire.

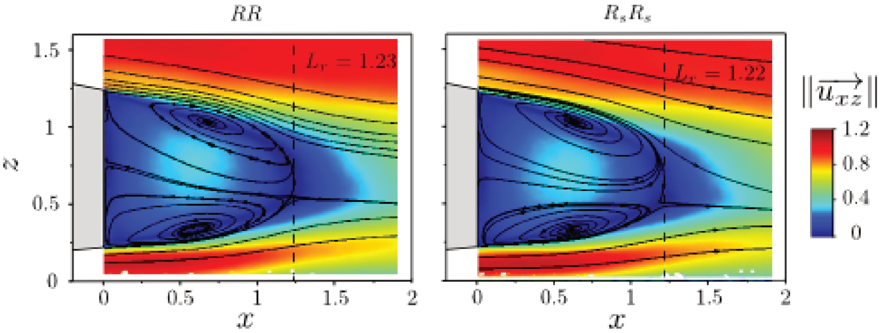

Figure 5.23: The PIV measurements of the velocity magnitude overlaid with 2D streamlines in the symmetrical plane of mean vehicle wake, for RR and R_sR_s.

Their aerodynamic lift and drag coefficients and integrated underbody and base pressure are reported for stationary (Table 5.5) and rotating states (Table 5.6). The aerodynamic coefficients display minor differences between the two types of tires, except for the lift coefficients of four wheels configurations, which are very close to zero.

	$SCz(m^2)$	δ/SCz	$SCx(m^2)$	δ/SCx	$SCp_{\mathrm{U}}(m^2)$	δ/SCp_{U}	$SCp_{\mathrm{B}}(m^2)$	δ/SCp_{B}
XS	-0.225	-	0.445	-	-2.662	-	-0.260	-
XS_s	-0.214	-4.9%	0.444	-0.2%	-2.647	-0.6%	-0.261	0.4%
SS	0.083	-	0.448	-	-2.256	-	-0.263	-
S_sS_s	0.103	24.1%	0.451	0.7%	-2.214	-1.9%	-0.266	1.1%

Table 5.5: Full scale lift and drag coefficients, integrated underbody and base pressure for stationary wheels with the reference tire and the slick tire. The relative differences are equally given with respect to the reference tire configurations (*XS* and *SS*).

	$SCz(m^2)$	δ/SCz	$SCx(m^2)$	δ/SCx	$SCp_{\mathrm{U}}(m^2)$	δ/SCp_{U}	$SCp_{\mathrm{B}}(m^2)$	δ/SCp_{B}
XR	-0.379	-	0.390	-	-2.768	-	-0.232	-
XR_s	-0.350	-7.7%	0.397	1.8%	-2.767	-0.04%	- 0.235	0.4%
RR	0.020	-	0.393	-	-2.274	-	- 0.234	-
R_sR_s	0.051	155.0%	0.399	1.5%	-2.247	-1.2%	- 0.233	-0.3%

Table 5.6: Full scale lift and drag coefficients, integrated underbody and base pressure for rotating wheels with the reference tire and the slick tire. The relative differences are equally given with respect to the reference tire configurations (*XR* and *RR*).

5.2.3 Wheelhouse contribution

Hitherto we have focused on the vehicle surface pressure variation and the associated mean wake modification related to another two different types of tires, the sidewall 'marking' tire and the slick tire. It is sufficient to remark that the relative difference of integrated base pressure is not always consistent with the change in drag coefficient. For instance, in Table 5.4, R_cR_c has a lower drag than RR (-1.8%) while subject to higher base suction (1.3%). On the flip side, in Table 5.6, R_sR_s has a higher drag than RR (1.5%) while with sightly higher base pressure (-0.3%). Meanwhile, we have also observed local effect of different tire inside the wheelhouses. For example, the front rotating wheel with sidewall 'marking' tire increases the pressure at the front region of the wheel arch while decreases the pressure at the rear part (Figure 5.16 (e)). A resultant pressure force of the front wheelhouse is thus reckoned to be an additional 'thrust' when compared to the baseline configuration. It counteracts the base suction, which seems to be in good consistent with the fact that R_cR_c has lower base pressure but smaller drag coefficient. Besides, the front rotating wheel with slick tire is likely to create higher wheelhouse drag as lower pressure is discernible at the front region of the wheel arch (Figure 5.22). Whereupon, it is worth taking into account the wheelhouses and assessing their contribution to the drag coefficient in addition to the base contribution. Theoretically, as the drag measurement covers only the vehicle not the wheels, the vehicle drag F_x can thus be written as:

$$F_x = F_f + F_v + F_{\mathrm{whh}} - F_{\mathrm{B}} \tag{5.1}$$

where F_f symbolizes the integrated frontal force, F_v stands for the viscous force, F_{whh} is the integrated pressure force of the four wheelhouses projected onto the x-axis, and F_B represents the force exerting on the base. Applying time-averaging we have:

$$\overline{F_x} = \overline{F_0} + \overline{F_{\mathrm{whh}}} - \overline{F_{\mathrm{B}}} \tag{5.2}$$

where we denote the sum of the mean frontal and frictional force by $\overline{F_0}$. Normalized by $\dfrac{1}{2}\rho V_0^2$ gives:

$$SCx = SCx_0 + SCp_{\mathrm{whh}} - SCp_{\mathrm{B}} \tag{5.3}$$

In each term the subscript of the surface S is omitted for the sake of brevity, while each S represents the corresponding integrated surface. If we posit that the frontal forces summed with frictional force is quasi-stationary, it can thus be said that the change in drag is correlated to 100% of the modification in base pressure plus wheelhouse pressure.

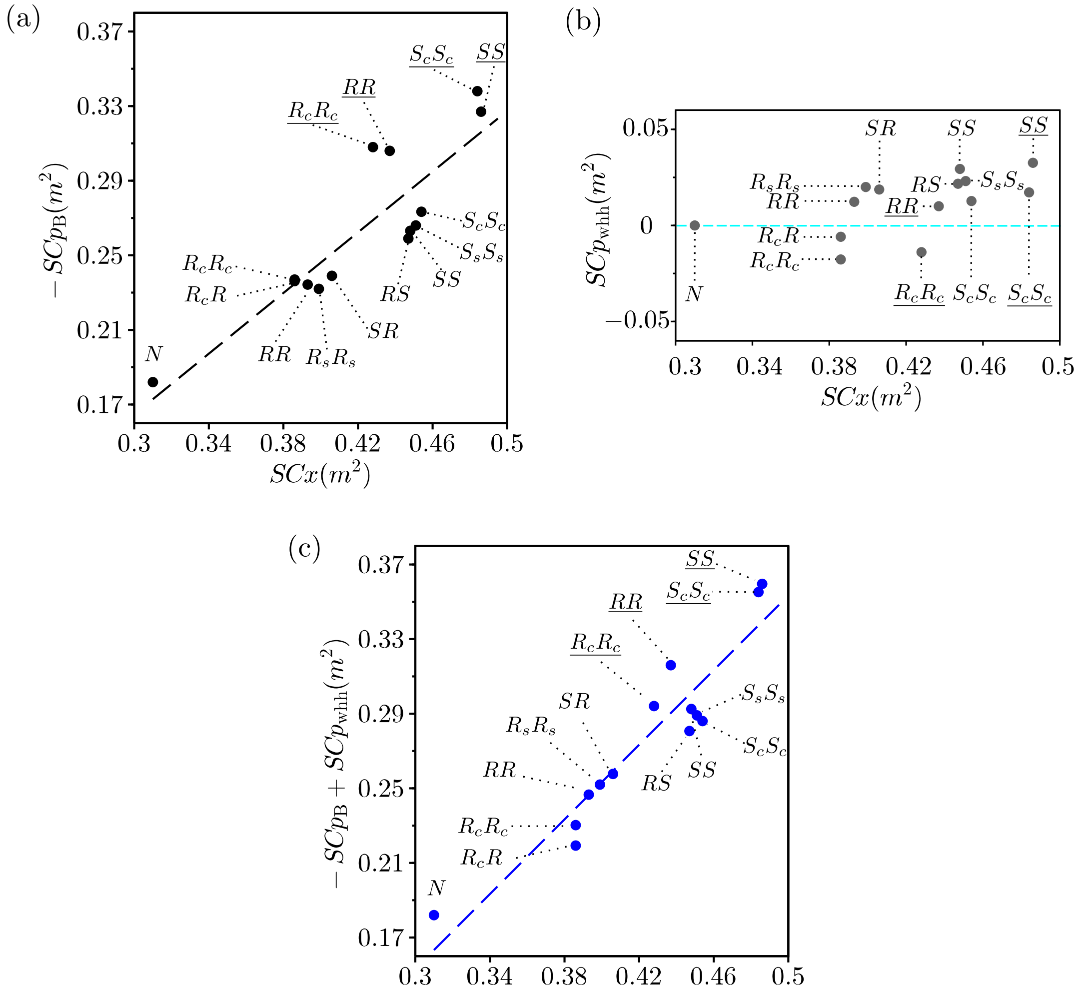

Figure 5.24: (a) SCx versus $-SCp_{\mathrm{B}}$, with fit function $-SCp_{\mathrm{B}} = 0.81SCx - 0.08$ ($R^2 = 0.77$) depicted in dash line; (b)SCx versus SCp_{whh}; (c) SCx versus sum of $-SCp_{\mathrm{B}}$ and SCp_{whh}, with fit function $-SCp_{\mathrm{B}} + SCp_{\mathrm{whh}} = 1.00SCx - 0.15$ ($R^2 = 0.89$) depicted in dash line; for all the configurations with measurements inside the wheelhouses and on the base.

To further confirm this point, the two terms $-SCp_{\mathrm{B}}$, SCp_{whh} and their sum will be plotted as a function of SCx in Figure 5.24 for all the configurations considered in this study with measurements in the wheelhouses and on the base. A good correlation between the drag and base pressure is demonstrated by Figure 5.24(a). The slope of 0.81 emphasizes a dominant contribution of the base surface to the vehicle drag. And overall the base pressure drives the variations of drag recorded for different combinations of the wheels and vehicle geometry, consistent to the recent studies of Littlewood & Passmore (2012), Grandemange *et al.* (2014), Perry *et al.* (2015) and Perry *et al.* (2016).

Figure 5.24(b) gives the wheelhouse drag as a function of SCx. The blue dash line indicates zero wheelhouse drag. Configuration N is the case as a consequence of the plugged wheelhouses. Below this line, the resultant pressure force of the wheelhouses can be viewed as a 'thrust'. The rotating wheel with sidewall 'marking' tire can provide this additional 'thrust', which mainly due to the higher pressure it creates at the front bottom surface of the wheel arch, and higher suction at the rear bottom surface of the wheel arch (Figure 5.16), when compared to RR whose wheelhouse drag is slightly positive.

On one hand, the coefficient of determination R^2 of the fit function ($SCx\ vs.\ -SCp_{\mathrm{B}}$) is 0.77, suggesting a certain incoherence as mentioned in the first paragraph of this section. On the other, no evident correlation can be found for $SCx\ vs.\ SCp_{\mathrm{whh}}$. However, when summing up the two terms, an excellent correlation is unfolded, with a slope of one and a higher coefficient of determination (0.89), which strongly corroborates Eq. 5.3. And the constant 0.15 in the fit function corresponds the contribution of the frontal and frictional force, which is constant at first order.

Summary In this section, the tire with sidewall 'marking' and the slick tire are investigated, in comparison with the reference tire. As opposed to wheel state change or vehicle geometry change, the aerodynamic coefficient measurements reveal a general smaller order of magnitude of the variations induced by the tire modification, especially for rotating states.

When compared to the reference cases, the stationary wheel with sidewall 'marking' seems to increase the underbody blockage rate by enhancing the ground counter rotating vortices downstream the wheels, therefore leading to higher lift and underbody pressure, higher drag and base suction. The stationary wheel with slick tire is likely to bring about similar modification while with smaller impact.

Applying sidewall 'marking' tires on the rear rotating wheels decreases the base centerline pressure gradient to zero. Correspondingly, in the vehicle wake the upwash from the underbody is reduced. While the front rotating wheel with sidewall 'marking' tire does not greatly influence the wake balance. These results demonstrate a high dependence of the wake wall-normal balance on the rear tire (when the vehicle is equipped with an underbody diffuser). The reduced upwash by these tires seems to be in accordance with the less inward defecting rear wheel wakes. The pressure measurements in the rear wheelhouse agrees well with this point, as it can be detected a decreased inward-pointing pressure gradient in the vicinity of the wheel's rear bottom. The increase of the wake size by this tire is still open issues. It can probably be related to the enhanced vorticity in the shear layers developing at the two sides of the wheel.

A reduction of the base centerline pressure gradient and an increase in wheel wake size is also observed for rotating wheel with slick tire, while with smaller amplitude than tire with sidewall 'marking'. The increase of wheel wake size is probably attributed to the completely blocked contact patch. Contrary to the reference wheel with three longitudinal grooves, there is a jet-like flow passing through the grooves and directed into the wheel wake region, evidenced by the numerical results, which may ultimately reduce the wake size.

At last, the wheelhouse contribution is investigated for all the measured configurations. The rotating wheel with sidewall 'marking' tire appears to bring about wheelhouse 'thrust', counteracting the base suction. The vehicle drag and the sum of base and wheelhouse drag follow a linear dependence. The slope of one indicates that the change in drag is correlated to approximately 100% of the modification in base pressure plus wheelhouse pressure. The affine function between base pressure and vehicle drag exhibits a slope of 0.81. Thus roughly speaking, the wheelhouse drag variation represents nearly 19% of the vehicle drag modification.

Chapter 6

Conclusions and perspectives

6.1 Concluding remarks

It has long been established in the literature that the aerodynamic characteristics of the wheels themselves, and in turn their interaction with the vehicle, are a crucial area of understanding for car manufactures. The well-balanced wake built into a basic vehicle body can be deteriorated by interaction with the four wheels in the underbody. On these grounds, the vehicle model that we employed throughout the study is a geometry having a balanced wake [1] including four rotating wheels with standard tires. Nonetheless, this wake balance can be easily modified by wheel state (Section 4.3) or tire modification (Section 5.2). By eliminating front wheels (Section 4.1), four wheels (Section 3.1), or underbody diffuser (Section 5.1), the underbody flow momentum is much increased or decreased. The vehicle wake develops into a non-balanced topology, whereas the wake organization seems more robust towards underbody perturbations. A general picture of the wake balance as a function of underbody flow momentum, quantified roughly by the base vertical pressure gradient and the integrated underbody pressure, is given in Figure 6.1.

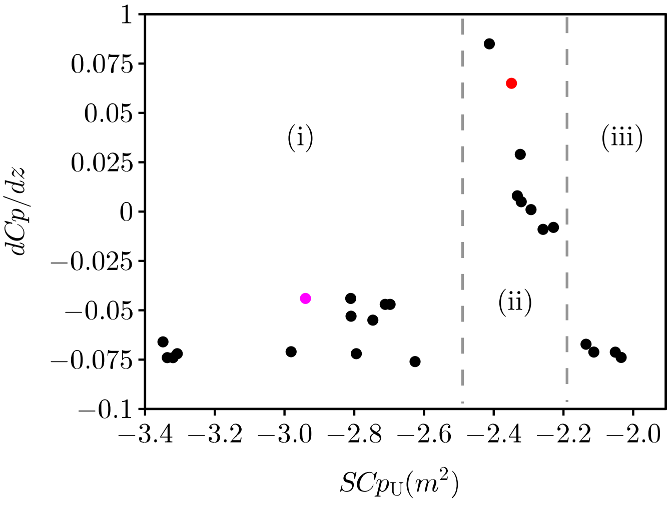

Figure 6.1: The integrated underbody pressure versus base vertical pressure gradient, for all the configurations measured in the experiment. The red and magenta points are respectively the baseline configuration with four rotating wheels and the smooth vehicle configuration with plugged wheelhouses.

- At important underbody flow momentum (i), it is when only two rear wheels or rear obstacles are mounted, or the case of the smooth vehicle model with plugged wheelhouses,

---

[1] in a viewpoint of turbulent kinetic energy in the upper and lower shear layers

the downwash from the roof prevails the upwash from the underbody. The measured base vertical pressure gradient is around -0.075 to -0.04.
- At moderate underbody flow momentum (ii), it is when four wheels are employed. The mean wake balance is very sensitive to the state of the wheel and type of the tire, and the base vertical pressure gradient varies from -0.008 to 0.085. The well-balanced configuration has a vertical pressure gradient of 0.065, with important upwash from the underbody.
- At even lower underbody flow momentum (iii), it is when the diffuser is eliminated with four wheels configurations, the downwash dominates the vehicle wake. The base vertical pressure gradient is around -0.075.

The vehicle model originates from ASMO model (Section 2.1.2) and has been optimized with reference four rotating wheels. Whereas intrinsically the smooth model has a reversed wall-normal wake balance (base vertical pressure gradient being -0.044) compared to the baseline configuration, due to its larger roof angle (10°) and the smaller diffuser angle (5°). This emphasizes the importance of optimizing the model's rear geometry (spoiler and diffuser angle) with four rotating wheels. In addition, the wake balance inversion is believed to be the result of the modified underbody flow momentum, coupled with the diffuser (see Section 4.2). While eliminating the diffuser, the vehicle wake is once again subject to important downwash from the roof.

The non-balanced while robust wake organization allows us to investigate more easily the local perturbations, which leads to one of the fundamental results of this work: the identification of two flow regimes depending on the streamwise development of the underbody obstacle wakes (Section 3.2).

The experimental investigation of underbody blockage controlled by obstacle pair at the rear underbody of the vehicle model shows similar vehicle wake organizations, dominated by upper larger clockwise recirculating structure in the mean wake. While with increasing obstacle size, a shortening of the mean recirculation bubble is evidenced. Furthermore, two regimes depending on the obstacle size, can be identified:
- At small blockage (obstacles of small width), only local effects are observed. Downstream of the obstacles, their local pressure imprint on the vehicle base decreases with the increasing width. While the pressure on the symmetrical plane of the vehicle remains unaffected.
- At large blockage range (obstacles of large width), the enlarging size leads to a more global modification, manifested by the pressure augmentation at the rear underbody and an increasing suction on the entire base.

The experiment using fixed obstacle size with varying streamwise position in the rear underbody of a Windsor-type model, also brings to evidence two regimes, in terms of lift and drag coefficients [2]. The two regimes of 'small' and 'large' blockage rates in the previous experiment, can be analogously referred to as 'far away from' and 'close to' the model base in this experiment (Figure 3.27 and 3.28).

Generally speaking, with the increase in obstacle size or the approach of the obstacles towards the base, both the base suction (or drag) and underbody pressure (or lift) increases. At the first regime, the closure of the obstacle wake is upstream the end of the underbody, in a mean point of view. While in the second regime, with the 'merging' of the 'unclosed' obstacle wake with the vehicle wake, the sensibility of the global aerodynamic coefficients towards the size of the obstacles or the distance of the obstacles to the base, are significantly increased.

---

[2] Their surface pressure and mean wakes were not measured but does not affect the following conclusion.

Given the different approach in the two experiments with independent measurements (pressure and force), the result is thus believed to be universal.

Such phenomenon can also be applied to more complex situations, from replacing the rear obstacle pair by rear wheels to vehicle model including four wheels, with different vehicle shapes. The stop of the rear wheel rotation, in Section 4.1 (two rear wheels configurations), Section 4.3 (four wheels configurations) and Section 5.1 (vehicle without diffuser, four wheels configurations), all amount to an increase in underbody blockage, in terms of global aerodynamic coefficients, at first order. The change in tire, with carborundum powder glued on the flank or the use of a slick tire, can also be interpreted as increase in underbody blockage, typically with small amplitude, compared to the reference tire with three longitudinal grooves (Section 5.2). The configuration with two rear wheels equipped with carborundum powder glued on the tire flank in stationary state appears to be the only one that can be classified into the second regime, as only in its horizontal PIV plane at the half of the ground clearance, reversed flow is measured.

At this stage, it is important to note that, setting 'non-closed' obstacle/wheel wakes at the end of the underbody as the criteria to separate the second regime from the first might be lack of precision, as their wakes may not be homogeneous in the vertical direction, and in the experiment only the horizontal plane at the half of the ground clearance is measured. The mechanisms responsible for the 'separation' of the two regimes due to the 'merging' of the underbody obstacle/wheel wakes with the vehicle wake also remain to be further explored.

The experiments investigating the modifications around the well-balanced wake configuration, *i.e.* the baseline configuration including four rotating wheels with standard tires, demonstrate that, depending on whether at front or rear axle the wheel rotation is inhibited, either local or global effect of the wheel is highlighted (Section 4.3).

The front stationary wheels create larger wake and lower pressure in their wakes, compared to front rotating wheels. Thus they primarily contribute to a lower lift coefficient owing to the lower pressure imprint on the underbody. However, the front wheel state has little influence on the wake topology and therefore on the base pressure, as well as on the drag. We believe that this finding is important as the variation of the global lift of the vehicle can be attributed to very different effects: on the one hand, the local pressure imprint by the wheel wakes; on the other hand, the global variation of underbody flow momentum. Typically, the stationary rear wheels mainly decrease the underbody flow momentum, compared to rotating rear wheels, owing to the blockage effect coupled with the vehicle diffuser. They importantly increase the underbody pressure at the entrance of and in the diffuser, therefore leading to higher lift coefficient. The upwash from the underbody is reduced. The mean reciruclation bubble of the vehicle is thus diverted more towards the ground (Figure 4.34), with a shortened length and enhanced turbulent kinetic energy in the lower shear layer (Figure 4.36).

In parallel, changing the tire at either front or rear wheels compared to the baseline configuration, also suggests higher impact of the rear tire on the wake-balance. Furthermore, the tire with side wall carborundum powder can bring about higher modification in terms of surface pressure distribution than the slick tire. However, it is found that the blockage effect of the rear rotating wheel with side wall carborundum powder is still smaller than stop of the rear wheel rotation, as visible in Figure 5.8 and 5.14. Whereas the two modifications increase the wake wall-normal asymmetry to almost the same level. Other mechanism apart from the underbody blockage effect, responsible for the wall balance modification, is proposed according to the pressure measurements inside the rear wheelhouses in Figure 5.16. The reduced inward-pointing pressure gradient in the vicinity of the wheel's rear bottom, which is a local effect of the tire, might be linked to the less inward deflection of the rear wheel wakes, and the reduced upwash from the underbody. The increase in the turbulent activity in the shear layers of the wheels with side wall carborundum powder is also likely to modify the wake balance, and needs to be further investigated. Nevertheless, this observation points out again the sensitivity of the well-balanced wake towards underbody perturbations.

To summarize our findings, the wheel-vehicle aerodynamic interactions can be split into three distinct but interrelated aspects:

- local effect: in the near wakes of the wheels is low pressure region. The wakes of front and rear wheels can impact the underbody pressure. The near wakes of the rear wheels can interact with the vehicle wake, and impact the base pressure. Particularly, the merging of non-closed mean wakes of the rear wheels with the vehicle wake gives rise to strong penalty in drag. This has a first order effect on aerodynamic forces.
- global effect: depending on the presence of the wheels, wheels states, or types of the tires, the underbody flow momentum can be modified. Front wheels have, of course, a major influence on the underbody flow momentum. While as far as the rear wheels are concerned, this effect is particularly emphasized if the vehicle has a underbody diffuser. This also has a first order effect on aerodynamic forces.
- wake balance effect: for a given geometry of the rear part of the vehicle (angle of the roof, of the diffuser), a modification of the underbody flow momentum and orientation or of the turbulent states of the separating shear layers, can modify the mean wake balance of the vehicle. Therefore, the base pressure distribution can be modified, which has a second order effect on aerodynamic forces. The minimum base drag is obtained in the present case for a positive vertical pressure gradient in the base centerline.

6.2 Perspectives

In the scope of this work, we made use of a vehicle model that was designed and manufactured prior to the current research. The three dimensional complexity of its wake flow has been highlighted in Section 3.1. Moreover, Chapter 4 and 5 have shed light on the significant impact of the vehicle's underbody diffuser. Thus, further work is recommended to investigate the generality of the wheel-vehicle interactions with other vehicle geometries, or applying movable rear flaps to set different flow separation angles at the vehicle's trailing edge.

In terms of the drag reduction strategies, the existence of the two regimes controlled by obstacle pair at the rear underbody is of crucial interest, which provides some guidelines to improve vehicle drag. Considering the two regimes depicted in Figure 3.28(b), it is thus preferable to keep a distance of larger than 1.5 times of the rear wheel width between the vehicle base and the end of the wheel, to mitigate the drag penalty. It could be done by mounting the rear axle more upstream [3] or using thinner wheels, meanwhile ensuring not much deterioration of other performance as security and stability. The use of thinner wheels should also take into account the relatively increased wheelhouse volume, which might in turn increase the vehicle drag (Regert & Lajos, 2007; Fabijanic, 1996; Thivolle-Cazat & Gilliéron, 2006). Experimentally, it could be interesting to extend the rear obstacle parametric study with obstacle pair or wheels at the front axle.

Additionally, in the last section of this work (Section 5.2.3), the wheelhouse contribution to the vehicle drag was brought to light. For the rotating wheel with sidewall carborundum powder tire, the small increase of the base drag is compensated by the decrease of wheelhouse

---

[3] this might not be easily applied in reality, as the wheelbase and other geometry parameters are highly constrained by the vehicle's functional aspects

drag, ultimately leads to lower vehicle drag. The increase of base drag is related to the slight deterioration of the mean wake balance. While the decrease of the wheelhouse drag arises from the local suction created at the rear bottom surface of the wheel arch. A drag reduction strategy will be taking advantage of the wheelhouse drag reduction by these tires, meanwhile applying movable flaps, synthetic jets or other control devices to improve the vehicle wake balance.

Eventually, the focus of this work concentrates on the time-averaged flow field. It is suggested to extend the understanding of the wheel-vehicle interaction from an unsteady flow scope. The work of Bonitz *et al.* (2018) reported coherent structures emanating from the top of the front wheel arch, at the wheel rotating frequency. Although the rear wheelhouse was not the concern of their work, it is believed that similar dynamics could be observed at the rear wheel arch. Indeed, in our work, outflow from the top of the rear arch and their downstream convection were captured by the numerical results (Figure 4.26). Our work mainly reveals the primary impact of the rear wheels/wheelhouses, in particular their wakes convecting in the underbody and interacting with the vehicle wake downstream. It can thus be anticipated that the structures created from the upper part of the rear wheelhouses, at the side-body, would also modify the vehicle wake. Assuming that these coherent structures propagate downstream until the trailing edge, a Strouhal number based on the rotating frequency (dominant frequency of the coherent structures evidenced by Bonitz *et al.* (2018)), the width of the base, and the freestream velocity gives $St \approx 0.5$. According to the research on periodic forcing at the rear Ahmed body by Barros *et al.* (2016); Li (2017), such low frequency structures might enhance the shear layer turbulence from the side wall separation, therefore contribute to base pressure drag. While with the parametric study using underbody obstacles beneath smooth vehicle model, this contribution can not be evaluated [4].

In parallel, other dominant peaks were detected in the frequency spectrum behind the rotating wheels. For instance, the experimental measurements and RANS simulations in Croner (2014) reported flow structures emanating from the rear wheelhouse cavity at the second harmonic of the rotating frequency. Heyder-Bruckner (2011) pointed out a vortex shedding of $300Hz$ at the lower wake of an isolated rotating wheel using DES. It would be of value to investigate the impact of these multi-frequency structures created at the rear wheel/wheelhouse on the vehicle wake development.

---

[4] This might also account for the higher base drag of the configuration with two rear rotating wheels than that with obstacle pair of similar physical blockage rate (Section 4.1.3).

References

Afzal, Noor 1996 Wake layer in a turbulent boundary layer with pressure gradient- a new approach. In *IUTAM Symposium on Asymptotic Methods for Turbulent Shear Flows at High Reynolds Numbers, Bochum, Germany*, pp. 95–118.

Ahmed, S. R., Ramn, G. & Faltin, G. 1984 Some salient features of the time averaged ground vehicle wake. *SAE Tech. Report. No. 840300. Society of Automotive Engineers. Inc.. Warrendale. PA* .

Aljure, DE, Lehmkuhl, O, Rodriguez, I & Oliva, A 2014 Flow and turbulent structures around simplified car models. *Computers & Fluids* **96**, 122–135.

Avadiar, T, Thompson, MC, Sheridan, J & Burton, D 2018 Characterisation of the wake of the drivaer estate vehicle. *Journal of Wind Engineering and Industrial Aerodynamics* **177**, 242–259.

Axerio, John & Iaccarino, Gianluca 2009 Asymmetries in the wake structure of a formula 1 tire. In *TSFP DIGITAL LIBRARY ONLINE*. Begel House Inc.

Balachandar, S, Mittal, R & Najjar, FM 1997 Properties of the mean recirculation region in the wakes of two-dimensional bluff bodies. *Journal of Fluid Mechanics* **351**, 167–199.

Barros, D. 2015 Wake and drag manipulation of a bluff body using fluidic forcing. PhD thesis, École Nationale Supérieure de Mécanique et d'Aérotechnique, Poitiers, France.

Barros, Diogo, Borée, Jacques, Cadot, Olivier, Spohn, Andreas & Noack, Bernd R 2017 Forcing symmetry exchanges and flow reversals in turbulent wakes. *Journal of Fluid Mechanics* **829**.

Barros, Diogo, Borée, Jacques, Noack, Bernd R, Spohn, Andreas & Ruiz, Tony 2016 Bluff body drag manipulation using pulsed jets and coanda effect. *Journal of Fluid Mechanics* **805**, 422–459.

Bastian, Schnepf, Gregor, Tesch & Thomas, Indinger 2015 On the influence of ride height changes on the aerodynamic performance of wheel designs. *International Journal of Automotive Engineering* **6** (1), 23–29.

Berg, Henrik & Brandt, Adam 2018 Investigation of aerodynamic wheel design. PhD thesis, Master's thesis, Chalmers University of Technology.

Bonitz, Sabine, Larsson, Lars & Sebben, Simone 2018 Unsteady pressure analysis of the near wall flow downstream of the front wheel of a passenger car under yaw conditions. *International Journal of Heat and Fluid Flow* **73**, 188–198.

CASTELAIN, THOMAS, MICHARD, MARC, SZMIGIEL, MATHIEU, CHACATON, DAMIEN & JUVÉ, DANIEL 2018 Identification of flow classes in the wake of a simplified truck model depending on the underbody velocity. *Journal of Wind Engineering and Industrial Aerodynamics* **175**, 352–363.

CHEN, HUDONG, CHEN, SHIYI & MATTHAEUS, WILLIAM H 1992 Recovery of the navier-stokes equations using a lattice-gas boltzmann method. *Physical Review A* **45** (8), R5339.

CHEN, HUDONG, TEIXEIRA, CHRIS & MOLVIG, KIM 1997 Digital physics approach to computational fluid dynamics: some basic theoretical features. *International Journal of Modern Physics C* **8** (04), 675–684.

CHEN, SHIYI, CHEN, HUDONG, MARTNEZ, DANIEL & MATTHAEUS, WILLIAM 1991 Lattice boltzmann model for simulation of magnetohydrodynamics. *Physical Review Letters* **67** (27), 3776.

CHEN, SHIYI & DOOLEN, GARY D 1998 Lattice boltzmann method for fluid flows. *Annual review of fluid mechanics* **30** (1), 329–364.

CHIKATAMARLA, SHYAM S 2008 Hierarchy of lattice boltzmann models for fluid mechanics. PhD thesis, ETH Zurich.

COOPER, KEVIN R, BERTENYI, TAMAS, DUTIL, GENEVIEVE, SYMS, J & SOVRAN, G 1998 The aerodynamic performance of automotive underbody diffusers. *Tech. Rep.*. SAE Technical Paper.

COOPER, KEVIN R, SYMS, J & SOVRAN, G 2000 Selecting automotive diffusers to maximise underbody downforce. *Tech. Rep.*. SAE Technical Paper.

CRONER, EMMA 2014 Etude de l'écoulement autour des ensembles roulants d'un véhicule en vue de l'optimisation aérodynamique du pneumatique. PhD thesis, ISAE Institut Supérieur de l'Aéronautique et de l'Espace.

DIASINOS, SAMMY, BARBER, TRACIE J & DOIG, GRAHAM 2015 The effects of simplifications on isolated wheel aerodynamics. *Journal of Wind Engineering and Industrial Aerodynamics* **146**, 90–101.

ELENA, LAURENT 2001 Aérodynamique automobile. *Mécanique & industries* **2** (3), 199–210.

ELOFSSON, PER & BANNISTER, MARK 2002 Drag reduction mechanisms due to moving ground and wheel rotation in passenger cars. *Tech. Rep.*. SAE Technical Paper.

EU, LEGISTATION 2018 Reducing car emissions: new CO2 targets for cars explained. `http://www.europarl.europa.eu/news/en/headlines/society/20180920STO14027/reducing-car-emissions-new-co2-targets-for-cars-explained/`.

FABIJANIC, JOHN 1996 An experimental investigation of wheel-well flows. *Tech. Rep.*. SAE Technical Paper.

FACKRELL, JE & HARVEY, JK 1975 The aerodynamics of an isolated road wheel. In *Proceedings of the Second AIAA Symposium of Aerodynamics of Sports and Competition Automobiles, Los Angleles, California, USA*, , vol. 11, pp. 119–125.

FILIPPOVA, OLGA & HÄNEL, DIETER 1998 Grid refinement for lattice-bgk models. *Journal of Computational physics* **147** (1), 219–228.

Frisch, Uriel, Hasslacher, Brosl & Pomeau, Yves 1986 Lattice-gas automata for the navier-stokes equation. *Physical review letters* **56** (14), 1505.

Fuller, Joshua & Passmore, Martin A 2014 The importance of rear pillar geometry on fastback wake structures. *Journal of Wind Engineering and Industrial Aerodynamics* **125**, 111–120.

Grandemange, M, Gohlke, M & Cadot, O 2013*a* Bi-stability in the turbulent wake past parallelepiped bodies with various aspect ratios and wall effects. *Physics of Fluids* **25** (9), 095103.

Grandemange, M., Gohlke, M. & Cadot, O. 2013*b* Turbulent wake past a three-dimensional blunt body. part 1. global modes and bi-stability. *J. Fluid Mech.* **722**, 51–84.

Grandemange, Mathieu, Gohlke, Marc & Cadot, Olivier 2014 Turbulent wake past a three-dimensional blunt body. part 2. experimental sensitivity analysis. *Journal of Fluid Mechanics* **752**, 439–461.

Grandemange, Mathieu, Mary, Axel, Gohlke, Marc & Cadot, Olivier 2013*c* Effect on drag of the flow orientation at the base separation of a simplified blunt road vehicle. *Experiments in fluids* **54** (5), 1529.

Gulyás, András, Bodor, Ágnes, Regert, Tamas & Jánosi, Imre M 2013 Piv measurement of the flow past a generic car body with wheels at les applicable reynolds number. *International Journal of Heat and Fluid Flow* **43**, 220–232.

Heft, Angelina 2014 Aerodynamic investigation of the cooling requirements of electric vehicles. PhD thesis, Technische Universität München.

Heyder-Bruckner, Jacques 2011 The aerodynamics of an inverted wing and a rotating wheel in ground effect. PhD thesis, University of Southampton.

Hobeika, Teddy & Sebben, Simone 2018 Cfd investigation on wheel rotation modelling. *Journal of Wind Engineering and Industrial Aerodynamics* **174**, 241–251.

Hobeika, Teddy, Sebben, Simone & Landström, Christoffer 2013 Investigation of the influence of tyre geometry on the aerodynamics of passenger cars. *SAE International Journal of Passenger Cars-Mechanical Systems* **6** (1), 316–325.

Howell, JP 1994 The influence of ground simulation on the aerodynamics of simple car shapes with an underfoor diffuser. In *RAes Conference on Vehicle Aerodynamics*, pp. 36–1.

Hucho, W. H. & Sovran, G. 1993 Aerodynamics of road vehicles. *Ann. Rev. Fluid. Mech.* **25**, 485–537.

Huminic, Angel & Huminic, Gabriela 2017 Aerodynamic study of a generic car model with wheels and underbody diffuser. *International Journal of Automotive Technology* **18** (3), 397–404.

IPCC 2018 IPCC special report on global warming of 1.5^o C. `http://www.ipcc.ch/report/sr15/`.

JAKIRLIC, SUAD, KUTEJ, LUKAS, HANSSMANN, DANIEL, BASARA, BRANISLAV & TROPEA, CAMERON 2016 Eddy-resolving simulations of the notchback ‘drivaer’model: Influence of underbody geometry and wheels rotation on aerodynamic behaviour. *Tech. Rep.*. SAE Technical Paper.

JOWSEY, LYDIA 2013 An experimental study of automotive underbody diffusers. PhD thesis, © Lydia Jowsey.

KATZ, JOSEPH 1995 Race car aerodynamics. *Robert Bentley* .

KNOWLES, ROBIN DAVID 2007 Monoposto racecar wheel aerodynamics: investigation of near-wake structure and support-sting interference .

KOITRAND, SOFIE & REHNBERG, SVEN 2013 A computational investigation of wheel and underbody flow interaction.

KRAJNOVIÄ, SINIĹA & DAVIDSON, LARS 2005 Flow around a simplified car, part 2: understanding the flow. *Journal of Fluids Engineering* **127** (5), 919–928.

KRAJNOVIĆ, SINIŠA & DAVIDSON, LARS 2005 Influence of floor motions in wind tunnels on the aerodynamics of road vehicles. *Journal of wind engineering and industrial aerodynamics* **93** (9), 677–696.

KRAJNOVIĆ, SINISA, SARMAST, SASAN & BASARA, BRANISLAV 2010 Les of the flow around a generic wheel in a wheelhouse. In *ASME 2010 3rd Joint US-European Fluids Engineering Summer Meeting collocated with 8th International Conference on Nanochannels, Microchannels, and Minichannels*, pp. 2681–2692. American Society of Mechanical Engineers.

KRENTEL, DANIEL, MUMINOVIC, RIFET, BRUNN, ANDRÉ, NITSCHE, WOLFGANG & KING, RUDIBERT 2010 Application of active flow control on generic 3d car models. In *Active flow control II*, pp. 223–239. Springer.

KROOK, PL BHATNAGAR-EP GROSS-M, BHATNAGAR, PL & GROSS, EP 1954 A model for collision processes in gases. *Phy. Rev* **94**, 511–524.

KUTHADA, TIMO & WIEDEMANN, JOCHEN 2008 Investigations in a cooling air flow system under the influence of road simulation. *Tech. Rep.*. SAE Technical Paper.

LANDSTRÖM, C, JOSEFSSON, L, WALKER, T & LÖFDAHL, L 2011*a* An experimental investigation of wheel design parameters with respect to aerodynamic drag. In *8th FKFS Conference*.

LANDSTRÖM, CHRISTOFFER, LÖFDAHL, LENNART & WALKER, TIM 2009 Detailed flow studies in close proximity of rotating wheels on a passenger car. *SAE International Journal of Passenger Cars-Mechanical Systems* **2** (2009-01-0778), 861–874.

LANDSTRÖM, CHRISTOFFER, SEBBEN, SIMONE & LÖFDAHL, LENNART 2010 Effects of wheel orientation on predicted flow field and forces when modelling rotating wheels using cfd. In *8th MIRA International Vehicle Aerodynamics Conference*.

LANDSTRÖM, CHRISTOFFER, WALKER, TIM, CHRISTOFFERSEN, LASSE & LÖFDAHL, LENNART 2011*b* Influences of different front and rear wheel designs on aerodynamic drag of a sedan type passenger car. *Tech. Rep.*. SAE Technical Paper.

Latt, Jonas 2007 Hydrodynamic limit of lattice boltzmann equations. PhD thesis, University of Geneva.

Lévêque, Emmanuel, Toschi, Federico, Shao, Liang & Bertoglio, J-P 2007 Shear-improved smagorinsky model for large-eddy simulation of wall-bounded turbulent flows. *Journal of Fluid Mechanics* **570**, 491–502.

Li, Ruiying 2017 Aerodynamic drag reduction of a square-back car model using linear genetic programming and physic-based control. PhD thesis, ISAE-ENSMA Ecole Nationale Supérieure de Mécanique et d'Aérotechique-Poitiers.

Li, Yanbing, Shock, Richard, Zhang, Raoyang & Chen, Hudong 2004 Numerical study of flow past an impulsively started cylinder by the lattice-boltzmann method. *Journal of Fluid Mechanics* **519**, 273–300.

Littlewood, Rob & Passmore, Martin 2010 The optimization of roof trailing edge geometry of a simple square-back. *Tech. Rep.*. SAE Technical Paper.

Littlewood, Rob, Passmore, Martin & Wood, Daniel 2011 An investigation into the wake structure of square back vehicles and the effect of structure modification on resultant vehicle forces. *SAE International Journal of Engines* **4** (2), 2629–2637.

Littlewood, RP & Passmore, Martin A 2012 Aerodynamic drag reduction of a simplified squareback vehicle using steady blowing. *Experiments in fluids* **53** (2), 519–529.

Lucas, J-M, Cadot, O, Herbert, V, Parpais, S & Délery, J 2017 A numerical investigation of the asymmetric wake mode of a squareback ahmed body–effect of a base cavity. *Journal of Fluid Mechanics* **831**, 675–697.

Mack, Oliver 2003 The non-linearity of piezoelectric force transducers and their analytical modelling. In *Proceedings of the 17th World Conference–Metrology in the 3rd Millenium*, pp. 22–27.

Marklund, Jesper & Lofdahl, Lennart 2012 Influence of a diffuser to the wake flow of a passenger car. In *ASME 2012 Fluids Engineering Division Summer Meeting collocated with the ASME 2012 Heat Transfer Summer Conference and the ASME 2012 10th International Conference on Nanochannels, Microchannels, and Minichannels*, pp. 53–62. American Society of Mechanical Engineers.

McArthur, Damien, Burton, David, Thompson, Mark & Sheridan, John 2016 On the near wake of a simplified heavy vehicle. *Journal of Fluids and Structures* **66**, 293–314.

McManus, James & Zhang, Xin 2006 A computational study of the flow around an isolated wheel in contact with the ground. *Journal of Fluids Engineering* **128** (3), 520–530.

Mears, AP, Crossland, SC & Dominy, RG 2004 An investigation into the flow-field about an exposed racing wheel. *Tech. Rep.*. SAE Technical Paper.

Mlinaric, Peter 2007 *Investigation of the influence of tyre deformation and tyre contact patch on CFD predictions of aerodynamic forces on a passenger car*. Chalmers tekniska högskola.

Morelli, A 1969 Aerodynamic effects on an automobile wheel. *ATA Rev* **22** (6), 281–288.

Morelli, Alberto 2000 A new aerodynamic approach to advanced automobile basic shapes. *Tech. Rep.*. SAE Technical Paper.

Nakashima, Takuji, Tsubokura, Makoto, Nouzawa, Takahide, Nakamura, Takaki, Zhang, Huilai & Oshima, Nobuyuki 2008 Large-eddy simulation of unsteady vehicle aerodynamics and flow structures. In *BBAA VI International Colloquium-2008, Honoshima Univ., Division of Mechanical and Space Engineering*.

Österh, J., Noack, B. R., Krajnović, S., Barros, D. & Borée, J. 2014 On the need for a nonlinear subscale turbulence term in pod models as exemplified for a high-reynolds-number flow over an ahmed body. *J. Fluid Mech.* **747**, 518–544.

Passmore, MA & Le Good, GM 1994 A detailed drag study using the coastdown method. In *IMechZ Autotech Congress*.

Patel, VC & Sotiropoulos, F 1997 Longitudinal curvature effects in turbulent boundary layers. *Progress in Aerospace Sciences* **33** (1-2), 1–70.

Pavia, Giancarlo & Passmore, Martin 2017 Characterisation of wake bi-stability for a square-back geometry with rotating wheels. In *FKFS Conference*, pp. 93–109. Springer.

Peng, Chen 2011 The lattice boltzmann method for fluid dynamics: theory and applications. *M. Math, Department of Mathematics, Ecole Polytechnique Federale de Lausanne* .

Perry, Anna-Kristina & Passmore, Martin 2013 The impact of underbody roughness on rear wake structure of a squareback vehicle. *Tech. Rep.*. SAE Technical Paper.

Perry, Anna-Kristina, Passmore, Martin & Finney, Ashley 2015 Influence of short rear end tapers on the base pressure of a simplified vehicle. *SAE International Journal of Passenger Cars-Mechanical Systems* **8** (2015-01-1560), 317–327.

Perry, Anna-Kristina, Pavia, Giancarlo & Passmore, Martin 2016 Influence of short rear end tapers on the wake of a simplified square-back vehicle: wake topology and rear drag. *Experiments in Fluids* **57** (11), 169.

Perzon, Sven & Davidson, Lars 2000 On transient modeling of the flow around vehicles using the reynolds equation. In *International Conference on Applied Computational Fluid Dynamics (ACFD) Beijing China*, pp. 720–727.

Pfadenhauer, M, Wickern, G & Zwicker, K 1996 On the influence of wheels and tyres on the aerodynamic drag of vehicles. In *MIRA International Conference on Vehicle Aerodynamics*.

PIRELLI 2018 F1 tires range. `https://www.pirelli.com/tires/en-us/motorsport/homepage-f1/`.

Pirozzoli, Sergio, Orlandi, Paolo & Bernardini, Matteo 2012 The fluid dynamics of rolling wheels at low reynolds number. *Journal of Fluid Mechanics* **706**, 496–533.

Purvis, AR 2003 The wake behind a deformable racing tyre. PhD thesis, MSc thesis, Cranfield University.

Qian, YH & Orszag, SA 1993 Lattice bgk models for the navier-stokes equation: Nonlinear deviation in compressible regimes. *EPL (Europhysics Letters)* **21** (3), 255.

Regert, Tamas & Lajos, Tamas 2007 Description of flow field in the wheelhouses of cars. *International Journal of Heat and Fluid Flow* **28** (4), 616–629.

Roshko, Andrey 1993 Perspectives on bluff body aerodynamics. *Journal of Wind Engineering and Industrial Aerodynamics* **49** (1-3), 79–100.

Rossitto, Giacomo 2016 Influence of afterbody rounding on the aerodynamics of a fastback vehicle. PhD thesis, Chasseneuil-du-Poitou, Ecole nationale supérieure de mécanique et d'aérotechnique.

Rossitto, Giacomo, Sicot, Christophe, Ferrand, Valérie, Borée, Jacques & Harambat, Fabien 2016 Influence of afterbody rounding on the pressure distribution over a fastback vehicle. *Experiments in Fluids* **57** (3), 43.

Roumeas, Mathieu, Gilliéron, Patrick & Kourta, Azeddine 2009 Analysis and control of the near-wake flow over a square-back geometry. *Computers & Fluids* **38** (1), 60–70.

Sprot, Adam Joseph 2013 Open-wheel aerodynamics: effects of tyre deformation and internal flow. PhD thesis, Durham University.

Succi, Sauro & Succi, Sauro 2001 *The lattice Boltzmann equation: for fluid dynamics and beyond*. Oxford university press.

Thivolle-Cazat, Emmanuelle & Gilliéron, Patrick 2006 Flow analysis around a rotating wheel. In *13th Int. Symposium on Applications of Laser Techniques to Fluid Mechanics, Lisbon, Portugal*, pp. 26–29. Citeseer.

Tsubokura, Makoto, Kobayashi, Toshio, Nakashima, Takuji, Nouzawa, Takahide, Nakamura, Takaki, Zhang, Huilai, Onishi, Keiji & Oshima, Nobuyuki 2009 Computational visualization of unsteady flow around vehicles using high performance computing. *Computers & Fluids* **38** (5), 981–990.

Wagner, Alexander J 2008 A practical introduction to the lattice boltzmann method. *Adt. notes for Statistical Mechanics* **463**, 663.

Wäschle, Alexander 2006 *Numerische und experimentelle Untersuchung des Einflusses von drehenden Rädern auf die Fahrzeugaerodynamik*. expert Verlag.

Wäschle, Alexander 2007 The influence of rotating wheels on vehicle aerodynamics-numerical and experimental investigations. *Tech. Rep.*. SAE Technical Paper.

Wäschle, Alexander, Cyr, Stephane, Kuthada, Timo & Wiedemann, Jochen 2004 Flow around an isolated wheel-experimental and numerical comparison of two cfd codes. *Tech. Rep.*. SAE Technical Paper.

Wassen, Erik, Eichinger, Sándor & Thiele, Frank 2010 Simulation of active drag reduction for a square-back vehicle. In *Active Flow Control II*, pp. 241–255. Springer.

Wickern, Gerhard & Lindener, Norbert 2000 The audi aeroacoustic wind tunnel: Final design and first operational experience. *Tech. Rep.*. SAE Technical Paper.

Wiedemann, Jochen 1996 The influence of ground simulation and wheel rotation on aerodynamic drag optimization-potential for reducing fuel consumption. *Tech. Rep.*. SAE Technical Paper.

WITTMEIER, FELIX, WIDDECKE, NILS, WIEDEMANN, JOCHEN, LINDENER, NORBERT & ARMBRUSTER, RENE 2013 Reifenentwicklung unter aerodynamischen aspekten. *ATZ-Automobiltechnische Zeitschrift* **115** (2), 144–150.

XFLOW 2010 Aerodynamic analysis involving moving parts with xflow. *Tech. Rep.*.

Experimental study of wheel-vehicle aerodynamic interactions

The thesis aims to provide a better understanding of the wheel-vehicle interaction, via experimental investigations on a 2/5-th scale vehicle with an underbody diffuser and 2/5-th scale wheels equipped with Michelin tires. The vehicle geometry, based on ASMO model, was modified prior to the PhD work, in order to achieve a reasonable front wheel yaw angle, and a realistic wake balance with four rotating wheels. It is the baseline configuration in the scope of this work.

The findings demonstrate that the well-balanced wake of the baseline configuration can be easily modified by different wheel states or tire modifications, especially at the rear axle. This results from a global effect of the underbody momentum modifications, i.e. a high wake sensitivity to the underbody flow. On the contrary, when the vehicle mean wake develops into a non-balanced topology, it is more robust towards underbody perturbations such as different wheel states or tire modifications. By eliminating four wheels or front wheels, the underbody momentum flux is vastly increased; by eliminating the underbody diffuser, which is a vehicle geometry modification, the underbody momentum flux is significantly reduced. In these two circumstances, one can observe a robust downwash from the roof, independent of the wheel states or tire modifications.

Besides, there is a more local effect of the wheels near wakes on the aerodynamic lift and drag of the vehicle. Low pressure regions in the underbody downstream the front wheels have an effect on vehicle lift. The rear wheels impose pressure conditions on the vehicle base, influencing the vehicle drag. Particularly, the merging of non-closed mean wakes of the rear wheels with the vehicle wake can give rise to strong penalty in vehicle drag.

Key words: Motor vehicles—Tires, Automobiles—Aerodynamics, Wakes (Aerodynamics), Drag (Aerodynamics), Lift (Aerodynamics), Turbulence

Etude des interactions aérodynamiques roue-véhicule

L'objet de la thèse est de mieux comprendre l'interaction entre la roue et le véhicule, à travers des expérimentations sur une maquette à l'échelle 2/5ième équipée d'un diffuseur et de pneus Michelin. La géométrie du véhicule, basée sur le modèle ASMO, a été modifiée précédemment à ce travail afin d'obtenir un angle d'attaque de l'écoulement sur les roues avant et un équilibre du sillage réaliste en présence de quatre roues tournantes. Cette configuration a servi de référence dans le cadre de cette étude.

Il a été mis en évidence que la configuration de base avec un sillage équilibré peut facilement être modifiée d'un point de vue aérodynamique en changeant l'état des roues (en rotation ou pas) et le type de pneumatique, en particulier sur l'essieu arrière. Cela provient d'un effet global et d'une sensibilité importante de l'équilibre du sillage aux changements de débit au soubassement. A contrario, lorsque le sillage du véhicule se trouve déséquilibré, il devient plus robuste par rapport à des perturbations de soubassement comme un changement d'état des roues ou une modification des pneumatiques. Si l'on supprime les quatre roues ou uniquement les deux roues avant, le débit de quantité de mouvement au soubassement est grandement augmenté. Par contre, si l'on supprime le diffuseur (changement important de la géométrie du véhicule), celui-ci s'en trouve nettement réduit. Dans ces deux configurations, le sillage est très fortement déséquilibré vers le sol et devient indépendant aux modifications apportées sur les roues.

Il a également été mis en évidence un effet plus local du sillage des roues sur la portance et la traînée du véhicule. En effet, la zone de dépression dans le sillage des roues avant a un effet sur la portance alors que le sillage des roues arrière pilote en partie la pression au culot et donc la traînée. Il a ainsi été observé une augmentation importante de la traînée du véhicule lorsque le sillage des roues arrière, non fermé, venait en interaction directe avec le sillage du véhicule.

Mots clés: Véhicules automobiles—Pneus, Automobiles—Aérodynamique, Sillage (aérodynamique), Traînée (aérodynamique), Portance (aérodynamique), Turbulence